Waste Cassava Peel and Almond Hull Valorisation via Microwave Processing: A Source of Chemicals, Materials and Bioenergy

Allyn Pramudya Sulaeman

Doctor of Philosophy

University of York

Chemistry

March 2020

"To get the truth,

we cannot blame the wrong because we get the truth from mistakes."

(Allyn)

Abstract

Unavoidable food supply chain wastes are an under-utilised source of renewable materials, chemicals and (bio)energy. This thesis investigates the microwave processing (both conventional pyrolysis and hydrothermal) of waste cassava peel (CP) and almond hull (AH) as a source of microfibrilated celluloses (MFCs) (materials), sugars and bio-oil (chemicals) and biochar (bio-energy). Particular focus is given to the production of MFC and their application as adsorbents for Cr(VI) and methylene blue (MB) remediation.

A range of MFC's was prepared via acid-free hydrothermal microwave processing at different temperatures (120, 170 and 220 ^{o}C) of both virgin CP or AH and their residue from pretreatment with either ethanol or heptane. ATR-IR, TGA, XRD, solid-state ^{13}C CPMAS NMR, zeta potential, HPLC, CHN, TEM and SEM analyses were performed to ascertain structural changes in the production of MFCs. Significant changes were seen between MFCs processed at 170 ^{o}C with respect to 220 ^{o}C, *i.e*. significant increases in the Crystallinity Index, thermal decomposition by TGA and visual darkening of the materials synonymous with the leaching of amorphous cellulose and possible pyrolytic processes. AH MFCs presented excellent hydrogel and film forming capabilities.

CP MFC (CP 220 ^{o}C-30 minutes) was shown to have superior performance in the adsorption of Cr (VI) reaching 180.73 mg/g via ultrasound treatment at pH 2. However, in the uptake of MB, CP MFC (CP120 ^{o}C-30 minutes) had a superior performance (199.06 mg/g). It was found that for both MFCs, the kinetic processes can be accurately predicted by *pseudo*-second order rate kinetics.

Bio-oil produced via the microwave pyrolysis of AH had a high heating value of 34.37 MJ/kg whilst char derived from CP gave a value 25.64 MJ/kg by bomb calorimetry, indicating that both have potential as alternative biofuels.

List of Contents

List of Tables

List of Figures

Acknowledgements

Firstly and foremost, I would like to express my deep gratitude to my supervisor, Dr Avtar Matharu, for continuous support for my PhD study. His suggestion, wise and fatherly guidance motivated me to finish this research within four years.

My sincere thanks also go to Dr Javier Remòn Nunez for introducing me to the almond hull and Dr Eduardo Melo for sharing knowledge about nanocellulose, and all the staff of GCCE and technicians; Dr Hannah Briers, Dr Tom Dugmore, Dr Richard Gammons and Paul Elliott, who promotes pleasant working atmosphere and makes me welcomed as a family.

Many thanks to my supportive Green Chemistry fellows for discussions and friendship we have had in the last four years; Thank you very much to Andrew J. Maneffa for proof-reading the thesis, Yang Gao, Jaspreet Kaur, Iris Yu, Yann Lie, Zia Chowdhury, Amadou Oumarou, Hao Xia, Chaiwat Ngasan, Roxana Milescu, Alisa Doroshenko, Konstantina Sotiriou.

Financially, I would like to thank Lembaga Pengelola Dana Pendidikan (LPDP) scholarship, Ministry of Finance, Indonesia, for giving me this opportunity.

Last but not least, I would like to thank my parents, Tati Sutarsih and Sulaeman, for supporting me spiritually from Indonesia and my family, Dina, Laudi, Ravel, Raes who always patience facing this life together.

Thank you all. May God always bless you.

Declaration

I declare that this thesis is a presentation of original work, and I am the sole author. This work has not previously been presented for an award at this, or any other, University. All sources are acknowledged as *References.*

Collaboration	Sections	Collaborator	Institution
MFCs production	3.2.1	Dr Eduardo Melo Dr Javier Remon Nuñez	University of York
Electron spectroscopy	3.2.6	Dr Meg Stark	University of York
CHN analysis	3.1.2	Dr Graeme McAllister	University of York
HPLC analysis	3.2.8	Dr Hannah Briers Dr Richard Gammons	University of York
Zeta potential	3.2.9	Dr Buthaina Albanyan	University of York
XPS analysis	3.3.2.2	Dr David Morgan	Cardiff University
^{13}C CP-MAS NMR	3.2.5	Dr Heather Fish	University of York

Chapter 1: Introduction

1.1 Food Waste: A Modern-Day Dilemma

The inefficiency in the food system from farm to fork generates approximately 1.3 billion tonnes per year in food waste (both avoidable and unavoidable).[1,2] Food waste accounts for almost $936 billion in economic loss notwithstanding negative environmental, and social impact.[3,4] Figure 1.1 shows the farm to fork supply chain with the type of losses incurred.[5] In the UK alone, the Waste and Resources Action Programme (WRAP) reported that households contributed to 70% of food waste (6.6 million tonnes) besides manufacturing, retail, and HRI (hotel, restaurant and institution). One-fifth of the total household food waste was classified unavoidable and valued at approximately £14 billion.[6]

Greenhouse gas (GHG) emissions produced from food production, food waste and the uncontrolled expansion in land use are significant contributors to climate change. Climate change has a significant impact on topsoil nutrient depletion and land use, as the second-largest natural carbon sink from the atmosphere after the ocean.[7] GHG emissions such as methane (CH_4) and nitrous oxide (N_2O), dominate at the farm stages (fertiliser use and anaerobic soil process) while carbon dioxide (CO_2) emissions arise from burning inedible materials or use of fossil fuel-driven farm machinery. The GHG emissions contribution along the supply chain (fertiliser manufacture, planting, processing, distribution, consumption stages and waste disposal) are estimated at about 19-29% (9100-16900 $MtCO_2$ equivalent/year) of the total global emission.[8,9] Unsustainable global food supply also indirectly impacts the availability of freshwater, oceans, forestry, biodiversity and ecosystems.[10]

Strategies for reducing unavoidable and avoidable food waste need identifying and implementing where waste reduction and recycling are a global obligation. Educating consumers and retailers, proper management practices, excellent transport, logistics and storage, and efficient technologies to reduce and recycling waste are some examples to reduce food waste.[11] Based on the food waste hierarchy, namely: prevention; recycling; recovery, and; disposal, the recovery often implies waste to energy either via incineration or anaerobic digestion.[12]

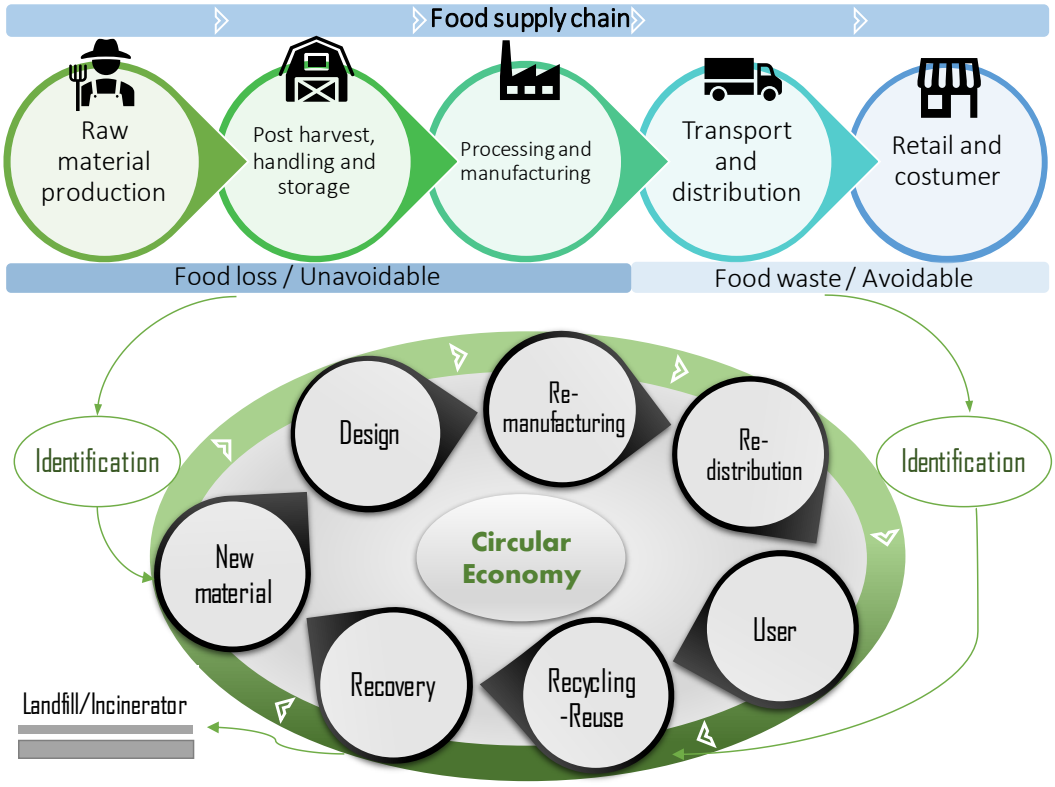

Figure 1. 1 Food supply chain in the circular economy concept [5] (original in colour)

Committing to Courtauld 2025 food waste prevention program, the UK aims to be a pioneer by launching the first food waste reduction roadmap in the world. The roadmap will target a 20% reduction in food waste equating to £20 billion to the UK economy by 2025.[13] This program strengthens the development of a circular economy (see Figure 1.1)

and meets the Agenda 2030 Sustainable Development Goal (SDG) 12.3, "to halve, per capita, food waste at the retail and consumer level, and reducing food losses as well as production and supply chains including post-harvest losses by 2030" .[14] Implementing their Sustainable Food Program and EU Food Policy, the food manufacturing sector will reduce carbon emissions, use less water and reduce waste. Furthermore, EU food and drink policy must maintain the global need (between customer satisfaction and global market competitiveness) whilst focusing on the innovation (R & D) and sustainable ecosystem.[15,16]

Adaptation of circular economy concept represents the best platform for mitigating negative environmental impact such as, GHG emissions and squandering wastage of natural resources from the food supply chain.[17] The circular economy offers an efficient and effective use of natural resources.[18] The Paris Agreement in 2015 highlighted reinforcing a global response combating climate change toward a low-carbon circular economy.[18,19] According to the EC, a circular economy maintains product value as long as possible in order to reduce the waste until it cannot be used again. The main principle of the circular economy is to maintain and tighten the circle by continuing recirculating resources.[20]

The circular economy concept constructs in our mind to raise responsibility and awareness of scarce natural resources and excessive exploitation. Transformation into a bioeconomy with high-efficiency on consumption and production of material can address global issues in the future, such as population growth, natural resources, fossil depletion and climate change.[21] The key challenge for running the model is an assessment platform with a multi-dimensional indicator and the creation of benefits from the efficiency use of resources that can be felt by all the collaborative parties. Commitment to circular, closed-

loop principles, the food security system helps to strengthen sustainable agricultural resources and food chain system. [22–24] Thus, food waste is a global, highly topical, modern-day dilemma because of its negative economic, environmental and social impact. Our current food supply chain is often linear, *i.e.* from the cradle to the grave (C2G), where considerable resources are lost.[25] A change to a circular economy is required where the resources are retained. In the case of food waste, we need to explore its valorisation into chemicals, materials and (bio)energy.

1.2 Prospective Food Waste

1.2.1 Opportunities from cassava peel waste

Cassava (*Manihot esculenta Crantz*) is one of Indonesia's main commodities widely grown to produce tapioca flour (tapioca starch) for traditional food, sweet pudding, glucose syrup, chips and as a thickening ingredient.[26] The chemical composition of cassava peel is 4.88% cellulose, 11.9% hemicellulose, 3.62% lignin, 4.85% crude protein [27], 51.93% starch, 8.73% moisture and 3.27% ash[28]. Cassava is a reliable traditional crop for food security, especially in Asia and Africa, with low energy production per hectare.[29] The advantage of cassava plantation is its adaptability and tolerance in areas with low nutrient soils, poor soil fertility, arid soils and pest and disease resistance.[29,30] The mature root can retain nutritional value without water for a long period.[31] In 2018, the global production of cassava amounted to 277 million tonnes (fresh root equivalent), with Nigeria, Thailand and Indonesia being the top three producers.[32] Thus, as cassava is widely grown and processed (peeled and chopped), its peel has the potential to be an important natural resource for

chemical, materials and (bio)energy enabling to the development of bio-based circular economies.

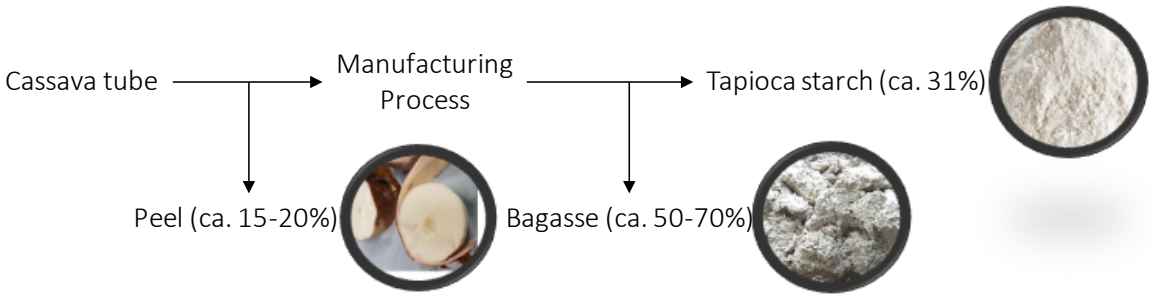

Figure 1. 2 Manufacturing process of cassava starch (original in colour)

Cassava peel represents approximately 15% to 20% of the tuber and the residual bagasse from starch production is around 50-70 % (see Figure 1.2).[33,34] The main process of the cassava industry is the extraction of cassava into white tapioca flour, and other industries widely use starch for other products such as in bioethanol, adhesive (glue) production, animal feed coating, paper and textile yarn.[29] Besides the peel product generated from the starch industry, the residual fibre material from the extraction starch process can be used for bioethanol or cattle feed.[35]

Cassava waste used to be as a substitute for maise in animal diet. However, cassava tuber and peel waste cannot be added directly to the animal meal because of high levels of glucocyanide (400 mg/kg). The drying process is the most common method to decrease cyanide content. Alternatively, fermentation or cooking and frying can remove the HCN content.[36] Both cassava tuber and peel have low protein content, approximately 3.6 and 5.5 %, respectively. Interestingly the leaves possess around 21% protein.[36]

The tuber is starch-rich (31% of fresh weight).[37] A mixture of cassava starch with hot water has a chewy, smooth and elastic texture with a translucent appearance.[38] Cassava

starch comprises 17 % amylose and 83 % amylopectin. However, cassava starch is also highly resistant because it is folding of the amylopectin and amylose branches coupled with hydrogen bonding. Thus, cassava starch is more resistant in the intestine digestion.[36] Cassava starch could be an appropriate option for gluten-free patients.[39]

1.2.2 Opportunities from almond hull waste

The world demand for tree nuts, especially almonds, continues to rise year after year, favourable for its taste and nutritional density, lipid profile, vitamin E and polyphenol content.[40] In 2019, the United States - led global almond production (80% market share), followed by the European Union and Australia.[41,42] The processing of almond crops contributes to the production of 1.4 million tonnes of almond by-products per year, including shells, hulls, pruning waste, leaves, skin, and inedible kernel.[43]

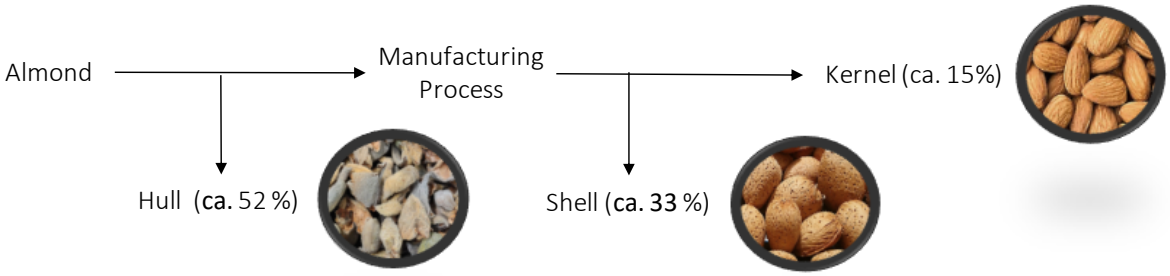

Figure 1. 3 Manufacturing process of almond production (original in colour)

As shown in Figure 1.3, during the processing of almonds the kernel, shell and hull represent 15%, 33% and 52%, respectively.[44] The latter (hull) is unavoidable and has the potential to be a value-added renewable material due to its high content of sugar (18-30%), cellulose (21-35%), lignin (7-15%) and other valuable organic compounds.[45,46] At present, the almond hull by-product from the hulling process is often used as an animal feed substitute for alfalfa or corn and not valorised to any great extent.[47]

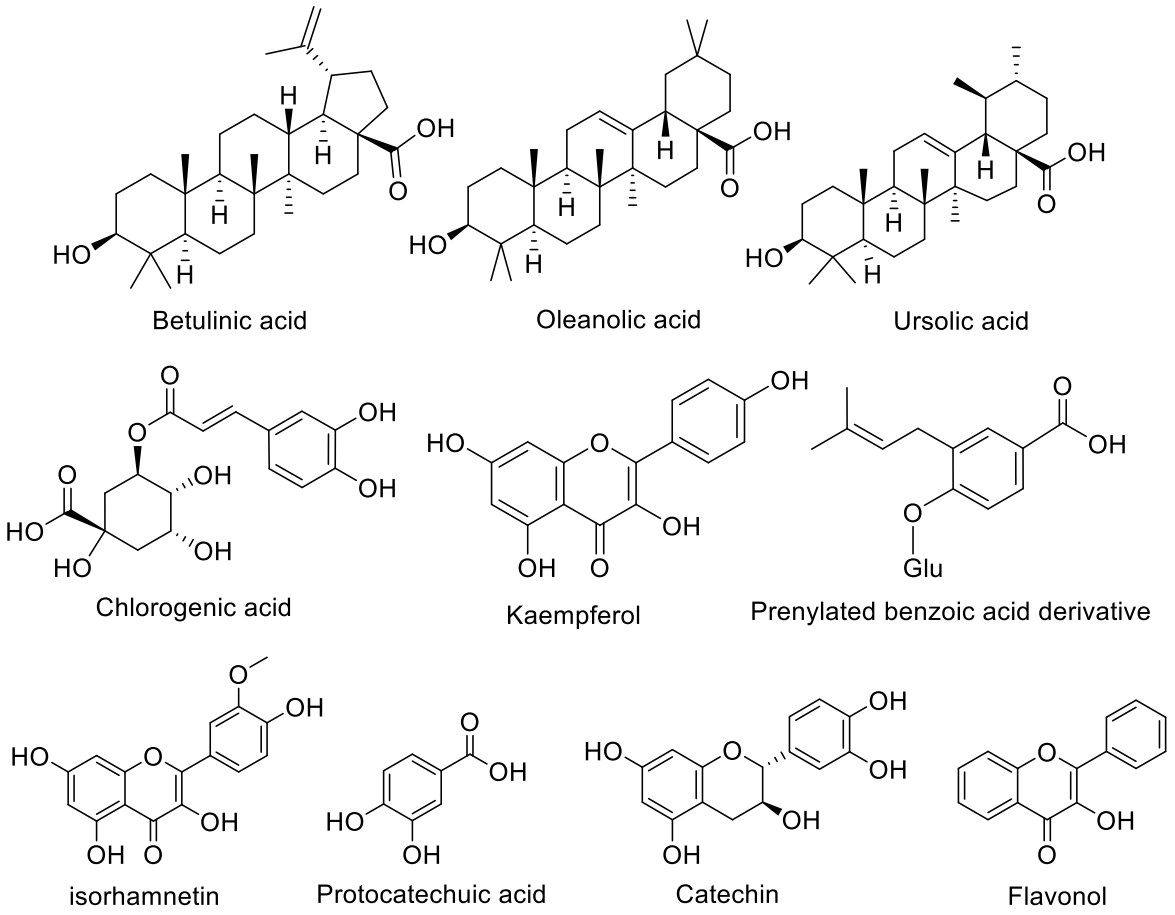

Figure 1. 4 Chemical structures found in the almond hull

Almond hulls (*Prunus amygdalus*) are abundant series of polyphenols and sterol-like compounds (see Figure 1.4) such as betulinic acid, oleanolic acid, ursolic acid, flavonol, flavonol glycosides, chlorogenic acid, kaempferol, isorhamnetin, protocatechuic acid, catechin, and prenylated benzoic acid derivative (3-prenyl-4-*O*-β-D-glucopyranosyloxy-4-hydroxylbenzoic acid).[48–50] Almond hulls are used as a bioenergy source in the manufacturing plant itself; however, their calorific value is relatively low, ranging between 16-18 MJ/kg.[51]

1.3 Cellulose and Nanocellulose

Cellulose is a semi-crystalline polysaccharide composed of a linear chain of β-D-glucopyranose units linked each other by β-(1-4)-glycosidic bonds (Figure 1.5) Cellulose is hydrophobic because of extensive inter-and intramolecular hydrogen bonding.[52–54]

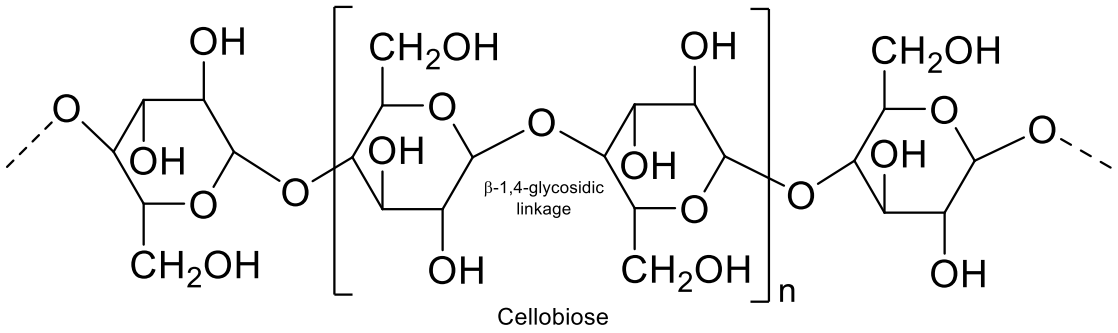

Figure 1. 5 Cellulose structure

Cellulose comprises both crystalline and amorphous region (see Figure 1.6). There are four different cellulose polymorphs: Cellulose I, is native cellulose that exists in two types allomorphic I_α and I_β; Cellulose II, also known as regenerated cellulose, is from NaOH solution treatment of cellulose I. Cellulose II is the most stable form of crystalline cellulose and has inter-sheet hydrogen bonding in antiparallel strands whereas cellulose I has a parallel direction; Cellulose III, is obtained by ammonia treatment of cellulose I and II, and; Cellulose IV, extracted from modified cellulose III with glycerol at high temperatures.[55]

Chemical pretreatment of cellulose fibres has a major impact on the fibre network as it causes hydrogen bonds to break, allows hydroxyl groups to be more accessible and improves reactivity for the next hydrolysis step.[56] The hierarchical defibrillation process of natural fibres using top-down destruction enables the production of micro- and nano-

cellulose. A wide variety of methods, including chemical treatment, enzyme treatment, and physical treatment allow for nanofibrillated cellulose (NFC) isolation from the cellulosic materials (Figure 1.7). Chemical treatments such as alkaline-acid treatment, 2,2,6,6-tetramethylpiperidine-1-oxyl radical (TEMPO) oxidation, enzymatic hydrolysis and ionic liquids facilitate the accessibility of hydroxyl groups, increase the internal surface of cellulose fibres improve crystallinity, and break cellulose hydrogen bonds, resulting in increased fibre reactivity.[57] There are a range of physical methods for transforming cellulose to nanocellulose, such as homogenisation, steam explosion, microfluidization, grinding, cryocrushing, microwave and ultrasound.[58]

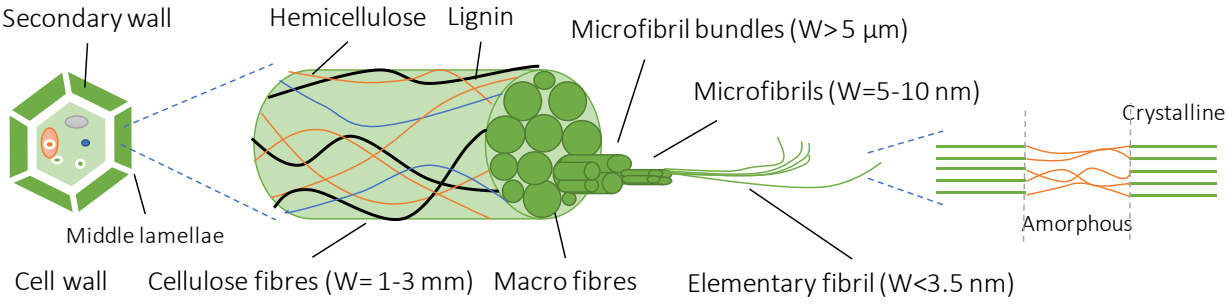

Figure 1. 6 Macro- and micro-cellulose [59] (original in colour)

Cellulose nanocrystals (CNCs) are typically made using acid hydrolysis of water-dispersed cellulosic materials where the length and diameter of CNCs usually range from 200–500 nm in length to 3–35 nm in diameter. Cellulose nanofibril (CNFs) are long and strong network fibrils (µm) with a nanometer range of diameter usually formed through mechanical or physical processes, but it possible through a chemical process to produce individual fibril with TEMPO method.[58,60] Bacterial cellulose (BC) is formed from the primary extracellular metabolite by bacteria such as *Acetobacter xylinum* secreting a ribbon-shaped fibril, smaller than 100 nm long, consisting of 2–4 nm diameter nanofibrils. [61]

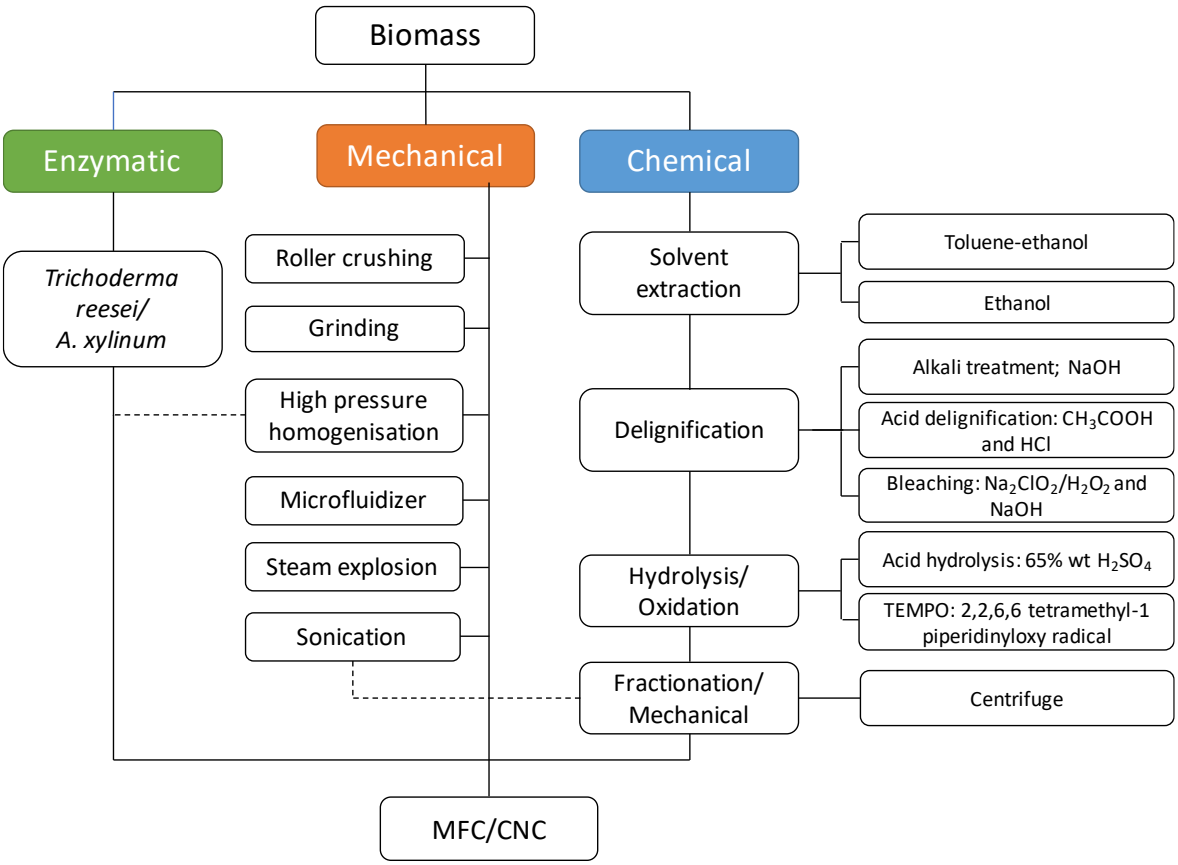

Figure 1. 7 Several methods to obtain nanocellulose (Original in colour)

In 1983, the term of microfibrillated cellulose (MFC) was introduced Turbak *et al*.[62], to describe a smooth and stable gel product of wood cellulose pulp (2% w/v suspension of microfibrilated cellulose) widely used as an emulsifier in food, paint, emulsion and cosmetics. In contrast to CNCs, MFC consists of long, flexible and entangled nanofibers containing both amorphous and crystalline forms.[63] MFCs exhibit more water-retention capability, shear-thinning (*pseudo*plasticity), high viscosity and yield stress after homogenisation. The microfibrils have strong entanglement to each other forming networks at low concentration due to the high aspect ratio of the fibres. [64,65]

1.4 Microwave as heat generation

The use of microwaves offers several advantages over conventional heating, such as rapid and selective heating, providing internal heating from substances, shorter reaction time, and controllable stop/start.[66] Heat transfer via microwave irradiation (usually at the frequency of 915 MHz and 2.45 GHz) to materials causes kinetic molecular movement of the alternating electrical field compartment of migration of the ionic species (conduction mechanism) or dipolar species (dipolar polarisation mechanism) under the passage of microwave radiation attempts to rotate or reorient the lag behind the electric field oscillations and causes polarisation losses and/or also friction between the molecules to generate heat.[67,68] The material ability to adsorb microwave electromagnetic and degree of microwave heating can be determined by the term "loss tangent" as (tan δ) which is the ratio of the dielectric loss factor (ε") to the dielectric constant (ε') as shown in Table 1.1.[69,70] The loss tangent depends on the working temperature and frequency applied material absorbers can generally be divided into three types depending on their tangents of loss; high (> 0.5), medium (0.1-0.5) and low (< 0.1).[69]

Dielectric constant (ε') describes as the measure of the ratio electrical permeability material to the free space electric permeability (similar to relative permittivity of a capacitor). The change in the dielectric constant relies on the ability of the molecular structure of the materials to resist or hold the molecular formation under the induction of an electrical field to be polarised, as a function of the temperature and frequency of the electrical field applied.[71] At the higher-frequency of electric field oscillations, the dipole molecules are unable to follow the field oscillations, and when the permeability drops, the substances will behave like non-polar materials. The dielectric loss factor (ε") could reach

maximum at the specific frequency (*e.g.*, water at approx. 20 GHz) along with the permeability (ε') decreases gradually, and ε" value indicates the material ability to dissipate energy into the surrounding system (heat generation).[71]

General changes of some materials in the temperature respect to dielectric properties, *e.g*. polar solvents, the dielectric materials become poorer as temperature increases or both dielectric constant and dielectric loss factor decrease with temperature increases. However, for example, in lossy material and wood, the dielectric constant and/or the loss factor increase with temperature.[72] Ionic liquids (ILs) under microwave through ionic conduction exhibit the absorption microwave irradiation ability increasing with increasing temperatures or rapidly heated.[73] Effect of addition salt (1-2% NaCl) on a solution under microwave irradiation, the loss factor (ε") increase linearly but the dielectric constant (ε') did not change significantly, indicating a positive correlation with temperature.[74] Microwave vessels of plastic materials due to temperature resistance in which most plastic materials have low dielectric constant values of 2-3.[71]

Table 1. 1 Loss tangent and dielectric constant of various solvents[70]

Solvent	**Loss tangent (tan δ) at 2.45 GHz, 20°C**	**Dielectric constant (ε')**
Ethylene glycol	1.350	37.4
Methanol	0.659	32.6
2-butanol	0.447	18.4
Acetic acid	0.174	6.2
Water	0.123	80.4
Acetonitrile	0.062	37.5
Acetone	0.054	21
Toluene	0.040	2.38
Hexane	0.020	1.88

1.5 Aims and Objectives

The overall aim of this thesis is to explore the potential of cassava peel and almond hull as exploitable renewable resources-chemicals, materials and bioenergy via microwave processing. The materials in the form of microfibrilated cellulose (MFC) will be achieved via acid-free microwave-assisted hydrothermal processing, whilst conventional microwave pyrolysis will also be considered to affect the production of biochar (bioenergy) and bio-oil (chemicals). The MFC's will be investigated for the potential to form hydrogels, films and, in particular as potential biobased adsorbents for removal of Cr(VI) and methylene blue from aqueous environments (Figure 1.8).

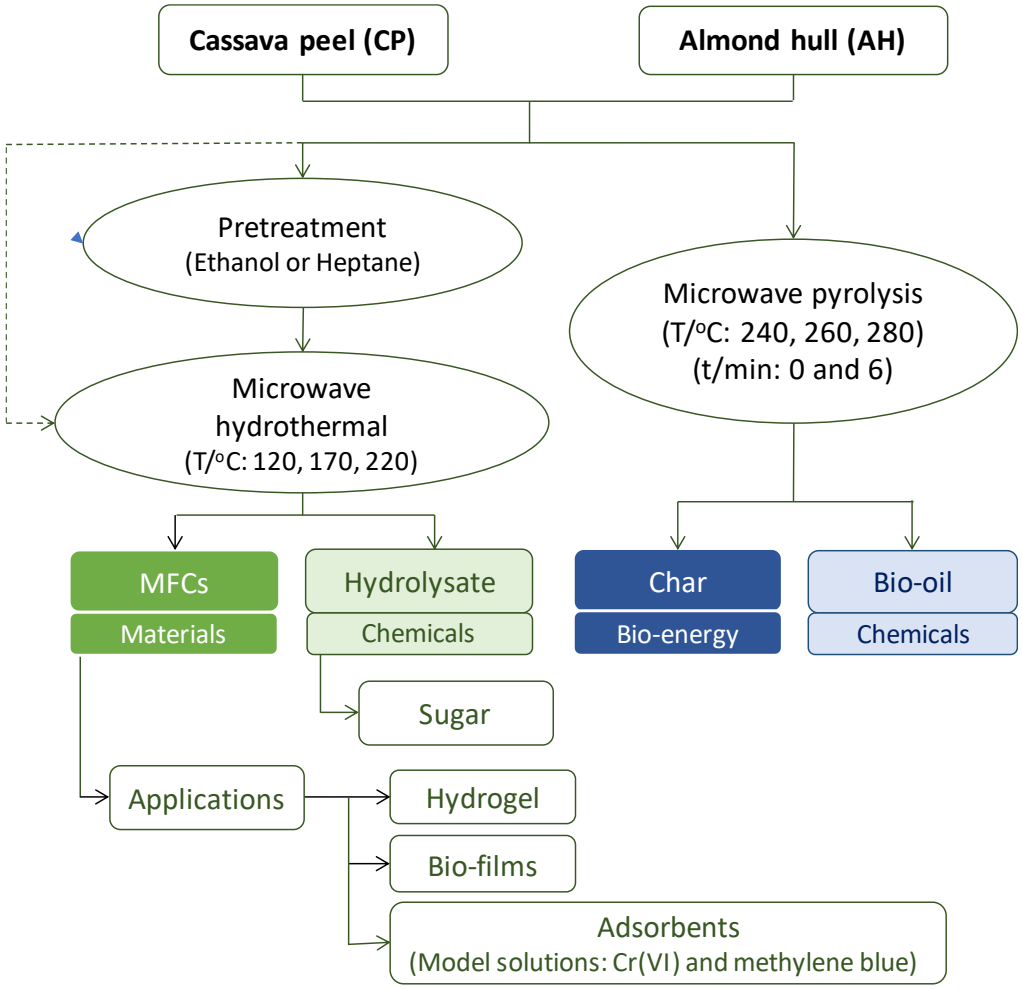

Figure 1. 8 Biomass microwave treatment respective to their products (original in colour)

The specific objectives of this research are:

I. Preliminary analysis of the chemical composition of cassava peel and almond hull biomass to determine cellulose, hemicellulose and lignin content and CHN content.

II. The production of acid-free microwave hydrothermal microfibrillated celluloses. Initially, the cassava peel (CP) and almond hull (AH) will be pretreated in hot solvent (either ethanol (CPET or AHET) or heptane (CPHP or AHHP) to remove extractives. Thereafter, acid-free microwave hydrolysis will be conducted from 120, 170 and 220 ^{o}C. For comparison, peel and hulls without pretreatment will also undergo acid-free microwave processing to investigate the influence of extracting. The samples will be analysed by ATR-IR, TGA, XRD, ^{13}C CPMAS NMR, SEM, Zeta potential, CHN, TEM and SEM. The microfibrilated cellulose produced will be investigated for their potential as hydrogels and biobased films.

III. The influence of acid-free microwave processing on the hydrolysate sugar content will be investigated.

IV. The ability of MFCs to remediate hexavalent chromium and methylene blue from model solutions at different concentrations will be investigated. Several isotherm models will be applied; Langmuir, Freundlich, Temkin and Dubinin-Radushkevich in order to understand the binding mechanism. Conventional stirring (CT) with respect to ultrasound (US), the latter is expected to give better results due to its microscopic rather than macroscopic effect. The effect of pH will be investigated. The MFC loaded

chromium for cassava peel and almond hull will be analysed by XPS to identify the changes oxidation state of chromium and cellulose before and after adsorption. The thermodynamic parameters involved in adsorption of the methylene blue at different temperature with respect to microfibrilated of cassava peel and almond hull. A kinetic study of chromium and methylene blue adsorption with respect to microfibrilated cellulose of cassava peel and almond hull will be conducted. *Pseudo*-first order, *pseudo*-second order, Elovich, and intra-particle diffusion model will be explored. A comparison will also be made of the agitation process by which the contaminants were taken up for both traditional stirring and sonication in the kinetic study.

V. The microwave pyrolysis of cassava peel and almond hull will be investigated in order to produce bio-oil and biochar as a source of bioenergy and chemicals, respectively. The biomass will be subjected to closed vessel microwave pyrolysis at temperature of 240, 260 and 280 ^{o}C and reaction time (0 and 6 minutes).

Chapter 2: Experimental

2.1 Materials and Reagents

Fresh cassava tubers were purchased from Kirkgate Market, Leeds, England. The tubers were peeled, and the white inner layers were chopped into small pieces using a knife mill, dried, ground (coffee grinder) into a fine powder and stored until further required. Almond hulls were harvested and collected from 'Marcona Almonds' producer farms in Zaragoza, Spain and sent to the GCCE by Dr Javier Remon. On receipt, the hulls were sprayed with ethanol to prevent mould growth during storage. The dried hulls were chopped with a knife mill, milled (coffee grinder) into medium-fine powder and stored until further required.

All solvents and reagents, *i.e.* ethanol, heptane, ethyl acetate, acetone, sodium hydroxide, sodium bicarbonate, sodium carbonate, sulfuric acid, nitric acid, magnesium sulphate, potassium dichromate, methylene blue, ammonium ferrous sulphate hexahydrate, acetic acid, calcium nitrate and sodium thiosulfate were obtained from Sigma Aldrich (now known as Merck) and used as supplied without further purification.

2.2 Methods

2.2.1 Pretreatment biomass

The appropriate solvent (100 mL, either ethanol or heptane) was added to either cassava peel or almond hull powder (20 g) contained in a round-bottomed flask equipped with a reflux condenser. The slurry was heated under reflux for 2 h. Thereafter, the mix-

ture was cooled and filtered. The residue was isolated and dried for analysis and experiment whilst the filtrate was evaporated to dryness *in vacuo*. The yields are reported in the section of Chapter 3.2.

2.2.2 Cellulose, hemicellulose and lignin determination[75]

2.2.2.1 Cellulose content

Overview: Biomass powder is treated with a mixture of a hot nitric-acetic acid mixture which dissolves intercellular substances to separate cellulose from hemicellulose and lignin. Starch and pentosan are hydrolysed. After washing with water, these impurities are removed, and an excess of acidified $K_2Cr_2O_7$ is added to the remaining cellulose effecting oxidation to carbon dioxide and water (Eq. 2.1).

$$(C_6H_{10}O_5)_n + 4K_2Cr_2O_7 + 16H_2SO_4 \rightarrow 6CO_2 + 4Cr_2(SO_4)_3 + 4K_2SO_4 + 21H_2O \quad \text{(Eq.2. 1)}$$

Unreacted (excess) acidified $K_2Cr_2O_7$ is titrated with Mohr's salt $(NH_4)_2Fe(SO_4)_2$ solution (Eq. 2.2). The same amount of acidified $K_2Cr_2O_7$ without cellulose is also titrated with $(NH_4)_2Fe(SO_4)_2$ solution as a control. The cellulose content was determined based on titer differences of the volume of $(NH_4)_2Fe(SO_4)_2$ solution used.

$$K_2Cr_2O_7 + 6FeSO_4 + 7H_2SO_4 \rightarrow 3\ Fe_2(SO_4)_3 + Cr_2(SO_4)_3 + K_2SO_4 + 7H_2O \quad \text{(Eq.2. 2)}$$

Method: The appropriate biomass (approx. 0.03 g, either cassava peel or almond hull) was placed in a glass centrifuge tube, mixed with conc. HNO_3: glacial acetic acid (11:1, 5 mL) and placed in boiling water for 25 minutes. Thereafter, the mixture was cooled, spun (3500 rpm, 10 minutes) and the supernatant was removed and discarded. The pellet was washed with distilled water and decanted thrice (3 x 10 mL). The pellet was oxidised with

acidified potassium dichromate solution (0.2 N $K_2Cr_2O_7$, 10 mL; H_2SO_4 95%, 8.09 mL) by heating in boiling water for 10 minutes. The cooled solution was transferred into an Erlenmeyer flask containing ferrous indicator (7 drops) and the excess of potassium dichromate solution was titrated with Mohr's reagent (0.10 N) until endpoint was achieved (red-brown to dark green). The titre volume was recorded as *b* mL. A blank titration was conducted in the absence of pellet (to check) and the titre volume recorded as *a* mL. The cellulose content (%) was then determined according to equation 2.3.

$$Cellulose\ content\ (\%) = \frac{0.00675xKx(a-b)}{n} x100\% \quad \text{(Eq.2. 3)}$$

Where:

m = volume of Mohr salt (mL)

K = coefficient (~0.103) of blind test 25 mL Mohr salt with 25 mL 0.10 N $K_2Cr_2O_7$

a = volume of 0.1N Mohr salt consumed by $K_2Cr_2O_7$ control solution (mL)

b = volume of 0.1N Mohr salt consumed by the remaining $K_2Cr_2O_7$ after oxidation cellulose

n =cellulose weight (g)

0.00675 = standard titer of cellulose

2.2.2.2 Hemicellulose content

Overview: Starch and other water-soluble carbohydrates are dissolved by boiling in 80% $Ca(NO_3)_2$ solution. After washing with distilled water, the precipitate is treated with aqueous HCl to hydrolyse the hemicellulose to a sugar solution. The total sugar content was determined by the copper-iodine method after neutralising with NaOH. Sugar from the hydrolysed hemicellulose reduces Cu(II) to Cu_2O. The amount of Cu(I) determines the hemicellulose content through the iodometric method. The KIO_3 and KI solution release iodine under acidic conditions (Eq 2.4).

$$KIO_3 + 5KI + 3H_2SO_4 \rightarrow 3I_2 + 3K_2SO_4 + 3H_2O \qquad \text{(Eq.2. 4)}$$

After the addition of oxalic acid, iodine reacts with Cu_2O (eq. 2.5).

$$Cu_2O + I_2 + H_2C_2O_4 \rightarrow CuC_2O_4 + CuI_2 + H_2O \qquad \text{(Eq.2. 5)}$$

The excess of iodine is titrated with $Na_2S_2O_3$ solution (eq. 2.6).

$$2Na_2S_2O_3 + I_2 \rightarrow Na_2S_4O_6 + 2NaI \qquad \text{(Eq.2. 6)}$$

Method: The appropriate biomass (approx. 0.1 g, either cassava peel or almond hull) was placed in a glass centrifuge tube. 80%-Aqueous calcium nitrate solution (15 mL) was added and placed in boiling water for 5 minutes. Thereafter, the mixture was cooled, distilled water (20 mL) was added to the centrifuge tube, spun (3500 rpm, 10 minutes) and the supernatant was removed and discarded. The pellet was washed with water and decanted thrice (3 x 10 mL), soaked in 2 N-aqueous HCl (10 mL) and placed in boiling water for 45 minutes. The mixture was cooled, spun (3500 rpm, 10 mins), and the supernatant was isolated and kept aside. The pellet washed with distilled water thrice (3 x 10 mL). Each time the supernatant was isolated and combined with previous isolated fractions. Phenolphthalein indicator (1 drop) was added to the combined supernatant isolate followed by sufficient 2 N-aqueous NaOH solution to affect a colour change from colourless to pink. The total volume of this solution was made up to 100 mL with the addition of distilled water.

An aliquot of this solution (10 mL) was transferred into an Erlenmeyer flask containing a copper-iodine solution (10 mL: 1.41 N-aqueous Na_2CO_3; 0.1 N-aqueous $CuSO_4$; 0.28 N-aqueous tartaric acid; 0.025 N-aqueous KIO_3 and 0.025 N-aqueous KI) and heated in boiling water for 15 minutes. The mixture was cooled and acidified (conc. H_2SO_4) 1 N

oxalic acid solution (5 mL) and 0.5%-aqueous starch solution (0.5 mL) were added. The resultant dark blue/black mixture was titrated with 0.01 N-aqueous sodium thiosulfate solution (0.01 N) until the blue light/black colour disappeared. The titre volume was recorded as *b* mL. A blank titration was conducted in the absence of supernatant isolate (to check) and the titre volume recorded as *a* mL. The hemicellulose content (%) was then determined according to equation 2.7.

$$Hemicellulose\ content\ (\%) = \frac{0.009\ x\ 100\ x\ [248-(a-b)]\ x\ (a-b)}{10000\ x\ 10\ x\ n\ x\ 100} \qquad \text{(Eq.2. 7)}$$

Where:

n = sample weight/g

a = volume of 0.01 N sodium thiosulfate consumed by control solution /mL

b = volume of 0.01 N sodium thiosulfate consumed by analysis solution /mL

0.009 = the conversion factor for hexose to cellulose

2.2.2.3 Lignin content

Overview: Acetic acid (1% by volume) is added to the appropriate biomass to separate sugars, organic acids and other soluble compounds. Acetone removes chlorophyll, lipids, fats and other fat-soluble compounds. After rinsing the precipitate with water, the pellet is oxidised with acidified $K_2Cr_2O_7$ solution (Eq. 2.8)

$$C_{11}H_{12}O_4 + 8K_2Cr_2O_7 + 32H_2SO_4 = 11CO_2 + 8K_2SO_4 + 8Cr_2(SO_4)_3 + 32H_2O \quad \text{(Eq.2. 8)}$$

The excess of acidified $K_2Cr_2O_7$ is titrated with Mohr's solution.

Method: The appropriate biomass (approx. 0.03 g, either cassava peel or almond hull) was placed in a glass centrifuge tube. Glacial acetic acid (1%, 10 mL) was added, the tube was shaken for 5 minutes and then spun (3500 rpm, 10 minutes). The supernatant

was removed and discarded whilst the pellet was washed with acetone and decanted thrice (3 x 4 mL). Whilst in the centrifuge tube, the pellet was dried (105 ^{o}C) overnight, soaked in concentrated H_2SO_4 (73%, 3 mL) and kept in this state for 16 h. Thereafter, distilled water was added (10 mL) to the tube, heated in boiling water for 5 minutes and cooled. Aqueous $BaCl_2$ solution (10%, 0.5 mL) was added and the mixture was spun (3500 rpm, 10 mins). The supernatant was isolated and discarded whilst the pellet washed with distilled water thrice (3 x 10 mL). Each time the supernatant was discarded. An appropriate volume of acidified potassium dichromate solution (0.2 N $K_2Cr_2O_7$, 10 mL; H_2SO_4 95%, 8.09 mL) was added and heated to dissolve the pellet. The cooled solution was transferred into an Erlenmeyer flask containing ferrous indicator (7 drops), and the excess of potassium dichromate solution was titrated with Mohr's reagent (0.10 N) until endpoint was achieved (red-brown to dark green). The titre volume was recorded as *b* mL. A blank titration was conducted in the absence of pellet (to check) and the titre volume recorded as *a* mL. The lignin content (%) was then determined according to equation 2.9.

$$\text{Lignin content}(\%) = \frac{0.433 \text{ x K x (a}-\text{b)}}{n \; x \; 100\%} \qquad \text{(Eq.2. 9)}$$

Where:

K = coefficient (~0.103) of blind test 25 mL Mohr salt with 25 mL 0.10 N $K_2Cr_2O_7$

a = volume of 0.1 N Mohr salt solution consumed by $K_2Cr_2O_7$ control (mL)

b = volume of 0.1 N Mohr salt solution consumed by the remaining $K_2Cr_2O_7$ of lignin determination (mL)

n = sample weight (g)

0.433 = standard titer of lignin

2.2.3 Acid-free microwave-assisted hydrolysis

2.2.3.1 MFC production

The acid-free microwave-assisted hydrolysis was performed on cassava peel (CP) and almond hull (AH) from three different samples: residue without pretreatment, ethanol extracted residue (ET) and, heptane extracted residue (HP). All samples were processed in a CEM Mars 6 closed vessel microwave system with an energy maximum of 600 W and a ramp time of 20 minutes. The operating condition was set up with a temperature of 120, 170, 220 ^{o}C with 0 minutes holding time and 5% (w/v) concentration biomass ratio to the deionised water. The slurry was filtered, and then the residue washed with water first, hot ethanol (2x) and acetone. Thereafter, the residue was dried at approximately 40 ^{o}C for 72 h or until constant weight was achieved. The filtered solution of all samples was analysed with HPLC for sugar content. The yield (%) of dry MFC was calculated according to Eq.2.10 and the dried samples were coded based on their source biomass and processing temperature. For example, CP 120 is cassava peel processed at 120 ^{o}C and AH 120 is almond hull processed at 120 ^{o}C.

$$\text{Yield (\%)} = \frac{Weight\ sample\ after\ hydrolysis\ (g)}{Weight\ sample\ before\ hydrolysis\ (g)} x\ 100 \quad \text{(Eq.2. 10)}$$

2.2.3.2 MFC for adsorption study

The microwave set up was similar for MFC production as reported earlier in section 2.2.3.1 For the adsorption study, the raw material for adsorbent was used from biomass without pretreatment. The operating condition for hydrolysis was at the temperatures between 120 and 220^{o}C, with holding time of 30 minutes and a concentration of 5% (w/v).

2.2.3.3 Chromium adsorption study

A chromium stock solution (2000 mg/L) was prepared by dissolving $K_2Cr_2O_7$ (2.8286 g, $2.719x10^{-2}$ mol of Cr(VI)) in 500 mL deionisation water. The calibration standard curve for chromium was produced at 540 nm with Cr(VI) concentration of 0.10, 0.50, 1.0, 1.5, and 2.0 mg/L (Figure 2.1). The working concentrations were prepared from the stock solution by dilution and re-checked to ensure actual concentration before the experiment conducted.

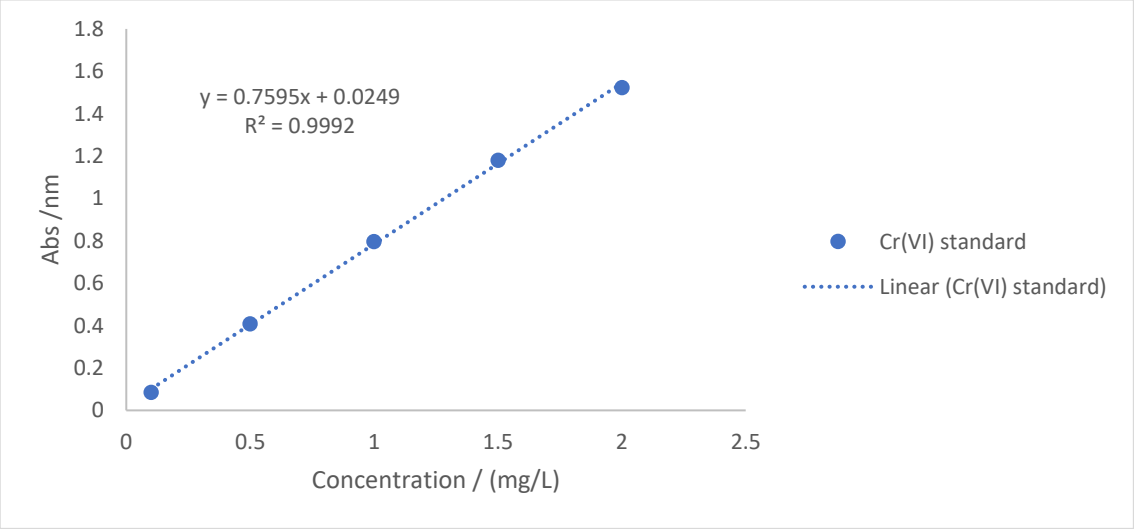

Figure 2. 1 Calibration standard solution for Cr(VI) (Original in colour)

Stirring mode (ST)

The appropriate dried MFC (0.5% (w/v) or 0.025 mg) and the appropriate concentration of Cr(VI) solution (4.975 mL) were placed in a small vial (7 mL). The batch experiments were conducted under magnetic stirring (agitation speed, 250 rpm) and the contact time of 2 h. Optimisation of various parameters for isotherm study were initial chromium concentration ranging 0.5–1000 mg/L, pH medium at 7 and pH 2 and four types of adsorbents (CP 120 and CP 220 for cassava peel and AH 120 and AH 220 for almond hull)

while for kinetic study the varying contact time between 30 minutes and 12 h at pH 2. The pH medium was adjusted by 10% H_2SO_4 until pH 2 was reached. After the adsorption study finished, the nanocellulose in the solution was centrifuged at 3500 rpm, and the supernatant was collected by pipette. The concentration of the remaining Cr(VI) in the solution after adsorption was determined with colorimetric method 7196A[76] using 1.5-diphenylcarbazide by UV/Vis (Jasco v-550) at 540 nm. The absorbance of the remaining ion Cr(IV) after absorption was extrapolated to the standard curve in Figure 2.1 and multiplied with its dilution factor. Each parameter experiments were repeated at least two times.

Ultrasound mode (US)

The ultrasound equipment (Sonic vibra-cell VCX 130, 20 kHz) was set up at 65 % amplitude and a pulse cycle of 3 seconds on and 1 second off. All experiments were performed in a 7 mL vial with the appropriate MFC (0.5% (w/v)) in the appropriate concentration of Cr(VI) solution (4.975 mL) with 30 minutes contact time by sonication, and then the vial was immediately placed an ice-cold bath. The different parameters of the isotherm study were: (i) initial Cr(VI) concentration was ranging from 1 to 1200 mg/L, (ii) the medium solution of pH 7 and pH 2 while for the kinetic studies were performed by varying contact time ranging from 1 to 60 minutes in medium pH 2. The sample was transferred to the centrifuge tube and centrifuged at 3500 rpm for 10 minutes. The remaining Cr(VI) was pipetted and determined with the colourimetric method 7196A[76] using 1.5-diphenylcarbazide by UV/Vis (Jasco v-550) at 540 nm. The absorbance of the remaining Cr(IV) solution after absorption was extrapolated to the standard curve in Figure 2.1 and multiplied with its dilution factor. Each parameter experiments were repeated at least two times.

2.2.3.4 Methylene blue adsorption study

Methylene blue solution preparation

Methylene blue ($C_{16}H_{18}ClN_3S$) stock solution (2000 mg/L) was prepared by dissolving methylene blue (600 mg, $1.87x10^{-3}$ mol) in 300 mL deionised water. The calibration standard curve for methylene blue was produced at absorbance 664 nm with a concentration of 0.5, 1.0, 2.0, 3.0, 4.0 and 5.0 mg/L (Figure 2.2). The working concentrations were prepared by dilution from the stock solution and re-checked to ensure actual concentration before the experiment conducted.

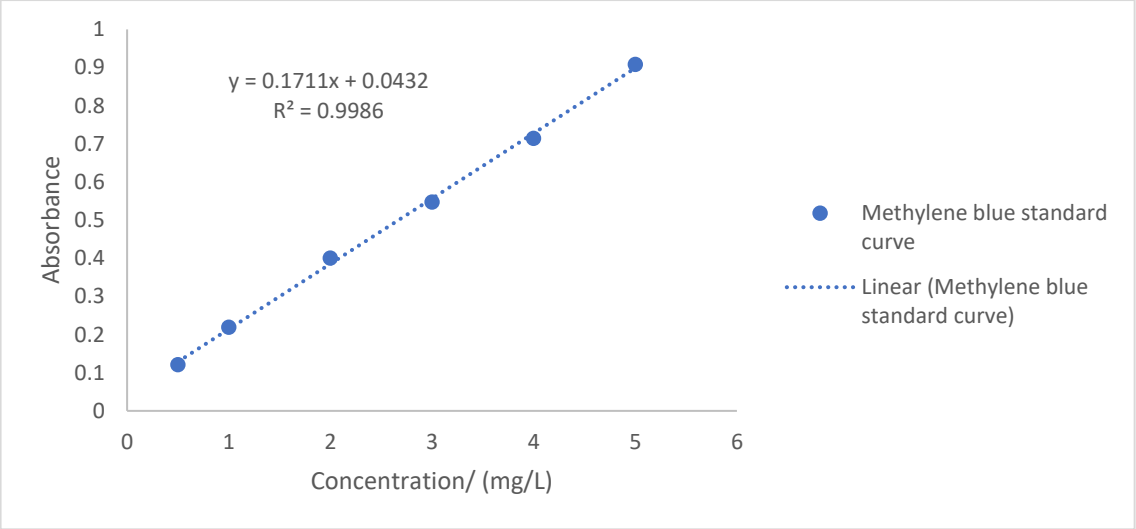

Figure 2. 2 Calibration standard solution for methylene blue (Original in colour)

Stirring mode (ST)

The appropriate dried MFC (0.5% (w/v) or 0.025 mg) in the appropriate concentration of methylene blue solution (4.975 mL) were added into a vial 7mL. The batch experiments were conducted using a magnetic stirrer with 250 rpm agitation speed and 2 h contact time with the different isotherm parameters: (i) initial concentration (150–1500

mg/L), (ii) five types of adsorbent (CP 120, CP 220, AH 120, AH 220 and activated carbon (Norit™)), while for kinetic study, the varying contact time between 30 and 6 h. The thermodynamic parameters were carried out at the temperature of 22^{o}C, 35^{o}C, and 45°C. After the adsorption process was complete, the MFC solution was centrifuged at 3500 rpm, and the concentration of the remaining methylene blue solution was determined with the colourimetric method by UV/Vis (Jasco v-550) at 664 nm. The absorbance of the remaining methylene blue solution after absorption was extrapolated to the standard curve in Figure 2.2 and multiplied with its dilute on factor. Each parameter experiments were repeated at least two times.

Ultrasound mode (US)

The ultrasound experiments (Sonic vibra-cell VCX 130, 20 kHz) were set up at 65% amplitude with a pulse cycle of 3 seconds on and 1 second off. All batch experiments were performed in a 7 mL vial with the appropriate MFC (0.5% (w/w) or 0.025 mg) in the appropriate concentration of methylene blue solution (4.975 mL). The vials were sonicated for 30 minutes and then placed in an ice-cold bath. For the optimisation of isotherm parameters; (i) different MB concentration effect of uptake was ranging from 150 to 1500 mg/L, (ii) five types of adsorbent (CP 120, CP 220, AH 120, AH 220 and activated carbon (Norit™)), were investigated whilst for the kinetic studies were performed with varying contact time from 1 minute to 1 h. After sonication, the sample was transferred to the centrifuge tube and was centrifuged at 3500 rpm for 10 minutes. The remaining MB concentration was determined with the colourimetric method by UV/Vis (Jasco v-550) at 664 nm. The absorbance of the remaining methylene blue solution after absorption was

extrapolated to the standard curve in Figure 2.2 and multiplied with its dilution factor. Each parameter experiments were repeated at least two times.

The percentage MB removal or the adsorption efficiency was calculated using the following equation (eq. 2.11):

$$\%\, removal\ of\ MB = \frac{C_0 - C_e}{C_0}\ x\ 100 \qquad \text{(Eq.2. 11)}$$

where C_o is the initial concentration (mg/L) and C_e is the equilibrium concentration (mg/L) of MB.

The equilibrium adsorption (q_e) was calculated using equation (2.12):

$$q_e(\frac{mg}{g}) = \frac{C_0 - C_e}{m}\ x\ V \qquad \text{(Eq.2. 12)}$$

where q_e is the equilibrium adsorption of the Cr(VI) per unit mass of the adsorbent (mg/g), m is the weight of the adsorbent (g), and V is the volume of the solution (L).

2.2.4 Hydrogel formation

The MFC hydrogels were produced at different concentrations ranging 2 to 7 % (w/v) by adding deionised water to CP120 or AH120 (microwave hydrolysed at 120^{o}C of cassava peel or almond hull) in 7 mL vial. The mixture was homogenised using Ystral Homogenizer D-79282 Dottingen X10/20 E3 for 5 minutes at 20,000 rpm. Thereafter, the gel was allowed to cool to ambient temperature. The resultant gel formation was assessed qualitatively through a tube inversion test, in which the vial was turned was upside down. A real-gel is strong, -supportive where it will not flow.

2.2.5 MFC-based films

MFC-based films were produced at a concentration of 0.2% (w/v) in deionised water. The mixture homogenised using Ystral Homogenizer D-79282 Dottingen X10/20 E3 for 5 minutes at around 20,000 rpm and sonicated for 10 minutes to break any large lumps and intent to more homogenous dispersion. Subsequently, the suspensions were poured into a short-stem sintered glass filter with 40 mm diameter, pore size 3 covered with a PTFE membrane filtered with glass suction vacuum and air-dried. The wet MFC films were dried at around 40 °C and stored in plastic petri dishes. The morphology and cross-section film were analysed by SEM.

2.2.6 Microwave-assisted pyrolysis

Dried cassava peel powder (CP) or dried almond hull powder (AH) (1.0 g) without pretreatment was placed in 35 ml microwave glass tubes. Microwave-assisted pyrolysis with a CEM Discover microwave reactor was set in dynamic mode at different temperature (240, 260, and 280 ^{o}C) and holding time (0 and 6 minutes). After heating was complete, the biochar (solid fraction) was further washed by ethyl acetate (5 mL) then dried and its calorific value determined via oxygen bomb calorimetry. Bio-oil was extracted into ethyl acetate and evaporated to give a viscous brown oil. The oil chemical component was analysed GC-MS.

2.2.7 Theoretical higher heating value (HHV)

The estimation of high heating value (HHV) of the crude biomass and biochar post microwave pyrolysis were calculated using modified Channiwala's formula is shown in Eq. 2.13:[77,78]

HHV (MJ/kg) = 0.3491 x C (wt.%) + 1.1783 x H (wt.%) − 0.1034 x O (wt.%) − 0.015 N (wt.%)

(Eq.2. 13)

where the oxygen content was calculated by the difference, *i.e*., oxygen (%) = 100% - C (wt.%) – H (wt.%) - N (wt.%)

The element ratio H/C and O/C were calculated as shown in equations 2.14 and 2.15:

$$\mathrm{H}/_{\mathrm{C}}\ \text{ratio} = \frac{\frac{\text{Weight hydrogen \%}}{\text{Atomic weight hydrogen}}}{\frac{\text{Weight carbon \%}}{\text{Atomic weight carbon}}} \qquad \text{(Eq.2. 14)}$$

$$\mathrm{O}/_{\mathrm{C}}\ \text{ratio} = \frac{\frac{\text{Weight oxygen \%}}{\text{Atomic weight oxygen}}}{\frac{\text{Weight carbon \%}}{\text{Atomic weight carbon}}} \qquad \text{(Eq.2. 15)}$$

2.3 Instrumental Analysis

2.3.1 Elemental analysis (CHN)

The carbon, hydrogen and nitrogen content were analysed with A CE-440 elemental analyser (EAI Exeter Analytical) was linked with a Sartorius S2 balance. The samples were placed in a nickel sleeve, combusted at 975 °C under pure oxygen, and the combustion products were analysed with a very high coefficient of thermal conductivity detectors. The analysis was conducted twice. Elemental analysis was performed by Dr Graeme McAllister, Department of Chemistry, University of York.

2.3.2 Attenuated total reflectance infrared spectroscopy (ATR-IR)

ATR-IR was carried out using a Perkin Elmer Spectrometer (Spectrum 400 FT-IR/FT-NIR). Prior to recording a spectrum, a background scan was set up from 4000 cm^{-1} to 600

cm^{-1} and the spectral resolution of 4 cm^{-1}. Thereafter, the amount of sample was placed on the sapphire window and spectrum recorded with 4-time scans.

2.3.3 Thermogravimetric Analysis (TGA)

The cellulosic samples (9-10 mg) was placed into a small aluminium pan in each experiment. TGA was carried out using on a PL Thermal Science STA 625 under a flow of nitrogen gas from 20 to 625 °C at a heating rate of 10 $^{o}C\ min^{-1}$.

2.3.4 Solid-state ^{13}C CP-MAS nuclear magnetic resonance

^{13}Carbon NMR analysis was conducted using a 400 MHz Bruker Avance III HD spectrometer with solid-state ^{13}C Cross Polarization Magic Angle Spinning (CP-MAS) NMR (SSNMR) spectra method connected to a 4 mm Bruker H(F)/X/Y triple-resonance probe and 9.4T Ascend superconducting magnet. Each MFC sample was set with spinning rates of 10,000 ± 2 Hz by a 1 ms linearly-ramped contact pulse, and 3 seconds optimised recycle delays, and 2,000 scans numbers. The ^{13}C-NMR chemical shifts reported respect to TMS and were referenced using adamantane (29.5 ppm) as an external secondary reference.

2.3.5 X-Ray diffraction

XRD pattern analysis measured with a Bruker-AXS D8 Advance Diffractometer equipped Cu monochromatic K-α radiation (λ =1.54184 Å) and a PSD Lynx eye detector. The fine powder of MFC sample was run with the settled voltage of 40 kV and current of 40 mA, the rate scan speed of 2 sec/step with increment 0.100194 over a 2θ range between 5 and 37° in a locked coupled scan mode. The data processing included background signal subtraction and trace smoothing. According to Segal equation (Eq.2.16), the crystalline index (CrI) of MFC samples was calculated.

$$\text{Crystallinity index (\%)} = \frac{(I_{200} - I_{am})}{I_{200}} x100 \qquad \text{(Eq.2. 16)}$$

where:

I_{200} = intensity of the crystalline material peak at 2θ = 22°

I_{am} = intensity of amorphous contribution at 2θ = 18 °

2.3.6 Scanning electron microscopy (SEM)

SEM images of MFC morphology were conducted in a JEOL JSM-7600F SEM instrument. MFC suspension of the sample (0.2% w/v) was either, directly air-dried on the SEM grid or freeze-dried. When freeze-dried, a small amount of the gel or suspension was placed on a copper shim and excess of liquid was removed with filter paper. The sample was then frozen in liquid nitrogen slush (-210 °C, so it does not form a bubble, achieving better cooling rate and better preserving the original structure of the material).The shim plus gel was transferred to the cooled Peltier stage in a Polaron coating unit, and the air was pumped out. The temperature was kept around. -55 °C and the vacuum was maintained around 10^{-4} mBar. After a few hours, the sample was warmed to room temperature, and the gel was knocked off the shim. The remaining scraps of gel were imaged after mounting the shim plus scraps on a stub and coating with gold/palladium (4 nm thick). The SEM analysis was performed by Meg Stark, Department of Biology, University of York.

2.3.7 Transmission electron microscopy (TEM)

TEM images of cellulosic fibres dimension were analysed using a TEM FEI Tecnai 12 G^2 operating at an acceleration voltage of 120 kV with BioTWIN for high contrast imaging coupled on a digital imaging system SIS Megaview III camera. Sample preparation prior to

the analysis, MFC was diluted samples (0.2%) (w/v) with ionised water were sonicated for 30 minutes under an ice-cold ultrasound batch. A drop of the sample (8 µL) was left on the grid for five minutes then negatively stained with 1% uranyl acetate and finally glow discharged. Copper grids with a formvar/carbon support film which had been previously glow discharged were used. The TEM analysis was performed by Meg Stark, Department of Biology, University of York.

2.3.8 Gas chromatography-mass spectroscopy (GC-MS)

Gas chromatography-mass spectrometry (GC-MS) is an analytical method to separate, identify, and quantify a mixture of chemicals combining gas-chromatography and mass spectrometry. Microwave pyrolysis bio-oil from the CEM Discover microwave reactor was diluted in ethyl acetate and filtered prior to injection. The samples were analysed on Clarus 500 Gas Chromatograph and Clarus 560 S Mass Spectrometer of Perkin Elmer Company. Samples method used the general-1 method with duration 13.33 minutes, initial temperature 50 ^{o}C, hold time 0 minute, ramping rate 30 ^{o}C/ minutes, temperature 300^{o}C with holding time 5 minutes, split ratio 5:1 and injector temperature 300^{o}C and general-2 method, duration 38 minutes, initial temperature from 50 ^{o}C, holding time 4 minutes, ramp rate 10 ^{o}C/minutes, end temperature at 290 ^{o}C with 10 min holding time, split ratio 5:1, and injector temperature 300 ^{o}C.

2.3.9 High-performance liquid chromatography (HPLC)

Sugars (cellobiose, glucose, xylose/ fructose, arabinose and levoglucosan), sugar acids (glucuronic acid and galacturonic acid), soluble organic acids (lactic acid, formic acid, levulinic acid and acetic acid), furans (HMF and furfural) and levoglucosenone present in

the microwave hydrolysate were quantified by HPLC. The analysis was performed by Dr Hannah Briers and Dr Richard Gammons, Department of Chemistry, University of York.

Sugars and acids were analysed by using an Agilent 1260 equipped with a reverse-phase Hi-Plex H (300 × 7.7 mm, 8 µm particle size) column, using 0.005 M H_2SO_4 as mobile phase, isocratic mode (no gradient), 0.4 mL/min flow-rate, column temperature at 60 °C, refractive index detector (55 °C), 5 µl injection and a total run time of 35 min.

Furans were analysed by using an ACE C18 (250 × 4.6 mm, 5 µm particle size) column, acetonitrile: water (25/75) as mobile phase, isocratic mode, flow-rate of 0.8 mL/min., column temperature at 30 °C, a diode-array detector (DAD) at 220 nm, injection volume of 5 µl and the total run time of 22 minutes. The hydrolysate microwave was collected, filtered via a disk filter (0.22 µm pores) and analysed in the HPLC.

2.3.10 X-Ray photoelectron spectroscopy (XPS)

To obtain XPS spectra using monochromatic Al Kα X-ray source operating at 120 W (10 mA x 12 kV) a Kratos Axis Ultra DLD system was employed. Data were acquired with pass energies of 160 eV for survey spectra, and 20 eV for high resolution scans with phase sizes of 1 eV and 0.1 eV respectively. The process was operated in the hybrid operating mode, using a combination of magnetic and electrostatic lenses to collect electrons over an analytical area of approximately 300 x 700 μm^2. To minimise the charge of the sample surface, a magnetically confined charge compensation system was used, and all spectra were taken with an angle take of 90°. During spectra processing, a pressure of 1 x 10^{-9} Torr was maintained, with system base pressure of 5 x 10^{-10} Torr. Data were quantified using

CasaXPS (v2.3.23) using modified Wagner Sensitivity Factors as provided by the manufacturer after subtraction of the Shirley background.

2.3.11 N_2 porosimetry

The porosity of the materials was analysed using a TriStar Micromeritics Surface Area and Porosity Analyser based on nitrogen adsorption and desorption. The cellulose sample was degassed at 90 °C for 6 h under vacuum prior to analysis, and the mass of the glassware and sample was measured. The appropriate MFC sample or activated carbon (~50 mg) was put inside a clean porosimetry tube. The data was processed using TriStar software, where specific surface areas were calculated using the Brunauer-Emmett-Teller (BET) equation, and desorption pore volume and average pore size were calculated using Barrett-Joyner-Halenda (BJH) equations.

2.3.12 Boehm titration

Overview: The oxygen-containing surface group quantification of the MFC adsorbent was determined by the Boehm acid-base titration method. The total acidic and basic sites were neutralised with NaOH and HCl solutions, respectively. The total acidic sites included the carboxylic, phenolic and lactonic sites. The carboxylic sites were neutralised with 0.01 M $NaHCO_3$ solution, the lactonic sites with 0.01 M Na_2CO_3 solution and the phenolic sites were estimated by subtracting the carboxylic and lactonic sites from the total acidic sites.[79]

Method: The appropriate nanocellulose sample (0.25 g) was placed in 100 ml glass conical flask and added 30 mL of 0.1 M NaOH, 0.1 M $NaHCO_3$, and 0.05 Na_2CO_3 to each glass conical flask for acid group determination. For the basic group determination, added 30 mL

of 0.1 M HCl solution. The mixture solution was shaken for 24 hours. Subsequently, 5 mL aliquot was pipetted from the flask solution, and the excess of basic was titrated by 0.01 M HCl, vice versa for the total basic group, the excess of 0.1 HCl was titrated by 0.01 NaOH with Tashiro indicator. Tashiro indicator is a mixture ratio (1:1) between 0.1% methylene blue and 0.01% methyl red in ethanol (pH value ranged 4.4-6.2). The equivalent point of titration the solution colour change from green to purple for acid group determination. Each experiment was conducted duplicate. The acid group and basic group was calculated according to equations 2.17-2.18, 2.20, 2.21, and 2.22:

$$n_{carboxyl}\left(\frac{mmol}{g}\right) = \frac{\left(V_{\text{HCl blind test of } NaHCO_3} - V_{\text{HCl mixture solution}}\right) \text{x } 0.01 \text{ M HCl x } 6}{0.25 \text{ g sample}} \quad \text{(Eq.2. 17)}$$

$$n_{lactones}\left(\frac{mmol}{g}\right) = \frac{\left(V_{\text{HCl blind test of } Na_2CO_3\ H} - V_{\text{HCl mixture solution}}\right) \text{x } 0.01 \text{ M HCl x } 6}{0.25 \text{ g sample}} \quad \text{(Eq.2. 18)}$$

$$Lactonic\ site = n_{lactones} - n_{carboxyl} \quad \text{(Eq.2. 19)}$$

$$n_{phenols}\left(\frac{mmol}{g}\right) = \frac{\left(V_{\text{HCl blind test of NaOH}} - V_{\text{HCl mixture solution}}\right) \text{x } 0.01 \text{ M HCl x } 6}{0.25 \text{ g sample}} \quad \text{(Eq.2. 20)}$$

$$Phenolic\ site = n_{phenols} - n_{lactones} - n_{carboxyl} \quad \text{(Eq.2. 21)}$$

$$n_{basic}\left(\frac{mmol}{g}\right) = \frac{\left(V_{\text{NaOH blind test of HCl}} - V_{\text{NaOH mixture solution}}\right) \text{x } 0.01 \text{ M NaOH x } 6}{0.25 \text{ g sample}} \quad \text{(Eq.2. 22)}$$

2.3.13 Zeta potential

The zeta potentials of MFC cellulosic samples at pH 2 and pH 7 were analysed using Malvern Zetasizer Nanoseries Nano-Z5, UK. The sample preparation, MFC sample (0.005-0.01 %) (w/v) was mixed in 30 mL vial with deionised water by homogeniser for 5 minutes, and the dispersed solution transferred into a capillary cell by pipette. The zeta potentials were determined in duplicate.

2.3.14 Bomb calorimetry

The gross heat of biochar was determined using a Parr 6200 Calorimeter with a standard 1108 Oxygen Bomb. Dry char or biomass sample (0.3 g) was placed in an iron pan inside the bomb cylinder and placed firing wire into the bomb head. The temperature of bucket water (2809 g) and jacket temperature will be stabilised to the burning process for determining the calorific value.

Chapter 3: Results and Discussion

This chapter is divided into four parts, namely:

I. Compositional analysis

II. Production of microfibrillated celluloses (MFCs)

III. Chromium (VI) and methylene blue adsorption study

IV. Microwave pyrolysis

3.1 Compositional Analysis

3.1.1 Cellulose, hemicellulose and lignin content.

The overall mean cellulose, hemicellulose and lignin content (Table 3.1) of virgin cassava peel (CP) and almond hull (AH) were calculated by classical titration according to Hu *et al.* [75] The lignin content appears to be the most significant difference between the two samples. The lignin content of almond hulls (11.41%) was found to be almost four times higher than for cassava peel (3.09%).

Table 3. 1 Cellulose, hemicellulose and lignin content (%)

Raw biomass	**Composition/%**		
	Cellulose	**Hemicellulose**	**Lignin**
Cassava peel (CP)	11.30±0.8	22.39±1.9	3.09±0.8
Almond hull (AH)	13.38±0.8	24.06±3.7	11.41±2.0

In comparison, Aderemi *et al*.[80] and Onyelucheya *et al*.[81] reported that cassava peel comprises cellulose (3.05-5.4%), hemicellulose (21.65-29.81%) and lignin (2.65-4.81%) based on acid detergent fibre (ADF) and neutral detergent fibre (NDF) isolation, degradation or oxidation as reported by van Soest.[82] The hemicellulose and lignin content

of cassava peel from NDF/ADF technique are quite similar with classical titration but the cellulose content is lower. The acid detergent is usually a mixture of H_2SO_4, as acid, and cetyltrimethylammonium bromide (CTAB), as detergent. The neutral detergent is a mixture of sodium lauryl sulfate (SLS), as detergent, disodium ethylenediaminetetraacetatic acid (EDTA), sodium borate, disodium hydrogen phosphate and 2-ethoxyethanol. ADF comprises cellulose, lignin, and insoluble ash (mainly silica) whilst NDF which contains hemicellulose, cellulose, lignin, and insoluble ash.

Yalchi *et al*.[47] report almond hulls to comprise ADF (13.7-29.9%), NDF (28-38.49%) and acid detergent lignin (ADL) or crude lignin content (4.1-14.9%). The cellulose content of the almond hull is assumed to be 8.9-15% calculated as the difference between ADF and ADL, whilst the hemicellulose content is NDF – ADF predicted to be 8.59-14.68%. Compared with classical titration, the content of cellulose and lignin is in range of NDF/ADF but the content of hemicellulose is different. NDF/ADF method evaluates the nutritive value of feeds and digestibility in rumen[47,83] which has different routes with the classical method in cellulose, hemicellulose and lignin analysis. However, it gives a picture of the carbohydrate component and composition of the almond hull. The differences in composition are also dependent on several factors such as species, growing conditions and environment, maturity, time of harvest and length of storage.[84]

3.1.2 Elemental analysis, protein content and higher heating value (HHV)

The CHN analysis, protein content and higher heating value (HHV) of virgin cassava peel (CP) and almond hulls (AH) are reported in Table 3.2. The %C and %H are comparable for both feedstocks, but there is a significant difference in their %N. Cassava peel contains significantly more nitrogen than almond hulls. %N is a very good proxy for protein content.

Multiplication of %N by 6.25 (plant protein factor) affords the crude protein content.[85] Thus, the crude protein content of cassava peel and almond hull was 9.81% and 5.38%, respectively.

The CHN analysis provides an approximate estimate of the biomass composition, and the chemical composition such as cellulose, lipid or protein is related linearly to elemental CHN content. The fraction of carbon and hydrogen contents of cassava peel (Table 3.2) were slightly higher than the almond hull, and the nitrogen percentage of cassava almost doubled that of the almond hull. The CHN analysis of lignocellulose gave the estimated crude protein content calculated from the conversion factor plant protein via multiplication by 6.25.[85] Using this factor, the protein content of cassava peel and almond hull were 9.8% and 5.3% respectively.

Table 3. 2 CHN analysis of cassava peel and almond hull raw material

Raw biomass	%C	%H	%N	%O	Protein/%	HHV/(MJ/kg)
Cassava peel (CP)	41.63	6.114	1.57	50.85	9.81	16.47
Almond hull (AH)	41.26	5.71	0.86	52.16	5.38	15.72

The theoretical HHV can be calculated from CHN data using a modified form of Channiwala's formula, [77] (see Chapter 2: Experimental, Section 2.2.7). Cassava peel has a slightly higher HHV than almond hulls. The Channiwala formula is a good proxy for the actual calorific value as determined by bomb calorimetry. The measured calorific value for cassava peel and the almond hull was 15.5 MJ/kg and 14.8 MJ/kg, respectively.

3.2 Production of Microfibrillated Celluloses (MFCs)

MFCs were produced from virgin cassava peel (CP) and almond hull (AH) and solvent extracted (pretreatment with either hot ethanol (ET) or hot heptane (HP)) cassava peel and almond hulls. Pretreatment with hot heptane (HP) was used to extract non-polar and/or weakly polar compounds such as waxes or lipids, whilst hot ethanol (ET) pretreatment was used to remove polar compounds such as water, sugars, phenols, tannins, *etc.*[86] The average yield of sugar extracted from ethanol pretreatment were 8.15% and 14.29 % (w/w) while the oil fraction from heptane pretreatment was 0.35% and 1.38% (w/w) for cassava peel and almond hull, respectively. In the scope of this thesis, the extractives were not further analysed.

3.2.1 MFC yield

Table 3.3 lists MFC yield (%) concerning microwave processing temperature (^{o}C) for virgin cassava peel (CP), ethanol extracted cassava peel (CPET), heptane extracted cassava peel (CPHP), virgin almond hulls (AH), ethanol extracted almond hulls (AHET) and heptane extracted almond hulls (AHHP) (The images of the resultant MFCs are shown in Appendix I: Figure A. 1, which depict differing degrees of colour according to processing temperature and pretreatment method). The MFC yield for almond hulls was always higher than for cassava peel at all processing temperatures indicating more hydrolysis of cassava peel than for almond hulls. MFC yields decreased with increasing microwave processing temperature from 120 ^{o}C to 170 ^{o}C to 220 ^{o}C irrespective of feedstock type. It is well known that hemicelluloses are leached/decomposed in the region 120-150 ^{o}C under microwave conditions whilst leaching of cellulose and especially leaching of amorphous cellulose

occurs at above 180 °C.[87] These changes are manifested, for example, in the crystal structure and crystallinity index (CI), thermogravimetric analysis profiles, ^{13}C CPMAS NMR, ATR-IR and hydrolysate profile as discussed later.

Table 3. 3 MFCs of cassava peel and almond hull yield (%) of microwave hydrothermal

Cellulosic samples	Temperature/°C		
	120	170	220
	Yield/%		
CP	46.64	31.42	15.04
CPET	43.93	28.34	22.21
CPHP	47.54	21.14	19.13
AH	73.27	50.90	30.93
AHET	66.31	45.14	33.43
AHHP	50.22	42.90	33.59

3.2.2 ATR-IR analysis

The ATR-IR spectra of MFCs produced at different processing temperatures (120 °C, 170 °C and 220 °C) from virgin cassava peel (CP, without pretreatment), ethanol- (CPET) and heptane- (CPHP) pretreatment are presented in Figures 3.1, 3.2 and 3.3, respectively and, those for virgin almond hull (AH, without pretreatment), ethanol- (AHET) and heptane- (AHHP) pretreatment are shown in Figures 3.4, 3.5, and 3.6, respectively. Table 3.4 summarises the common assignment bands observed.

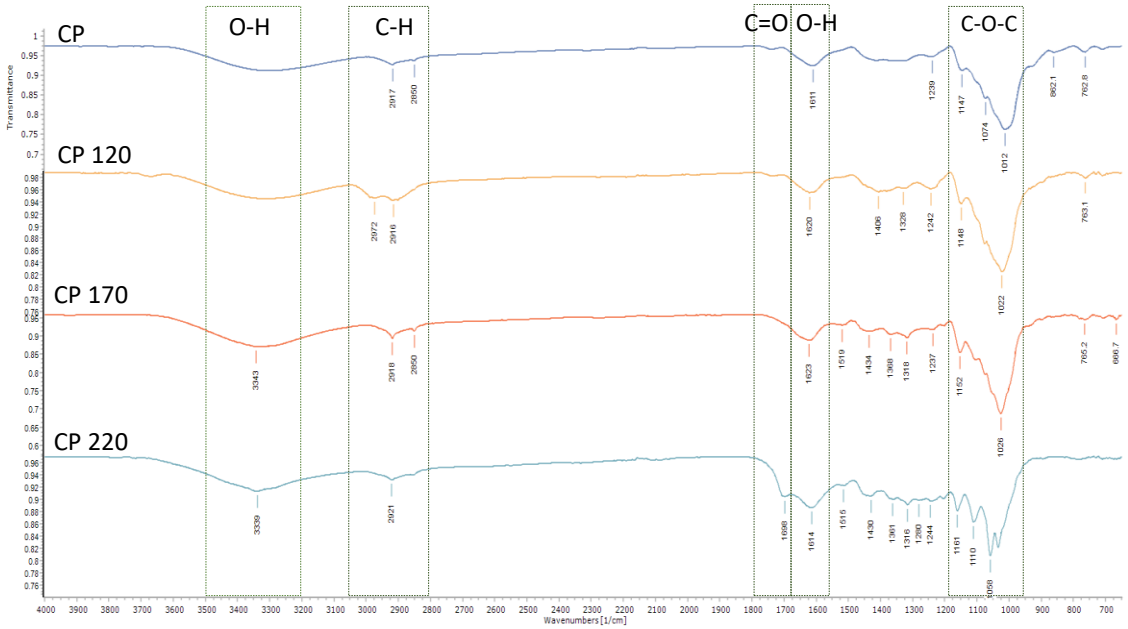

Figure 3. 1 ATR-IR spectra of MFC produced from CP at different processing temperature (Original in colour)

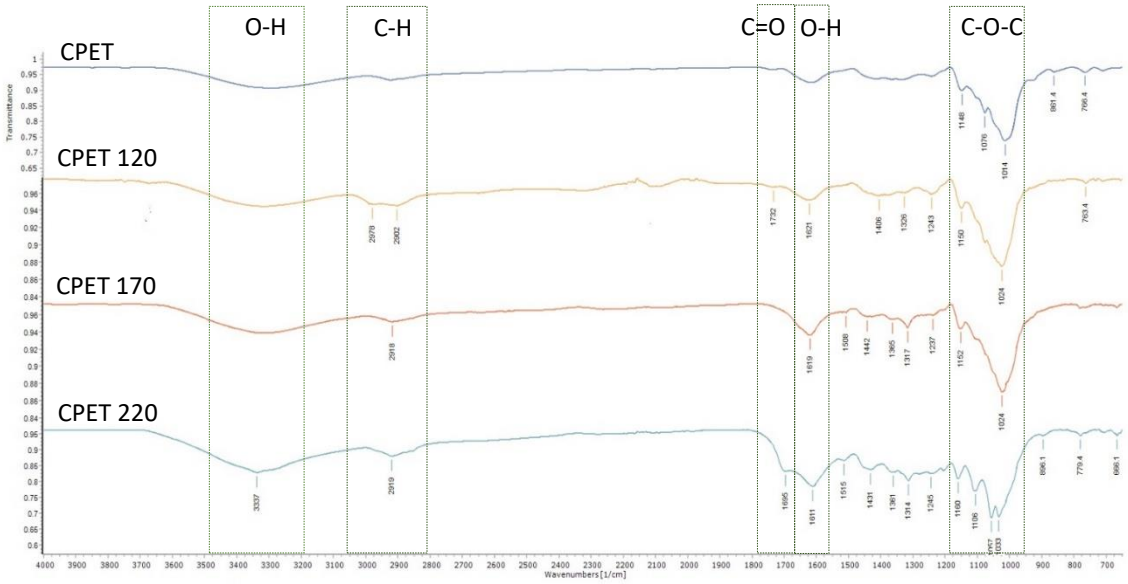

Figure 3. 2 ATR-IR spectra of MFC produced from CPET at different processing temperature (Original in colour)

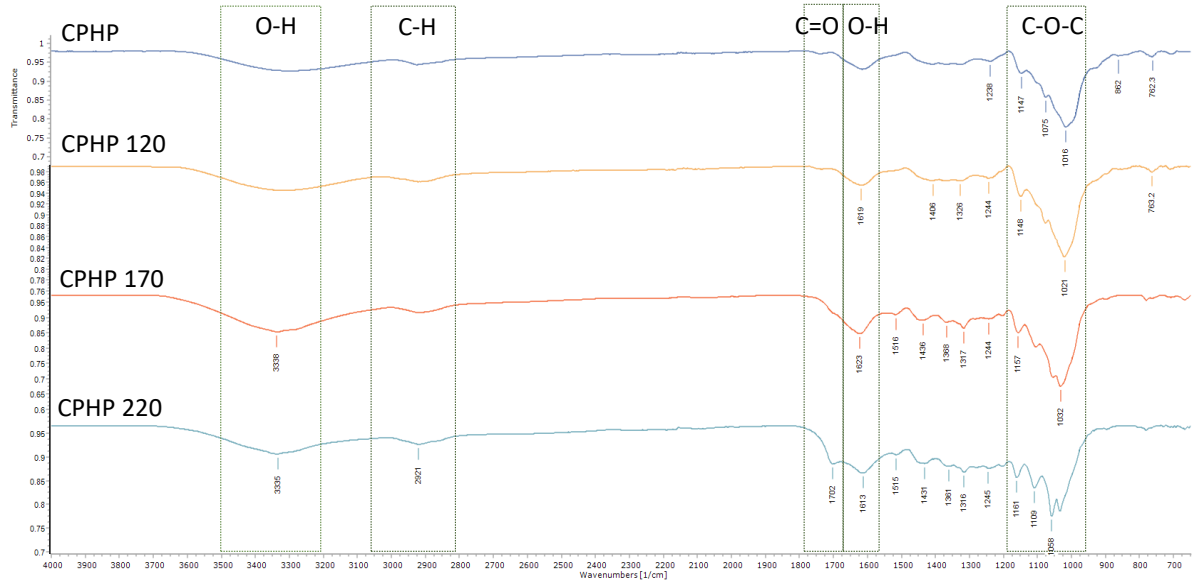

Figure 3. 3 ATR-IR spectra of MFC produced from CPHP at different processing temperature (Original in colour)

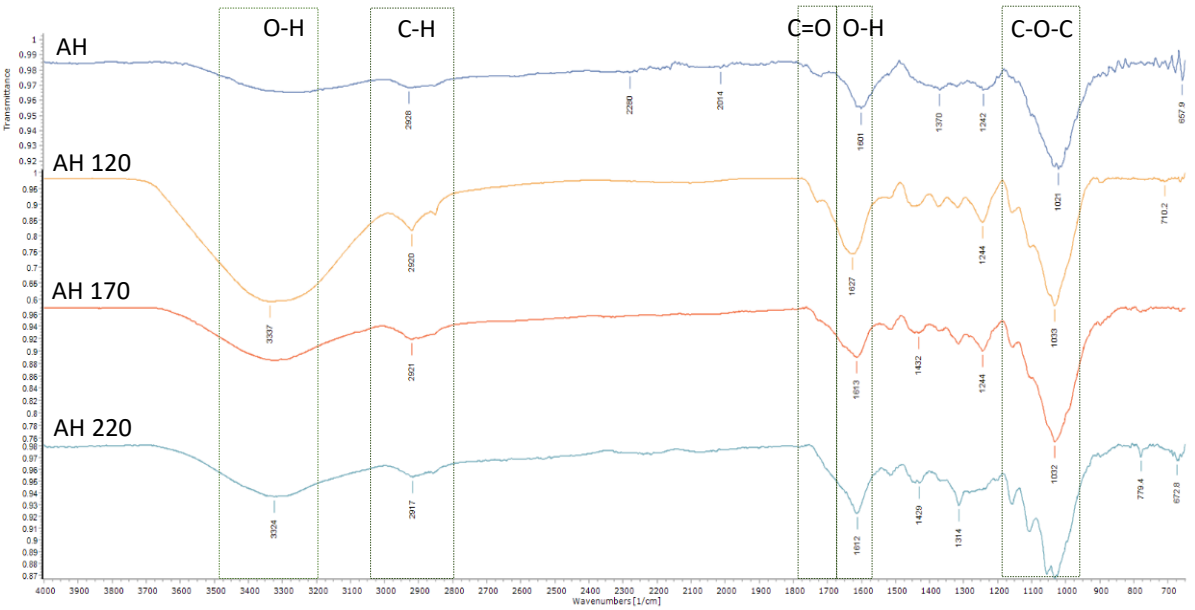

Figure 3. 4 ATR-IR spectra of MFC produced from AH at different processing temperature (Original in colour)

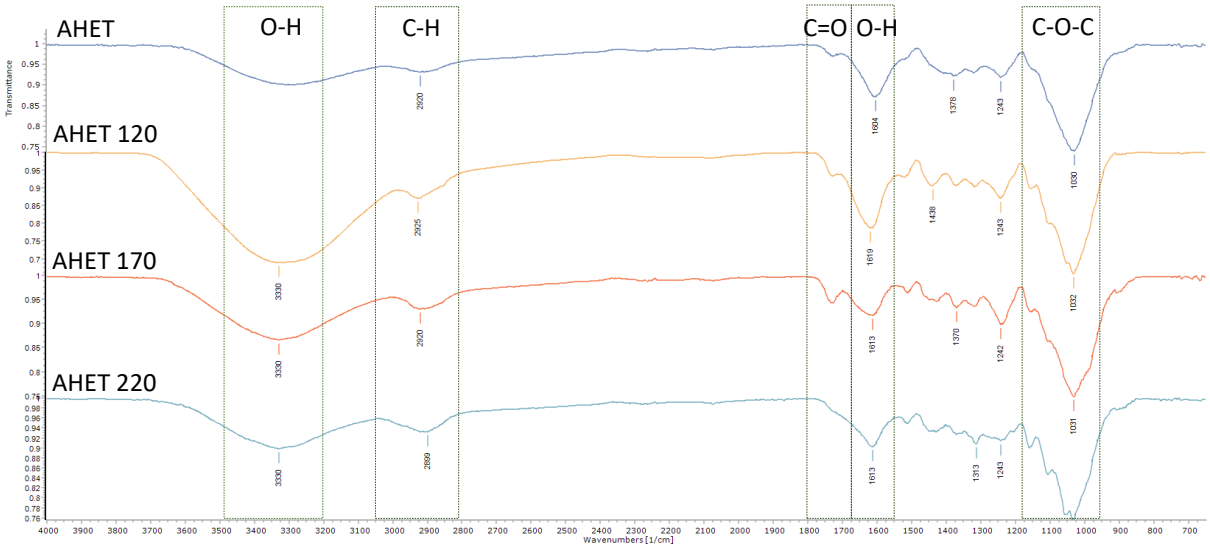

Figure 3. 5 ATR-IR spectra of MFC produced from AHET at different processing temperature (Original in colour)

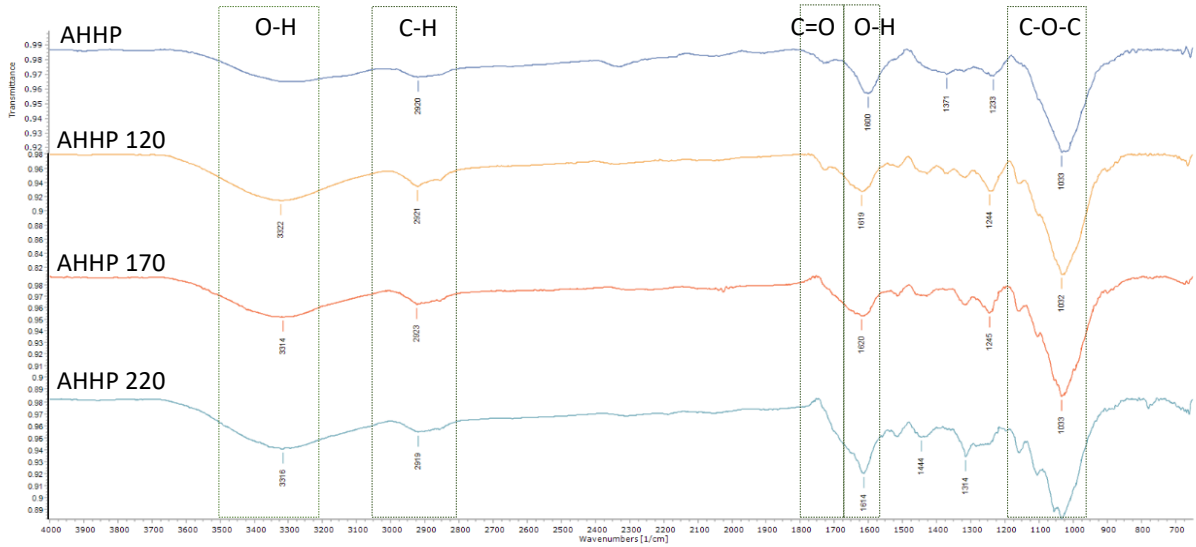

Figure 3. 6 ATR-IR spectra of MFC produced from AHHP different processing temperature (Original in colour)

The ATR-IR spectra of all virgin samples (both untreated: CP (Figure 3.1) and AH (Figure 3.4), and; pretreated: CPET (Figure 3.2), CPHP (Figure 3.3), AHET (Figure 3.5) and AHHP (Figure 3.6)) exhibit characteristic broad absorption band centred at approximately 3300 cm^{-1} corresponding to the O–H stretching vibration synonymous with hydroxyl groups

within cellulose at residual or inherent trapped water. The broadness of this absorbance band is indicative of extensive hydrogen bonding.[88] The C-O polysaccharide skeletal structure is evidenced by very strong absorbance bands in the region 1200-1000 cm^{-1} associated with C-O stretching mode. Specifically, the broad, prominent band at approximately 1150 cm^{-1} is assigned to the glycosidic linkages (C-O-C) between the glucose units and the ring stretching of glucose leads to absorbance bands at 1175 and 895 cm^{-1}.[89] C-H bonding is evidenced by C-H stretching vibrations at approx. 2900 cm^{-1}.[90,91] Often trapped water is detected by the O-H deformation mode, which is observed at approximately 1600 cm^{-1}.[92]

Table 3. 4 Common ATR-IR bands of cassava peel and almond hull MFCs

Infrared band/cm^{-1}	**Functional group assignment**
3345-3300	OH stretching
2980-2850	CH stretching
1735-1695	C=O stretching
1630-1600	O-H of water adsorbed on cellulose
1530-1500	C=C stretching
1450-1425	CH_2 deformation
1380-1310	C-H deformation
1250-1235	O-H deformation
1175-1100	C-O-C stretching
1060-1000	C-O stretching
910-895	C-H ring stretching [89]
895-885	C-H out of plane bending [91]
670-650	C-OH out of plane bending

The effect of microwave processing temperature on cassava peel, either virgin untreated (CP, see Figure 3.1) or pretreated (CPET (Figure 3.2), CPHP (Figure 3.3)) with respect to changes in functional groups, as analysed by ATR-IR, reveals disappearance of the weak carbonyl absorption centred at approximately 1730 cm^{-1} coupled with an increase

and sharpening of the C-O and C-O-C absorption bands in the region 1200-1000 cm^{-1} as the temperature increases from 120 ^{o}C to 170 ^{o}C. These changes are attributed to leaching of hemicellulosic and/or pectinaceous substances from the biomass. The carbonyl absorption (1700 cm^{-1}) reappears in samples processed at 220 ^{o}C (CP 220, CPET 220 and CPHP 220) which may be attributed to leaching of amorphous cellulose coupled with cellulose decomposition to afford *pseudo*-lignins that migrate to the surface of the material. On visual inspection, samples processed at 220 ^{o}C were darker in colour than their lower temperature counterparts. Alternatively, this absorbance band may be attributed to condensed tannins and/or migration of lignins from with cell walls to the exterior surface. Thus, the absorbance band at approx. 1720 cm^{-1} may correspond to carbonyl stretching vibrations associated with ferulic and *para*-coumaric acid lignin.[93,94]

A similar effect of microwave processing temperature with respect to changes in functional groups, as analysed by ATR-IR, with almond hulls, either virgin untreated (AH, see Figure 3.4) or pretreated (AHET (Figure 3.5), AHHP (Figure 3.6)) was noted. Subtle changes include a stronger carbonyl absorbance band which persists up to 170 ^{o}C.

3.2.3 Crystallinity index

The X-ray diffraction (XRD) patterns were analysed with an X-ray diffractometer (Bruker Powder XRD) at room temperature. The cellulose was scanned with a monochromatic Cu-Kα radiation source (λ= 0.1539 nm) in the step-scan mode with a 2θ angle ranging from 5° to 38° with a step of 0.1 and scanning time of 2.0 min. Using the Segal method (Eq. 3.1), the total intensity after the subtraction of the background signal (measured without cellulose), the crystallinity index (CI) can be identified from the heights of the 200 peak and the intensity minimum from 200 to 110 bands [95,96]. I_{002} represents a

crystalline region at 2θ= 22.3°, while I_{am} represents the amorphous region at 2θ=18.1°. The value of the crystallinity index (CI) for cassava peel and almond hull MFC at different processing temperature was calculated and summarized in Table 3.5.

$$\text{Crystallinity index /\%} = \frac{(I_{002} - I_{am})}{I_{002}} x100 \qquad \text{(Eq. 3. 1)}$$

Table 3. 5 Crystallinity Index (%) of cassava peel and almond hull MFCs

MFC samples	Hydrothermal treatment temperature/°C		
	120	170	220
	Crystallinity index/%		
CP	12.7	41.3	63.1
CPET	18.3	44.7	63.9
CPHP	17.1	50.6	65.7
AH	36.6	42.7	54.4
AHET	45.2	45.4	61.5
AHHP	45.8	53.2	55.2

The crystallinity index of all MFCs increases with increasing temperature. The highest crystallinity index was achieved for cassava peel MFCs (63.1 – 65.7%). Interestingly, cassava peel MFCs have the lowest crystallinity index at 120 °C but have the highest crystallinity at 220 °C. For example, the crystallinity index of CPHP at 120 °C changes from 17.1% to 65.7% at 220 °C equating to the difference of |48.6%|. The almond hull samples at 120 °C possess crystallinity indexes from 36.6 – 45.8% and increase to 54.4 – 61.5% at 220 °C. The difference from the initial (120 °C) to final temperature (220 °C) is far less drastic, for example, AHHP shows a difference of 9.4%. Thus, the constituents within cassava peel, irrespective of pretreatment or not, are more sensitive to leaching under microwave hydrolysis than are almond hulls. More hemicellulosic matter and amorphous cellulose are lost giving a higher final %-age of crystalline cellulose. Interestingly, as shown

in Table 3.1 (see earlier) the hemicellulose and cellulose composition of virgin, raw, almond hulls and cassava are very similar. The only difference being the lignin content, which is significantly higher in almond hulls. Thus, the higher amount of lignin in almond hulls may be preventing, shielding or blocking hydrolysis of hemicellulose and amorphous cellulose.

The XRD patterns for all samples at different stages of treatment is shown in Figure 3.7. As for most polymers, cellulose can be crystalline, semi-crystalline or amorphous. The MFC of cassava peel and almond husk shows a characteristic peak corresponding to the so-called cellulose I polymorph. Cellulose I can be found in native cellulose and consists of two different crystalline allomorphic forms of cellulose; I_α that can be founded from bacteria or algae and I_β which can be sourced from higher plants.[97] The XRD patterns at 170 ^oC and 220 ^oC shows that MFC resulting from microwave hydrothermal is cellulose I. There is no evidence of a split peak between 2θ = 20.1^o and 21.53^o assigned for 110 and 220 cryptographic planes of crystalline cellulose II.[94,98] From Figures 3.7 A, a characteristic diffractogram pattern of cellulose I_β can be found at the 14.8° (2θ) reflection which is assigned to the ($1\bar{1}0$) crystallographic plane. At 16° (2θ) the reflection is assigned to the (110) crystallographic plane. At 18° (2θ) the reflection is assigned to the amorphous phase. At 22.0-22.6° (2θ) the reflection is assigned to the (200) crystallographic plane and 34.5^o (2 θ) is assigned to the 004 plane.[97,99,100].

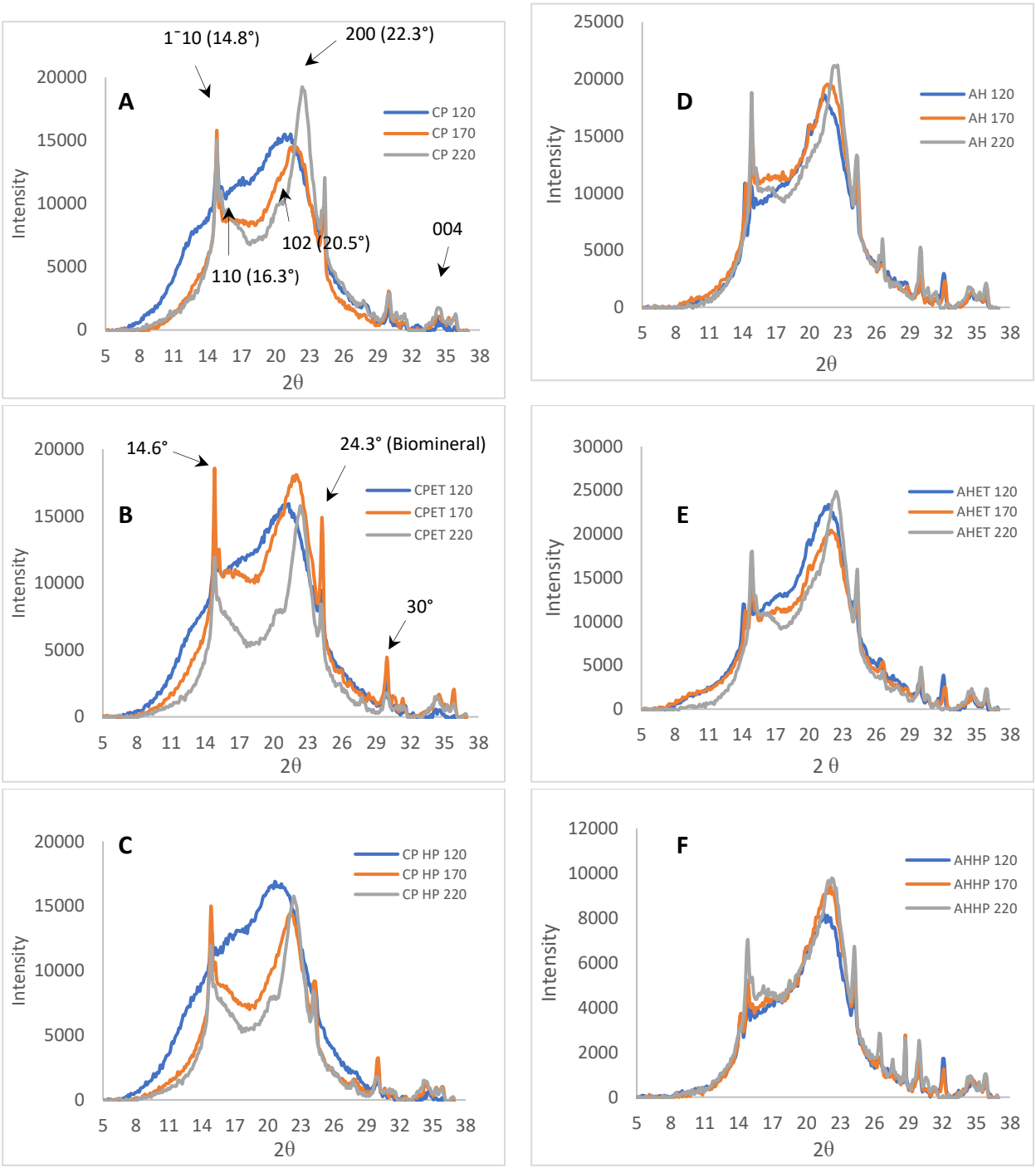

Figure 3. 7 XRD spectra of cassava peel and almond hull MFC; A) CP, without pretreatment B) CPET, ethanol pretreatment C) CPHP, heptane pretreatment D) AH, without pretreatment E) AHET, ethanol pretreatment F) AHHP, heptane pretreatment (Original in colour)

The sharp peaks found during XRD are likely to arise from mineral impurities. Tazaki *et al*.[101] studied crystalline cellulose from Kurugaki trunk trees and was able to identify bio-minerals in the wood using XRD. A similar pattern of sharp peaks at 14.6°, 24.3° and 30° as shown on Figure 3.7B suggested the presence of kaolinite ($Al_2Si_2O_5{\cdot}(OH)_4{\cdot}H_2O$), cristobalite ($SiO_2$), and apatite ($Ca_5(PO_4)_3$(F, Cl, OH) which may originate from the soil with clay and weathered rocks.[101] Melo *et al.*[102] also reported the presence of biominerals, such as calcium oxalate, in MFCs prepared via acid-free microwave hydrolysis of citrus peels.

3.2.4 Thermal stability

Thermogravimetry analysis (TGA) was performed to investigate the thermal stability of cellulose under N_2 gas as shown in Figure 3.8 and 3.9 The maximum thermal degradation temperatures of cellulose in cassava peel and almond hull with respect to microwave processing temperature has been extracted from these figures and are summarised in Table 3.6.

Table 3. 6 Thermal stability cellulose (°C) of cassava peel and almond hull

Cellulosic samples	**Microwave-assisted hydrolysis temperature/°C**			
	Raw	**120**	**170**	**220**
	Cellulose decomposition temperature/°C			
CP	299.40	306.83	358.20	372.13
CPET	304.50	320.34	360.28	369.26
CPHP	298.17	309.36	362.17	374.15
AH	303.21	347.53	351.68	363.28
AHET	300.42	346.18	346.77	364.03
AHHP	304.12	349.79	353.56	359.43

Biomaterial thermal depolymerisation occurs in multiple stages, depending on the thermal stability of each chemical component and composition in the biomass.[93] From

figures 3.8 and 3.9, the initial mass loss seen in all samples from 60 to 160°C can be attributed to the vaporisation of water and/or volatiles from the biomaterial amounting to approximately 10% mass. Thereafter, there is a distinct difference in the degradation of cassava peel with respect almond hulls. The latter (see Figure 3.9A (AHNT), 3.9B (AHET) and 3.9C (AHHP)) shows a strong thermal event between 170 and 220 °C which may be due to pectinaceous-like matter or an unidentified high-molecular weight flavonoid or polyphenol. This thermal event is not seen in cassava peel. Thereafter, both cassava peel (CP, CPET and CPHP) and almond hulls (AHNT, AHET and AHHP) show a thermal event at approximately 220 ^{o}C which is more akin to the decomposition of pectinaceous matter.[103,104] This thermal event is much weaker for cassava peel. The next major thermal event occurs in the region 298-372^{o}C characteristic of decomposition of a mixture of hemicellulose and cellulose.[98] This decomposition temperature moves towards higher temperatures with respect to increasing microwave processing temperature, *i.e*, the samples are tending towards crystalline cellulose which correlates well the crystallinity index data reported earlier and the thermal stability gap for AH cellulosic matter is less dramatic than for CP.

Hemicellulose is more easily hydrolysed than cellulose due to the amorphous structure while cellulose has a long crystalline chain of glucose polymer, enhancing its thermal stability.[105] It can be seen clearly that a notable shoulder corresponding to the depolymerisation of hemicellulose in the untreated (the raw fibres) almond hull (225^{o}C-290^{o}C) in Figure 3.9 which disappears following pretreatment. Meanwhile, lignin content decomposition occurs from 250 ^{o}C to 500 ^{o}C where the thermal decomposition lignin is

very high due to the cross-linking of phenylpropane units and other high molecular weight groups. [98,106]

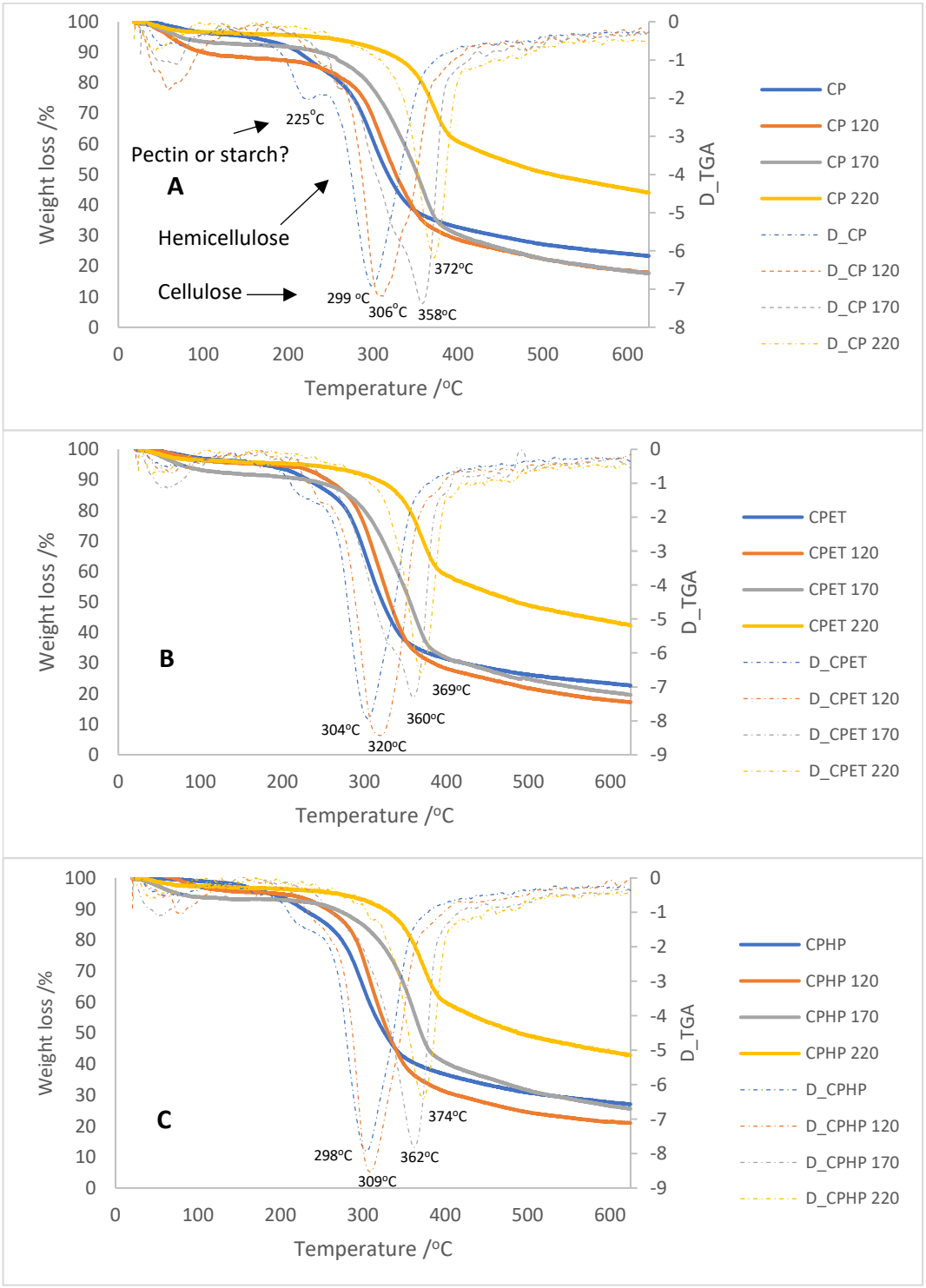

Figure 3. 8 TGA results of cassava peel A) without pretreatment B) pretreatment with ethanol C) pretreatment with heptane (Original in colour)

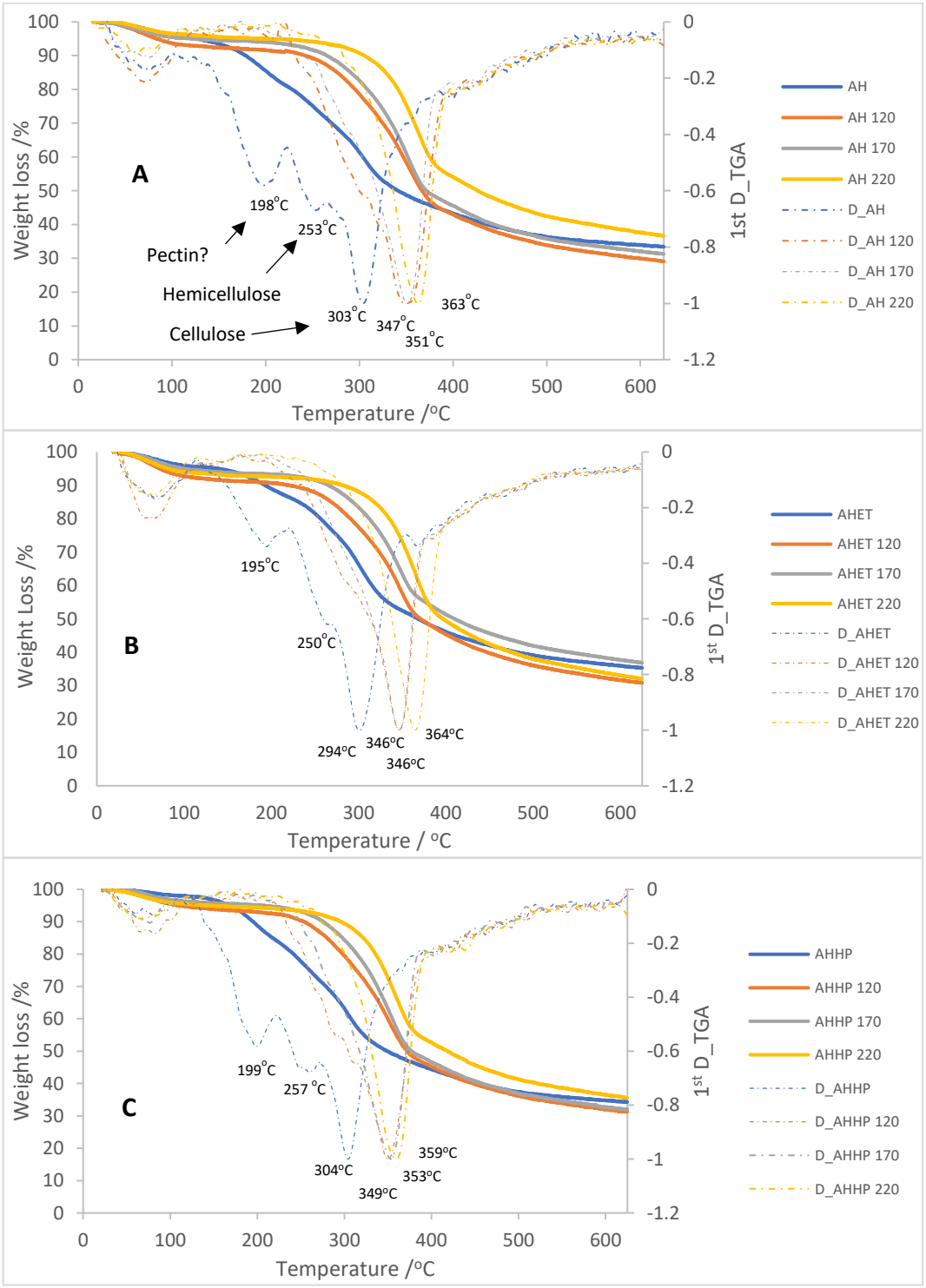

Figure 3. 9 TGA results of almond hull A) without pretreatment B) pretreatment with ethanol C) pretreatment with heptane (Original in colour)

Interestingly, there appears to be a significant change in the amount of residue left at 625 ^{o}C for all cassava peel samples processed at 220^{o}C (CP, CPET and CPHP) in Figure 3.8. Samples processed at 120 ^{o}C and 170 ^{o}C (and virgin CP) afford 20-25% by wt. residue whilst at 220 ^{o}C approx. 40-45% by wt, residue remains. This material may have undergone significant hydrolytic pyrolysis to afford a *pseudo*char *or pseudo*lignin-like material. As discussed previously, significant darkening of samples processed at 220 ^{o}C is observed. This significant change in residue content was not observed in almond hulls samples. The residue content was approx. 35%.

3.2.5 ^{13}C Solid-state CPMAS NMR analysis

Table 3.7 summarises the deconvoluted chemical shifts (ppm) for the anhydroglucose portion of cellulose in virgin cassava peel (CP), virgin almond hull (AH), ethanol pretreated (CPET or AHET), heptane pretreated (CPHP or AHHP) and their respective MFCs obtained at 120 ^{o}C, 170 ^{o}C and 220 ^{o}C. The corresponding full NMRs are shown in Figures 3.10 to 3.15, which reveal additional resonances at approx. 165-180 ppm, 110-160 ppm and 25-40 ppm (see later for discussion).

The resonances identified in table 3.7 are characteristic of an anhydroglucose unit synonymous with carbohydrate polymers. For example, starch shows resonances at: C1(100 ppm), C4(82 ppm) C2, C3, C5 (74-70 ppm) and C6 (61 ppm).[107,108] CP 120 shows a series of resonances: C1(103 ppm), C4(82 ppm), C2,3,5 (72-74 ppm), and C6 (64 ppm) possibly corresponding to hemicellulose of composed 1-4-linked β-D-xylopyranose units.[109] The virgin almond hull appeared to contain 4-*O*-methyl glucuronic acid from hemicellulose where the chemical carbon shift of C1 (98 ppm), C4 (83 ppm) C3 (73 ppm) as reported by Lyu *et al*.[109] The chemical shift of crystalline cellulose I_{β} signals are C1 (106 and 104 ppm),

C2 (71 ppm), C3 (74.9 ppm), C4 (88.9 ppm), C5 (72 ppm), C6 (65 ppm)[110], those resonances are corresponding with all MFCs produced at a temperature of 220 ^{o}C.

Table 3. 7 Deconvoluted ^{13}C CPMAS NMR spectra (ppm) of cassava peel and almond hull MFCs

Cellulosic samples	**Resonances/ppm**					
	C1	**C4**	**C2, C3, C5**			**C6**
CP	104.65, 100.44	82.75	-	72.62	75.76	62.66, 60.48
CP 120	105.71, 103.34	82.86	-	72.74	75.74	62.98, 60.63
CP 170	104.41	88.91, 82.85	-	72.69	75.37	65.53, 62.84
CP 220	106.16, 104.69	88.98, 84.83	71.96	72.99	75.33	65.47, 63.39
CPET	104.63, 100.76	82.94	-	72.64	75.46	62.67
CPET 120	103.52	82.97	-	72.66	75.09	62.94, 60.92
CPET 170	105.18	89.22, 83.75	-	72.66	75.34	65.42, 62.70
CPET 220	106.05, 104.60	88.94, 84.04	71.89	72.89	75.29	65.53, 65.26
CPHP	104.24, 100.33	82.73	-	72.65	75.65	62.58
CPHP 120	103.50	82.88	-	72.74	75.22	61.90
CPHP 170	105.90, 104.54	88.95, 84.33	-	72.57	75.31	65.51, 62.73
CPHP 220	106.03, 104.60	89.33, 84.26	71.90	73.02	75.28	65.52, 63.32
AH	105.26, 99.28	83.34	-	72.32	75.23	65.15, 62.67
AH 120	105.28	89.12 83.73	-	72.55	75.16	65.20, 62.94
AH 170	105.36	89.14, 83.95	-	72.29	75.12	65.28, 62.63
AH 220	106.01, 104.61	89.07, 84.15	71.84	72.87	75.33	65.42, 62.74
AHET	105.13, 98.87	83.87	-	72.35	75.32	65.34, 63.04
AHET 120	105.27	88.97, 83.34	-	72.29	75.16	65.25, 62.63
AHET 170	105.51	89.07, 82.86		72.40	75.28	65.29, 62.54
AHET 220	106.00, 104.60	89.13, 83.95	71.80	72.87	75.23	65.33, 62.73
AHHP	105.45, 99.04	83.47	-	72.39	75.41	65.13
AHHP 120	105.85	89.40, 84.03	-	72.61	75.51	65.39, 62.90
AHHP 170	105.58	89.27, 83.91	-	72.56	75.46	65.38, 62.78
AH HP 220	105.92, 104.70	89.04, 84.12	71.91	72.85	75.4	65.99, 62.99

Effective removal of hemicellulose from cellulose and the increase in the degree of crystallinity can be observed by analysis of the resonances for C4 (82-89 ppm) and C6 (62-66 ppm) which are indicative of amorphous and crystalline cellulose. On increasing the

processing temperature from 120 °C to 170 °C to 220 °C these resonances start to split into two and become sharper. The resonances associated with amorphous cellulose decrease in intensity whilst those for crystalline cellulose increase.[111] Additionally, the C2, C3 and C5 resonances also become sharper and separated with respect to increasing temperature. For example, a clear resonance can be observed at approx. 71 ppm in all samples processed at 220 °C. Interestingly for cassava peel MFC at 220 °C, the broad resonances at 173-178 ppm, 160-110 ppm and 21-30 ppm may be attributed to lignin and/or *pseudo*lignins.[112–114] Again, this supports previous data (crystallinity index, ATR-IR and TGA) and the notion that above 170 °C significant leaching of amorphous cellulose takes place coupled with lignin either moving to surface or decomposition of cellulose to afford *pseudo*lignins.

Of particular note on comparing the differences in the spectra of virgin cassava peel (CP) and virgin almond hull (AH) is the significant presence of resonances in the aromatic region (110-160 ppm) and alkyl region (20-40 ppm) in the latter. This analysis may also confirm our original compositional data analysis (see Table 3.1) which revealed that virgin almond hull possesses significantly more lignin (ca. 11%) compared to cassava peel (ca. 3%). The resonances for lignin remain for all AH samples processed and CP at 220 °C will also include resonances associated with *pseudo*lignins.

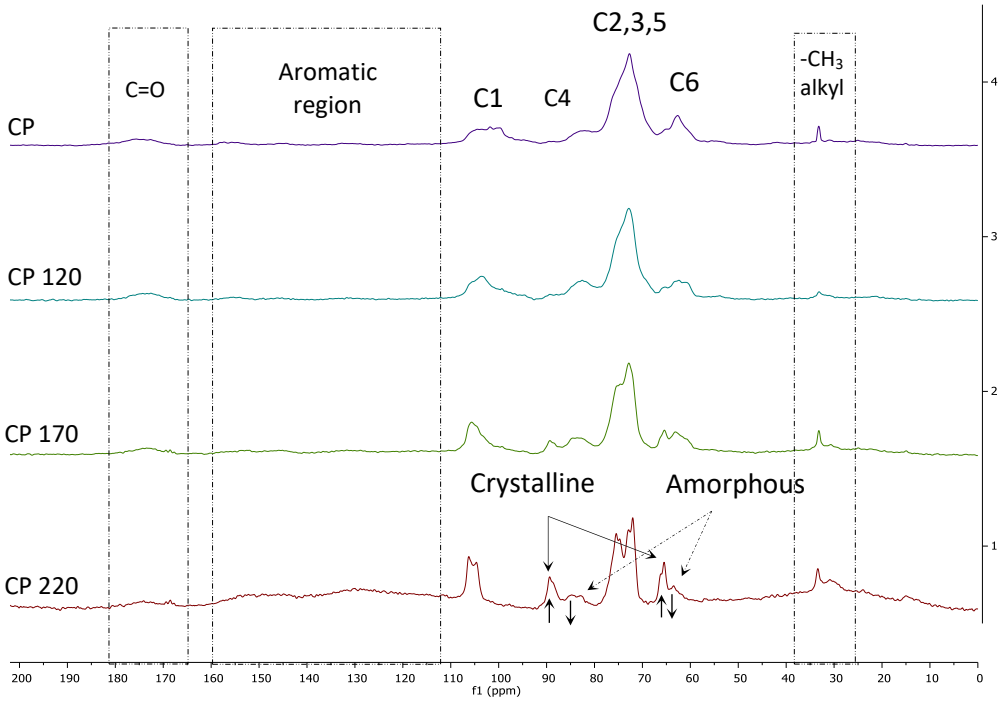

Figure 3. 10 ^{13}C CPMAS NMR spectra of virgin CP and its corresponding MFCs (Original in colour)

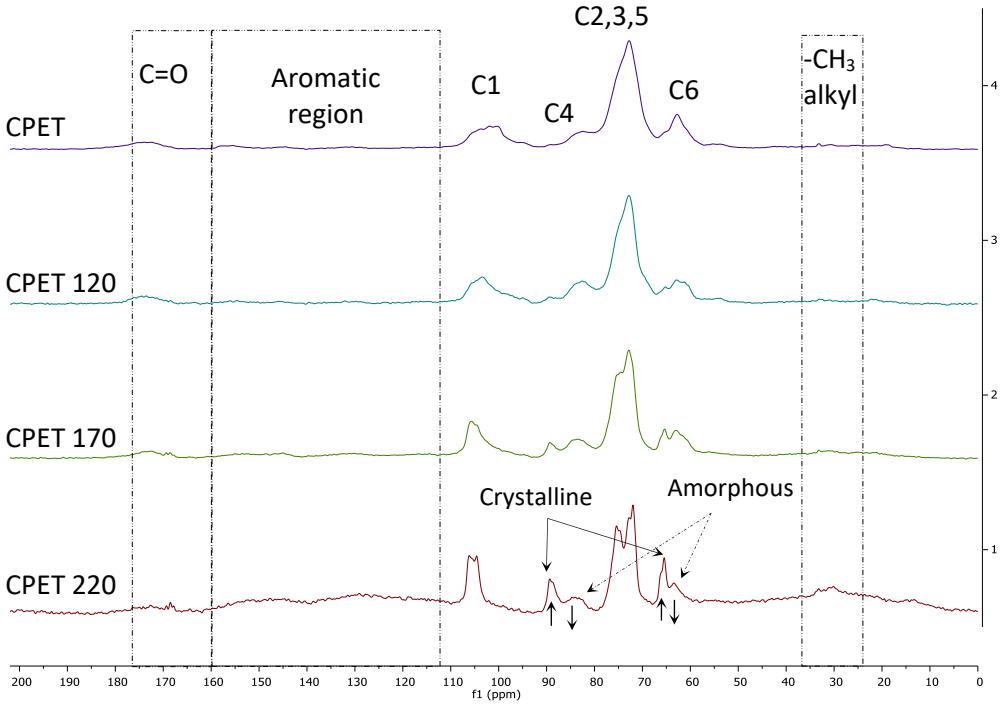

Figure 3. 11 ^{13}C CPMAS NMR spectra of CPET and its corresponding MFCs (Original in colour)

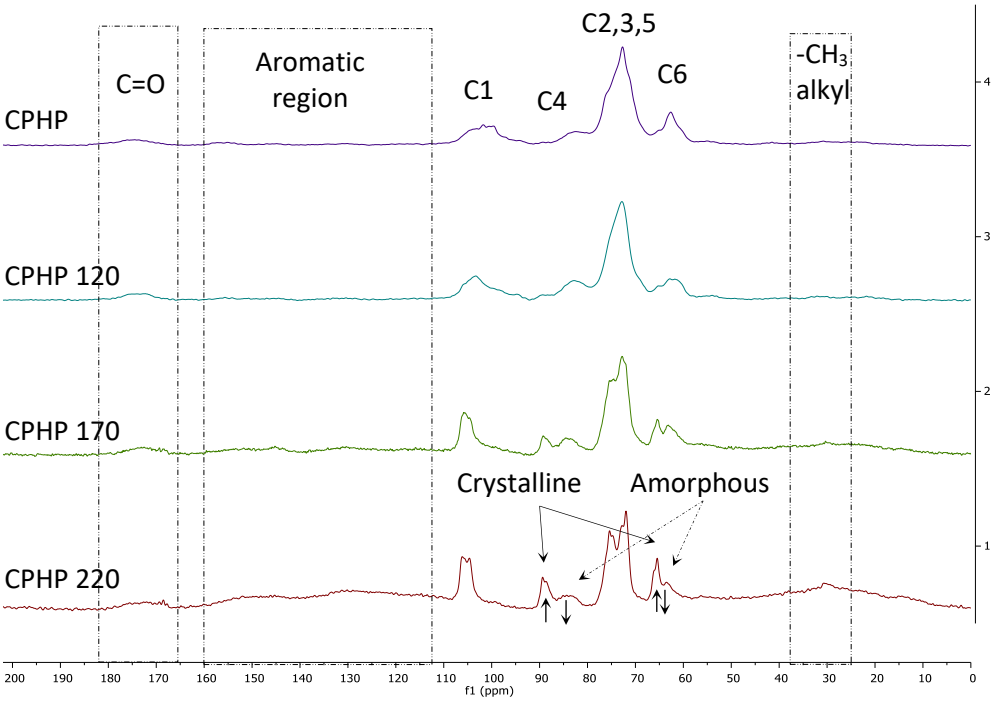

Figure 3. 12 ^{13}C CPMAS NMR spectra of CPHP and its corresponding MFCs (Original in colour)

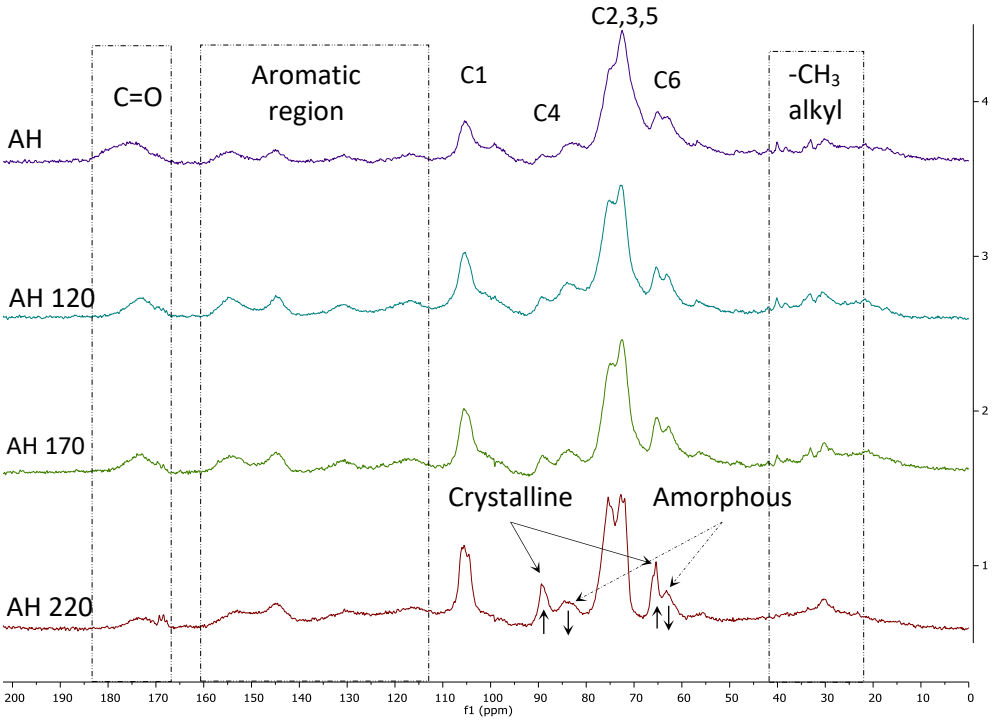

Figure 3. 13 CPMAS NMR spectra of virgin AH and its corresponding MFCs (Original in colour)

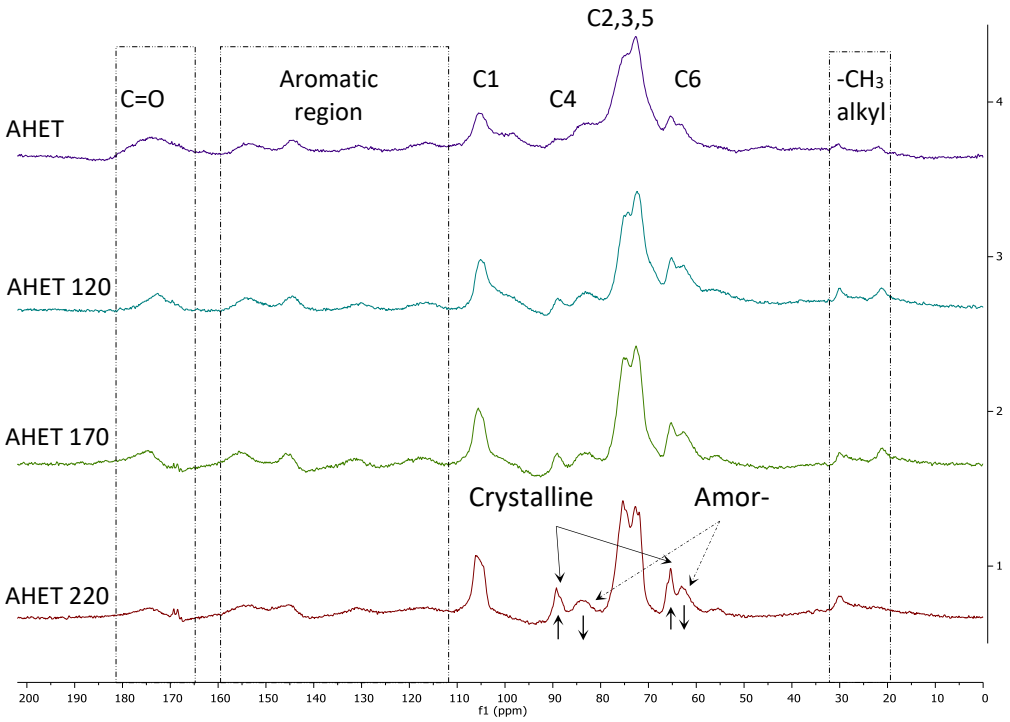

Figure 3. 14 ^{13}C CPMAS NMR spectra of AHET and its corresponding MFCs (Original in colour)

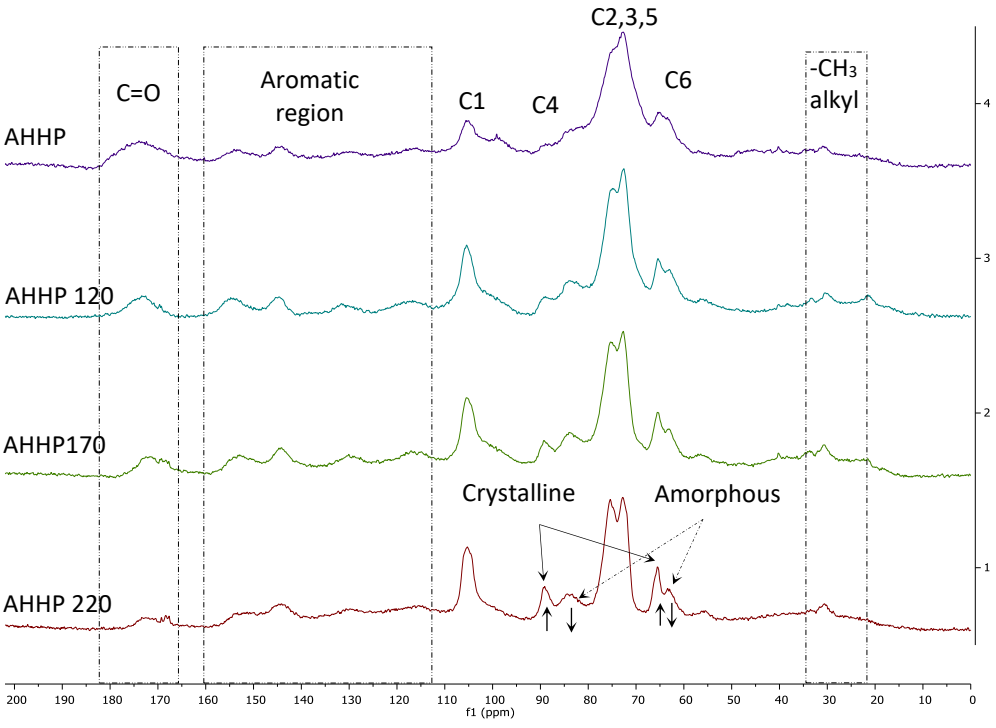

Figure 3. 15 ^{13}C CPMAS NMR spectra of AHHP and its corresponding MFCs (Original in colour)

3.2.6 TEM analysis

According to TAPPI WI3021,[115–117] the hierarchical structure of cellulose fibres can be classified into nano-objects (cellulose nanocrystal (CNC), cellulose nanofibril (CNF)) and nanostructured cellulose (cellulose microcrystal (CMC), cellulose microfibril (CMF). CNC is pure crystalline fibres with W = 3-10 nm and aspect ratio L/W = 5-50 while CNF is fibrous cellulose of plant material that contains both crystalline and amorphous regions (W=5-30 nm, aspect ratio L/W > 50). Cellulose microcrystal (CMC) is depolymerised high purity cellulose (DP < 400) with structured bundle of cellulose (W 10-15 µm, aspect ratio L/W < 2) while CMF or microfibrillated cellulose (MFC) is purified wood or non-wood producing multiple elementary fibrils with both crystalline and amorphous regions which typically still contains residual hemicellulose (W= 10-100 nm, L =0.5 -10 µm). The summary of standard terms for nanocellulose is shown in Figure 3.16.

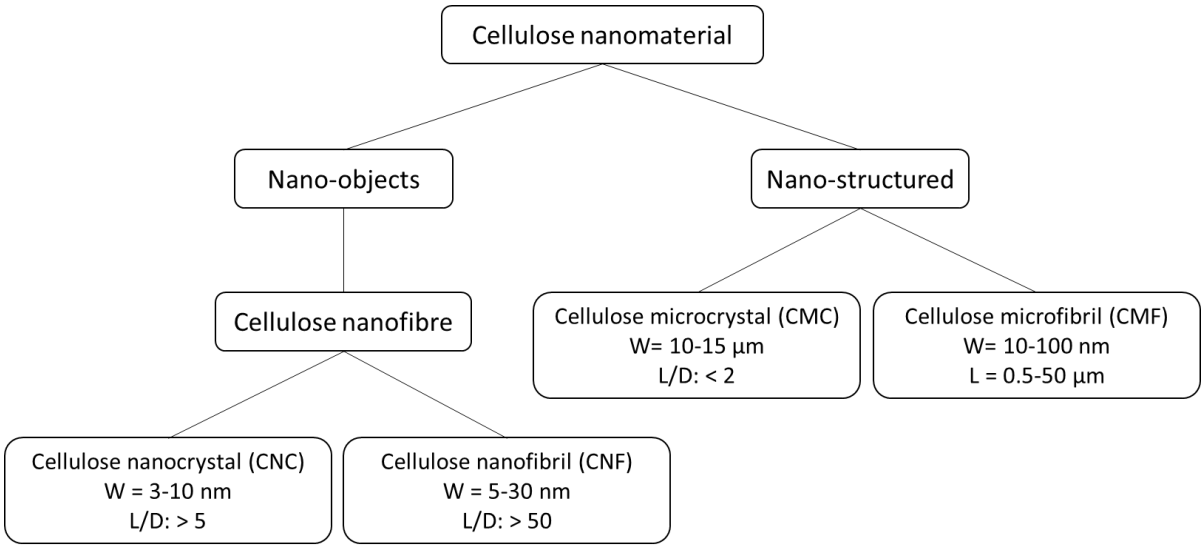

Figure 3. 16 Standard terms for nanocellulose [117]

Figure 3.17 shows the TEM images for virgin cassava peel (CP), with ethanol pretreatment (CPET) and with heptane pretreatment (CPHP). The black arrow on each image highlights the microfibril width as calculated through the ImageJ software. A progressive (de)fibrillation of fibres into individualized microfibrils with increasing microwave processing temperature can be observed. It can also be seen that the width of all fibres is relatively similar and less than 11 nm when prepared using microwave treatment with operating temperatures from 120 ^{o}C to 220 ^{o}C. Thus, according to TAPPI WI3021 our method of microwave-assisted hydrolysis of cassava peel actually produces nanocellulose.[118] The microfibril is split into smaller aspect ratios [119] and some elementary fibres (W < 3.5nm) can be found at 170 ^{o}C.[120,121] Nanocrystal-like or needle-like fibres (lower aspect ratio) [122] are observed at 220 ^{o}C from all sources with shorter length ranging 0.5-2.7 µm. The summary of the average fibre width of cassava peel MFCs is listed in Table 3.8.

Table 3. 8 The average width (nm) of cassava peel MFCs

MFC samples	**Microwave Processing Temperature/^{o}C**		
	120	**170**	**220**
	Average width/nm		
CP	7.2	4.8	4.9
CPET	4.0	3.8	4.1
CPHP	5.1	4.1	3.6

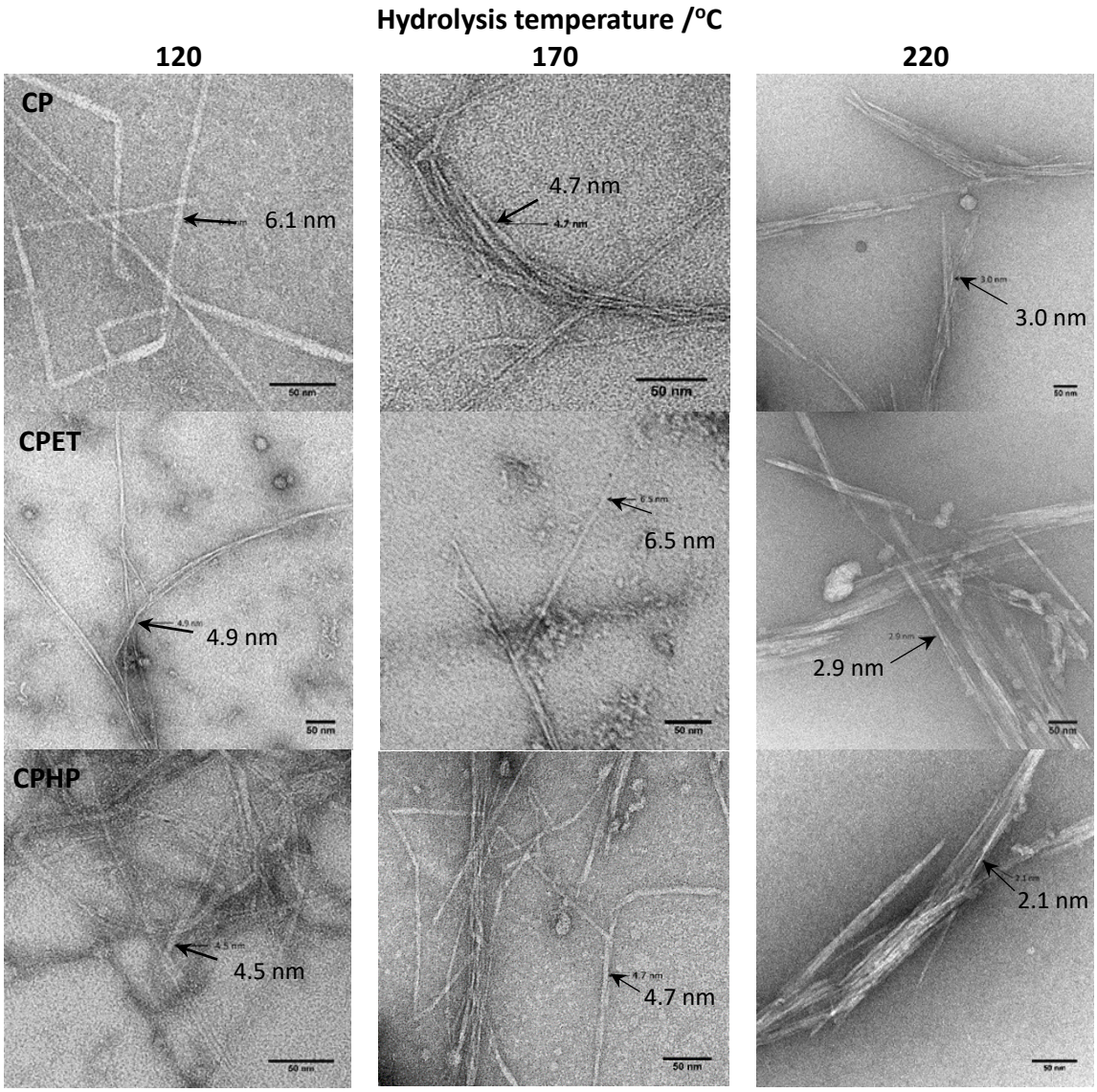

Figure 3. 17 TEM images of cassava peel MFCs at different processing temperatures

The TEM images of microfibrils obtained from microwave processing of almond hulls are shown in Figure 3.18 and their widths listed in Table 3.9. After microwave hydrolysis treatment average widths measured between 2.9 and 6.0 nm (Figure 3.18). Similar to cassava peel reported earlier, increasing microwave processing temperature induces defibrillation to microfibrils to nanofibers and nanocrystals.

Table 3. 9 The average of width (nm) of almond hull MFCs

MFC samples	Microwave Processing Temperature/°C		
	120	170	220
	Average width/nm		
AH	3.7	3.2	3.3
AHET	6.0	5.9	4.9
AHHP	4.8	3.4	2.9

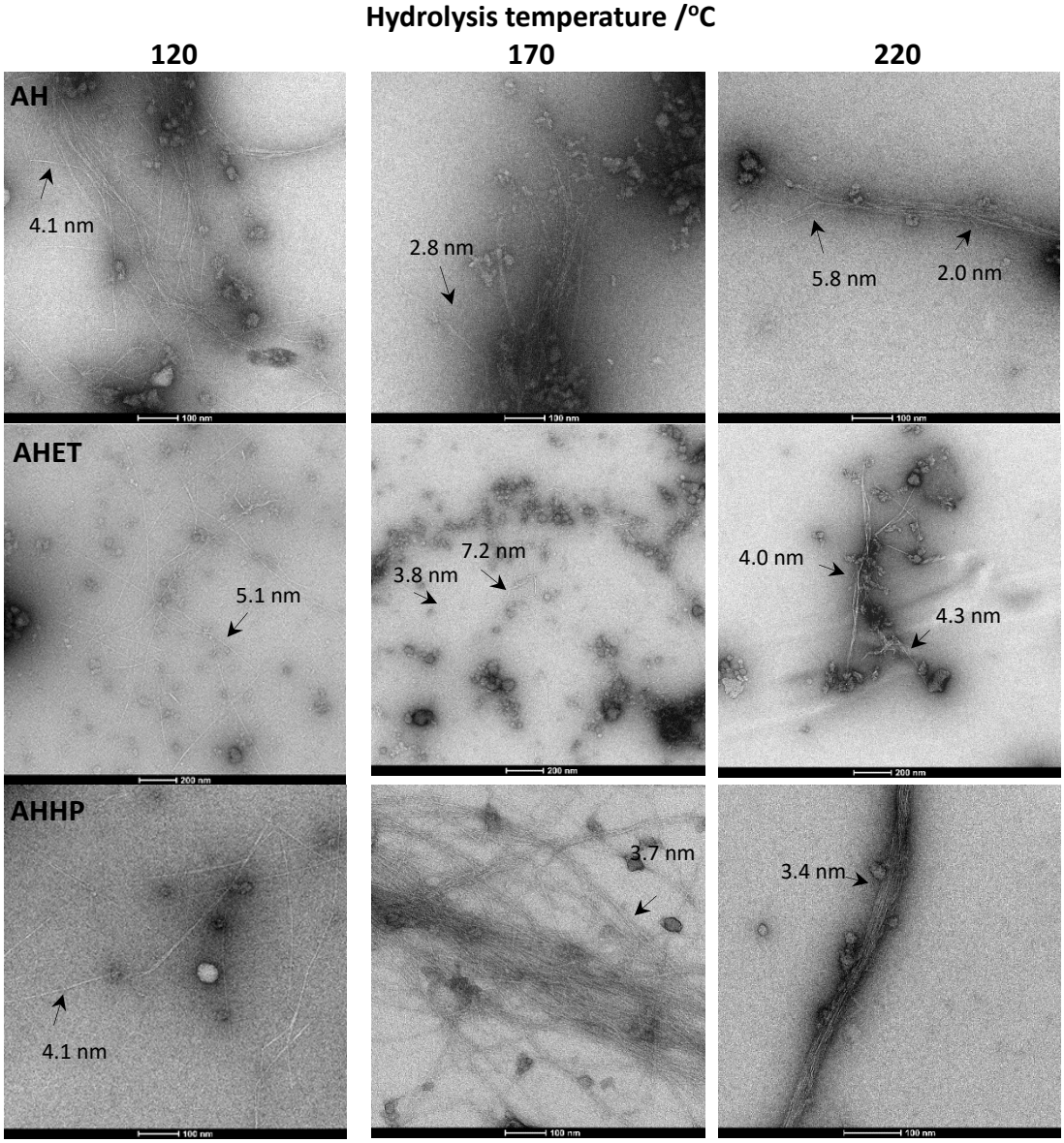

Figure 3. 18 TEM images of almond hull MFCs produced at different temperatures

Some residual amorphous matter entangled amongst the fibres was also present. The dark grey amorphous clusters are assumed to be *pseudo*lignin that cover the fibres at a temperature of 120 ^{o}C and 170 ^{o}C, while at 220°C, these recalcitrant clusters were hydrolysed at high temperature and were mainly composed of residual lignin-like fragments. [123]

3.2.7 SEM analysis

SEM micrographs were utilized for visualisation and investigation of the microstructural morphology of the MFCs.[124] Figure 3.19 shows a series of SEM images of MFCs derived from cassava peel, both with and without either ethanol or heptane pretreatment, processed at 120 ^{o}C. The surface morphology of CPHP 120 consists of a network of microfibrils that clearly cover the outer wall layer. An increase in temperature led to observable structural changes, as shown in Figure 3.19, with the disintegration of cellulose fibres into their structural components (microfibrils). Microfibrils are the main component of microfibrillated cellulose (MFC), although several studies have shown that fibrillation produces a material which may be composed of inhomogeneous fibres, e.g. fibres, fibre fragments, fines and fibrils.[121]

The SEM image of MFCs from the almond hull is shown in Figure 3.20. Microwave hydrothermal treatment appears to affect the structural and chemical characteristics of the fibres. The SEM images of AHET 220 (2000x magnification) showed the network of structured nanofiber-like cellulose due to the removal of amorphous components, but the rough surface attached on the microcellulose fibre was attributed to residual of lignin or *pseudo*lignin. [118] However, the surface of the cellulose cluster was still covered by residue from other materials (hemicellulose or lignin) in the images of AH 120 and 170.

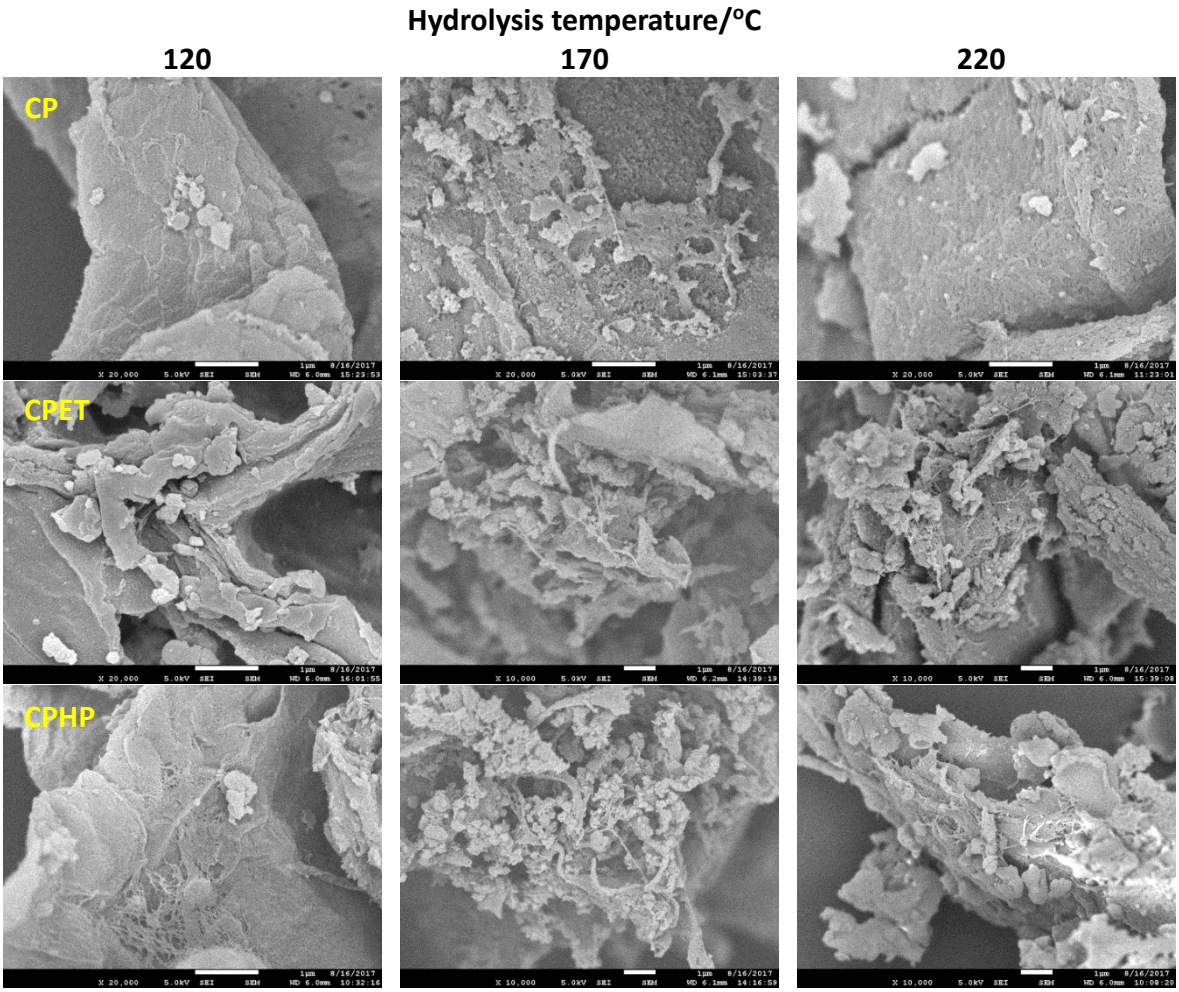

Figure 3. 19 TEM images of cassava peel MFCs with respect to processing temperature

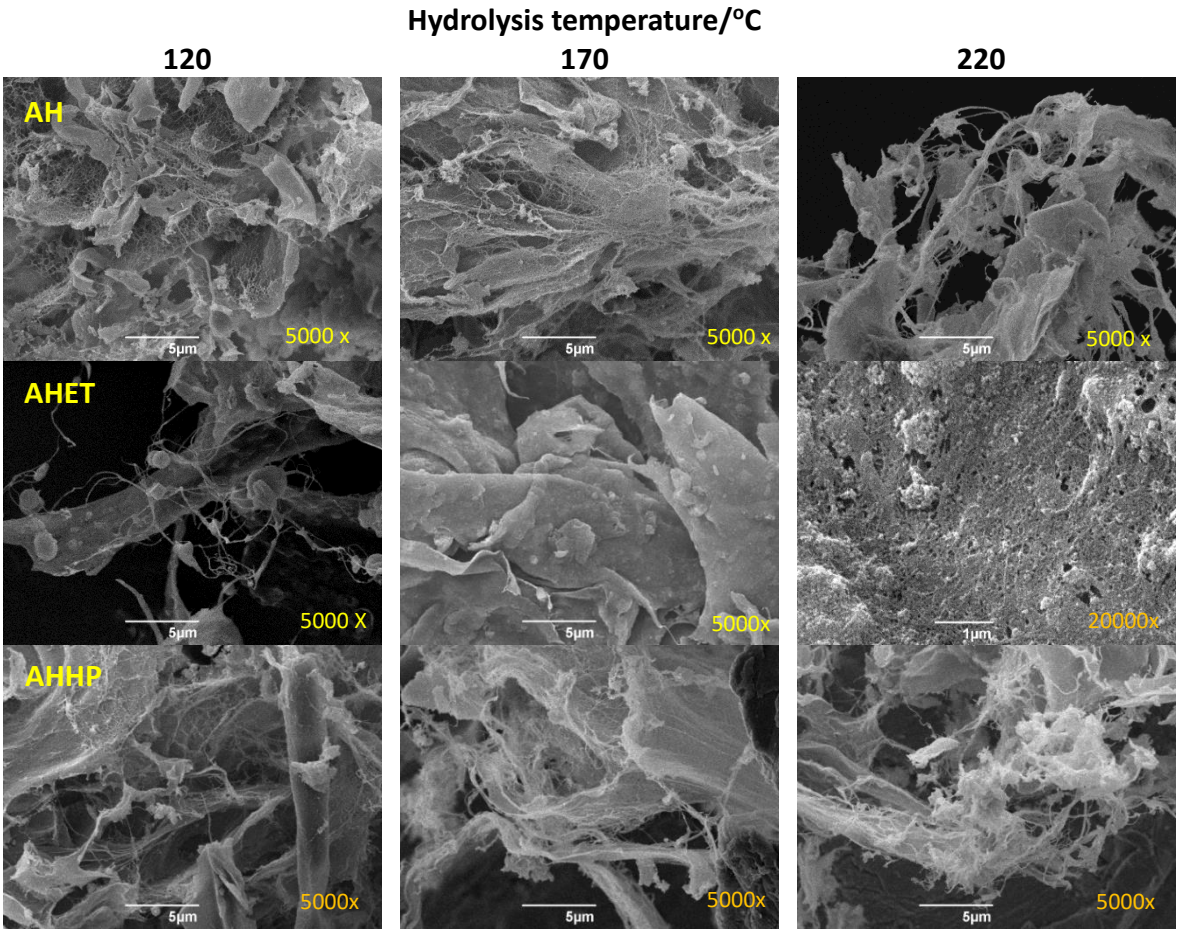

Figure 3. 20 TEM images of almond hull MFCs with respect to processing temperature

3.2.8 Sugar analysis of supernatant

Following microwave treatment, the resulting aqueous fraction was analysed by HPLC in order to understand the composition of sugar and other derivatives produced during the thermal hydrolysis. The hydrothermal microwave-assisted selective scissoring concept gradually scissors cellulose leaching its amorphous content.[123] Pretreatment of the biomass is presumed to impact the recovery of sugar content following microwave processing due to change the original structure of the original lignocellulosic biomass. This is predominantly due to the extraction of specific compounds in the cell wall which were

entangled and or embedded of the amorphous region to the primary crystalline cellulose fibres but were removed by the solvent during pretreatment.

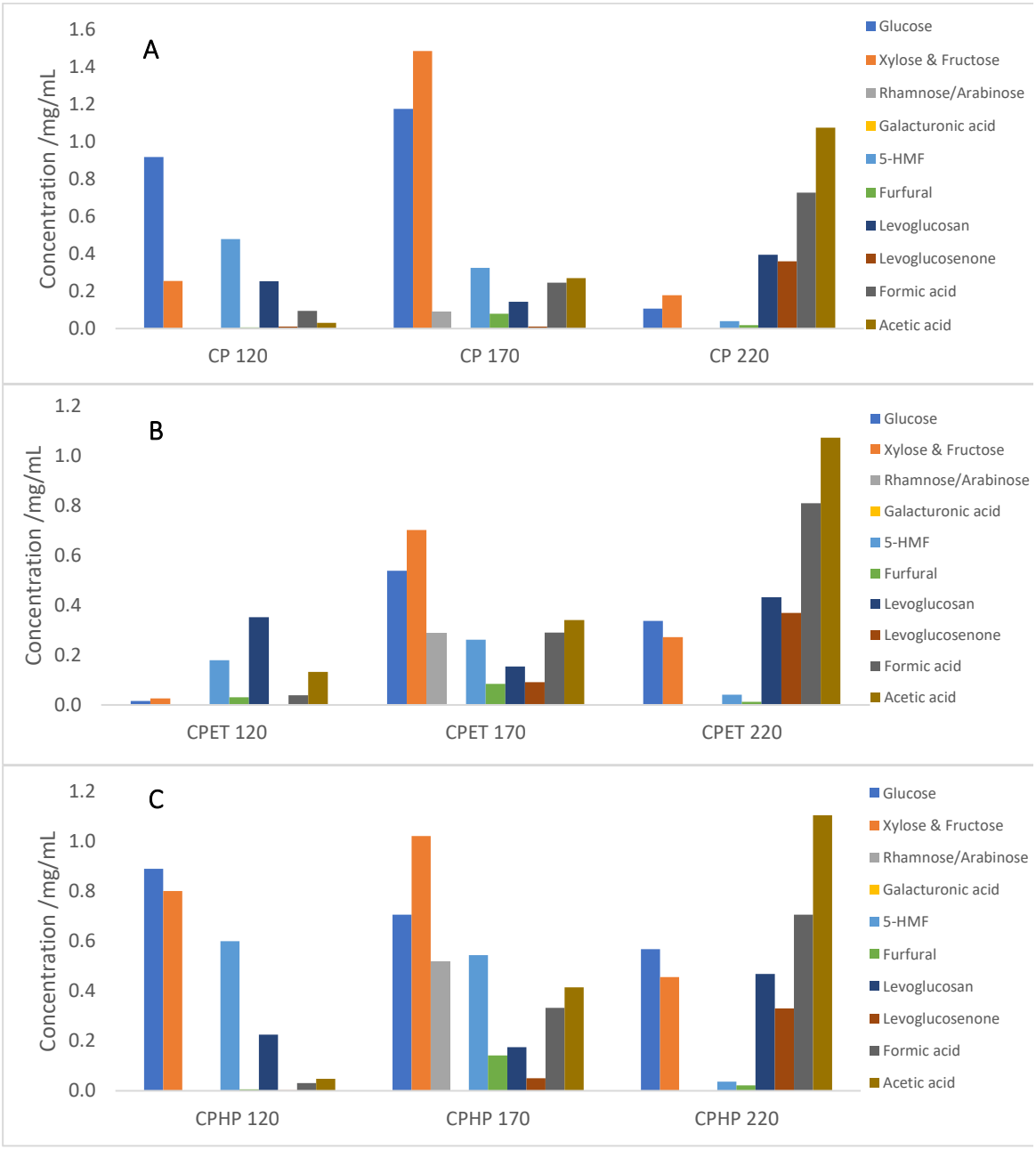

Figure 3. 21 HPLC analysis of cassava peel sugar hydrolysate; A) non-treatment B) ethanol pretreatment C) heptane pretreatment (Original in colour)

As shown in Figure 3.21, by HPLC, the hydrolysate of all cassava peel did not detect the galacturonic acid concentration in the sample indicated that cassava peel does not

contain this sugar acid. The polymer of galacturonic acid is part of pectinaceous matter which is linked by α-1,4 glycosidic bonds. [125] In Figure 3.21 B shows the sugar analysis of supernatant derived from cassava peel that had undergone ethanol pretreatment (CPET 120), it detected only a small amount of xylose and glucose compared to CP 120 or CPHP 120, indicating that ethanol pretreatment could remove xylose and α-glucose effectively before the hydrolysis process. The removed sugars produced from cassava peel are not only components from the polysaccharides of hemicellulose but also starch which is a polymer of α-glucose and mainly comprises amylose and amylopectin.[126,127]. Cassava peel is with rich in starch, with concentrations of 42-60.6% (w/w) depending on the isolation method used, variety and the age of roots [128–130]

Moorthy *et al*.[131] reported ethanol-soluble extraction on cassava flour and found that the sugar was identified as sucrose and ranged from 0.9 to 3.7%. Ethanol extraction through low-pressure steam explosion recovered more than 30 g/L sugar and 80% of hemicellulose from wheat straw.[132] The solubility of the hemicellulose monomers xylose and galactose increases with increased temperature and water fraction.[133,134] These facts indicated that even though most sugar is insoluble with cold or ambient temperature ethanol, as Soxhlet extraction occurs at close to the boiling point of the solvent, the ethanol never reached saturated due to the recycling of fresh ethanol from the reflux condenser.[135]

As reported by Lu *et al*.[136] the recovery of xylose from cassava for bioethanol production via enzymatic hydrothermal with an optimum operating temperature of 180 ^{o}C reached 54.44 %, indicating cassava is xylose-rich. The microwave hydrolysate component of cassava peel showed good agreement with the results of the aforementioned work as the hydrolysate of hemicellulose hydrolysis products was more abundant in constituent

monosaccharides (specifically xylose/fructose) and effective hydrolysis temperature at 170 ^{o}C on untreated and heptane sample.

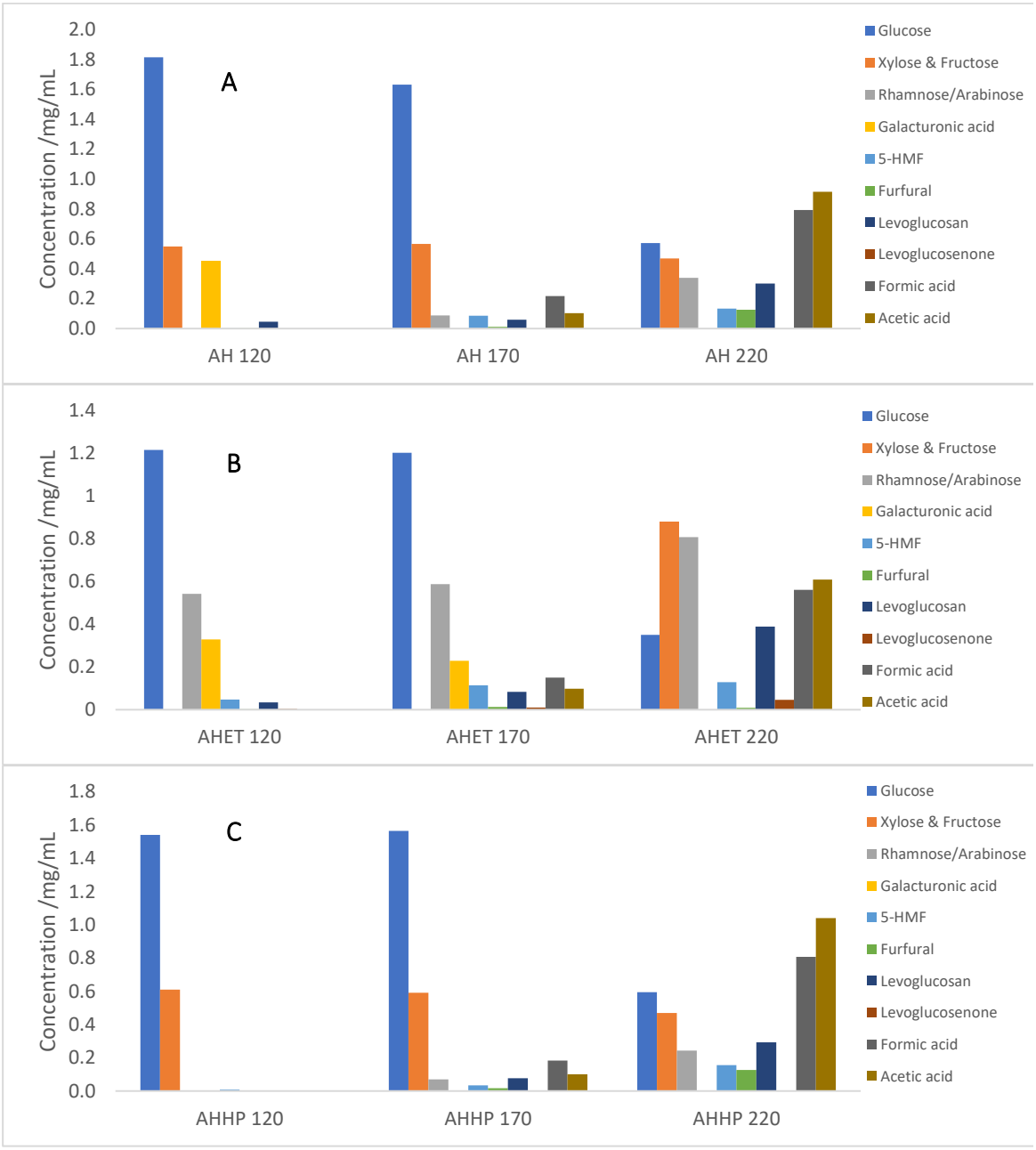

Figure 3. 22 HPLC analysis of the almond hull sugar hydrolysate A) non-treatment B). ethanol pretreatment C) heptane pretreatment (Original in colour)

HPLC analysis of hydrolysate on treated ethanol derived from almond hull after microwave hydrolysis 120-170 ^{o}C revealed the absence of xylose compared to hydrolysate

from without pretreatment and heptane pretreatment (Figure 3.22 B). Partially the amount of xylose already extracted when ethanol pretreatment could reduce the furfural production as a dehydration product. Pretreatment by ethanol indirectly helped to reduce some heteropolymer bonding of hemicellulose sugars (glucose, xylose, mannose, galactose, arabinose, fructose, galacturonic acid and glucuronic acid) to the lignin before the hydrolysis process.[137] In addition to this, ethanol pretreatment was also used to depolymerise lignin and other phytoconstituents as it is particularly efficient for extraction of phenol, tannin, alkaloid, saponin, flavonoid and coumarin compounds. [86,138–140]

Heptane pretreatment assisted the removal of soluble sugar from almond hull indirectly, with evidence the disappearance of rhamnose/arabinose and galacturonic acid during an operating temperature of 120 ^{o}C (Figure 3.22C). Undergone heptane treatment was suggested extracted of short or long-chain free fatty acid able to change the medium environment (*e*.*g*, *p*Ka) during Soxhlet extraction that may affect to sugar-acid [141,142] and also could possibly from water contained on the sample.

Microwave-assisted hydrolysis improved on the selective scissoring of non-cellulosic compounds depending on operating temperature.[102,143] Some glucose and xylose monomers were detected in the supernatant produced at hydrolysis temperatures (120-220^{o}C). Rhamnose/arabinose and galacturonic acid (the main monomers of pectin and correlates well with TGA data discussed earlier) can be found in the hydrolysate of the almond hull only at a temperature below 170^{o}C.[144] At higher temperatures, although a considerable amount of glucose, xylose and fructose could be identified, there was also the evident formation of 5-hydroxymethyl furfural (5-HMF), furfural, levoglucosan and levoglucosenone which were identified as value-added chemical products from the

conversion of derivative sugars.[145–147] Figure 3.23 shows the possible pathways for cellulose and hemicellulose conversion to value-added chemical products. The first main hydrolysis products are glucose and xylose, which can be derived from amorphous cellulose and hemicellulose by applying a temperature of 170 ^{o}C or below. The non-crystalline cellulosic content is converted into the sugar hydrolysate whilst the crystalline cellulose would not participate in the hydrothermal reaction.[148] However, as postulated Jiang *et al*.[149], the crystalline part of cellulose could lead to the formation of levoglucosan. Hydrothermal conversion after 170 ^{o}C resulted in the generation of byproducts such as formic acid, levulinic acid and acetic acid. The formation of acetic acid was attributed to the dehydration of xylose as it was concurrent with declining xylose concentration at high temperature while by-production of formic acid and levulinic acid was generated from the degradation of further glucose reaction.[150,151]

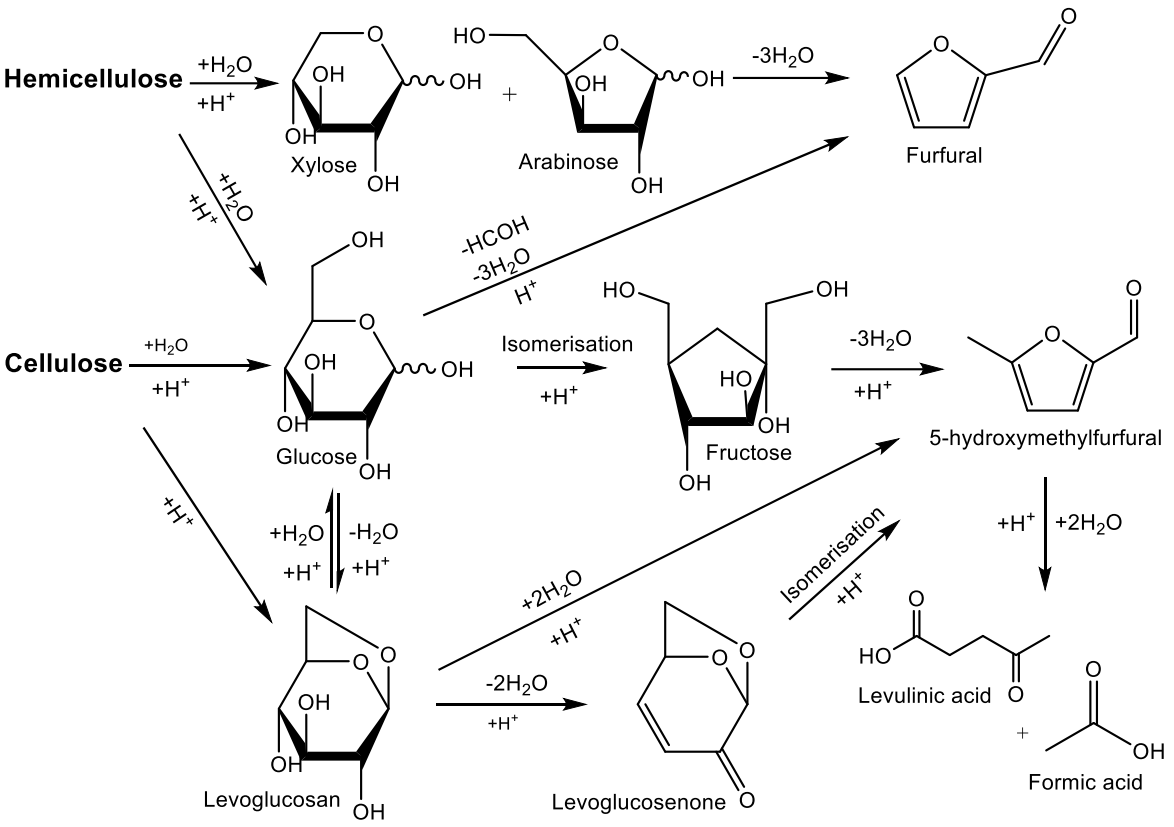

Figure 3. 23 Chemical conversion pathways to furfural, 5-HMF, levoglucosan and levoglucosenone [145,152,153]

3.2.9 Zeta potential

Zeta potential is one region interface of the electrical double layer distribution electrical charges where the first layer is the Stern layer, the particles firmly bonded to ion charge, the second boundary layer is a diffuse layer, the layer of fewer firmly ions attached and this line differentiates the moving ion and the stationary ion and the last region layer is a slipping plane as hydrodynamic shear potential or called *zeta potential* which is the potential difference area between stationary layer and the medium dispersion.[154]

The zeta potential describes the net surface charge of a colloid dispersed in water and can be used to determine the physical stability of an emulsion or suspension.[154] A high zeta potential value indicates electrostatic repulsion between particles leading to the prevention of aggregation (good colloid ζ = ± 40-60 mV). Conversely, a low zeta potential value of the colloid indicates that the suspended particles have high electrostatic attraction and low repulsion and thus, tend to flocculate – especially over extended periods (rapid coagulation, ζ = ± 0-5 mV).[155,156] The magnitude of zeta potential is easily modified to become more positive or negative depending on the solution pH or occurrence of salt ions and can lead to an unstable MFC dispersion.[157–159]

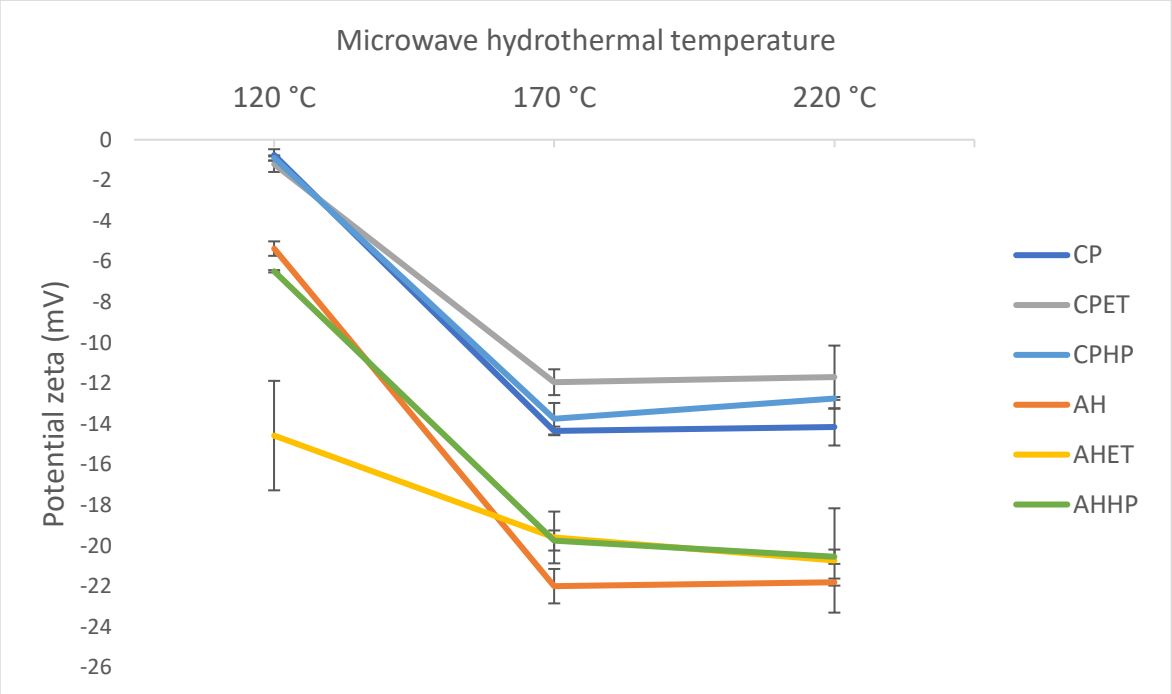

Figure 3. 24 Zeta potential of MFCs at pH neutral (Original in colour)

The determination of the zeta potential value of lignocellulosic materials is useful in helping to understand the behaviour of dispersions containing cellulose particles with

application in the field of adsorption, paper making and composite material synthesis. As shown in Figure 3.24, the microwave processing temperature affects the zeta potential value in neutral water (pH 7), *i.e*., increasing temperature decreases zeta potential value up until a temperature of 170 ^{o}C whereafter, the zeta potential remains relatively constant. All fibres exhibited a negative zeta potential in which cassava peel MFC consistently displayed a stronger zeta potential than almond hull fibres, *i.e*., more negative. At a hydrolysis temperature of 120 ^{o}C, the zeta potential of cassava peel ranged between -0.8 and -1.2 mV and almond hull non-treatment and heptane treatment was quite similar between -5.4 and -6.5 mV except ethanol treatment turned to be more negative at the temperature of 120 ^{o}C by -14.6 mV. A hydrothermal treatment at 170 ^{o}C and 220 ^{o}C caused a slight significant change to zeta potential of pre-treatment and without treatment fibres, where cassava peel ranged between -11.7 and -14.4 mV and almond hull between -19.6 and -22.0 mV. The more negative value of zeta potential MFC in water indicates a high repulsion between particles, implying increasing hydrophobic cellulose behaviour.[159] In comparison, isolated nanofibers from banana peel waste produced through a series of chemical processes (alkaline, bleaching and acid hydrolysis), followed high-pressure homogenisation, exhibited a zeta potential of -28.4 to -44.1 mV and -16 mV without homogenisation.[156] Moreover, Rubio *et al*.[160] reported that the zeta potential of hydrolysis cassava bark residue produced by 0.1 M NaOH solution and 0.1 M H_2SO_4 treatment for 24 h, was between -5 mV and -30 mV.

3.2.10 Hydrogel formation

The term 'hydrogel' describes a swollen polymer that retains a large amount of water (at least 90% of water) by maintaining the three-dimensional (3D) network of

hydrophilic chains that are suspended in aqueous solution.[161,162] Forming a gel can be predicted and controlled from polymer structure, molecular symmetry and medium by the presence of hydrophilic groups attached to the polymeric backbone such as -COOH, -OH, -NH_2, -$CONH_2$, -CONH and -SO_3H.[162,163] The crosslinking chemical network supports the 3D network when the osmotic pressure from water-swollen regions arises and prevention the dissolution of the hydrogel.[164,165].

Polysaccharides-based hydrogel including; starch, cellulose, chitosan, pectin, chitin can be extracted from natural sources (*e.g*. plant, food waste, animal by-products as renewable resources) and have become popular due to exciting properties such as biodegradability, high-water retention capacity, high crystallinity, high surface to volume ratio, degree flexibility fibre network, and high tensile strength.[166,167] Cellulose alone is not soluble in solely water, and most cellulose-based hydrogels are generated within a hybrid system by surface modification with different matrix (*e.q*. methylcellulose, carboxymethyl cellulose, hydroxy ethylcellulose, etc.) in order to improve polymer cross-linkage features depending on the application.[163,165,168,169] To reach maximum trapped water, the sol-gel phase transition subjected by physical and or chemical stimuli; physical stimuli include heating, magnetic field, light, pressure, sonication, and homogenisation while chemical stimuli include pH medium-responsive (depend on expansion and elongation of ionic state fibres), via ions of salt addition (as counterion, balancing radii fibre to increase gel stiffness) and chemical addition network trigger.[162,168,170–173] As shown in Figure 3.27**,** the illustration of the hydrogel 3D network structure is driven by chemical and physical interactions. The chemical network was built through a covalent bond to improve the stability and strengthening of the network when space is filled with water while the physical forces

cause entanglement or junction fibres via ionic bonding, hydrogen bonding, or van der Waals where the molecular self-assembly depend on environment changes helping to trap the liquid.[174]

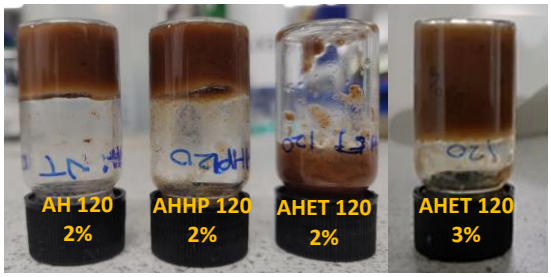

Figure 3. 25 The inversion test of AH120, AHHP, AHET hydrogels at 2% and AHET at 3% (w/v) (Original in colour)

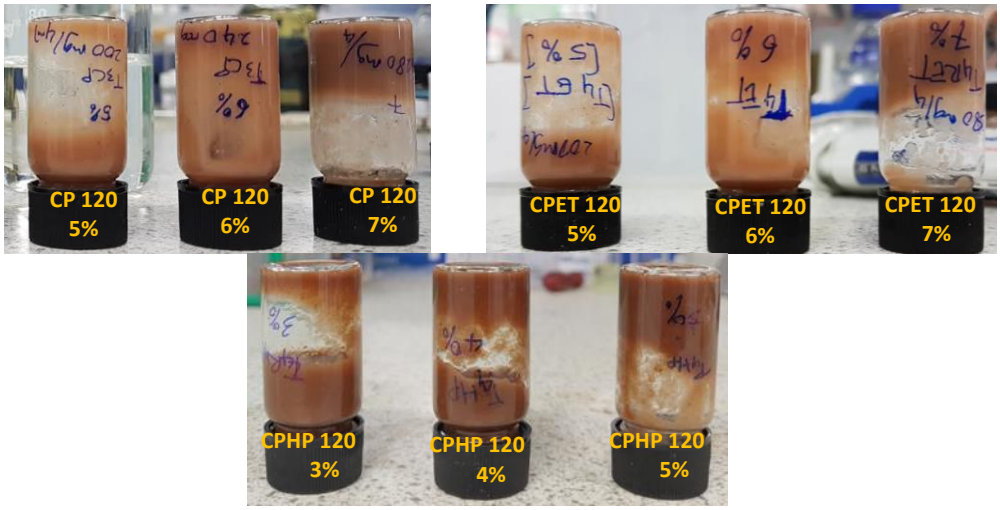

Figure 3. 26 The inversion test of CP 120 and CPET 120 hydrogels at 5%, 6% and 7% and CPHP at 3%, 4% and 5% (w/v) (Original in colour)

Physical stimuli used in the present work to stimulate the formation of hydrogel were comprised homogenisation for 5 minutes, followed by ultrasound treatment for 5-10 minutes, with an amplitude of 65%. The minimum concentration of almond hull MFC required to form a stable hydrogel was identified 2% (w/v) for AH 120 and AHHP 120, whilst for AHET120 the minimum concentration was 3% (w/v) as determined by an inversion test (see Figure 3.25). Interestingly, CP120 and CPET120 produced hydrogels at significantly

high concentration needed for gelation of 7% (w/v) whilst CPHP120 was able to form a gel at 5% (Figure 3.26). The high concentration of gelation cassava peel that could be related to the absence of galacturonic acid and/or pectinaceous matter (from HPLC analysis in Figure 3.21). Galacturonic acid/pectinaceous matter was evident (TGA and HPLC) in almond hull MFCs but also a significant amount of lignin or condensed tannins. If, the latter, then they may be able to enhance hydrogen-bonding with water to afford gels at a lower concentration. Furthermore, the HPLC analysis of almond husk hydrolysate was found to contain monomeric sugar units of rhamnose, another key fragment within pectin.[175] Polysaccharide domains of native pectin are composed of homogalacturonan (HGA), rhamnogalacturonan I (RG-I), rhamnogalacturonan II (RG-II), xylogalacturonan, and apiogalacturonan.[144] Ionically crosslinked pectin builds strong networks with covalent polysaccharide domain bonds.[144] A small number of anionic surface charges from residual hemicellulose made a strong gel, forming the entangled network at lower concentration when compared to pure nanocrystal cellulose (CNC) itself [168]. In a previous study by Melo, the hydrogel of pure CNC reached a concentration of 3% where the best performance swelling from orange peel residue of microwave hydrothermal at 120°C was 2% (w/v).[87]

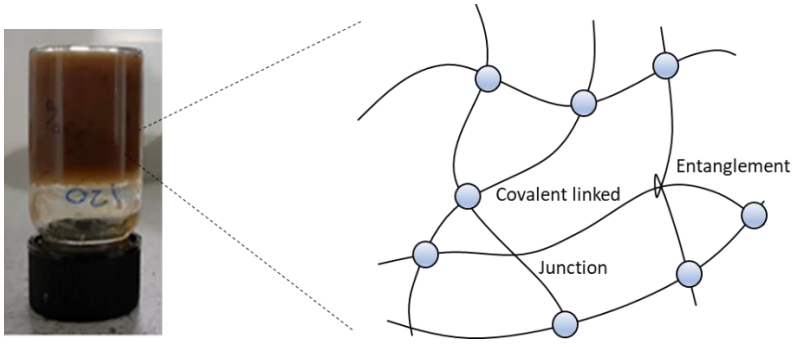

Figure 3. 27 Illustration of the hydrogel 3D network [173,174] (Original in colour)

MFC 120°C exhibited excellent dispersion in water, demonstrating a higher hydrophilic interaction compared to MFC from produced at 170°C and above which tended to less hydrophilic, and resulted in low swelling. Hydrophobicity increased of MFC as the higher temperature hydrolysis was suggested to form *pseudo*lignin that has a lower negative surface charge, and is insoluble with water due to the presence of carbonyl, methoxy and polyaromatic structures.[176,177] *Pseudo*lignin is derived via polymerisation reactions from furfural and 5-hydroxymethyl furfural (5-HMF) has been reported as spherical lignin-like droplets that block and deposit on the surface of cellulose. [176–179]

3.2.11 MFC-based films

The MFCs derived from AH and CP were used to fabricate films which are shown in Figure 3.28. The films were prepared using 0.2% (w/v) of MFC dispersed in deionised water. Only AHET 120 was able to successfully make a film, with the other samples being easy to break when peeled from the PTFE membrane (see Figure 3.28). All films from cassava peel MFC 120 became stuck to the membrane and were also brittle with the structure cracking very easily upon drying (not shown). However, all MFCs from microwave hydrolysis at 170 °C and 220 °C quickly dried and formed a structured film. This could be related to decreased water retention and swelling of the fibres with increasing temperature during the hydrolysis process.[180] The fibres tend to increase the hydrophobic characteristic as hydrolysis temperature is increased, where the hornification phenomenon of fibres upon drying readily facilitates film formation.[181] The transparency the film depends on the treatment of the fibre source can be seen in the aforementioned image, *i.e*., the light brown films at low temperature turned to black films at high temperature.

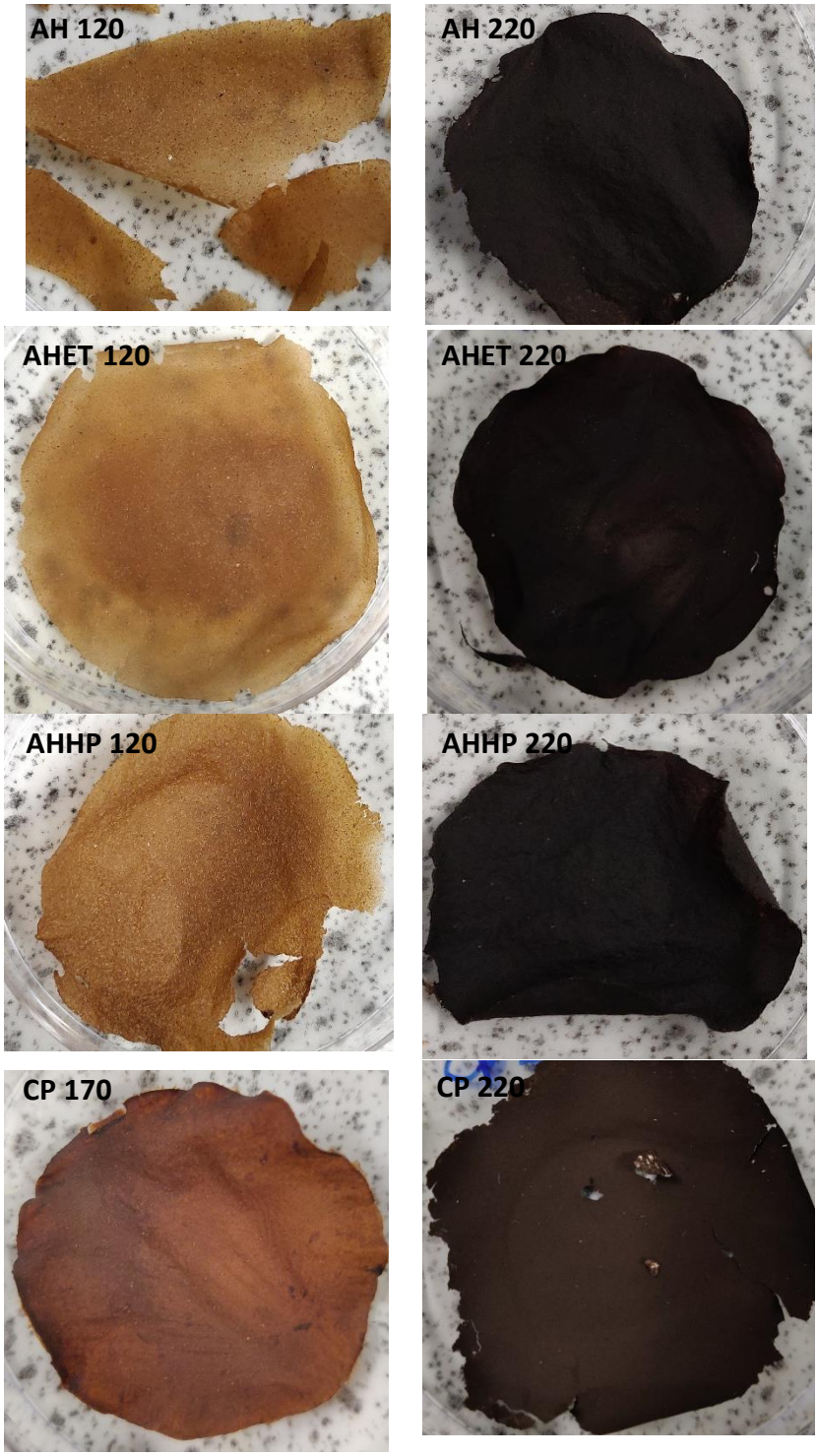

Figure 3. 28 The films produced using the almond hull and cassava peel MFC (Original in colour)

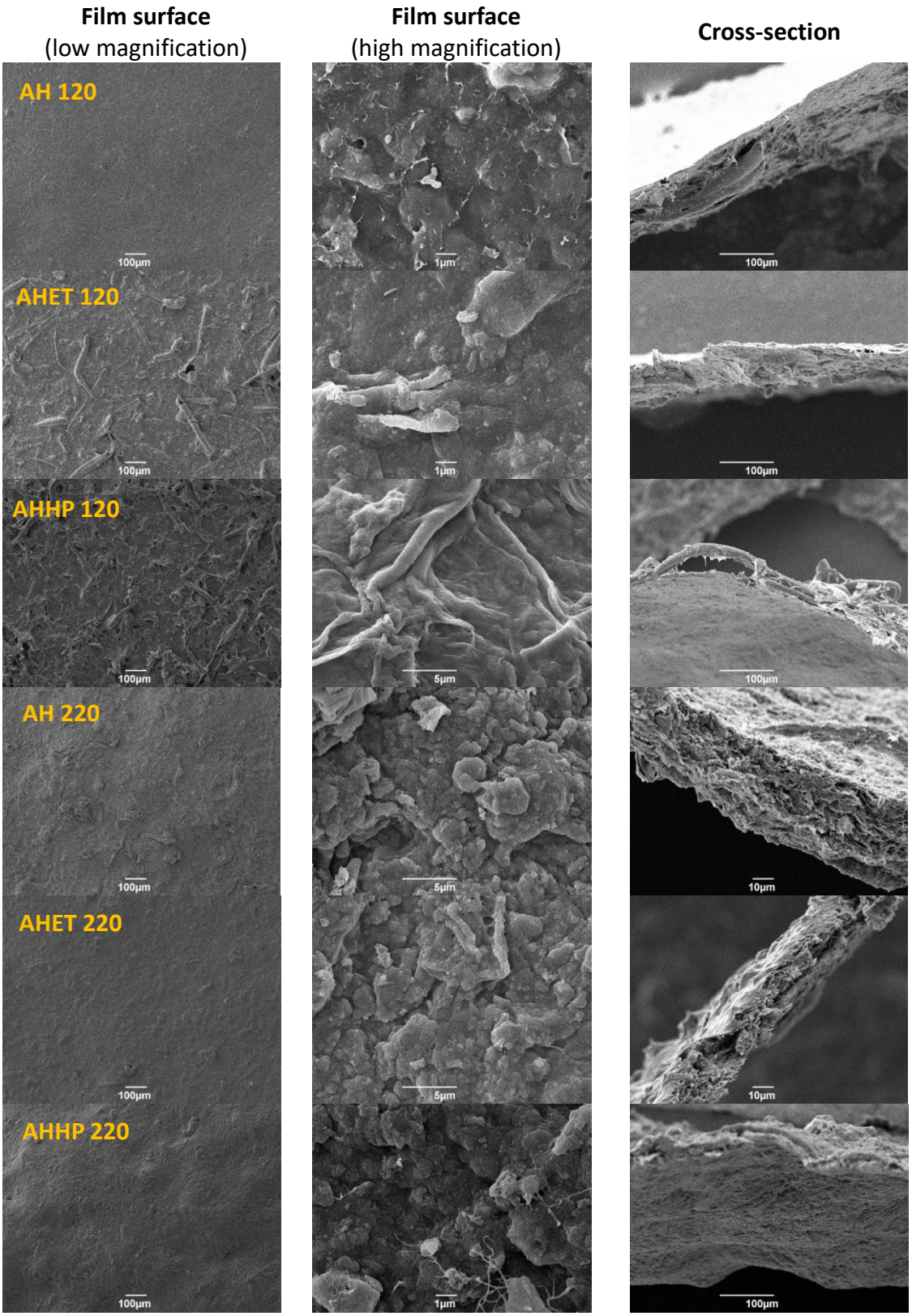

Figure 3. 29 SEM images of almond hull films

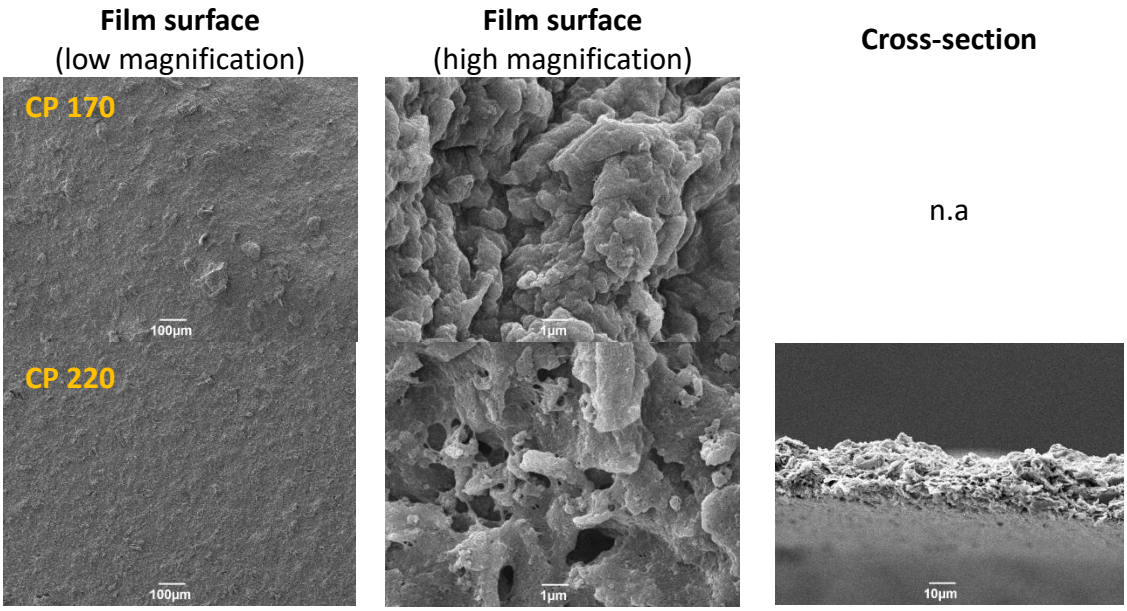

Figure 3. 30 SEM images of cassava peel films

The surface texture of the MFC film produced at low temperatures was found to be rough as can be seen in Figures 3.29 (AH) and 3.30 (CP) and appear visually similar to a chunk of wood-like material or flax fibres and bundles of fibres crossing over each other - especially on the surface and cross-section of AHET 120 and AHHP 120 films with the width ranging between 9 and 18 µm roughly. In comparison, fibre bundles of sugar palm cellulose produced via delignification and mercerisation method have a diameter of approximately 11.8 µm.[182] Surface roughness became small with increasing temperature, MFC produced at high temperature generated a film which was visibly smoother than films produced using materials prepared at low temperatures. Incomplete removal non-cellulosic materials may have influenced the roughness of the film, many fibril bundles result in the surface being irregular.

Sabbah *et al*. [154] highlighted a correlation between preparation of bio-film and zeta potential if, the particles suspended in the water (for mixture or single component) have a zeta potential between lower than +10 mV or less negative than -10mV, then the film will

become unstable and tough. This conclusion is in agreement with our results of zeta potential, where MFC 120 from AHET 120 (ζ = -14.6 mV) showed the lowest zeta potentials and could be formed into a good film (not easily ripped when peeled from membrane). In addition, the roughness of MFC film morphology can also be linked to zeta-potential changes as an increase in salt or surfactant (mixture) concentration increases the film's roughness.[183]

3.3 Chromium (VI) and Methylene Blue Adsorption Study

Among the separation methods used to remedy polluted wastewater, adsorption is considered to be the most desirable, efficient and effective process for dealing with various unwanted materials in a large wastewater volume.[184] The removal of contaminant using bio-based nanofibres as green adsorbents has been increasingly explored in purification technology due to their natural abundance, high surface area, high mechanical strength and flexibility and versatility for use in composite materials.[185,186] Recently, the use of waste food as a source of biobased adsorbents has attracted attention due to the fact that such materials tend to inexpensive, abundant, renewable and environmentally friendly, especially in applications in which universal adsorbent such as activated carbon is expensive.[187] The utilisation of plant-based nanomaterials (mainly nanocellulose fibres) as promising alternative adsorbent is currently being investigated low cost, eco-friendly, high surface area, nanopore size and flexibility functional surface in the chemical modification to improve loading capacity.[187,188]

The contamination of aquatic ecosystems from synthetic dyes and heavy metal dyes produced as by-products of various industries such as textile, leather, cosmetic, printing,

paint etc. is currently considered a serious risk to the environment and water quality for daily use.[189] Hexavalent chromium is known to be a highly toxic and carcinogenic pollutant which is currently released into the environment, as are various dyes such as methyl orange and methylene blue depending on their relative concentrations.[184,190] Interestingly, in aqueous solution, chromium ion and methylene blue have different charges. Chromium can take various forms in solution such as $HCrO_4^-$, CrO_4^{2-}, $HCrO_7^-$ and $Cr_2O_7^{2-}$ and the anionic species $HCr_2O_4^-$ and or $Cr_2O_7^-$ can be found at low pH[191,192] while methylene blue is a heterocyclic aromatic cationic dye ($C_{16}H_{18}N_3SCl$) with *p*Ka = 5.6, mainly at high pH value (positive charge).[193]

In this study, to understand the adsorption properties of cassava peel and almond hull MFC produced using microwave hydrothermal treatment at the temperatures of 120 ^oC and 220 ^oC, a series of experiments involving adsorption of chromium ions and methylene blue as model contaminants over a 30-minute holding time were undertaken. The mechanism by which contaminants were adsorbed in the presence of either conventional stirring (ST) or ultrasound-mediated (US) were also compared. The effect at different pH was conducted only on cassava peel MFC with respect to chromium uptake, and a thermodynamic study was performed on methylene blue adsorption only. Finally, decolourisation of methylene blue from containing the aforementioned MFC adsorbents was compared with commercial activated carbon (Norit™).

3.3.1 Adsorbent properties

For the adsorption experiment, MFC derived from cassava peel and almond hull without pre-treatment at hydrothermal temperatures of 120 ^oC and 220 ^oC with a holding

time of 30 minutes was used as adsorbents. Addition of holding time of 30 minutes during microwave treatment was found to improve their surface area and the pore diameter was closer to the mesoporous region (2 to 50 nm) with respect to MFC materials that were produced without this extra treatment period.[194] For example, for CP 120 with 0 minutes holding the BET surface area was 0.273 m^2/g whilst for CP120-30' (*i.e*. with 30 minutes hold) it was 2.847m^2/g. The porosity analysis of CP and AH is summarised in Table 3.10.

Table 3. 10 Porosity characteristic of MFCs with additional holding time

Adsorbents	**BET surface area/(m^2/g)**	**BJH pore volume /(cm^3/g)**	**BJH adsorption pore diameter /(nm)**	**BJH desorption pore diameter /(nm)**	**BET pore diameter /nm**
CP 120-30'	2.85	0.002	11.18	52.80	2.94
CP 220-30'	20.17	0.122	14.44	10.00	24.24
AH 120-30'	1.03	0.014	-	-	55.67
AH 220-30'	17.86	0.076	-	-	16.85
Activated carbon	505.60	0.304	5.06	4.78	1.90

*BET= Brunauer-Emmett-Teller, BJH=Barret-Joyner-Halenda

MFC can be described as a *soft* material that is very flexible. Even though the exact porosity, when dispersed in water, cannot be determined for adsorption purposes due to the hornification phenomena of the fibre after microwave hydrothermal or shrinkage of the diameter fibre pores after the drying process, it can at least give a picture that the MFC produced is a mesoporous material, especially that which was generated at low temperature. The fibre pore size distribution decreased, becoming narrower when it was subjected to drying or pressing; hence the moisture content reduces as reflected in the decrease in water retention.[195,196]

3.3.1.1 pH effect on zeta potential of MFC adsorbents

The zeta potential was analysed in order to understand the fundamental properties of the net surface charge content on the performance of the adsorbents under investigation, *i.e*., CP120 and AH120.[197] The measured charge for an MFC implies information concerning the electrostatic sign charge of the same MFC when dispersed in the water at different pH before interaction with the contaminant. The adsorbent electrostatic forces demonstrate liability for interaction to a contaminant in predicting or controlling the interaction between the colloid system.[198]

The zeta potential of CP 120 and AH 120 held an additional 30 minutes with respect to pH 2 and pH 7 are plotted in Figure 3.31. The MFCs of cassava peel and almond hull have a negative zeta potential at neutral pH and its zeta potential value increased with decreasing pH. For MFCs produced at 120 ^{o}C, almond hull (AH 120,30') had the lowest zeta potential (-18.7 mV) but, at 220 ^{o}C, this was true for cassava peel (CP 220, 30'; -27.1 mV). Increasing hydrolysis temperature of the almond hull from 120^{o}C to 220^{o}C did not change the zeta potential significantly, suggesting that the raw material from the almond hull was lignin-rich from deprotonated carboxylic acid and the aromatic phenolic content[199], as corroborated by the relevant ^{13}C CPMAS NMR, TGA and compositional data reported earlier. At low pH, the zeta potential of CP 220, 30' presented a positive charge at 6.1 mV followed by AH 220, 30' with a zeta potential value of 2.0 mV. Thus, the nature of the surface charge can be drastically altered with respect to pH. The nature of the surface of our MFCs was further investigated by conducting a Boehm titration as described next.

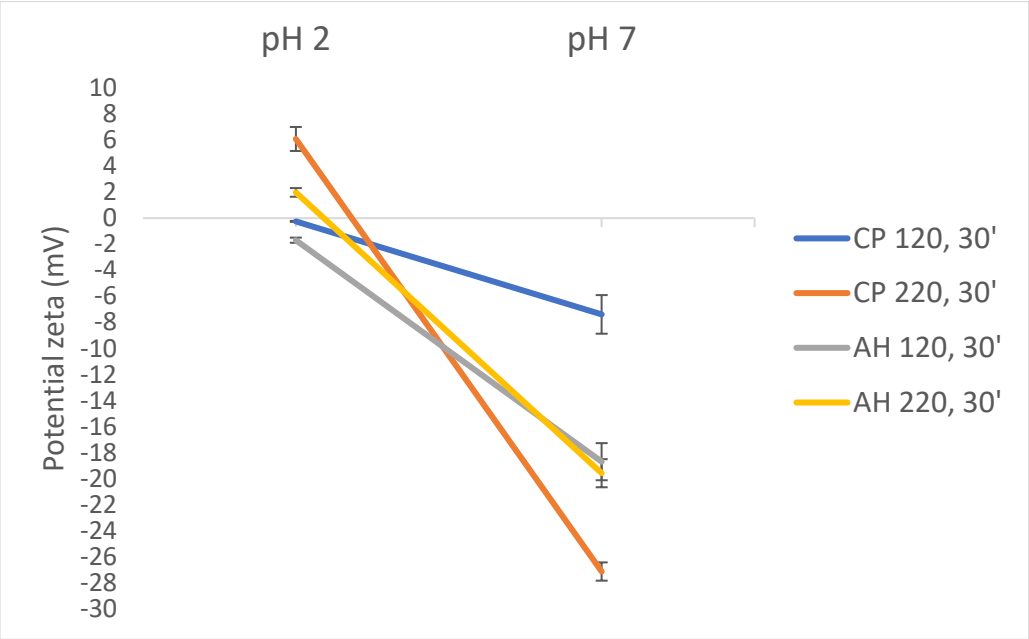

Figure 3. 31 pH effect on zeta potential of MFC adsorbents (Original in colour)

3.3.1.2 Boehm titration

Table 3.11 summarise Boehm titration results for CP120, 30' and AH120, 30' MFCs. Boehm titration was adopted as one of the standard methods for characterizing cellulose surface functions such as carboxylic, lactonic and phenolic hydroxyl groups and total basic groups (based on oxygen moieties such as quinone, pyrones, chromones, and π–π bonds).[79,200,201] Boehm suggested that selective neutralization of each functionality could be achieved using different strength base solutions called reaction bases; *i.e.*, sodium hydroxide (*p*Ka, 15.7) which neutralises all of three functionalities whilst sodium carbonate (*p*Ka, 10.3) neutralises carboxylic and phenolic groups, and sodium bicarbonate (*p*Ka, 6.4) only deprotonates carboxyl groups.[202] Furthermore, it was also found that due to the high lignin, cellulose, and hemicellulose content in both adsorbents but especially for almond hulls, high adsorption efficiency would be obtained because all of these polymers are well-

known for their large quantities of hydroxyl, methoxyl, and carbonyl groups -which favour the adsorption of metals via electrostatic and $\pi - \pi$ interaction.[203]

It was presumed that both the nature and quantity of the surface oxygen groups of the MFC should influence the adsorption process. From Table 3.11 it can be seen that AH120, 30' has the highest concentration of total acid groups (2.36 mmol/g) commensurate with high initial lignin content in the virgin almond hull (approx. 11% as reported earlier). A significant proportion of phenolic groups are detected (0.57 mmol/g) which also correlates well with the presence of lignin. Interestingly, virgin cassava peel which has a relatively low lignin content (approx. 3%) did not show presence of phenolic groups but did show acidic groups. The total acidic group concentration was far less than that for almond hull (CP120, 30' 0.88 mmol/g versus AH120, 30', 2.36 mmol/g). However, on processing cassava peel at 220 ^{o}C, the total acidic group concentration increased significantly to 2.58 mmol/g indicative of extensive oxidation and degradative processes occurring. In particular, a high concentration of phenolic groups was detected (0.8 mmol/g), the *trapped* lignin may have leached and/or extensive formation of *pseudo*lignins has occurred. Such a significant change was not observed for AH220, 30' showing only a marginal increase to 2.36 from 2.58 mmol/g.

Table 3. 11 Boehm titration values (mmol/g) for CP and AH MFC adsorbents

Adsorbents	Carboxylic group/ (mmol/g)	Lactonic group/ (mmol/g)	Phenolic group/ (mmol/g)	Total acid group/ (mmol/g)	Total basic group/ (mmol/g)
CP 120, 30'	0.62	0.25	0.00	0.88	0.69
CP 220, 30'	0.82	0.51	0.80	2.14	0.42
AH 120, 30'	1.34	0.45	0.57	2.36	0.36
AH 220, 30'	1.46	0.52	0.60	2.58	0.30

3.3.2 Construction of adsorption isotherms

3.3.2.1 Chromium adsorption isotherm models

Adsorption isotherm experiments were conducted, and the results analysed using several leading models; Langmuir, Freundlich and Temkin, and Dubinin-Radushkevich in order to obtain information concerning the maximum loading capacity and to better understand the interaction of Cr (VI) with cassava peel and almond hull MFC. The optimisation condition of media, such as pH, in addition to the properties of the adsorbent/adsorbate, requires an understanding of the driving forces involved during the adsorption process. The attraction is driven by surface area and pore volume of the adsorbent and electrical charge of the adsorbate site to create new balance equilibrium.[204]

Langmuir model

Langmuir adsorption model is valid as a description for the formation of an adsorbate monolayer on the surface due to homogeneous adsorbent sites or uniform energies adsorption, and the interaction forces between adsorbent and adsorbate decrease rapidly when the relative pressure of unity is achieved, or no further migration of adsorbate occurs when saturation is reached.[205–208] The Langmuir model was initially purposed in order to describe chemisorption (ionic or covalent bonding), but this model can be applied for many systems of adsorption to describe the mechanism in a binary system.[205]

The Langmuir adsorption isotherm and its linear form of are expressed in Eq.3.2 and Eq. 3.3 respectively.[209] Wherein, q_e is the theoretical amount of adsorbate adsorbed at equilibrium (mg/g), q_m is maximum adsorption capacity (mg/g), K_L is Langmuir isotherm

constants related to the free energy of adsorption (L/mg), and C_e is the concentration of adsorbate at equilibrium (mg/L). [207,208,210]

$$q_e = \frac{q_m K_L C_e}{1+K_L C_e} \quad \text{(Eq. 3. 2)}$$

$$\frac{1}{q_e} = \frac{1}{q_m K_L C_e} + \frac{1}{q_m} \quad \text{(Eq. 3. 3)}$$

Freundlich model

The Freundlich isotherm model describes the sorption on heterogeneous surfaces as well as the multilayer sorption at different affinities site. Freundlich model is an exponential distribution expression of adsorption as the adsorbate concentration increases, the concentration of adsorbate on the adsorbent surface increases so that the stronger binding sites are occupied first and then the binding strength decreases with increasing degree of adsorption.[207,211,212] The mathematical equation for the Freundlich model in Eq. (3.4) and the linearised logarithmic form (Eq. 3.5) are represented as:

$$q_e = K_F \, x \, C_e^{1/n} \quad \text{(Eq. 3. 4)}$$

$$\log q_e = \log K_F + \frac{1}{n} \log C_e \quad \text{(Eq. 3. 5)}$$

Where K_F is a constant indicative of the relative adsorption capacity of the adsorbent [(mg/L)(L/g)$^{1/n}$], C_e is the concentration of adsorbate at equilibrium (mg/L), and n is the Freundlich exponent constant indicating of the intensity of the adsorption and the magnitude the exponent when n > 1 indicates favourability of adsorption.[207,213]

Temkin model

The Temkin isotherm equation assumes that the heat of adsorption of all the molecules in the layer decreases linearly with coverage due to adsorbent–adsorbate interactions by ignoring the concentration value. The adsorption is characterised by a

uniform distribution of the binding energies by plotting the q_e against ln C_e to determine the Temkin constant.[207,208] The linear form of the Temkin model equation (Eq 3.8) is given by:

$$q_e = \frac{RT}{b} \ln K_T\, C_e \qquad \text{(Eq. 3. 6)}$$

$$q_e = \frac{RT}{b} \ln K_T + \frac{RT}{b} \ln C_e \qquad \text{(Eq. 3. 7)}$$

$$q_e = B \ln K_T + B \ln C_e \ , B = \frac{RT}{b} \qquad \text{(Eq. 3. 8)}$$

where q_e is the theoretical fractional coverage (mg/g), R the universal gas constant (8.314 J/mol K), T the absolute temperature (K), b is Temkin isotherm constant, B is constant related to heat sorption (J/mol), and K_T is the Temkin equilibrium constant related to maximum binding energy (L/g).[207,214]

Dubinin-Radushkevich (D-R) Isotherm.

Dubinin-Radushkevich (D-R) isotherm model is an empirical adsorption model that was developed for porous materials and is generally applied to express the adsorption mechanism with Gaussian micropore size distribution into both heterogeneous or uniform surfaces.[208,215] This model is adapted from Polanyi potential theory to investigate physical sorption on porous material, and it postulates that the adsorption mechanism in micropores, such as activated carbon is a pore-filling mechanism rather than layer by layer surface coverage involving Van Der Waal's forces.[215] The D-R model explains the gas-solid interface where this equation does not reduce to Henry's laws at low pressure, that has thermodynamic consistency in the region of Henry for gas adsorption explanation in microporous material.[215,216] Dubinin-Radushkevich isotherm (non-linear and linear form) (Eq.3.9 and 3.10) and the Polanyi adsorption potential are expressed as follows (Eq.3.11):

$$q_e = q_m \exp(-\beta\varepsilon^2) \quad \text{(Eq. 3. 9)}$$

$$\ln q_e = \ln q_m - \beta\varepsilon^2 \quad \text{(Eq. 3. 10)}$$

$$\varepsilon = RT \ln\left(1 + \frac{1}{C_e}\right) \quad \text{(Eq. 3. 11)}$$

Where q_m is the theoretical saturation capacity(mg/g), β is the Dubinin-Radushkevich coefficient constant related to the adsorption mean free energy (mol^2/j^2), and C_e is the equilibrium concentration at temperature T.[217]

The approach was usually applied to distinguish free energy of physical and chemical adsorption with adsorbate, the energy per molecule can be determined by the relationship D-R constant (Eq.3.12):

$$E = \left[\frac{1}{\sqrt{2\beta}}\right] \quad \text{(Eq. 3. 12)}$$

The tabulated data summarising experimental adsorption of Cr(VI) with 0.5% (w/v) of two types of cassava peel MFC (CP 120 and CP 220) at pH 7 and pH 2, and almond hull MFC at pH 2 via stirring and sonication is presented in Table 3.12, 3.13, and 3.14. It also includes isotherm constants and a correlation coefficient (R^2) for each model which allows for evaluation of the best model and also the prediction of maximum loading capacity (mg/g) via the Langmuir and D-R model depending on the closest regression value.

MFC adsorbents microwave treatment, *i.e.* CP 120^{o}C, 30' (CP120), CP 220^{o}C, 30' (CP220), AH 120^{o}C, 30' (AH120), and AH 220^{o}C, 30' (AH220) were produced for adsorption study with comparing the agitation technique between conventional stirring (ST) and ultrasound (US). As shown in Table 3.12, only a small amount of Cr(VI) can be absorbed by MFC of cassava peel at pH 7. The highest uptake of chromium uptake ions was obtained using CPUS 220 with a value of 2.24 mg/g with the experimental data showing a good fit to

the Freundlich model. The MFC of CP 120 both through stirring and sonication followed the Langmuir model, indicating monolayer formation on the outer surface of the absorbent. From the q_m data, the interaction between chromium ions and MFC of CP 120 was quickly saturated with low loading capacity, both through stirring and sonication. Adsorption of Cr(VI) at neutral pH with all MFCs was very low at Cr(IV) uptake and has not yet achieved satisfactory results, although CPUS 220 has a high potential affinity to react with chromium ions supported by the ultrasound process.

Table 3. 12 Isotherms modelling of Cr(VI) on cassava peel MFC at pH 7 and 21°C

Isotherm models	**Unit**	**Stirring**		**Ultrasound**	
		CPST 120	**CPST 220**	**CPUS 120**	**CPUS 220**
Langmuir	K_L (L/mg)	0.28	0.45	0.60	5.28
	q_m (mg/g)	0.47	0.42	0.82	2.24
	R^2	0.9881	0.9680	0.9864	0.7741
Freundlich	K_F (L/mg)	0.10	0.11	0.25	1.52
	n	1.69	1.54	1.69	4.49
	R^2	0.9055	0.9960	0.9766	0.9527
Temkin	B (kJ/mol)	0.12	0.13	0.23	0.43
	b	20308.5	19181.0	10666.9	5734.4
	K_T (L/mg)	2.58	3.32	4.50	45.28
	R^2	0.7948	0.9152	0.8868	0.9412
D-R	K_{DR} (mol^2KJ^{-2})	1.91E-07	1.51E-07	1.03E-07	3.36E-08
	E (kJ/mol)	1617.42	1819.40	2204.61	3857.56
	q_m (mg/g)	0.28	0.33	0.58	2.23
	R^2	0.7558	0.7749	0.7698	0.6055

The pH (of the medium under investigation) is one of the most important experimental parameters that can be used to probe adsorption mechanisms and phenomena, sorbent surface loading, ionization and sorbate species. Low electrostatic attraction between MFC cassava peel and ion chromium at pH 7 is due to the negative

charge exhibited by both the adsorbent and adsorbent as the surface net charge of the cellulose adsorbent was negatively charged, and the dissociation formation of chromium at neural pH was an anion of CrO_4^{2-}.[212,218,219] Under neutral or higher pH condition, the electrostatic forces will be weakened, resulting in reduced binding with the metal adsorbate.[220] Moreover, the ion CrO_4^{2-} that exists above pH 6 is a weak oxidizing agent (the potential reduction value = -0.13 V) suggesting insufficient energy or partial interaction with the adsorbent through electrostatic attraction.[221,222]

$$CrO_4^{2-} + 4H_2O + 3e^- \leftrightarrow Cr(OH)_3 + 5OH^- \qquad E^0 = -0.13\ V \qquad \text{(Eq. 3. 13)}$$

The pH of the medium does not only affect the surface charge of the adsorbent but also ionization and speciation of chromium. In order to maximise the uptake of chromium, it is vital to understand which species of chromium ion exist in solution at the pH under study. The solubility of $K_2Cr_2O_7$ is dependent on pH and the solution when dissociation of Cr(VI) in the pH value range from 6.5 to 12 is virtually solely as chromate, (CrO_4^{2-}). Conversely, when the pH range is between 0.7-6.5, the chromium ions instead form hydrogen chromate ($HCrO_4^-$) and dichromate ($Cr_2O_7^{2-}$) ions and when the pH value is < 0.7, the Cr(VI) ions convert to chromic acid (H_2CrO_4).[223] From the equilibrium constant (K) (Eq. 3.14-3.17) for various oxy-anions form of chromium equilibrium constant (*K*) as pH function solution, we can predict the direction of chromium ions favoured and abundance as follows:[224,225]

$$H_2CrO_4 \leftrightarrow HCrO_4^- + H^+ \qquad K = 4.1 \qquad \text{(Eq. 3. 14)}$$

$$HCrO_4^- \leftrightarrow CrO_4^{2-} + H^+ \qquad K = 10^{-5.9} \qquad \text{(Eq. 3. 15)}$$

$$HCr_2O_7^- \leftrightarrow Cr_2O_7^{2-} + H^+ \qquad K = 10^{0.85} \qquad \text{(Eq. 3. 16)}$$

$$Cr_2O_7^{2-} + H_2O \leftrightarrow 2HCrO_4^- \qquad K = 10^{-2.2} \qquad \text{(Eq. 3. 17)}$$

As such, different chromium ions species could be distinguished within three separate pH regions, as reported by Tandon *et al.*[226] and similarly by Hu *et al.* [227] as depicted in Figure 3.32.

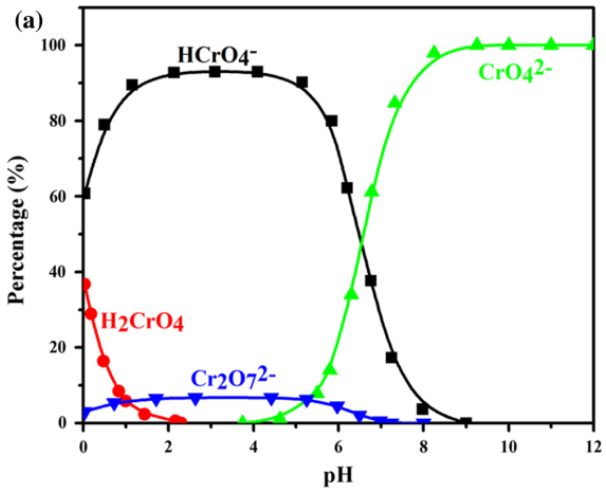

Figure 3. 32 Chromium(VI) form distribution as a function of solution pH [227] (Original picture)

The electrostatic attraction between cellulose and chromium increased when the aqueous medium was changed to pH 2, which has also been reported by Nasseh *et al*. [228], as the pH optimum for chromium adsorption. The adsorption of chromium is favoured at lower pH and the solubility equilibrium of chromium ions shifted, dominated by a form of $HCrO_4^-$ at pH 2.[212] As a response, the MFC cassava peel surface at pH 2 is positively charged, with the hydroxyl and carboxyl (*p*Ka = 3.0) group on the MFC surface tending to be protonated. [213] Generating a surface that is positively charged that would, in turn, more greatly attract negatively charged chromium ions.[229] Moreover, $HCrO_4^-$ species is a negatively monovalent ion, occupying the least active sites and requiring the minimum adsorption free energy.[218]

Table 3. 13 Isotherm modelling of Cr(VI) uptake by cassava peel MFC at pH 2 and 21°C

Isotherm models	Unit	Stirring (ST)		Ultrasound (US)	
		CPST 120	CPST 220	CPUS 120	CPUS 220
Langmuir	K_L (L/mg)	0.72	2.13	0.43	0.03
	q_m (mg/g)	22.99	46.04	45.76	193.51
	R^2	0.7782	0.8090	0.8702	0.9789
Freundlich	K_F (L/mg)	9.46	24.32	22.56	86.81
	n	5.03	5.46	6.64	8.51
	R^2	0.9547	0.9969	0.9639	0.9074
Temkin	B (kJ/mol)	3.73	6.81	5.76	19.56
	b	653.2	358.2	422.8	124.6
	K_T (L/mg)	7.20	37.16	27.22	19.79
	R^2	0.8719	0.9685	0.9093	0.9193
D-R	K_{DR} (mol^2KJ^{-2})	3.45E-07	7.97E-08	1.34E-06	6.12E-04
	E_D (kJ/mol)	1204.09	2504.24	611.90	28.58
	q_m (mg/g)	23.25	46.10	44.90	180.78
	R^2	0.6055	0.6354	0.7609	0.9981

Table 3. 14 Isotherm modelling of Cr(VI) uptake by almond hull MFC at pH 2 and 21°C

Isotherm models	Unit	Stirring ST		Ultrasound (US)	
		AHST 120	AHST 220	AHUS 120	AHUS 220
Langmuir	K_L (L/mg)	0.13	0.22	0.13	0.02
	q_m (mg/g)	83.57	104.47	99.01	167.95
	R^2	0.9352	0.8754	0.9246	0.9536
Freundlich	K_F (L/mg)	26.95	43.98	26.74	21.09
	n	4.45	5.62	4.32	2.91
	R^2	0.9770	0.9961	0.9865	0.9925
Temkin	B (kJ/mol)	14.33	15.22	17.83	39.27
	b	171.16	161.13	137.57	62.46
	K_T (L/mg)	2.25	7.718	0.86	0.14
	R^2	0.9607	0.9794	0.9656	0.9745
D-R	K_{DR} (mol^2KJ^{-2})	5.28E-05	3.25E-06	5.28E-05	2.82E-04
	E (kJ/mol)	287.48	392.23	97.33	42.11
	q_m (mg/g)	76.58	98.45	88.75	135.33
	R^2	0.7299	0.6568	0.7299	0.8003

The uptake of chromium by cassava peel and almond hull MFC increases at pH 2, as shown in Table 3.14. The maximum loading capacity of chromium ions was obtained using CPUS 220 (cassava peel with ultrasound) and AHUS 220 (almond hull with ultrasound) and corresponded to 180.73 mg/g and 167.95 mg/g respectively**.** The Dubinin-Radushkevich isotherm model gave a good description of the adsorption behaviour of CPUS 220 at pH 2 using the ultrasound method (R^2 = 0.9981) (see Appendix II: A.2 – a comparison of isotherm models for the uptake of Cr(VI) with CPUS 220 at pH 2 and the Dubinin–Radushkevich plot for CPUS 220). The mean free energy, E_D, was found to be 28.5 kJ/mol, which indicates a chemisorption process (E_D > 16 kJ/mol (if the E_D <8 kJ/mol physisorption occurs and 8>E_D<16 kJ/mol then adsorption follows ion exchange)[230–232] and a pore-filling mechanism for Cr(VI) adsorption on CPUS 220 occurs. Meanwhile, the isotherm for CPST 120, CPST 220 and CPUS 220 fitted well with the Freundlich model and value of n using the ultrasound method was higher (n>1) than for stirring indicating that ultrasound was favourable more adsorption and could lead to higher adsorption intensity.[212] Using ultrasound, the sorption of Cr(VI) increased loading capacity cellulose (mg/g) roughly four- and two-fold for CP 220 and CP 120, respectively, when compared to stirring. Ultrasonic cavitation facilitates the enhancement of mass transfer from solution to the adsorbent and breaking affinities between adsorbate and adsorbent.[233]

All MFC of the almond hull generated satisfactory fits with the Freundlich model for Cr(VI) sorption at pH 2. Using the Langmuir model, the maximum loading capacity (q_m) was predicted to be the highest for AHUS 220 followed by AHST 220, AHUS 120 and AHST 120 with uptakes of 167.95 mg/g, 104.47 mg/g, 99.01 mg/g and 83.57 mg/g respectively (see Appendix III. Figure A.3 – a comparison of isotherm models with AHUS 220 at pH 2 and the

Freundlich plot for AHUS 220). AH 220 had the best performance and AH 120 the worst, as predicted from zeta potential value of AH 220 (+2.0 ± 0.33 mV) more positively charged than AH 120 (-1.7 V ± 1.1 mV) at pH 2. Adsorption through the ultrasound method was greatly improved with respect to stirring, leading to an increase in uptake of 69% and 25% for AH 220 and AH 120 respectively.

3.3.2.2 XPS analysis-evidence of adsorbed chromium

The oxidation state of chromium following adsorption was determined by XPS analysis in order to gain insight into the adsorption mechanism, as displayed in Figure 3.33. The adsorption for XPS analysis was performed only using experiments involving Cr(VI) either at a concentration of 300 mg/L by stirring after 2 h and at 900 mg/L after contact for 30 minutes via sonication at pH 2. The analysis was conducted on the air-dried residue of the MFC of cassava peel (CPST 220 and CPUS 220) and almond hull (AHST 220 and AHUS 220) following adsorption. The deconvolution of the XPS spectrum for sorbed chromium is summarised in Table 3.15 and shows two distinct peaks with $2p^{3/2}$ and Cr $2p^{1/2}$ orbitals binding energies of around 577 eV and 587 eV, respectively, which is representative of the oxidation state +3 of Cr(III). These peak values are similar to the binding energy of Cr(III) species in the form of $Cr(OH)_3$ where the fitting peak for $Cr(OH)_3$ standard $2p^{3/2}$ is 577.3 – 577.7 eV.[234,235] This fact confirms during the adsorption process that the oxidation state hexavalent chromium was reduced to the trivalent form. Singh *et al*.[236] reported the removal of Cr(VI) by chitosan using XPS 90% of the chromium evidenced was as Cr(III) and the remaining 10% was Cr(VI) indicating that the reduction process did not reach completion. Conversion from Cr(VI) to Cr(III) can be inferred from the percentage of area corresponding to Cr(III) 2p which reached 76.8%, 79.8%, 83.0% and 70.0% for CPST 220,

CPUS 220, AHST 220 and AHUS 220, respectively. The deconvoluted Cr $2p^{3/2}$ and $Cr^{1/2}$ of Cr(VI) band at 580-581 eV and 588-589 eV through Casa XPS software as can be seen in Table 3.15, after comparison with the reference standard of Cr(VI) where the binding energies appear at bands of 579-581 and 588-590 eV, respectively.[237]

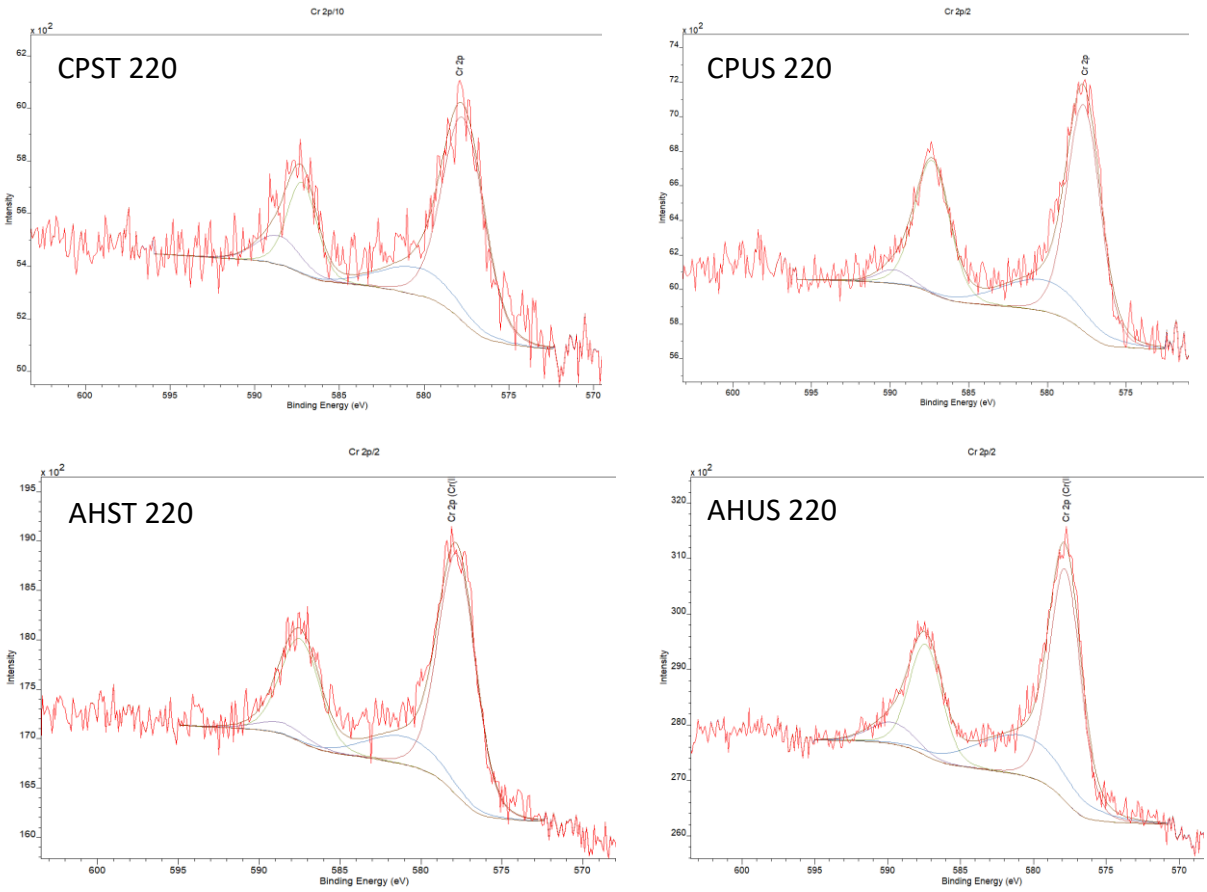

Figure 3. 33 XPS spectra of chromium after adsorption on the MFCs (Original in colour)

Table 3. 15 Deconvolution (eV) of XPC spectra of chromium $2p^{3/2}$ and $2p^{1/2}$ after adsorption

MFC loaded chromium	Cr(III) binding energy/eV		Cr(VI) binding energy/eV	
	$2p^{3/2}$	$2p^{1/2}$	$2p^{3/2}$	$2p^{1/2}$
CPST 220	577.68	587.19	580.38	588.59
CPUS 220	577.67	587.32	580.25	589.77
AHST 220	577.77	587.46	581.08	588.51
AHUS 220	577.81	587.39	580.74	589.70

The mechanism reduction of Cr(VI) to Cr(III) in acid medium is illustrated in Figure 3.34, where Cr(III) compound of adsorption product is less toxic than Cr(IV). The removal anion Cr(VI) formed monovalent of $HCrO_4^-$ at pH 2 following four-steps:

i. protonation of hydroxyl or carboxyl group on the cellulose surface;
ii. adsorbed anionic Cr(VI) to the protonated surface through the esterification of chromate;
iii. the reduction of Cr(VI) into Cr(III) followed the formation carboxyl group by the oxidation of cellulosic functional group or the adjacent donor electron from the cellulosic functional group (in a redox reaction, the acceptor electron must be bonded to cellulose first then Cr(VI) can be reduced to Cr(III), and;
iv. electrostatic attraction of Cr(III) or chelating Cr(III) with hydroxyl and or carbonyl group on the MFC surface [89,238,239].

According to Nakano *et al*.[239], reduction of Cr(VI) to Cr(III) in the acidic solution can contribute shifting pH from acid solution to neutral solution during adsorption and a substantial amount the decomposition recovery product of Cr(III) in form $Cr(OH)_3$ where the aforementioned result has similarity with the results of the present study with the Cr(III) form following adsorption also being detected as $Cr(OH)_3$ (BE $2p^{3/2}$=577 eV). [239,240]

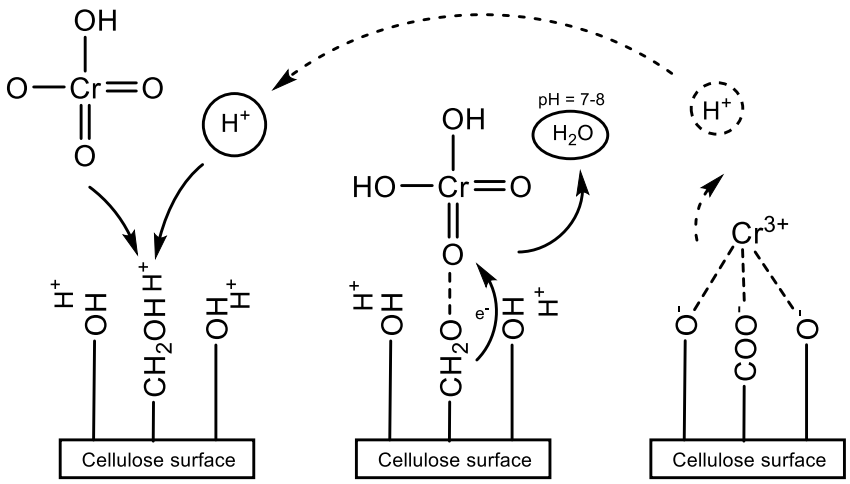

Figure 3. 34 The illustration of mechanism adsorption of Cr (VI) into the cellulose surface.

The reduction from Cr(VI) to Cr(III) contributes to the increase of pH as hydrogen ions are consumed in the reaction, the potential reduction value of chromium species (Eq. 3.18-3.21) based on the condition the pH solution and Cr(VI) concentration as follows: [241,242]

pH < 1, low conc.: $H_2CrO_4 + 6H^+ + 3e^- \leftrightarrow Cr^{3+} + 4H_2O$ $E^0 = +1.33$ V (Eq. 3. 18)

2≤ pH≤ 6, low conc.: $HCrO_4^- + 7H^+ + 3e^- \leftrightarrow Cr^{3+} + 4H_2O$ $E^0 = +1.35$ V (Eq. 3. 19)

High conc.: $Cr_2O_7^{2-} + 14H^+ + 6e^- \leftrightarrow 2Cr_3^+ + 7H_2O$ $E^0 = +1.33$ V (Eq. 3. 20)

pH > 6.5, low conc. $CrO_4^{2-} + 4H_2O + 3e^- \leftrightarrow Cr(OH)_3 + 5OH^-$ $E^0 = -0.13$ V (Eq. 3. 21)

Table 3. 16 Deconvolution (% area) of MFC C1s XPS spectra before and after adsorption

Peak C1s	B.E/eV	Chemical state	Cassava peel MFC/% area			Almond hull MFC/% area		
			CP 220	CPST 220	CPUS 220	AH 220	AHST 220	AHUS 220
I	285	C-C / C-H	50.85	57.98	31.21	55.12	51.33	49.97
II	286	C-O	36.92	29.9	54.74	31.05	33.47	38.01
III	287-288	C=O / O-C-O	7.83	5.58	13.52	7.92	9.45	9.51
IV	289	O-C=O	4.4	6.54	0.53	5.92	5.74	2.51

The changes in the functional group composition of MFC prepared via hydrothermal at a temperature of 220^{o}C both before and after adsorption was summarised Table 3.16 (see Appendix IV. Figure A. 4 - The deconvolution C1s XPS spectra of CP 220 before and after adsorption and Appendix V. Figure A.5 - The deconvolution C1s XPS spectra of AH 220 before and after adsorption)**.** The structural and composition transformation could occur at the active sites of the cassava peel and almond hull MFCs. Even though the mechanism of adsorption of Cr(VI) that has been proposed goes through an indirect mechanism via the active site of high-affinity donor electrons functional group such as hydroxyl, carbonyl, carboxyl and phenolic group [243], the composition of C-H could be considered having a role of Cr(VI) reduction. In acidic solution, the C-H group could influence the ability of the adsorbent to reduce Cr(VI) leading to the formation of oxidation product, C-OH, as described in the redox reaction (in Eq. 3.22). [237] In Table 3.16, the portion the functional group from C-H to C-OH increased following adsorption in the MFC of CPUS 220, AHST 220 and AHUS 220, *e.g.,* on CPUS 220 from 36.92% to 54.74%. Both MFC of cassava peel and almond hull treated via ultrasound, the C-H intensity decreased significantly via sonication by 19.64% and 5.15 %, respectively after adsorption. This indicates the application of ultrasound could be used as a trigger for more an intense reaction between adsorbent and adsorbate with respect to stirring, particularly for CPUS 220.

CPST 220 had the lowest uptake capacity of Cr(IV) when compared to MFC of CPUS 220, AHST 220 and AHUS 220. From the data for the C1s peak of cellulose, the percentage of C-H (B.E= 285 eV) in cassava peel (CPST 220) increased respect to the others by around 7.1 % using the stirring method from 50.85 % to 57.98%. It also displayed a decreased in terms of O-C-O intensity whilst the other MFC increased in this respect. Due to the increase

in C-H intensity after adsorption was suggested the mechanism for adsorption of CPST 220 and chromium on oxygenated carbon.

The possible redox reactions and regeneration of the active sites of the adsorbent could be described as shown in Eq.3.22-3.25:[237]

$$–C–H + Cr(VI) + H_2O \rightarrow –C–OH + Cr(III) + H^+ \quad \text{(Eq. 3. 22)}$$

$$–C–OH + Cr(VI) + H_2O \rightarrow –C=O + Cr(III) + H^+ \quad \text{(Eq. 3. 23)}$$

$$–C=O + Cr(VI) + H_2O \rightarrow –COOH + Cr(III) + H^+ \quad \text{(Eq. 3. 24)}$$

$$–C–COOH + Cr(VI) + H_2O \rightarrow –C–H + Cr(III) + H^+ + CO_2 \quad \text{(Eq. 3. 25)}$$

XPS spectra of the C1s band of cellulose revealed that not only the portion intensity on the specific functional group but also the changes of cellulose oxidation state. The surface-active site composition depends on the chemical component of raw biomass and the temperature applied during hydrolysis or other treatment. The surface function group composition shifted to a new equilibrium after adsorption wherein the oxygen-containing group (Lewis bases), such as C-OH, -COH, -COOH are likely to act as primary functional groups that the anionic chromium with the -C-H function group also possibly aiding Cr(VI) sorption under certain circumstance.[237,238]

3.3.2.3 Methylene blue adsorption isotherm models

A similar method that was used to study the adsorption of Cr(VI) was also used to investigate the interaction of methylene blue (MB) with MFCs derived from cassava peel and the almond hull and to subsequently compare the results with isotherm models of Langmuir, Freundlich, Temkin and Dubinin-Radushkevich.

Methylene blue is a cationic dye at neutral pH, whereas Cr(VI) instead forms different ions in solution. The adsorption of methylene blue was conducted at pH 7, which approaches the conditions used in the treatment of waste dyes within the industrial textile industry, even though it should be noted that sorption capacity could be increased at pH 10.[244]

The parameters of the various tested isotherm models derived from the aforementioned methylene blue removal experiments involving cassava peel MFC, almond hull MFC and activated carbon (Norit™) are shown in Table 3.17, Table 3.18 and Table 3.19 respectively. Interestingly, methylene blue uptake by MFC produced via microwave hydrothermal treatment at a temperature of 120 ^{o}C had a superior performance with respect to MFC generated at 220 ^{o}C. The highest equilibrium MB adsorption was reached using CPUS 120 (199.06 mg/g) and AHUS 120 (128.47 mg/g). The uptake of methylene blue using sonication could be improved by approximately 11.05% and 38 % for CP120 and CP 220, respectively and also by 7.5% and 10.9% in the case of AH 120 and AH 220, respectively.

The fitting parameter with four isotherm models showed CPST 120, CPUS 120 and CPUS 220 followed Langmuir (see Appendix VI. Figure A.6 - a comparison of isotherm model for uptake MB with CPUS 120 and Langmuir plot for CPUS 120), which indicates the formation monolayer coverage of methylene blue on the outer surface the adsorbent. Conversely, Temkin model gave the best representation for CPST 220, AHUS 120 and AHST 220 (see Appendix VII.Figure A.7 - a comparison of isotherm model for uptake MB with AHUS 120 and Temkin plot for AHUS 120) while and Freundlich model fitted with AHST 120 and AH 220. For CPST 220 and AHST 120, the coefficient correlation (R^2) results are very

close and could indeed be fitted using either the Freundlich or Temkin models. As can be seen in Table 3.19, the adsorption of MB by commercial activated carbon (AC) (Norit™) could be well fitted using the Langmuir model with the loading capacity via stirring (ACST) and ultrasound (ACUS) mode were 221.89 mg/g and 286.44 mg/g, respectively (see Appendix VIII. Figure A.8 - a comparison of isotherm model for MB uptake by ACUS and Langmuir plot for ACUS).

Table 3. 17 Isotherm modelling of MB uptake by cassava peel MFC

Isotherm models	**Unit**	**Stirring (ST)**		**Ultrasound (US)**	
		CPST 120	**CPST 220**	**CPUS 120**	**CPUS 220**
Langmuir	K_L (L/mg)	0.05	0.10	0.01	0.02
	q_m (mg/g)	171.57	51.52	199.06	83.42
	R^2	0.9808	0.9681	0.9876	0.9897
Freundlich	K_F (L/mg)	79.28	18.83	36.18	9.74
	n	8.22	5.45	3.85	2.66
	R^2	0.8574	0.9916	0.9586	0.9725
Temkin	B (kJ/mol)	17.42	7.35	37.062	18.84
	b	140.79	333.9	66.17	130.16
	K_T (L/mg)	30.17	4.433	0.25	0.20
	R^2	0.8821	0.9918	0.9741	0.9851
D-R	K_{DR} (mol^2KJ^{-2})	1.31E-04	1.46E-05	6.00E-04	9.90E-05
	E (kJ/mol)	61.88	184.93	28.87	71.05
	q_m (mg/g)	159.20	48.08	166.49	64.81
	R^2	0.9288	0.8402	0.9187	0.9288

Table 3. 18 Isotherm modelling of MB on almond hull MFC

Isotherm models	Unit	Stirring (ST)		Ultrasound (US)	
		AHST 120	AHST 220	AHUS 120	AHUS 220
Langmuir	K_L (L/mg)	0.17	0.16	0.17	0.05
	q_m (mg/g)	118.72	89.74	128.47	100.82
	R^2	0.9013	0.9241	0.9553	0.9291
Freundlich	K_F (L/mg)	59.45	45.19	52.89	41.40
	n	7.68	8.22	6.08	6.87
	R^2	0.9980	0.9826	0.9872	0.9974
Temkin	B (kJ/mol)	13.26	9.27	17.25	12.56
	b	184.96	264.54	142.14	195.35
	K_T (L/mg)	37.92	56.573	7.41	6.50
	R^2	0.9970	0.9865	0.9919	0.9945
D-R	K_{DR} (mol^2KJ^{-2})	1.77E-05	9.20E-06	1.77E-05	1.18E-04
	E (kJ/mol)	240.83	233.11	168.23	64.98
	q_m (mg/g)	113.28	86.52	119.18	94.03
	R^2	0.7972	0.7820	0.7972	0.7690

Table 3. 19 Isotherm modelling of MB on Norit™

Isotherm models	Unit	Stirring	Ultrasound
		ACST	ACUS
Langmuir	K_L (L/mg)	0.52	0.06
	q_m (mg/g)	221.89	286.44
	R^2	0.9919	0.9869
Freundlich	K_F (L/mg)	194.55	158.54
	n	44.83	10.98
	R^2	0.8926	0.8541
Temkin	B (kJ/mol)	4.789	22.684
	b	512.1125	108.1227
	K_T (L/mg)	3.60E+17	431.016
	R^2	0.8972	0.8717
D-R	K_{DR} (mol^2KJ^{-2})	7.70E-06	1.15E-04
	E (kJ/mol)	254.85	65.98
	q_m (mg/g)	219.60	272.86
	R^2	0.9145	0.9598

The above results suggest that highly efficient uptake of methylene blue can be achieved via the use of MFC adsorbents produced from microwave-assisted hydrolysis of waste biomass at a treatment temperature of 120°C. The mechanism of adsorption between cellulose and methylene blue depends on the surface structure of the active site belonging to the cellulosic matrix. The hydroxyl groups on cellulose play a vital role in inter/intramolecular bonding with MB through the formation of hydrogen bonds.[245]

It is known that the chemical form of MB in aqueous solution shifts between a cationic species (MB^+) and undissociated species (MB^0) depending on solution pH, as reported by Salazar-Rabago *et al.*[246] and shown in Figure 3.35. MB^0 predominated at pH < 3 and MB^+ form presents at pH > 6 where pH = *p*Ka =3.8. Due to the domination of MB^+ at neutral or higher pH, the adsorption mechanism of MB onto the negatively charged adsorbent surface (pH > pH_{pzc} adsorbent) is preferred through the electrostatic attraction with increasing pH causing the uptake of MB increase.[246]

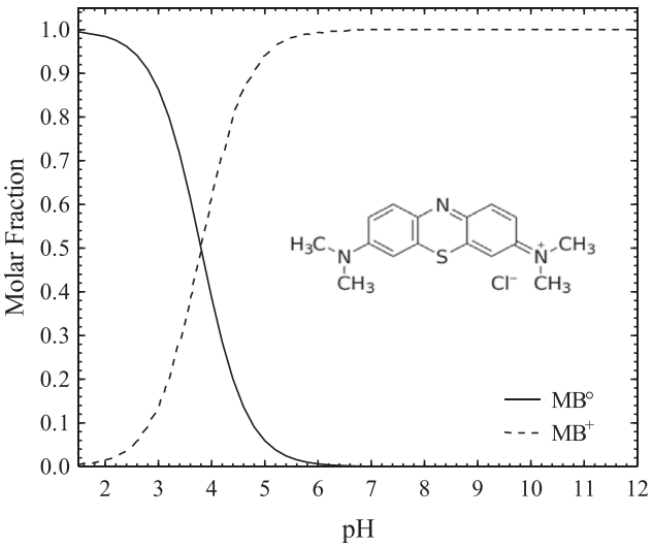

Figure 3. 35 The species of methylene blue as a function of pH [246] (Original picture)

However, from the adsorbent perspective according to the data presented herein, the order from highest to lowest MB adsorption capacity by stirring was CP 120 (191.06

mg/g) > AH 120 (118 mg/g) > AH 220 (89.74 mg/g) > CP 220 (51.52 mg/g). Based on the results of the zeta potential analysis, the charge of MFC 120 (-7.4 mV) was the less negative charge than MFC 220 at pH 7. In this case (at pH neutral), methylene blue is likely to be attracted to the hydroxyl at MFC surface, with the attraction being driven by dipole-dipole interaction between hydrogen group and the electropositive charge of methylene blue.[247] This statement correlates well with the C1s XPS spectra of MFC of CP 120, CP 220, AH 120 and AH 220 summarised in Table 3.20, (see Appendix IX. Figure A.9 – Deconvolution C1s XPS spectra for CP 120 and AH 220 before adsorption and for C1s XPS spectra for CP 220 and AH 220 in Appendix IV and V). It can be seen that the percentage area of the C=O or O-C-O group descended from highest to the lowest in the order of CP 120 (15.65%) > AH 120 (9.69%) > AH 220 (7.92%) > CP 120 (7.83%). The reaction which causes the high affinity of the carbonyl group with MB molecule is presented in the scheme below (Eq. 3.26): [247]

$$\mathrm{C=O^{\delta-}} + \mathrm{MB^{\delta+}} \quad \rightarrow \quad \mathrm{C=O \cdots\cdots MB} \qquad \text{(Eq. 3. 26)}$$

The composition of component cellulose could notice the abundance of the hydroxyl group, where C-O peak and C=O / O-C-O peaks of CP 120 was 65.49 % and 15.65% respectively. This could be one reason CP 120 was superior uptake MB than other cellulose. On the other hand, the weak electrostatic attraction of the surface could be generated by the carboxylic acid group. The carboxylic group should become predominantly negatively charged (-COO-) due to the fact that the pH of the solution used in this study was 7 and that the *p*Ka value of carboxylic acid is around 2-4 (pH solution > pH_{pzc} adsorbent).[248]

Table 3. 20 Composition (% area) of MFC adsorbents from the C1s XPS spectra

Peak	BE/eV	Chemical state	Cassava peel/% area		Almond hull/% area	
			CP 120	CP 220	AH 120	AH 220
I	285	C-C / C-H	19.18	50.85	54.53	55.12
II	286	C-O	62.49	36.92	32.08	31.05
III	288	C=O / O-C-O	15.65	7.83	9.69	7.92
IV	289	O-C=O	2.68	4.40	3.70	5.92

Parker *et al*.[247] and Tran *et al*.[249] reported that Yoshida bonding interaction (hydrogen bonding interaction) could contribute to the adsorption of dye molecules, where Yoshida bonding is known as the interaction between hydroxyl group (dipole H bonding) of cellulose surface and the aromatic ring of methylene blue. The n-π electron donor-acceptor interaction is the oxygen functional group (*i.e*., -COOH, -OH) of the cellulose surface interact with the aromatic ring of methylene blue. These forces may be limited to the carboxylic acid group as the primary mechanism for adsorption of cellulose and methylene blue due to deprotonation of carboxyl on pH adsorption. [247,249] Moreover, the carboxylic acid group CP 120 of the Boehm titration data is the lowest by 0.62 mmol/g (Table 3.11), and the percentage area of O-C=O is the lowest as well by 2.68 % (Table 3.20). This could be suggested the adsorption MB on the surface of CP 120 at pH 7 dominated by the functional group of hydroxyls.

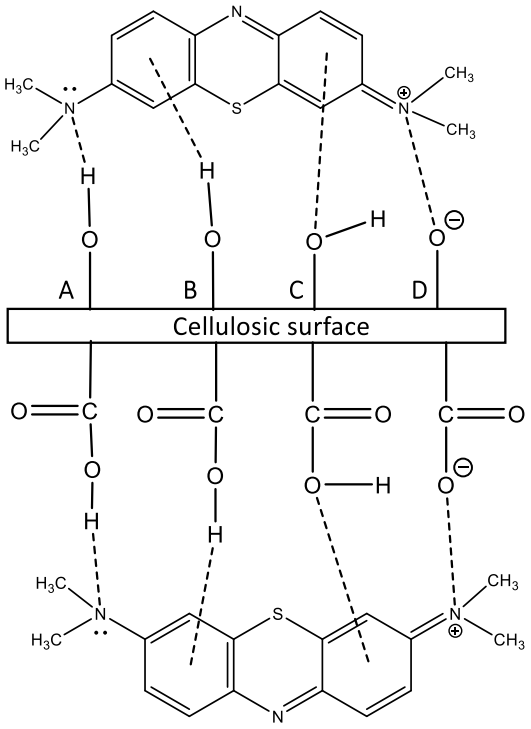

Figure 3. 36 Illustration of methylene blue interaction A) Dipole-dipole hydrogen bonding. B) Yoshida hydrogen bonding C) $n-\pi$ interaction. D) Electrostatic interaction[247,248]

The possible adsorption mechanism of methylene blue onto MFC cassava peel and the almond hull is likely to involve electrostatic attraction, hydrogen bonding, Yoshida hydrogen bonding and n-π interaction as illustrated in Figure 3.36.

3.3.3 Kinetic study of adsorbates onto MFC

A kinetic study was conducted in order to investigate the surface adsorption rate of Cr(VI) and methylene blue onto cassava peel and almond hull MFC by fitting with *pseudo*-first-order, *pseudo*-second-order, Elovich and intra-particle diffusion kinetic models. The correlation coefficient from these models gave the agreement between the experimental data and that predicted by the models. The adsorption kinetics of a system can be controlled by multiple steps, *i.e.*, the transfer of adsorbate to the adsorbent surface, transfer adsorbate on the adsorbent surface to the intra-particle active sites and retention

on the active sites, complexation or intra-particle precipitation phenomena. [250] During the kinetics studies, the adsorption rate was monitored at different time intervals (from 30 to 360 minutes) for stirring and for 5 to 60 minutes for ultrasound method.

Pseudo-first order

The *pseudo*-first order kinetic model is the earliest model from Lagergren in 1898 to describe the adsorption of liquid-solid adsorption between oxalic acid and malonic acid onto charcoal based on equilibrium adsorption of solid capacity. [251]. The adsorption mechanism is controlled by diffusion and mass transfer of the adsorbate to surface site [252]. The *pseudo*-first-order equation (Eq. 3.27), and the linearised form are expressed in (Eq. 3.28)

$$\frac{dq}{dt} = k_1(q_e - q_t) \qquad \text{(Eq. 3. 27)}$$

$$\log(q_e - q_t) = \log q_e - \frac{k_1}{2.303} t \qquad \text{(Eq. 3. 28)}$$

Where k_1 is the *pseudo*-first-order equation rate constant (min^{-1}), t is reaction time (min) q_e and q_t are the amounts of adsorbate adsorbed at equilibrium and at time t (mg/g), respectively. The value of k_1 was determined from the slope of the linear plots between log (q_e -q) and t.[212]

Pseudo second order

The *pseudo*-second order kinetic model assumes that the adsorption process is chemisorption in nature. The mechanism may involve the sharing of valence forces or the exchange of electrons between the adsorbent and the adsorbate.[253] The *pseudo*-second-order adsorption kinetic model is expressed in Eq. (3.29) and the linear form is shown in Eq. (3.30)

$$\frac{dq}{dt} = k_2(q_e - q_t)^2 \qquad \text{(Eq. 3. 29)}$$

$$\frac{t}{q_t} = \frac{1}{k_2 q_e^2} + \frac{t}{q_e} \qquad \text{(Eq. 3. 30)}$$

Where, k_2 (g^{-1}. min^{-1}) is the rate constant of *pseudo*-second order. The second-order sorption rate constant and q_e were determined from the slope and intercept of the plot between t/q_t and time.

Elovich

Elovich model is widely applied to describe the adsorption kinetics of various adsorbates on heterogeneous adsorbents, for instance of gases onto the solid system based on adsorption capacity.[254] The mathematical equation of Elovich model is represented in eq (3.32) as: [255]

$$\frac{dq}{dt} = \alpha\, exp^{-\beta q} \qquad \text{(Eq. 3. 31)}$$

$$q_e = \frac{1}{\beta}\ln(\alpha\beta) + \frac{1}{\beta}\ln t \qquad \text{(Eq. 3. 32)}$$

Where q is the quantity of adsorbate adsorbed at specific time α is the initial adsorption rate constant ($mg.g^{-1}min$) and β is the desorption rate constant during one experiment(g/mg).

Intra-particle diffusion model

The Weber-Morris intra-particle diffusion model was also employed in Eq. (3.33)

$$q_t = k_{id} t^{0.5} + C \qquad \text{(Eq. 3. 33)}$$

Where, K_{id} is the intra-particle diffusion constant, and C is a constant, which the intercept C describes the thickness of the boundary layer from the plot between q_t and $t^{0.5}$. Generally, the biosorption mechanism is presented by the transport of the adsorbate to the external

surface of the adsorbent, transport of the adsorbate within the pores of the adsorbent and sorption at the interior sites. [256,257]

3.3.3.1 Kinetic study of chromium uptake

The kinetic study for chromium for cassava peel was conducted at pH 2 with chromium concentration was either 337 mg/L for stirring or 1019 mg/L for ultrasound mode and the almond hull, chromium concentration was 492 mg/L for AHST 120 , 611 mg/L for AHST 220 and AHUS 120, and 704 mg/L for AHUS 220. In Table 3.21 (CP) and 3.22 (AH), the *pseudo*-second order model gave the best description for all experimental kinetic data of Cr(VI). The experimental data values of *pseudo*-second order rate constants gave strong correlation coefficients at $R^2 > 0.99$ (see Appendix X. Figure A.10- the plot of *pseudo*-second order for CPUS 220 and AHUS 220). Based on the *pseudo*-second-order assumption, it was suggested that in the medium pH 2, the interaction of Cr(VI) on the surface of MFC might be chemical sorption that involves two phases of rate-limiting steps (slow and fast step reaction).[252,258–260]

Table 3. 21 The kinetic modelling of Cr (VI) uptake by cassava peel MFC at pH 2 and 21°C

Kinetic models	Unit	Stirring		Ultrasound	
		CPST 120 at 337 mg/L	**CPST 220 at 1019 mg/L**	**CPUS 120 at 337 mg/L**	**CPUS 220 at 1019 mg/L**
Pseudo-first order	k_1 (min^{-1})	0.0083	0.0052	0.042	0.214
	q_e (mg/g)	10.02	45.11	19.28	169.79
	R^2	0.9498	0.9811	0.9390	0.9007
Pseudo-second order	k_2 (g/mg.min)	0.0035	0.00067	0.0079	0.0082
	q_e (mg/g)	35.47	153.44	51.31	163.61
	R^2	0.9997	0.9989	0.9996	0.9965
Elovich	α (mg/g.min)	0.3142	0.6393	0.555	0.698
	β (mg/g)	0.4216	0.1070	0.1830	0.0623
	R^2	0.9926	0.8518	0.9804	0.6264
Intraparticle diffusion	k_{id} ($mg/g.min^{0.5}$)	0.506	1.836	2.33	6.091
	C	24.399	153.443	29.177	124.042
	R^2	0.7333	0.8749	0.7952	0.4570

Table 3. 22 The kinetic modelling of Cr (VI) uptake by almond hull MFC at pH 2 and 21°C

Kinetic models	Unit	Stirring		Ultrasound	
		AHST 120 at 492 mg/L	**AHST 220 at 611 mg/L**	**AHUS 120 at 611 mg/L**	**AHUS 220 at 704 mg/L**
Pseudo-first order	k_1 (min^{-1})	0.0044	0.0057	0.198	0.098
	q_e (mg/g)	34.96	31.08	48.85	76.63
	R^2	0.9527	0.9810	0.9811	0.9858
Pseudo-second order	k_2 (g/mg.min)	0.0003	0.0005	0.0114	0.0025
	q_e (mg/g)	98.78	117.28	87.45	119.84
	R^2	0.9976	0.9994	0.9996	0.9963
Elovich	α (mg/g.min)	228.449	10668.1	63157.8	351.2
	β (mg/g)	0.1188	0.1188	0.150	0.063
	R^2	0.9733	0.9869	0.9365	0.9206
Intraparticle diffusion	k_{id} ($mg/g.min^{0.5}$)	1.451	1.228	3.696	9.37
	C	59.05	85.05	62.14	49.70
	R^2	0.9764	0.9469	0.8093	0.9018

3.3.3.2 Kinetic study of methylene blue uptake

In Table 3.23 and 3.24, the *pseudo*-second-order model revealed the best agreement for all experimental kinetic data of methylene blue adsorption with coefficient correlation value (R^2) were all greater than 0.99 (see Appendix XI Figure A.11 - *pseudo*-second order plot for CPUS 120 and AHUS 120). As well as the MFCs, the kinetic study of MB uptake by Norit™ could also be well fitted with the *pseudo*-second-order model (see Table 3.25). Similar to the adsorption of Cr(VI), the mechanism of adsorption of methylene blue onto MFC was based on chemisorption involving valency forces through sharing or exchange electron between adsorbent and adsorbate.[258]

However, the adsorption kinetic model is likely to be a complex process that could involve more than one mechanism. In Table 3.25, the adsorption MB by Norit™ in sonication could also be well fitted using *pseudo*-second order (R^2 value = 0.9975) or intra-particle diffusion model (R^2 value = 0.9972)The intercept, C, gives an idea about boundary layer thickness, the larger the value of the intercept, the higher the boundary effect.[261] According to Tan *et.al.*[262], intraparticle diffusion indicates two or more steps occurring in the adsorption process. The adsorption data indicated that the removal of dye from aqueous phase is a complex process, involving both boundary layer diffusion as well as intra-particle diffusion.[262,263]

Table 3. 23 The kinetic modelling of methylene blue on cassava peel MFC

Kinetic models	Unit	Stirring		Ultrasound	
		CPST 120 at 801 mg/L	**CPST 220 at 245 mg/L**	**CPUS 120 at 801 mg/L**	**CPUS 220 at 418 mg/L**
Pseudo first order	k_1 (min^{-1})	0.0111	0.0173	0.102	0.203
	q_e (mg/g)	2.64	8.48	16.92	6.15
	R^2	0.9671	0.9921	0.9537	0.9467
Pseudo second order	k_2 (g/mg.min)	0.0118	0.0042	0.0131	0.0808
	q_e (mg/g)	136.49	36.88	134.65	46.88
	R^2	1.0000	0.9999	1.0000	1.0000
Elovich	α (mg/g.min)	66.316	0.326	0.552	0.032
	β (mg/g)	1.2692	0.4096	0.186	0.748
	R^2	0.9358	0.9830	0.8289	0.6299
Intraparticle diffusion	k_{id} ($mg/g.min^{0.5}$)	0.123	0.492	2.158	0.51
	C	133.95	28.84	118.84	43.41
	R^2	0.8135	0.9293	0.6791	0.4617

Table 3. 24 The kinetic modelling of methylene blue on almond hull MFC

Kinetic models	Unit	Stirring		Ultrasound	
		AHST 120 at 736 mg/L	**AHST 220 at 736 mg/L**	**AH US 120 at 736 mg/L**	**AHUS 220 at 736 mg/L**
Pseudo-first order	k_1 (min^{-1})	0.0047	0.0053	0.055	0.029
	q_e (mg/g)	15.06	32.95	25.13	30.85
	R^2	0.8762	0.9318	0.8632	0.7031
Pseudo-second order	k_2 (g/mg.min)	0.0011	0.0004	0.0079	0.0042
	q_e (mg/g)	123.11	109.51	125.67	105.66
	R^2	0.9999	0.9998	0.9995	0.9933
Elovich	α (mg/g.min)	14307273.5	225.4	1696313.0	12667.1
	β (mg/g)	0.0871	0.0871	0.131	0.113
	R^2	0.9159	0.9600	0.9902	0.9459
Intraparticle diffusion	k_{id} ($mg/g.min^{0.5}$)	0.785	1.578	4.245	5.16
	C	103.52	69.34	95.16	65.11
	R^2	0.7765	0.8412	0.8606	0.8968

Table 3. 25 The kinetic modelling of methylene blue on activated carbon

Kinetic models	Unit	Stirring	Ultrasound
		ACST at 1286 mg/L MB	**ACUS at 1530 mg/L MB**
Pseudo-first order	k_1 (min^{-1})	0.0245	0.0347
	q_e (mg/g)	37.71	86.71
	R^2	0.9267	0.9931
Pseudo-second order	k_2 (g/mg.min)	0.0018	0.0010
	q_e (mg/g)	241.93	315.81
	R^2	1.000	0.9975
Elovich	α (mg/g.min)	0.570	0.034
	β (mg/g)	0.168742	0.745
	R^2	0.9374	0.9726
Intraparticle diffusion	k_{id} ($mg/g.min^{0.5}$)	1.0223	13.36
	C	223.33	200.84
	R^2	0.8278	0.9972

3.3.4 Thermodynamic study of MB sorption

The thermodynamic parameters related to the adsorption process including standard Gibbs free energy change ($\Delta G°$), standard enthalpy change ($\Delta H°$) and standard entropy change ($\Delta S°$) were calculated using standard methods. The Gibbs free energy change of the adsorption process is related to the equilibrium constant as given in Eq. 3.34 [264]:

$$\Delta G° = -RTlnK_{LE} \qquad \text{(Eq. 3. 34)}$$

where $\Delta G°$ is standard Gibbs free energy change of adsorption in kJ/mol, R is the universal gas constant (8.314 J/mol K), T is the temperature in Kelvin and K_{LE} is the thermodynamic equilibrium constant given as (Eq. 3.35):

$$K_{LE} = q_{max}\ x\ b \qquad \text{(Eq. 3. 35)}$$

In this equation, q_{max} is maximum Langmuir adsorption capacity, and b is Langmuir isotherm constant. Standard Gibbs free energy change is also related to the standard enthalpy change ($\Delta H°$) and standard entropy change ($\Delta S°$) at a constant temperature as given in equation (3.36):

$$\Delta G° = \Delta H° - T\Delta S° \qquad \text{(Eq. 3. 36)}$$

Now using the equations (3.34) and (3.36) we have equation (3.37)

$$Ln\ K_{LE} = \frac{\Delta S°}{R} - \frac{\Delta H°}{RT} \qquad \text{(Eq. 3. 37)}$$

Where, standard enthalpy change (ΔH°) in kJ/mol, and standard entropy change (ΔS°) in kJ/mol K has been calculated from Eq. 3.37. We can calculate the values of ΔH° and ΔS° from the slope and intercept of van't Hoff's plot of ln K_{LE} against 1/T, respectively.

Thermodynamic parameters associated with the temperature influence of cassava peel (CP), almond hull (AH) and activated carbon (AC) (Norit™) on methylene blue adsorption via stirring are shown in Table 3.26. The values of standard Gibbs free energy change (ΔG°) for the adsorption MB process were calculated by using K_{LE} values obtained from the Langmuir model at different temperatures of 22, 35 and 45°C, whilst enthalpy and entropy ΔH° from slope and intercept of plot K_{LE} against 1/T (see Appendix XII: Figure A.12 the plot of the thermodynamic parameter for CPST 120, AHST 120, and ACST).

The Gibbs free energy (ΔG°) values for MFC of cassava peel, almond hull and Norit™ were found to be negative for all studied temperature conditions, indicating the adsorption process is the spontaneous natural process and feasible at low temperature.[265] As the temperature increases, the ΔG° becomes higher (tending to positive) for CPST 120, CPST 220 (in Table 3.26) and Norit™ and can be associated with declining loading capacity of

adsorbate with increasing temperature. On the other hand, the ΔG° value of almond hull (AHST 120 and AHST 220) became lower (tending towards negative) as the temperature increased resulting in greater driving forces towards higher adsorption capacity at a higher temperature.[266] From the magnitude of Gibss free energy value, the interaction between adsorbent and adsorbate can be classified as the mechanism of physisorption (-20 to 0 kJ/mol) or chemisorption (-400 to -80 kJ/mol).[267] It was clear that all thermodynamic studies data, the criteria of the adsorption system pose a physisorption mechanism.

Table 3. 26 Thermodynamic parameters of methylene blue adsorption on cassava peel, almond hull and activated carbon

Adsorbent	T/K	ΔG° / (kJ/mol)	ΔH°/ (kJ/mol)	ΔS° /(kJ/mol.K)	R^2
CPST 120	295	-5.18	-17.74	-0.0428	0.9636
	308	-4.41			
	318	-4.22			
CPST 220	295	-4.09	-32.90	-0.0973	0.9655
	308	-3.20			
	318	-1.80			
AHST 120	295	-7.44	16.73	0.082	0.9846
	308	-8.63			
	318	-9.31			
AHST 220	295	-6.60	24.69	0.106	0.9719
	308	-7.72			
	318	-9.07			
AC ST	295	-11.62	-71.36	-0.2030	0.9851
	308	-8.45			
	318	-7.03			

The enthalpy (ΔH°) value of CPST 120, CPST 220 and Norit™ have a negative value that implies the exothermic character of the adsorption phenomena (ΔH° < 0). The exothermic process means the release of extra energy in the form of heat from the total energy absorbed in bond breaking is less than the total energy released in the bond making between adsorbate and adsorbent.[265] On the contrary, the enthalpy value of almond hull

was positive value where +16.73 kJ and +24.69 kJ/mol for AHST 120 and AHST 220 respectively, which indicates that the sorption of MB is an endothermic process. The uptake capacity of on the almond hull can be increased by increasing the temperature, and the adsorption followed physisorption because of the ΔH° value is less than 40 kJ/mol.[244,268,269]

The negative value of entropy change (ΔS°) on cassava peel MFC and activated carbon suggested decreasing randomness at the liquid-solid interface during adsorption, or that no significant change occurs in the internal structures of the adsorbent during the adsorption process (ΔS°< 0)[265,270] while the entropy change of almond hull has a positive value indicating increased randomness at the surface during the adsorption process as temperature increased.[270]

From thermodynamic parameters, it can be concluded that both enthalpy (ΔH°) and entropy (ΔS) contribute to the Gibbs free energy (ΔG°) of the adsorption process. The adsorption of MB onto cassava peel MFC and Norit™ were favourable at low temperature whereas for the adsorption of MB with MFC of the almond hull, the reaction to be appeared to more extensive at a higher temperature. This indicates an endothermic reaction (ΔH° > 0) with increasing entropy effect (ΔS°> 0) due to surface-structural changes which can be attributed to the loosening of the ordered water structure at the surface cellulose during adsorption.[271,272]

3.4 Microwave Pyrolysis

Concerning the depletion of fossil fuel and the effect of global climate change, biomass is one candidate as a source of renewable energy. It is believed that bioenergy sustainability will grow in the next few decades such that it can positively contribute to society's desire to reducing gas emissions by managing the supply chain feedstock

infrastructure. The abundance of food waste and agricultural residue has been recognised as a potential resource of biofuel production, and currently, various diverse technologies have been introduced to convert waste to biofuels.[273,274]

Pyrolysis is one method that involves the thermal decomposition of biomass without oxygen. The three main biomass pyrolysis products comprise char (solid), bio-oil(liquid) and gas; therefore, the pyrolysis process could include combustion, liquefaction and gasification. Combustion involves burning biomass conversion to energy storage or heat; liquefaction is the extraction of the biomass oil at relatively low temperature, and gasification is a conversion of solid biomass to fuel gas or syngas by heating such as CO, CO_2, CH_4 and H_2.[69,275] Conventional heating via pyrolysis requires higher energy up to the temperature of 600 ^oC whereas application of microwave-assisted pyrolysis reduces this temperature to between 200 ^oC and 300 ^oC whilst still producing biofuels (char, liquid fraction and gas) from biomass.[276] Most transfer heating source of conventional pyrolysis through biomass surface use electric and gas heaters; meanwhile, microwave heating is generated from the interaction of electromagnetic radiation with biomaterial.[67,274] Carbonaceous materials have a high capacity to absorb the electromagnetic field of the microwave and convert into the heat.[69]

In the present experiments, investigations of the yields, higher heating value (HHV) of the char and the bio-oil and identification of the compound present in the bio-oil that was resulted from microwave-assisted pyrolysis of virgin cassava peel and almond hull biomass with different temperature (240°C, 260°C and 280°C) and contact time (0 and 6 minutes). The energy determination of char was carried out by bomb calorimetry, and the bio-oils were identified by GCMS.

3.4.1 The yield fraction of microwave-assisted hydrolysis

In Table 3.27, the yield of cassava peel and almond hull microwave pyrolysis products were obtained (see Appendix XIII. Figure A.13 for the char appearance of cassava peel and almond hull). The yield represents an average of gravimetric measurements which were repeated at least three times. The yield of char results tended to decrease as temperature and reaction time increased, while the oil and gases tend to increase as the temperature and holding time increased. It can be seen, for example, that the char yield of cassava peel reduced from 72.14% to 62.16 % while the gas product consistently rose between 16.29 % and 22.94 % from the temperature of 240-280 ℃ and holding time of 0 and 6 minutes. The liquid fraction yield also increases with increasing temperature of operation. Cassava peel gave the highest bio-oil yield with up to 14.9% whereas the almond hull gave 11.73%.

Table 3. 27 The microwave pyrolysis yields of cassava peel and almond hull

Operational condition		**Cassava peel/%**			**Almond hull/%**		
T/ ºC	**t/min**	**Char**	**Oil**	**Gas**	**Char**	**Oil**	**Gas**
240	0	72.14	11.57	16.29	75.25	9.87	14.88
240	6	70.13	13.47	16.41	73.16	10.33	16.50
260	0	69.11	13.79	17.09	70.17	10.42	19.41
260	6	68.43	12.89	18.68	69.85	9.17	20.97
280	0	66.64	14.21	19.16	60.52	11.73	27.75
280	6	62.16	14.90	22.94	59.44	11.55	29.02

In comparison, the bio-oil yields of cassava peel and almond hull by microwave heating were somewhat lower than other conventional methods. For example, pyrolysis of cassava peel was performed in a fixed-bed tubular reactor at a temperature of 525 ºC resulting maximum bio-oil yield of 51.2%, while the solid and the gas yield were 24.3% and

24.5%, respectively as reported Ki *et al*.[277] However, the yield of liquid fraction in the present study of the almond hull is slightly lower than the results reported by Gonzalez *et al.*[278], who found that gasification of an almond peel with a fixed bed reactor at a temperature of 800^{o}C and 200 cm^{3}/min air flow rate, gave a residue yield of char, oil and gas was 19.0 %, 12.1 % and 68.9 % respectively. The bio-oil yield obtained from microwave pyrolysis is usually lower compared to conventional pyrolysis, but there is a possibility to increase bio-oil yield by maximising the heating rate at the same temperature. [276] Wu *et al.* [276] reported that the yield of oil fraction from wood biomass through the conventional method (fixed bed stainless steel reactor), and microwave pyrolysis was a similar value (~46%) and by microwave heating was a much faster reaction. In these experiments, the microwave pyrolysis power was performed with low or minimum fixed power of 125 watts and 75 watts for cassava peel and almond hull, respectively, in order to avoid the risk of an explosion associated with rapid releases of hot gases and build of pressure.

3.4.2 Elemental analysis of char and bio-oil

The elemental analysis of the char residue and the bio-oil derived from both cassava peel and the almond hull is shown in Tables 3.28 (CP) and 3.29 (AH). One purpose of biomass pyrolysis is to enrich the remaining solid product (biochar) in carbon content via devolatilization - consequently removing hydrogen and oxygen preferably over carbon through loss other constituents, *i.e*., as water and non-condensable gases (CO, CO_2, H_2).[279]

The H/C and O/C ratio value of char and bio-oil are the characteristics of valuable products for fuel application and could explain the degree of aromaticity and maturation as illustrated in the relevant van Krevelen diagram (see Figure 3.37).[279,280] Low-temperature pyrolysis typically has a high H/C and O/C of char quality.[279] The European Biochar

Certificate states that the value of H/C ratio < 0.7 is indicative of a good biochar quality and pyrolysis efficiency in soil management and carbon sequestration proxy while the ratio molar O/C < 0.4 indicates lower biochar stability.[281,282]

The average ratio H/C value of cassava peel and almond hull char was equal to 0.95 and 0.63, respectively, where the high degree of aromaticity of the almond hull biochar results in a material which meets the requirement regarding the H/C ratio. The lower H/C ratio material can be applied in the adsorption of organic pollutant through its properties such as hydrophobicity, hydrogen bonding, electrophilic interaction and π-π interaction. [283] On the other hand, the average of ratio O/C of almond hull and cassava peel char was around 0.45 and 0.46 of indicates that both can be considered as low stability biochar and with high contents of polar compounds. Due to the fact that the O/C ratio is higher than the standard value (O/C ratio > 0.4). These biochar could be classified as hydrochar, high oxygen-containing functional groups, higher cation exchange capacity (CEC), containing mostly alkyl moieties than aromatic structure, higher nutrient retention capacity than biochar in soil application and primary mesoporous material with high pore volume but lower specific surface area than biochar.[284] Hydrochar or hydrothermal carbonisation (HTC), otherwise known as wet torrefaction is normally produced via conventional heating (up to 300 ^{o}C) of biomass mixed with water under high pressure to retain the water act as pyrolytic compounds to produce charcoal-like.[279]

Table 3. 28 CHN analysis (%) of cassava peel biochar and bio-oil

Operational condition	T/°C	240	240	260	260	280	280
	t/min	0	6	0	6	0	6
Char - CHN analysis/%	C	57.17	60.72	54.97	58.76	61.45	58.87
	H	4.40	4.75	4.95	4.83	4.31	4.27
	N	0.99	1.43	1.36	1.53	1.09	0.79
	O*	37.44	33.11	38.72	34.87	33.15	36.07
	O/C	0.49	0.41	0.53	0.49	0.40	0.46
	H/C	0.92	0.94	1.08	0.99	0.84	0.87
Char/(MJ/kg)	HHV	21.25	23.35	21.00	22.58	23.09	21.85
Oil - CHN analysis/%	C	58.42	61.70	63.08	62.30	64.34	64.88
	H	6.97	7.18	7.70	7.38	7.85	7.75
	N	0.80	0.62	0.77	0.85	1.16	0.89
	O*	33.81	30.51	28.45	29.46	26.65	26.48
	O/C	0.43	0.37	0.34	0.35	0.31	0.31
	H/C	1.43	1.40	1.46	1.42	1.46	1.43
Oil /(MJ/kg)	HHV	25.10	26.83	28.13	27.39	28.94	29.03

*oxygen was calculated from mass balance

Table 3. 29 CHN analysis (%) of almond hull biochar and bio-oil

Operational condition	T/ °C	240	240	260	260	280	280
	t/min	0	6	0	6	0	6
Char - CHN analysis/%	C	60.95	59.04	60.15	60.42	58.55	60.14
	H	3.21	3.11	3.06	2.74	3.17	3.68
	N	0.83	0.79	1.07	0.72	1.08	1.47
	O*	35.01	37.07	35.73	36.12	37.20	34.71
	O/C	0.43	0.47	0.45	0.45	0.48	0.43
	H/C	0.63	0.63	0.61	0.54	0.65	0.73
Char/(MJ/kg)	HHV	21.42	20.42	20.89	20.57	20.31	21.72
Oil - CHN analysis/%	C	71.85	72.70	71.64	73.01	70.58	73.85
	H	8.64	8.70	8.64	8.59	8.57	8.66
	N	2.40	2.75	2.43	2.77	2.27	2.17
	O*	17.11	15.85	17.29	15.63	18.58	15.32
	O/C	0.18	0.16	0.18	0.16	0.20	0.16
	H/C	1.44	1.44	1.45	1.41	1.46	1.41
Oil/(MJ/kg)	HHV	33.46	33.95	33.36	33.95	32.78	34.37

*oxygen was calculated from mass balance

The estimation of high heating value (HHV) was calculated from the modified Channiwala's formula.[77] The higher heating value (HHV) of biochar was among 21.25-23.35 MJ/kg and 20.31- 21.72 MJ/kg for cassava peel and almond hull, respectively. Bio-oil phase from microwave hydrolysis results has a higher gross caloric value than the biochar product. The bio-oil HHV of cassava peel and the almond hull was ranging from 21.1 to 29.03 MJ/kg and from 32.78 to 34.34 KJ/mol. Almond hull bio-oil has higher gross calorific value over cassava peel bio-oil due to having lower O/C ratio (~0.17) compared cassava peel (~0.37) and presented higher carbon content [285].

From the theoretical HHV formula (Channiwala's method) could be summarised that the quality of char or bio-oil could be related to the abundance of the total carbon and hydrogen content of biomass composition.[286] By increasing thermal pyrolysis, the char and bio-oil quality will significantly improve *e.g.*, HHV of virgin raw cassava peel was 16.47 MJ/kg (Table.3.2) then after pyrolysis was 23.35 MJ/kg (Table 3.28). Depolymerisation and fragmentation the biomass component at high temperature could present lowering H/C and O/C ratio of biochar, and then, the heating value of the fuel increases [283,287]. In Figure 3.37, in comparison, the atomic ratio between the biochar CP and AH with commercial fuel such as coal and anthracite where anthracite is the lowest atomic ratio as increase the geological ages indicating the highest fuel energy content.[288]

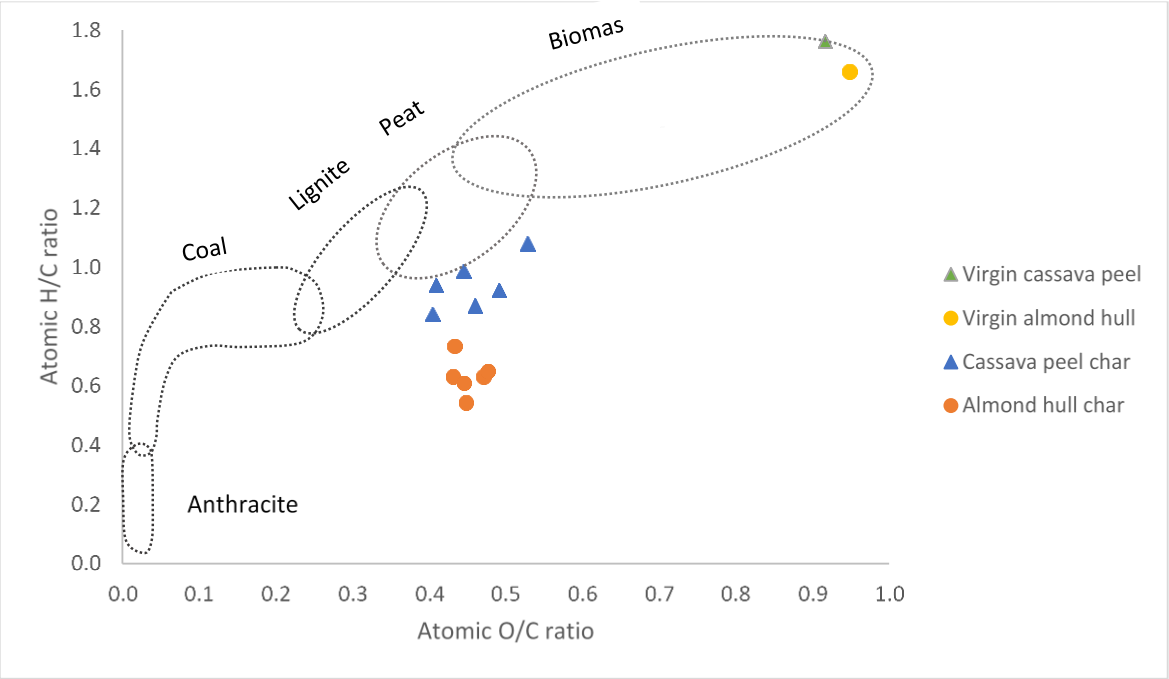

Figure 3. 37 A comparison char of cassava peel and almond hull with solid fuel in the van Krevelen diagram (Original in colour)

Although the bio-oil was quite low in yield, the quality of calorific value (HHV) was quite high ranging between 32.78 MJ/kg and 34.37 MJ/kg specifically for almond hull bio-oil. In comparison to Chen *et al*.[51] experiments on slow pyrolysis of the almond residue using fluidized bed reactor, the HHV ranged from 11.3 to 14.1 MJ/kg. The higher calorific value in the bio-oil is due to the concentration of organic compounds.[61] Moreover, pyrolysis with a slow heating rate is not only producing a high amount of the solid fraction but also producing energy-dense chars.[51]

Table 3. 30 The calorific value (MJ/kg) of biochar by bomb calorimetry.

Pyrolysis operational		Cassava peel char/(MJ/kg)	Almond hull char/(MJ/kg)
Temp/^{o}C	Holding time/min		
240	0	19.94	19.87
240	6	21.99	20.69
260	0	22.58	20.24
260	6	25.64	21.56
280	0	25.18	21.31
280	6	24.55	22.11

Table 3.30 shows the gross calorific value of biochar determined by bomb calorimetry. The calorific value trends increase with increasing temperature and reaction time. The results were quite similar to the theoretical HHV based elemental analysis in tendency and biomass source which the char of cassava peel was higher than the almond hull.

3.4.3 GC-MS analysis of bio-oils

The organic fraction of the bio-oil was collected using ethyl acetate extraction. The GC-MS chromatographs of cassava peel and almond hull bio-oil are shown in Figures 3.38 (CP) and 3.39 (AH). Table 3.31 (CP) and 3.32 (AH) lists identified compounds within the liquid fraction. The mass spectral data were compared with the NIST mass spectral database and their compound identification based on their time retention. NB – The data shown in indicative needs further substantiation and verification with known standards.

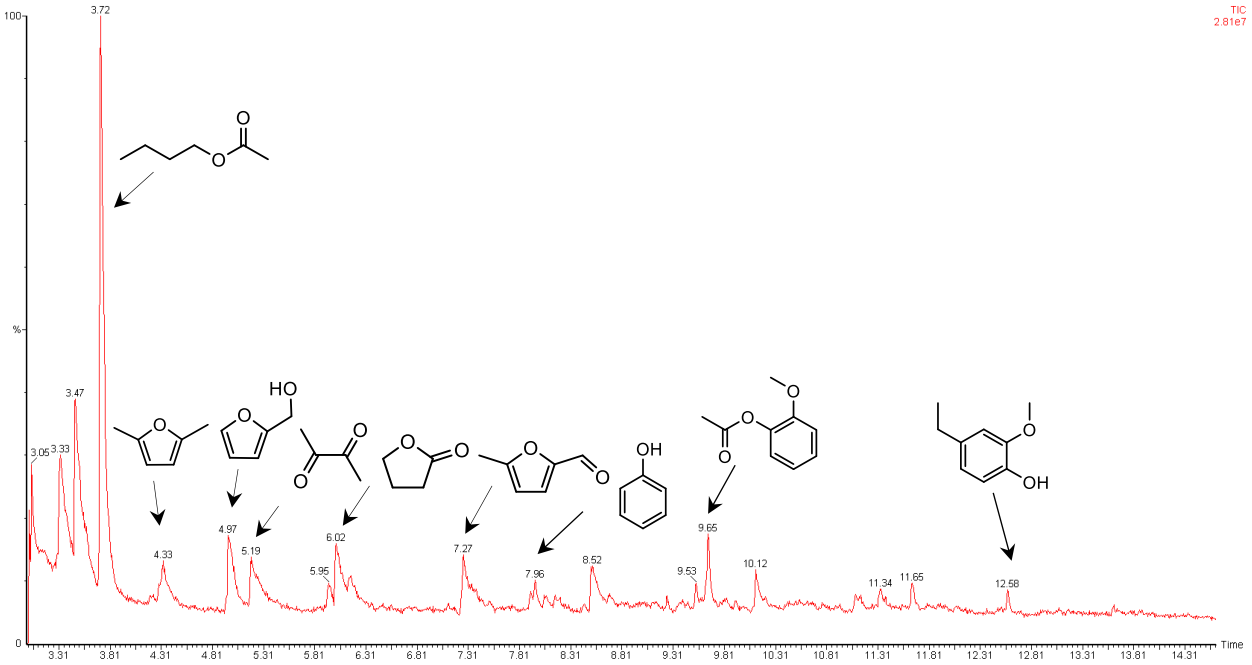

Figure 3. 38 The GC-MS chromatogram of bio-oil derived from cassava peel pyrolysis (Original in colour)

Table 3. 31 Chemical compounds of bio-oil cassava peel pyrolysis

Retention time/min	Identified compounds
3.72	Acetic acid
4.33	Furan, 2,5 dimethyl
4.97	2-Furanmethanol
5.19	2,3 Butanedione
6.02	γ- Butyrolactone
7.27	2-Furancarboxaldehyde, 5-methyl
7.96	Phenol
9.65	2-Methoxyphenyl acetate
12.58	Phenol, 4-ethyl-2-methoxy

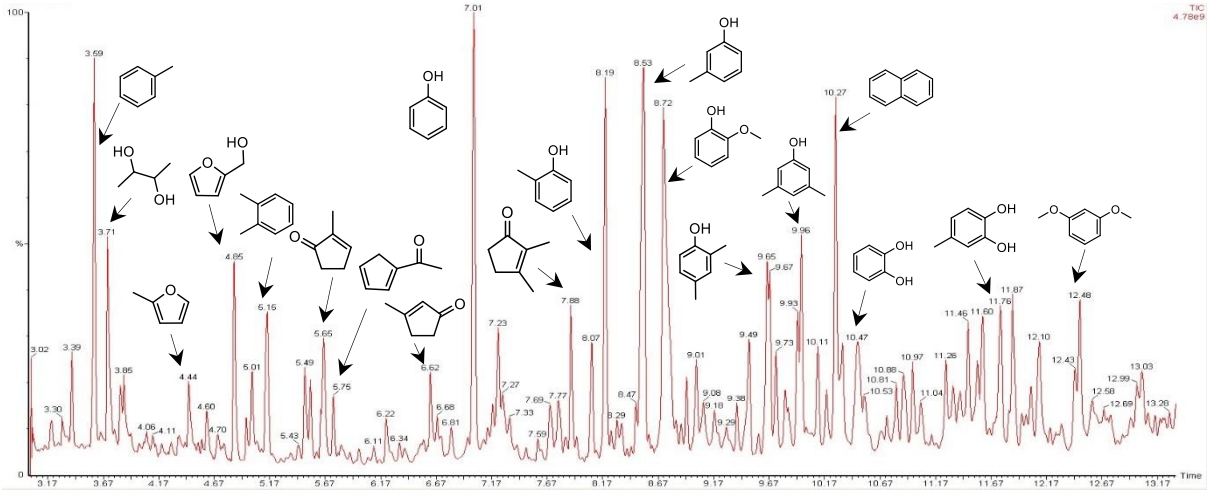

Figure 3. 39 The GC-MS chromatogram of bio-oil derived from almond hull pyrolysis (Original in colour)

Table 3. 32 Chemical compound of bio-oil almond hull pyrolysis

Retention time/min	Identified Compounds
3.59	Toluene
3.72	2,3-Butanediol
4.44	2-Methylfuran
4.85	2-Furanmethanol
5.15	o-Xylene
5.65	2-Methyl-2-cyclopenten-1-one
5.75	2-acetyl furan
6.62	3-Methyl-2-cyclopenten-1-one
7.11	Phenol
7.88	2,3-Dimethyl-2-cyclopenten-1-one
8.19	2-Methylphenol
8.54	3-Methylphenol
8.72	2-Methoxy phenol
9.65	2,4-Dimethylphenol
9.96	3,5-Dimethylphenol
10.27	Naphthalene
10.47	Pyrocatechol / Benzediol
11.73	4-Methylcatechol / 1,2-Benzenediol, 4-methyl-
12.48	2,6-Dimethoxyphenol

The primary constituents within the bio-oil were derivatives of furan and phenolic compounds. Hemicellulose thermochemical conversion products derived furfural and 2-furan methanol were abundant at the temperature ranging 240-260 ^{o}C, but their intensity decreased at high temperature. Sugar pyrolysate from hydrogenation reaction levoglucosan and hydroxyacetone such as gamma-butyrolactone and derivative from levoglucosan pyrolysis such as 2,3-butanedione were detected in the cassava peel oil fraction (Table 3.31).[289]

Chemical conversion of bio-oil was indicated the presence of 2,5-dimethylfuran which forms via the dehydration and hydrogenation of fructose from glucose isomerisation, while 2-methyl furan was produced from xylose polymer through the dehydration of furfural followed by hydrogenation.[290] Furanic compounds have a potential for use in biofuels blending due to their boiling point, high octane number, relatively high heating value and low solubility in water.[290]

Interestingly, a greater quantity of phenolic products could be observed in the bio-oil of the almond hull (Table 3.32) with respect to that derived from cassava peel with the main constituents being phenol, 2-methyl phenol (o-cresols), 3-methyl phenol, 2,4-dimethylphenol, 3,5 dimethyl phenol, and 2,6-dimethoxy phenol (syringols). These compounds are from the decomposition of lignin biomass components which was greater in the almond hull (~11.4% lignin of total biomass). Phenols and *o*-cresols are relatively stability from thermal decomposition.[291] According to Kelkar *et al*.[292], the biomineral from soil such as potassium are inherent in the biomass and can act as a catalyst of the reaction wherein the pyrolysis of cellulose and levoglucosan may produce cyclopentenone and phenol derivatives such methyl and dimethyl phenol. The softwood lignin composition is

largely dominated by the G unit, guaiacyl, (4-hydroxy-3-methoxyphenyl) and a small amount of S unit, syringyl, (3,5-dimethoxy-4-hydroxyphenyl). Kawamoto[291] reported that during the fast pyrolysis of wood lignin, there is temperature effect on the lignin cracking, which produces the aromatic methoxy predominantly guaiacols (2-methoxy phenols) from G-lignins syringols (2,6-dimethoxy phenols). The more the temperature is increased, guaiacols or syringols are converted to catechols (2-hydroxy phenols), pyrogallols (2,3-dihydroxy phenols), *o*-cresols (2-methyl phenols), xylenols (dimethylphenols). Volatisation of catechols and pyrogallols change to non-condensable gas around 550 °C and formation of polycyclic aromatic hydrocarbons (PAHs) at temperatures higher than 700 °C.[291] The lignin pyrolysis products of the almond hull found in this work are in good agreement with this mechanism as identified by the products observed via GC-MS. The use of phenolic molecules is suitable for reinforcing asphalt, plastic filler, and as polymeric adhesive resin.[287]

The formation of the aromatic fraction was detected from the almond hull bio-oil and included compounds such as toluene, xylene, naphthalene. These aromatic hydrocarbon products in the liquid fraction suggest that the reaction pathway from levoglucosan and cellulose during the pyrolytic process.[293] Uemura *et al*.[294] stated the primary precursor forming the aromatic hydrocarbon in bio-oil hydrolysate is suggested from volatiles compound of alkyne and diene such as acetylene, propyne and cyclopentadiene, these precursors are volatile products of cellulose degradation. Two routes to benzene being formed are (i) decomposition of toluene in which toluene alone is formed from the reaction of cyclopentadiene with ethylene, where cyclopentadiene could be formed from the combination of allyl radicals and acetylene, and (ii) from C_3

hydrocarbons such as propadiene and propyne.[294] On the other hand, Cheng *et al.* [295] presented two possible routes to form the other aromatics; (i) alkylation and cracking of an aromatic with allene (propadiene) or an olefin forming ethylene and another aromatic, (ii) Diels–Alder reaction between olefins and furan, such as the reaction between propylene and furan, producing toluene and water. The chemical precursor that form of the aromatic pathway during biomass pyrolysis can be described in Figure 3.40.

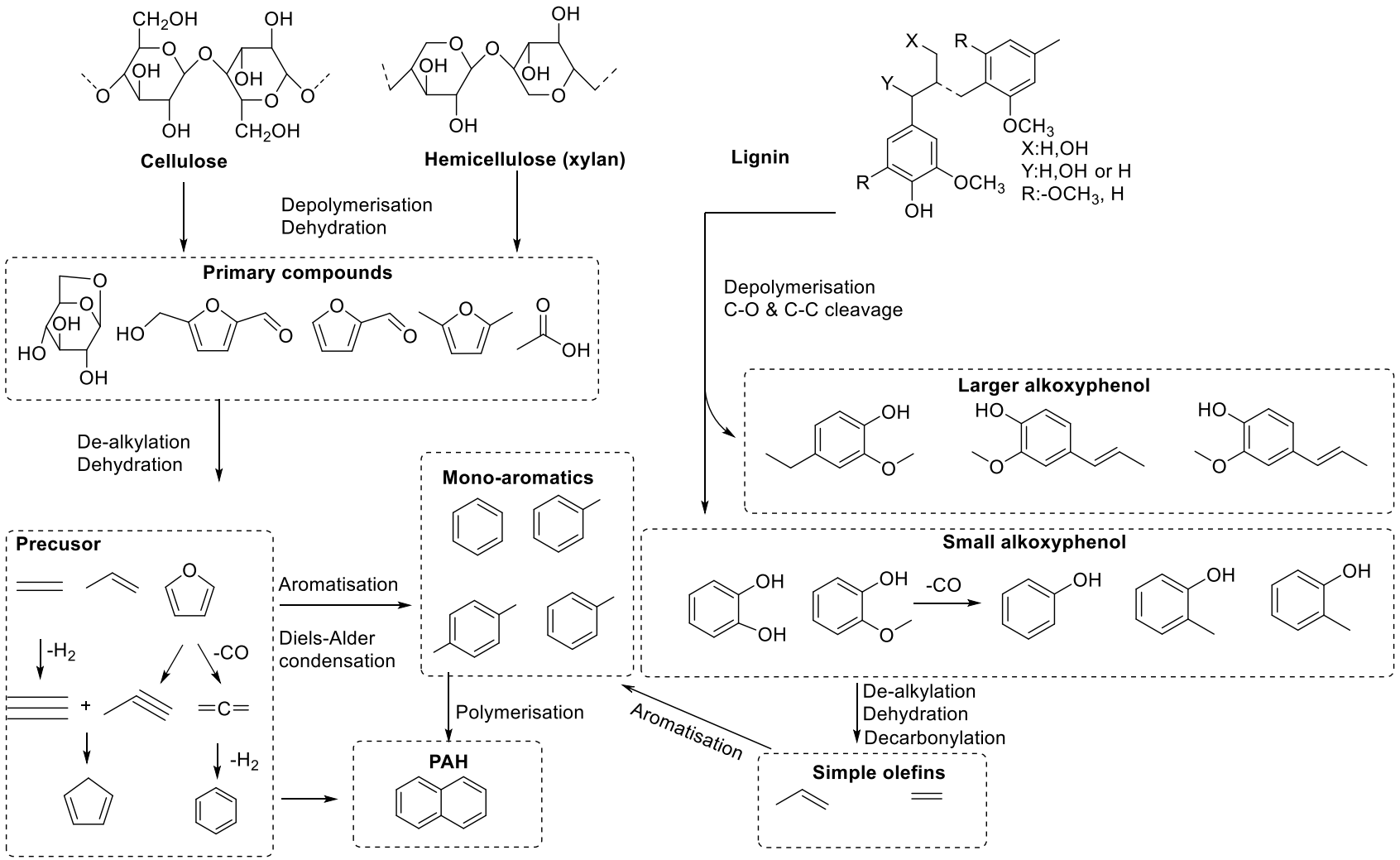

Figure 3. 40 Pyrolysis pathways forming aromatic compounds of the precursor biomass pyrolytic [294,295]

Chapter 4: Conclusions and Future Work

4.1 Summary of Results

In this study, waste cassava peel and almond hull have been subjected to microwave processing (both conventional pyrolysis and acid-free hydrothermal) with focus on their valorisation to materials (MFCs), chemicals (sugar hydrolysate and bio-oil) and (bio)energy (biochar). This work also investigated the influence of pretreatment (Soxhlet extraction using either ethanol or heptane) on the resultant microfibrilated cellulose/solid residues produced, their quantity and quality, and the composition of recovered sugars contained within the hydrolysates. Pretreatment could be an important factor in biomass hydrolysis, particularly concerning the generation of MFCs under low-temperature conditions and the applications thereof. This is exemplified in for instance, the production of biofilms by ethanol pretreatment on the almond hull which facilitated the easy formation of the structured film but hindered hydrogel formation (requiring 3 w/v % loading), whereas, untreated and heptane treatment led to excellent gel formation (even at 2 w/v %).

The valorisation approach via acid-free microwave-assisted hydrothermal processing (water alone) is a state-of-the-art concept for producing defibrillated celluloses akin to micro-fibrils, nanofibrils and nanocrystals. Unlike conventional production of nanocelluloses, which require intensive chemical and mechanical pretreatment mainly of wood pulp, our process is easily regulated and monitored in terms of the defibrillation of cellulose-based on hydrolysis temperature. The selective scissoring of non-cellulose compounds (residual sugar, hemicellulose and lignin) into MFC materials and valuable

compounds within a hydrolysate occurs. Water and microwave energy (temperature) are the only two main parameters used.

It was hypothesised that a pretreatment process may 'lighten the load' during hydrolysis processing, particularly at low temperatures between 120 ^{o}C and 170 ^{o}C via (partial) removal sugars, hemicellulose and the valuable organic compounds. Therefore, a pretreatment step could reduce temperature consumption in order to maximise the quality of the MFCs produced. This was verified by HPLC analysis of hydrolysate wherein pretreatment with ethanol aided extraction of xylose/fructose while heptane treatment indirectly facilitated the removal of rhamnose/arabinose and galacturonic acid.

TEM imaging was found to be an essential form of analysis with respect to the classification of defibrillated celluloses. Microwaves-assisted hydrolysis at low and medium temperature (< 170^{o}C) allowed the formation of microfibrillated cellulose (MFC) where the average fibre width fibres ranged from 7.2 to 3.6 nm for cassava peel and from 6.0 to 2.9 nm for the almond hull. Cellulose nanofibrils (CNF) (W= 3-10 nm, L/D > 50) could instead be found following microwave treatment at 220^{o}C, resulting in a shorter length ranging from 0.5 to 2.7 µm (higher aspect ratio). The splitting of microfibrils into elementary fibres (W < 3.5 nm) was found to occur mostly at high temperatures independent of pre-/treatment, but a small number of elementary fibres can be found starting at 170 ^{o}C especially in the cellulose produced after ethanol and heptane pretreatment.

ATR-IR was used to confirm the effect of thermal hydrolysis on the removal of hemicellulose as can be seen from the spectra following treatment of cassava peel at temperatures of 170^{o}C, according to a decrease in the signal intensity for C=O stretching at approximately 1730 cm^{-1}. Heptane pretreatment facilitated more easily removal of the C=O

signal from cassava peel and almond hull compared to the other treatment methods. XRD studies also verified that the MFC produced from cassava peel and almond hull in the heptane pretreatment group of 170 ^{o}C had the highest crystallinity index with respect to non-treatment and ethanol treatment. At 170 ^{o}C temperature applied, ^{13}C CPMAS NMR also showed an increase in crystallinity of C4 at 88-89 ppm and C6 at 65 ppm and a decrease in amorphous C4 at 82-84 ppm and C6 at 62-63 ppm. The aforementioned FTIR and XRD data which suggested that the hemicellulose and amorphous cellulose components were removed during processing are supported by TGA data which highlighted the presence of a strong thermal event starting from 170 to 220 ^{o}C.

The conditions of microwave hydrolysis processing were found to affect the zeta potential value of MFCs in neutral water (pH 7), with increasing temperature resulting in a material with decreased zeta potential up until a temperature of 170^{o} C where after, the zeta potential value remained relatively constant.

Experimental findings on the use of MFCs as adsorbents for Cr(VI) and methylene blue removal from aqueous systems showed that cassava peel has better performance than almond hull resulting in 180.73 mg/g Cr(VI) uptake by CPUS 220 (cassava peel from MHT at 220 ^{o}C and 30 minutes reaction time) via ultrasound at pH 2. The Dubinin-Radushkevich isotherm model gave a good description of the adsorption mechanism. Almond hull MFC of AHUS 220 (almond hull from MHT at 220^{o}C and 30 min reaction time) via ultrasound at pH 2 gave the highest Cr(VI) uptake by 167.95 mg/g, and the data fit well with the Freundlich model. It was found that for both MFCs, the kinetic processes can be accurately predicted by *pseudo*-second order rate kinetics. Deconvolution of obtained XPS spectra proved that there was a change of oxidation state during the adsorption process,

signifying the reduction from Cr(VI) to Cr(III) as $Cr(OH)_3$ which reached 79.8%, and 70% for CPUS 220 and AHUS 220 respectively. Ultrasound treatment has significant effects on Cr(IV) and methylene blue compared to stirring mode in uptake and time response.

The highest equilibrium adsorption of methylene blue was achieved using MFC of CPUS 120 (199.06 mg/g) and AHUS 120 (128.47 mg/g). The CPST 120 adsorption mechanism followed Langmuir model whereas the Temkin model gave the best representation for AHUS 120. Once again, the *pseudo*-second-order model revealed the best agreement for all experimental kinetic data of methylene blue adsorption with a correlation coefficient $R^2 > 0.99$. In comparison with activated carbon (Norit™), the adsorption of MB by Norit™ reached 286.44 mg/g via ultrasonic treatment and was fitted well using the Langmuir model. The best explanation of kinetic study of MB uptake by Norit™ in sonication mode was also found to be *pseudo*-second order. From a further thermodynamic study, the adsorption of MB onto cassava peel MFC and Norit™ was favourable at low temperature or ambient temperature at pH 7, whereas for the adsorption process of MB with almond hull MFC appeared to be more extensive at a higher temperature - this indicated an endothermic reaction and a positive value of entropy.

Virgin cassava peel (CP) and almond hull (AH) conversion to bioenergy (biochar and bio-oil) via microwave pyrolysis gave promising results. The actual calorific value of cassava peel and almond hull char as determined by bomb calorimetry was found to be relatively high value at 25.64 MJ/kg and 21.56 MJ/kg, respectively. The theoretical high heating value (HHV) of bio-oil derived from almond hull is higher than that produced from cassava peel is 34.37 MJ/kg. Pyrolysis of almond led to a bio-oil fraction which was comparatively richer

in phenolic products. Microwave pyrolysis allowed selective scissoring of the chemical compounds, which resulted in the formation of added-valuable chemicals *e.g*., furanics and/or phenolics.

4.2 Future Work

Acid-free microwave-assisted hydrolysis and microwave pyrolysis are promising green technologies for food waste valorisation given that they are; water-based (hydrolysis), less energy-consuming (30-50% lower) than conventional heating, efficient in terms of heat delivery, fast concerning reaction times, and easy to control or tailor.[87] In a wider context, support for research, technology advancement and more sustainable processing via the biorefining of renewable resources to gain economic, social and environmental helps to facilitate a broader, circular bio-economy concept. The development method of this technology is continually evolving, and there is plenty of room for improvements in the full valorisation of food waste. Regarding future works concerning the development of MFCs, more improvements could be made, as follows:

Biomass homogenisation resulting in a well-dispersion in water, this step could be attempted, before hydrolysing in order to enhance the processing of microwave hydrolysis into fibres. Such a pretreatment process could have a significant effect on the fibre network. By a physical process, enabling access to hydroxyl hydrogen bonding and making it much easier to extract non-cellulosic components. Moreover, optimisation of operational microwave temperature below 170 ^{o}C in the manufacturing of MFCs, should be tried in the future, in terms of energy consumption and appearance of MFCs. Besides, the reduction of solvent washing steps could further improve the overall greenness of the process.

Regarding the improvement in MFCs, *pseudo*lignin that resulted from the hydrolysis process between 170-220 ^{o}C should be better understood. Ideally, there is a strategy in reduction *pseudo*lignin formation. Because *pseudo*lignin alone is an unavoidable product during the hydrolysis process, from polymerisation of a significant decomposed carbohydrate fraction which is large enough to be the source of lignin-like structure.[296]

Improvement in the characterisation of mesoporous parameters for cellulose dispersion in water, *e.g.* surface area and pore diameter would also be helpful moving forward. This characterisation will be useful to understand the exact porosity of cellulose fibre when the MFCs are dispersed in water compared to in dried condition. For example, the highest uptake of methylene blue is cassava peel 120 (CP 120-30') but from porosity data of dried cassava peel 120 did not reflect a high surface area. Determination of porosity, when dispersed in water, will help to explain mechanism-driven adsorption forces, *i.e.* either pores or surface functional cellulose group, or both. Because cellulose is a soft, lightweight material that can be easily entangled when dispersed in water, it needs a strategy and development to understand the porosity of cellulose when dispersed in water compared to when it is dried. There are different drying methods for cellulose to minimise hornification phenomena, *i.e*., supercritical CO_2 drying, freeze-drying and vacuum drying that could all be tested in future work.[297]

Interestingly from data ^{13}C CPMAS NMR spectra at 220^{o}C, there was the splitting peak of C2, C3 and C5 with a clear resonance at approx. 71 ppm which could be possibly related TEM analysis at 220 ^{o}C of microfibres splitting into single fibre. However, a more detailed explanation of this phenomena could be provided using three-dimensional NMR

which can better probe the intra-intermolecular hydrogen bonding between C2, C3 and C5 of the cellulose.

References

1 A. S. Matharu, E. M. de Melo and J. A. Houghton, *Bioresour. Technol.*, 2016, **215**, 123–130.

2 FAO, Food wastage footprint-Impacts on natural resources, http://www.fao.org/3/i3347e/i3347e.pdf, (accessed 25 February 2020).

3 FAO, Glob. food losses food waste – Extent, causes Prev., http://www.fao.org/3/mb060e/mb060e00.htm, (accessed 20 February 2020).

4 FAO, Food Wastage Footprint: Full cost-accounting, http://www.fao.org/3/a-i3991e.pdf, (accessed 22 February 2020).

5 M. Gooch, M. Bucknell, D., LaPlain, D., Dent, B., Whitehead, P., Felfel, A., Nikkel, L., Maguire, *The Avoidable Crisis of Food Waste: Technical Report*, Ontario, 2019.

6 WRAP, UK progress against Courtauld 2025 targets and UN Sustainable Development Goal 12.3, https://wrap.org.uk/sites/files/wrap/Progress_against_Courtauld_2025_targets_and_UN_SDG_123.pdf, (accessed 20 February 2020).

7 European Environmental Agency, Soil, land and climate change, https://www.eea.europa.eu/signals/signals-2019-content-list/articles/soil-land-and-climate-change, (accessed 20 February 2020).

8 B. Notarnicola, G. Tassielli, P. A. Renzulli and A. Lo Giudice, in *Life Cycle Assessment in the Agri-food Sector*, eds. B. Notarnicola, R. Salomone, L. Petti, P. A. Renzulli, R. Roma and A. K. Cerutti, Springer International Publishing, Cham, 2015, pp. 1–56.

9 T. Garnett, *Food Policy*, 2011, **36**, S23–S32.

10 R. Ishangulyyev, S. Kim and S. H. Lee, *Foods*, 2019, **8**, 297.

11 P. Alexander, C. Brown, A. Arneth, J. Finnigan, D. Moran and M. D. A. Rounsevell, *Agric. Syst.*, 2017, **153**, 190–200.

12 ReFood, Vision 2020: UK roadmap to zero food waste to landfill, https://www.vision2020.info/assets/pdf/Vision_2020_roadmap.pdf, (accessed 23 February 2020).

13 WRAP, Courtauld Commitment 2025: Annual review 2017 - 18, http://www.wrap.org.uk/sites/files/wrap/Courtauld_2025_Annual_Review_2017_18.pdf, (accessed 22 February 2020).

14 FAO, SDG 12.3.1: Global Food Loss Index, http://www.fao.org/3/CA2640EN/ca2640en.pdf, (accessed 22 February 2020).

15 G. Lodorfos, A. Konstantopoulou, I. Kostopoulos and E. E. Essien, in *The Sustainable Marketing Concept in European SMEs*, Emerald Publishing Limited, 2018, pp. 121–140.

16 F. Galli, E. Favilli, S. D. Amico and G. Brunori, *A transition towards sustainable food systems in Europe*, Ass. Cult. Lab. di Studi Rurali Sismondi, Pisa, 2018.

17 SITRA, The circular economy - a powerful force for climate mitigation, https://media.sitra.fi/2018/06/12132041/the-circular-economy-a-powerful-force-for-climate-mitigation.pdf, (accessed 27 February 2020).

18 M. Cordella and R. Kaps, *Designing Sustainable Technologies, Products and Policies*,

Springer International Publishing, Cham, 2018.

19 F. C. F. Rei, A. F. Gonçalves and L. P. De Souza, *Veredas do Direito*, 2017, **14**, 81–99.

20 M. Paradowska, in *Sustainable Transport Development, Innovation and Technology*, ed. M. Suchanek, Springer International Publishing, Cham, 2017, pp. 245–269.

21 D. D'Amato, J. Korhonen and A. Toppinen, *Ecol. Econ.*, 2019, **158**, 116–133.

22 M. A. Camilleri, *Sustain. Dev.*, 2019, **27**, 530–536.

23 X. Li, B. Deng and H. Ye, *Energy Procedia*, 2011, **5**, 1399–1404.

24 S. Corrado and S. Sala, in *Designing Sustainable Technologies, Products and Policies*, Springer International Publishing, Cham, 2018, pp. 49–59.

25 T. Ronzon, M. Lusser, M. Klinkenberg, L. Landa, J. S. Lopez, R. M'Barek, G. Hadjamu and A. Belward, *Bioeconomy Report 2016*, 2017, vol. EUR 28468.

26 Y. Sudaryanto, S. B. Hartono, W. Irawaty, H. Hindarso and S. Ismadji, *Bioresour. Technol.*, 2006, **97**, 734–739.

27 G. O. Mbah, N. J. Edeani and M. . Onyiah, *Int. J. Curr. Res.*, 2013, **5**, 7.

28 O. O. Ezekiel, O. C. Aworh, H. P. Blaschek and T. C. Ezeji, *African J. Biotechnol.*, 2010, **9**, 187–194.

29 A. Parmar, B. Sturm and O. Hensel, *Food Secur.*, 2017, **9**, 907–927.

30 R. H. Howeler, in *Sweetpotato Research and Development: Its Contribution to the Asian Food Economy*, eds. A. Setiawan and K. O. Fuglie, 2005, pp. 17–51.

31 M. A. El-sharkawy, *Plant Mol. Biol. 56*, 2004, **56**, 481–501.

32 FAO, Food Outlook- Biannual report on global food markets, http://www.fao.org/3/CA2320EN/ca2320en.pdf, (accessed 3 March 2020).

33 A. O. Obadina, O. B. Oyewole, L. O. Sanni and S. S. Abiola, *African J. Biotechnol.*, 2006, **5**, 302–304.

34 A. Pandey, C. R. Soccol, P. Nigam, V. T. Soccol, L. P. S. Vandenberghe and R. Mohan, *Bioresour. Technol.*, 2000, **74**, 81–87.

35 S. Kajiwara and H. Maeda, *Agric. Biol. Chem.*, 1983, **47**, 2335–2340.

36 N. K. Morgan and M. Choct, *Anim. Nutr.*, 2016, **2**, 253–261.

37 A. Westby, *Cassava Biol. Prod. Util.*, 2002, **1**, 281–300.

38 Y. C. Fu, L. Dai and B. B. Yang, *Int. J. Food Sci. Technol.*, 2005, **40**, 119–132.

39 L. B. Milde, L. A. Ramallo and M. C. Puppo, *Food Bioprocess Technol.*, 2012, **5**, 888–896.

40 B. W. Bolling, *Compr. Rev. Food Sci. Food Saf.*, 2017, **16**, 346–368.

41 Almond Board of California, Almond Almanac 2019, https://www.almonds.com/sites/default/files/Almanac_2019_Web_0.pdf, (accessed 4 March 2020).

42 M. Shahbandeh, Almond production worldwide by country, 2018/2019, https://www.statista.com/statistics/632865/almond-production-worldwide-by-country/#statisticContainer, (accessed 5 March 2020).

43 K. M. Holtman, R. D. Offeman, D. Franqui-Villanueva, A. K. Bayati and W. J. Orts, *J.*

Agric. Food Chem., 2015, **63**, 2490–2498.

44 M. Ferrandez-Villena, C. E. Ferrandez-Garcia, T. G. Ortuño, A. Ferrandez-Garcia and M. T. Ferrandez-Garcia, *Agronomy*, 2019, **9**, 1–10.

45 H. Hasar and Y. Cuci, *Environ. Technol. (United Kingdom)*, 2000, **21**, 1337–1342.

46 I. Prgomet, B. Gonçalves, R. Domínguez-Perles, N. Pascual-Seva and A. Barros, *Molecules*, 2017, **22**, 1774.

47 T. Yalchi and S. Kargar, *J. Food, Agric. Environ.*, 2010, **8**, 781–784.

48 S. Sang, K. Lapsley, R. T. Rosen and C. T. Ho, *J. Agric. Food Chem.*, 2002, **50**, 607–609.

49 G. Takeoka, L. Dao, R. Teranishi, R. Wong, S. Flessa, L. Harden and R. Edwards, *J. Agric. Food Chem.*, 2000, **48**, 3437–3439.

50 M. N. Qureshi, S. Numonov and H. A. Aisa, *Int. J. Anal. Chem.*, 2019, **2019**, 1–7.

51 P. Chen, Y. Cheng, S. Deng, X. Lin, G. Huang and R. Ruan, *Int. J. Agric. Biol. Eng.*, 2010, **3**, 1–18.

52 K. C. C. De Carvalho, S. R. Montoro, M. O. H. Cioffi and H. J. C. Voorwald, in *Design and Applications of Nanostructured Polymer Blends and Nanocomposite Systems*, eds. S. Thomas, R. Shanks and S. B. T.-D. and A. of N. P. B. and N. S. Chandrasekharakurup, Elsevier, Boston, 2016, pp. 261–285.

53 R. Ibbett, S. Gaddipati, S. Hill and G. Tucker, *Biotechnol. Biofuels*, 2013, **6**, 1–15.

54 H. P. S. Abdul Khalil, C. K. Saurabh, M. Asniza, Y. Y. Tye, M. R. Nurul Fazita, M. I. Syakir, H. M. Fizree, A. F. I. Yusra, M. K. M. Haafiz, M. A. Kassim and N. L. M. Suraya, in

Cellulose-Reinforced Nanofibre Composites: Production, Properties and Applications, eds. M. Jawaid, S. Boufi and A. Khalil, 2017, pp. 1–24.

55 R. C. R. Nunes, in *Woodhead Publishing Series in Composites Science and Engineering*, eds. S. Thomas and H. J. B. T.-P. in R. N. Maria, Woodhead Publishing, 2017, pp. 463–494.

56 J. Lewandowska-Łańcucka, A. Karewicz, K. Wolski and S. Zapotoczny, in *Cellulose-Based Superabsorbent Hydrogels*, ed. M. I. H. Mondal, Springer, 2018, pp. 1–29.

57 H. P. S. Abdul Khalil, Y. Davoudpour, M. N. Islam, A. Mustapha, K. Sudesh, R. Dungani and M. Jawaid, *Carbohydr. Polym.*, 2014, **99**, 649–665.

58 M. Nasir, R. Hashim, O. Sulaiman and M. Asim, in *Cellulose-Reinforced Nanofibre Composites*, Elsevier, 2017, pp. 261–276.

59 M. A. Mohamed, M. Abd Mutalib, Z. A. Mohd Hir, M. F. M. Zain, A. B. Mohamad, L. Jeffery Minggu, N. A. Awang and W. N. W. Salleh, *Int. J. Biol. Macromol.*, 2017, **103**, 1232–1256.

60 T. Saito, S. Kimura, Y. Nishiyama and A. Isogai, *Biomacromolecules*, 2007, **8**, 2485–2491.

61 S. B. Kabakcı and Ş. Hacıbektaşoğlu, in *Pyrolysis*, InTech, 2017, vol. 1, p. 13.

62 A. F. Turbak, F. W. Snyder and K. R. Sandberg, in *J. Appl. Polym. Sci., Appl. Polym. Symp.*, United States, 1983, vol. 37, pp. 815–827.

63 P. Tingaut, T. Zimmermann and G. Sèbe, *J. Mater. Chem.*, 2012, **22**, 20105–20111.

64 K. Missoum, M. N. Belgacem and J. Bras, *Materials (Basel).*, 2013, **6**, 1745–1766.

65 A. Koponen, J. Lauri, S. Haavisto and T. Fabritius, *Appl. Sci.*, 2018, **8**, 755.

66 T. Sonobe, *2011 IEEE 1st Conf. Clean Energy Technol. CET 2011*, 2011, 297–299.

67 D. Beneroso, T. Monti, E. T. Kostas and J. Robinson, *Chem. Eng. J.*, 2017, **316**, 481–498.

68 S. S. Lam and H. A. Chase, *Energies*, 2012, **5**, 4209–4232.

69 S. L. Lo, Y. F. Huang, P. Te Chiueh and W. H. Kuan, *Energy Procedia*, 2017, **105**, 41–46.

70 R. O. M. A. De Souza, in *Production of Biofuels and Chemicals with Microwave*, eds. Z. Fang, R. L. Smith, and X. Qi, Springer Netherlands, Dordrecht, 2015, vol. 3, pp. 3–16.

71 D. Bogdal and A. Prociak, in *Microwave-Enhanced Polymer Chemistry and Technology*, eds. D. Bogda and A. Prociak, Blackwell Publishing Ltd, Oxford, UK, 2007, pp. 3–32.

72 J. Ilic, in *Encyclopedia of Materials: Science and Technology*, Elsevier, 2001, pp. 9629–9633.

73 M. A. P. Martins, J. Trindade, G. S., L. Buriol and C. P., in *Ionic Liquids - New Aspects for the Future*, InTech, 2013, vol. i, p. 13.

74 C. B. Koskiniemi, V. Den Truong, R. F. McFeeters and J. Simunovic, *Int. J. Food Prop.*, 2013, **16**, 917–927.

75 L. Hu, Y. Luo, B. Cai, J. Li, D. Tong and C. Hu, *Green Chem.*, 2014, **16**, 3107–3116.

76 U.S. EPA, *METHOD 7196A CHROMIUM,CHROMIUM, HEXAVALENT (COLORIMETRIC)*, U.S. Government Printing Office, Washington DC, Third Edit., 1992.

77 J. Remón, A. S. Matharu and J. H. Clark, *Energy Convers. Manag.*, 2018, **165**, 634–648.

78 S. A. Channiwala and P. P. Parikh, *Fuel*, 2002, **81**, 1051–1063.

79 J. Schönherr, *C*, 2018, **4**, 21.

80 F. a Aderemi and F. C. Nworgu, *Am. J. Agric. Environ. Sci.*, 2007, **2**, 308–311.

81 O. Okechukwu Elechi, N. Joseph Tagbo, O. Chioma Mary and A. Oluseun Emmanuel, *Int. J. Sci. Technol. Res.*, 2016, **5**, 184–187.

82 P. J. Van Soest, J. B. Robertson and B. A. Lewis, *J. Dairy Sci.*, 1991, **74**, 3583–3597.

83 Y. Taher, *African J. Biotechnol.*, 2011, **10**, 3022–3026.

84 C. M. Welker, V. K. Balasubramanian, C. Petti, K. M. Rai, S. De Bolt and V. Mendu, *Energies*, 2015, **8**, 7654–7676.

85 F. Mariotti, D. Tomé and P. P. Mirand, *Crit. Rev. Food Sci. Nutr.*, 2008, **48**, 177–184.

86 N. Thakur and V. Arya, *Middle - East J. Sci. Res.*, 2014, **19**, 1421–1424.

87 E. Melo, University of York, 2018.

88 V. Hospodarova, E. Singovszka and N. Stevulova, *Am. J. Anal. Chem.*, 2018, **09**, 303–310.

89 S. L. Wang and J. F. Lee, *Chem. Eng. J.*, 2011, **174**, 289–295.

90 O. Renê, S. D. Sommerfeld, K. Dube, O. De Freitas and J. Kohn, 2015, **38**, 902–909.

91 J. Coates, in *Encyclopedia of Analytical Chemistry*, John Wiley & Sons, Ltd, Chichester, UK, 2006, pp. 1–23.

92 A. Kumar, Y. S. Negi, V. Choudhary and N. K. Bhardwaj, *J. Mater. Phys. Chem.*, 2014, **2**, 1–8.

93 C. S. Julie Chandra, N. George and S. K. Narayanankutty, *Carbohydr. Polym.*, 2016, **142**, 158–166.

94 Q. Liu, Y. Lu, M. Aguedo, N. Jacquet, C. Ouyang, W. He, C. Yan, W. Bai, R. Guo, D. Goffin, J. Song and A. Richel, *ACS Sustain. Chem. Eng.*, 2017, **5**, 6183–6191.

95 O. J. Rojas, *Cellulose Chemistry and Properties : Fibers , Nanocelluloses and Advanced Materials*, 2016.

96 L. C. Segal, J. Jr Creely, A. E. J. Martin and C. M. Conrad, *An Empirical Method for Estimating the Degree of Crystallinity of Native Cellulose Using the X-Ray Diffractometer*, 1959, vol. 29.

97 D. J. Jeanmonod, Rebecca, K. et al. Suzuki, M. Hrabovsky, M. P. Mariana Furio Franco Bernardes and Lilian Cristina Pereira and Daniel Junqueira Dorta, *Intech open*, 2018, **2**, 64.

98 M. Poletto, H. L. Ornaghi Júnior and A. J. Zattera, *Materials (Basel).*, 2014, **7**, 6105–6119.

99 L. P. Novo, J. Bras, A. García, N. Belgacem and A. A. S. Curvelo, *ACS Sustain. Chem. Eng.*, 2015, **3**, 2839–2846.

100 K. Kafle, K. Greeson, C. Lee and S. H. Kim, *Text. Res. J.*, 2014, **84**, 1692–1699.

101 K. Tazaki, A. Fukuyama, F. Tazaki, T. Takehara, K. Nakamura, M. Okuno, Y. Hashida and S. Hashida, *Minerals*, 2017, **7**, 123.

102 E. M. De Melo, J. H. Clark and A. S. Matharu, *Green Chem.*, 2017, **19**, 3408–3417.

103 Y. Liu, Y. Sun, G. Ding, Q. Geng, J. Zhu, M. Guo, Y. Duan, B. Wang and Y. Cao, *J. Agric. Food Chem.*, 2015, **63**, 4263–4268.

104 A. S. Matharu, J. A. Houghton, C. Lucas-Torres and A. Moreno, *Green Chem.*, 2016, **18**, 5280–5287.

105 M. Poletto, A. J. Zattera, M. M. C. Forte and R. M. C. Santana, *Bioresour. Technol.*, 2012, **109**, 148–153.

106 H. Yang, R. Yan, H. Chen, C. Zheng, D. H. Lee and D. T. Liang, *Energy & Fuels*, 2006, **20**, 388–393.

107 Y. Yu, Y. Wang, W. Ding, J. Zhou and B. Shi, *Carbohydr. Polym.*, 2017, **174**, 823–829.

108 J. Guo, X. Lian, H. Kang, K. Gao and L. Li, *Eur. Food Res. Technol.*, 2016, **242**, 1485–1494.

109 G. J. Lyu, S. Bin Wu and R. Lou, *BioResources*, 2010, **5**, 1281–1291.

110 H. Kono and Y. Numata, *Cellulose*, 2006, **13**, 317–326.

111 S. Park, J. O. Baker, M. E. Himmel, P. A. Parilla and D. K. Johnson, *Biotechnol. Biofuels*, 2010, **3**, 1–10.

112 J. Ralph and L. Landucci, in *Lignin and Lignans*, CRC Press, 2010, pp. 137–243.

113 M. Y. Balakshin and E. A. Capanema, *RSC Adv.*, 2015, **5**, 87187–87199.

114 A. V. Ladesov, A. V. Belesov, M. V. Kuznetsova, A. S. Pochtovalova, A. V. Malkov, S. L. Shestakov and D. S. Kosyakov, *Russ. J. Appl. Chem.*, 2018, **91**, 663–670.

115 M. Hazwan Hussin, D. Trache, C. T. H. Chuin, M. R. Nurul Fazita, M. K. Mohamad Haafiz and M. S. Hossain, eds. Inamuddin, S. Thomas, R. Kumar Mishra and A. M. Asiri, Springer International Publishing, Cham, 2019, pp. 653–691.

116 A. Dufresne, *Handbook of Nanocellulose and Cellulose Nanocomposites*, 2017.

117 H. Kargarzadeh, M. Ioelovich, I. Ahmad, S. Thomas and A. Dufresne, *Handb. Nanocellulose Cellul. Nanocomposites*, 2017, 1–49.

118 J. Xie, C. Y. Hse, C. F. De Hoop, T. Hu, J. Qi and T. F. Shupe, *Carbohydr. Polym.*, 2016, **151**, 725–734.

119 M. Zhang, L. Xie, Z. Yin, S. K. Khanal and Q. Zhou, *Bioresour. Technol.*, 2016, **215**, 50–62.

120 R. K. Mishra, A. Sabu and S. K. Tiwari, *J. Saudi Chem. Soc.*, 2018, **22**, 949–978.

121 G. Chinga-Carrasco, *Nanoscale Res. Lett.*, 2011, **6**, 1–7.

122 L. Chen, Q. Wang, K. Hirth, C. Baez, U. P. Agarwal and J. Y. Zhu, *Cellulose*, 2015, **22**, 1753–1762.

123 E. M. De Melo, J. H. Clark and A. S. Matharu, *Green Chem.*, 2017, **19**, 3408–3417.

124 B. Deepa, E. Abraham, R. R. Koshy, L. A. Pothan and S. Thomas, *Handb. Polym. Nanocomposites. Process. Perform. Appl. Vol. C Polym. Nanocomposites Cellul. Nanoparticles*, 2015, 65–80.

125 L. Flutto, ed. B. B. T.-E. of F. S. and N. (Second E. Caballero, Academic Press, Oxford, 2003, pp. 4440–4449.

126 B. Biduski, W. M. F. da Silva, R. Colussi, S. L. de M. El Halal, L. T. Lim, Á. R. G. Dias and E. da R. Zavareze, *Int. J. Biol. Macromol.*, 2018, **113**, 443–449.

127 M. M. Burrell, *J. Exp. Bot.*, 2003, **54**, 451–456.

128 J. A. Montagnac, C. R. Davis and S. A. Tanumihardjo, *Compr. Rev. Food Sci. Food Saf.*, 2009, **8**, 181–194.

129 W. S. Ratnayake and D. S. Jackson, ed. B. B. T.-E. of F. S. and N. (Second E. Caballero, Academic Press, Oxford, 2003, pp. 5567–5572.

130 L. R. F. Souto, M. Caliari, M. S. Soares junior, F. A. Fiorda and M. C. Garcua, *Food Sci. Technol.*, 2016, **37**, 19–24.

131 S. N. Moorthy, J. Rickard and J. M. V Blanshard, in *CIAT publication (CIAT)*, Centro Internacional de Agricultura Tropical ; Montpellier (France) : Centre de Cooperation Internationale en Recherche Agronomique pour le Developpement, Department des Systemes Agroalimentaires et Ruraux, 1996, pp. 150–155.

132 D. Kim, *Molecules*, 2018, **23**, 309.

133 X. Gong, C. Wang, L. Zhang and H. Qu, *J. Chem. Eng. Data*, 2012, **57**, 3264–3269.

134 D. M. Gao, T. Kobayashi and S. Adachi, *Food Sci. Technol. Res.*, 2015, **21**, 801–803.

135 M. D. Luque de Castro and L. E. García Ayuso, ed. I. D. B. T.-E. of S. S. Wilson, Academic Press, Oxford, 2000, pp. 2701–2709.

136 H. Lu, C. Lv, M. Zhang, S. Liu, J. Liu and F. Lian, *Energy Convers. Manag.*, 2017, **132**, 251–260.

137 K. Inoue, K. I. Kitahara, Y. Aikawa, S. Arai and T. Masuda-Hanada, *Molecules*, 2011, **16**, 5905–5915.

138 R. El Hage, N. Brosse, L. Chrusciel, C. Sanchez, P. Sannigrahi and A. Ragauskas, *Polym. Degrad. Stab.*, 2009, **94**, 1632–1638.

139 E. Martino, I. Ramaiola, M. Urbano, F. Bracco and S. Collina, *J. Chromatogr. A*, 2006, **1125**, 147–151.

140 C. K. Nitsos, P. A. Lazaridis, A. Mach-Aigner, K. A. Matis and K. S. Triantafyllidis, *ChemSusChem*, 2019, **12**, 1179–1195.

141 S. Soltani Dashtbozorg, K. Invally, A. Sancheti and L.-K. Ju, *Microb. Biosurfactants their Environ. Ind. Appl.*, 2019, 56–80.

142 T. Kobayashi, H. Kuramochi, K. Maeda and K. Xu, *Energies*, 2017, **10**, 1–14.

143 H. Xia, J. A. Houghton, J. H. Clark and A. S. Matharu, *ACS Sustain. Chem. Eng.*, 2016, **4**, 6002–6009.

144 S. Y. Chan, W. S. Choo, D. J. Young and X. J. Loh, *Carbohydr. Polym.*, 2017, **161**, 118–139.

145 F. Cao, T. J. Schwartz, D. J. McClelland, S. H. Krishna, J. A. Dumesic and G. W. Huber, *Energy Environ. Sci.*, 2015, **8**, 1808–1815.

146 B. Danon, G. Marcotullio and W. De Jong, *Green Chem.*, 2014, **16**, 39–54.

147 N. Sweygers, N. Alewaters, R. Dewil and L. Appels, *Sci. Rep.*, 2018, **8**, 1–11.

148 Y. Gao, H. Xia, A. P. Sulaeman, E. M. de Melo, T. I. J. Dugmore and A. S. Matharu, *ACS Sustain. Chem. Eng.*, 2019, **7**, 11861–11871.

149 L. Jiang, N. Wu, A. Zheng, X. Wang, M. Liu, Z. Zhao, F. He, H. Li and X. Feng, *Polymers (Basel).*, 2017, **9**, 599.

150 S. Y. Yoon, S. H. Han and S. J. Shin, *Energy*, 2014, **77**, 19–24.

151 F. Delbecq, Y. Wang, A. Muralidhara, K. El Ouardi, G. Marlair and C. Len, *Front. Chem.*, 2018, **6**, 1–29.

152 P. L. Dhepe and R. Sahu, *Green Chem.*, 2010, **12**, 2153–2156.

153 A. Herbst and C. Janiak, *New J. Chem.*, 2016, **40**, 7958–7967.

154 M. Sabbah and M. Esposito, *J. Biotechnol. Biomater.*, 2016, **6**, 2–4.

155 M. Tholstrup Sejersen, T. Salomonsen, R. Ipsen, R. Clark, C. Rolin and S. Balling Engelsen, *Int. Dairy J.*, 2007, **17**, 302–307.

156 F. M. Pelissari, P. J. D. A. Sobral and F. C. Menegalli, *Cellulose*, 2014, **21**, 417–432.

157 G. V. Lowry, R. J. Hill, S. Harper, A. F. Rawle, C. O. Hendren, F. Klaessig, U. Nobbmann, P. Sayre and J. Rumble, *Environ. Sci. Nano*, 2016, **3**, 953–965.

158 L. Zhong, S. Fu, X. Peng, H. Zhan and R. Sun, *Carbohydr. Polym.*, 2012, **90**, 644–649.

159 Y. Huang, S. Sun, C. Huang, Q. Yong, T. Elder and M. Tu, *Biotechnol. Biofuels*, 2017, **10**, 1–11.

160 A. J. Rubio, I. Z. Silva, F. Gasparotto and A. S. Edneia, 2018, **65**, 751–756.

161 R. Cha, Z. He and Y. Ni, *Carbohydr. Polym.*, 2012, **88**, 713–718.

162 M. Bahram, N. Mohseni and M. Moghtader, in *Emerging Concepts in Analysis and Applications of Hydrogels*, InTech, 2016, vol. i, p. 13.

163 R. A. Shanks and I. R. M. Pardo, in *Cellulose-Based Superabsorbent Hydrogels*, 2018, pp. 1–26.

164 E. M. Ahmed, *J. Adv. Res.*, 2015, **6**, 105–121.

165 S. M. F. Kabir, P. P. Sikdar, B. Haque, M. A. R. Bhuiyan, A. Ali and M. N. Islam, *Prog. Biomater.*, 2018, **7**, 153–174.

166 S. Sezer, İ. Şahin, K. Öztürk, V. Şanko, Z. Koçer and Ü. A. Sezer, in *Cellulose-Based Superabsorbent Hydrogels*, 2018, pp. 1–27.

167 T. Ghosh and V. Katiyar, in *Cellulose-Based Superabsorbent Hydrogels*, 2018, pp. 1–25.

168 K. J. De France, T. Hoare and E. D. Cranston, *Chem. Mater.*, 2017, **29**, 4609–4631.

169 A. Koschella, M. Hartlieb and T. Heinze, *Carbohydr. Polym.*, 2011, **86**, 154–161.

170 S. Chatterjee and P. Chi-leung Hui, in *Hydrogels - Smart Materials for Biomedical Applications*, IntechOpen, 2019, vol. i, p. 13.

171 R. Soares, M. C. Carneiro, M. I. C. Monteiroa, S. de S. Henriquae, F. V. M. Pontes, L. I. Dias da Silva, A. A. Neto and R. E. Santelli, *Chem. Speciat. Bioavailab.*, 2009, **21**, 153–160.

172 P. A. G. Soares, A. I. Bourbon, A. A. Vicente, C. A. S. Andrade, W. Barros, M. T. S.

Correia, A. Pessoa and M. G. Carneiro-Da-Cunha, *Mater. Sci. Eng. C*, 2014, **42**, 219–226.

173 F. Ullah, M. B. H. Othman, F. Javed, Z. Ahmad and H. M. Akil, *Mater. Sci. Eng. C*, 2015, **57**, 414–433.

174 D. E. Ciolacu and D. M. Suflet, in *Biomass as Renewable Raw Material to Obtain Bioproducts of High-Tech Value*, Elsevier, 2018, pp. 401–439.

175 V. K. Thakur and M. K. Thakur, *Handbook of Sustainable Polymers*, Jenny Stanford Publishing, 2016.

176 P. Sannigrahi, D. H. Kim, S. Jung and A. Ragauskas, *Energy Environ. Sci.*, 2011, **4**, 1306–1310.

177 S. D. Shinde, X. Meng, R. Kumar and A. J. Ragauskas, *Green Chem.*, 2018, **20**, 2192–2205.

178 F. Hu, S. Jung and A. Ragauskas, *Bioresour. Technol.*, 2012, **117**, 7–12.

179 Y. Pu, F. Hu, F. Huang, B. H. Davison and A. J. Ragauskas, *Biotechnol. Biofuels*, 2013, **6**, 1.

180 A. S. Matharu, E. M. de Melo, J. Remón, S. Wang, A. Abdulina and E. Kontturi, *ChemSusChem*, 2018, **11**, 1344–1353.

181 J. M. B. F. Diniz, M. H. Gil and J. A. A. M. Castro, *Wood Sci. Technol.*, 2004, **37**, 489–494.

182 R. A. Ilyas, S. M. Sapuan, R. Ibrahim, H. Abral, M. R. Ishak, E. S. Zainudin, M. S. N. Atikah, N. Mohd Nurazzi, A. Atiqah, M. N. M. Ansari, E. Syafri, M. Asrofi, N. H. Sari

and R. Jumaidin, *J. Mater. Res. Technol.*, 2019, **8**, 4819–4830.

183 R. Prathapan, R. Thapa, G. Garnier and R. F. Tabor, *Colloids Surfaces A Physicochem. Eng. Asp.*, 2016, **509**, 11–18.

184 G. Z. Kyzas, J. Fu and K. A. Matis, *Materials (Basel).*, 2013, **6**, 5131–5158.

185 Y. Pan, F. Wang, T. Wei, C. Zhang and H. Xiao, *Chem. Eng. J.*, 2016, **302**, 33–43.

186 H. Sehaqui, U. P. de Larraya, P. Liu, N. Pfenninger, A. P. Mathew, T. Zimmermann and P. Tingaut, *Cellulose*, 2014, **21**, 2831–2844.

187 N. Isobe, X. Chen, U. J. Kim, S. Kimura, M. Wada, T. Saito and A. Isogai, *J. Hazard. Mater.*, 2013, **260**, 195–201.

188 A. W. Carpenter, C. F. De Lannoy and M. R. Wiesner, *Environ. Sci. Technol.*, 2015, **49**, 5277–5287.

189 N. Neethu and T. Choudhury, *Recent Pat. Nanotechnol.*, 2018, **12**, 200–207.

190 A. R. Netzahuatl-Muñoz, M. Del Carmen Cristiani-Urbina and E. Cristiani-Urbina, *PLoS One*, 2015, **10**, 1–23.

191 H. Zhu, Q. Kong, X. Cao, H. He, J. Wang and Y. He, *Desalin. Water Treat.*, 2016, **57**, 20368–20376.

192 Y. Huang, X. Lee, F. C. Macazo, M. Grattieri, R. Cai and S. D. Minteer, *Chem. Eng. J.*, 2018, **339**, 259–267.

193 G. L. Dotto, J. M. N. Santos, I. L. Rodrigues, R. Rosa, F. A. Pavan and E. C. Lima, *J. Colloid Interface Sci.*, 2015, **446**, 133–140.

194 M. Beaumont, A. Kondor, S. Plappert, C. Mitterer, M. Opietnik, A. Potthast and T. Rosenau, *Cellulose*, 2017, **24**, 435–440.

195 X. L. Luo, J. Y. Zhu, R. Gleisner and H. Y. Zhan, *Cellulose*, 2011, **18**, 1055–1062.

196 M. Häggkvist, T. Q. Li and L. Ödberg, *Cellulose*, 1998, **5**, 33–49.

197 P. Liu, H. Sehaqui, P. Tingaut, A. Wichser, K. Oksman and A. P. Mathew, *Cellulose*, 2014, **21**, 449–461.

198 D.-Q. Lin, L.-N. Zhong and S.-J. Yao, *Biotechnol. Bioeng.*, 2006, **95**, 185–191.

199 W. Xue, F. Lei, P. Li and J. Jiang, *BioResources*, 2018, **13**, 1510–1524.

200 J. M. Shannon, J. H. Clark, M. Ingrid De Heer, T. Ekblad and A. S. Matharu, *ACS Omega*, 2018, **3**, 18361–18369.

201 A. Pawlicka and B. Doczekalska, *Ann. Warsaw Agric. Univ. - For. Wood Technol.*, 2013, **14**, 11–14.

202 Y. S. Kim, S. J. Yang, S. W. Kim, H. J. Lim, T. Kim and C. R. Park, *ICCM Int. Conf. Compos. Mater.*, 2011, 0–3.

203 P. S. Thue, E. C. Lima, J. M. Sieliechi, C. Saucier, S. L. P. Dias, J. C. P. Vaghetti, F. S. Rodembusch and F. A. Pavan, *J. Colloid Interface Sci.*, 2017, **486**, 163–175.

204 M. Danish, T. Ahmad, R. Hashim, N. Said, M. N. Akhtar, J. Mohamad-Saleh and O. Sulaiman, *Surfaces and Interfaces*, 2018, **11**, 1–13.

205 L. Liu, X.-B. Luo, L. Ding and S.-L. Luo, in *Micro and Nano Technologies*, eds. X. Luo and F. B. T.-N. for the R. of P. and R. R. Deng, Elsevier, 2019, pp. 83–147.

206 M. A. A. Sayed and M. S. Khater, *Middle East J. Appl. Sci.*, 2013, **3**, 98–104.

207 O. Hamdaoui and E. Naffrechoux, *J. Hazard. Mater.*, 2007, **147**, 381–394.

208 A. O. Dada, F. A. Adekola and E. O. Odebunmi, *Cogent Chem.*, 2017, **3**, 38–45.

209 I. Langmuir, *J. Am. Chem. Soc.*, 1918, **40**, 1361–1403.

210 O. Hamdaoui, E. Naffrechoux, L. Tifouti and C. Pétrier, *Ultrason. Sonochem.*, 2003, **10**, 109–114.

211 K. Vijayaraghavan, T. V. N. Padmesh, K. Palanivelu and M. Velan, *J. Hazard. Mater.*, 2006, **133**, 304–308.

212 M. Akram, H. N. Bhatti, M. Iqbal, S. Noreen and S. Sadaf, *J. Environ. Chem. Eng.*, 2017, **5**, 400–411.

213 L. dos Santos Silva, J. de Oliveira Carvalho, R. D. de Sousa Bezerra, M. da Silva, F. Ferreira, J. Osajima and E. da Silva Filho, *Molecules*, 2018, **23**, 743.

214 R. I. Yousef, B. El-Eswed and A. H. Al-Muhtaseb, *Chem. Eng. J.*, 2011, **171**, 1143–1149.

215 N. D. Hutson and R. T. Yang, *Adsorption*, 1997, **3**, 189–195.

216 N. Ayawei, A. N. Ebelegi and D. Wankasi, *J. Chem.*, 2017, **2017**, 1–11.

217 J. N. Aningo, *J. Multidiscip. Eng. Sci. Technol.*, 2017, **4**, 7993–8000.

218 Y. Xu, J. Chen, R. Chen, P. Yu, S. Guo and X. Wang, *Water Res.*, 2019, **160**, 148–157.

219 I. Ullah, R. Nadeem, M. Iqbal and Q. Manzoor, *Ecol. Eng.*, 2013, **60**, 99–107.

220 D. W. O'Connell, C. Birkinshaw and T. F. O'Dwyer, *Bioresour. Technol.*, 2008, **99**, 6709–6724.

221 A. E. Chávez-Guajardo, J. C. Medina-Llamas, L. Maqueira, C. A. S. Andrade, K. G. B. Alves and C. P. de Melo, *Chem. Eng. J.*, 2015, **281**, 826–836.

222 D. Metze, N. Jakubowski and D. Klockow, in *Handbook of Elemental Speciation II - Species in the Environment, Food, Medicine and Occupational Health*, John Wiley & Sons, Ltd, Chichester, UK, 2005, pp. 120–135.

223 N. Unceta, F. Séby, J. Malherbe and O. F. X. Donard, *Anal. Bioanal. Chem.*, 2010, **397**, 1097–1111.

224 Y. Zhou, Q. Jin, T. Zhu and Y. Akama, *J. Hazard. Mater.*, 2011, **187**, 303–310.

225 J. Bajpai, R. Shrivastava and A. K. Bajpai, *Colloids Surfaces A Physicochem. Eng. Asp.*, 2004, **236**, 81–90.

226 R. K. Tandon, P. T. Crisp, J. Ellis and R. S. Baker, *Talanta*, 1984, **31**, 227–228.

227 H. Hu, Y. Gao, T. Wang, L. Sun, Y. F. Zhang and H. Li, *J. Radioanal. Nucl. Chem.*, 2019, **321**, 427–437.

228 N. Nasseh, L. Taghavi, B. Barikbin and A. R. Harifi-Mood, *J. Water Reuse Desalin.*, 2017, **7**, 449–460.

229 L. Zhou, Y. Liu, S. Liu, Y. Yin, G. Zeng, X. Tan, X. Hu, X. Hu, L. Jiang, Y. Ding, S. Liu and X. Huang, *Bioresour. Technol.*, 2016, **218**, 351–359.

230 S. Chakraborty, S. Chowdhury and P. Das Saha, *Appl. Water Sci.*, 2012, **2**, 135–141.

231 A. U. Itodo and H. U. Itodo, *Life Sci. J.*, 2010, **7**, 68–76.

232 A. Baldermann, A. Grießbacher, C. Baldermann, B. Purgstaller, I. Letofsky-Papst, S.

Kaufhold and M. Dietzel, *Geosciences*, 2018, **8**, 309.

233 G. Jing, Z. Zhou, L. Song and M. Dong, *Desalination*, 2011, **279**, 423–427.

234 J. T. Qi, T. Hashimoto, J. R. Walton, X. Zhou, P. Skeldon and G. E. Thompson, *Surf. Coatings Technol.*, 2015, **280**, 317–329.

235 M. C. Biesinger, C. Brown, J. R. Mycroft, R. D. Davidson and N. S. McIntyre, *Surf. Interface Anal.*, 2004, **36**, 1550–1563.

236 R. Singh, H. Dong, Q. Zeng, L. Zhang and K. Rengasamy, *Geochim. Cosmochim. Acta*, 2017, **210**, 25–41.

237 W. Zheng, Q. An, Z. Lei, Z. Xiao, S. Zhai and Q. Liu, *RSC Adv.*, 2016, **6**, 104897–104910.

238 Y. Zhang, J. Ou, Z. Duan, Z. Xing and Y. Wang, *Colloids Surfaces A Physicochem. Eng. Asp.*, 2015, **481**, 108–116.

239 Y. Nakano, K. Takeshita and T. Tsutsumi, *Water Res.*, 2001, **35**, 496–500.

240 R. S. Vieira, M. L. M. Oliveira, E. Guibal, E. Rodríguez-Castellón and M. M. Beppu, *Colloids Surfaces A Physicochem. Eng. Asp.*, 2011, **374**, 108–114.

241 X. F. Sun, Y. Ma, X. W. Liu, S. G. Wang, B. Y. Gao and X. M. Li, *Water Res.*, 2010, **44**, 2517–2524.

242 N. Fiol, C. Escudero and I. Villaescusa, *Bioresour. Technol.*, 2008, **99**, 5030–5036.

243 G. Choppala, N. Bolan and B. Seshadri, *J. Hazard. Mater.*, 2013, **261**, 718–724.

244 J. J. Salazar-Rabago, R. Leyva-Ramos, J. Rivera-Utrilla, R. Ocampo-Perez and F. J. Cerino-Cordova, *Sustain. Environ. Res.*, 2017, **27**, 32–40.

245 G. Labiebah, G. Gunawan, M. C. Djunaidi, A. Haris and D. S. Widodo, *J. Kim. Sains dan Apl.*, 2019, **22**, 23.

246 J. J. Salazar-rabago, R. Leyva-ramos, J. Rivera-utrilla, R. Ocampo-perez and F. J. Cerino-cordova, *Sustain. Environ. Res.*, 2017, **27**, 32–40.

247 H. L. Parker, A. J. Hunt, V. L. Budarin, P. S. Shuttleworth, K. L. Miller and J. H. Clark, *RSC Adv.*, 2012, **2**, 8992–8997.

248 H. N. Tran, S. J. You, T. V. Nguyen and H. P. Chao, *Chem. Eng. Commun.*, 2017, **204**, 1020–1036.

249 H. N. Tran, Y. F. Wang, S. J. You and H. P. Chao, *Process Saf. Environ. Prot.*, 2017, **107**, 168–180.

250 K. A. Shroff and V. K. Vaidya, *Chem. Eng. J.*, 2011, **171**, 1234–1245.

251 Y. S. Ho, *Scientometrics*, 2004, **59**, 171–177.

252 Q. Xu, Y. Wang, L. Jin, Y. Wang and M. Qin, *J. Hazard. Mater.*, 2017, **339**, 91–99.

253 S. Yadav, V. Srivastava, S. Banerjee, C. H. Weng and Y. C. Sharma, *Catena*, 2013, **100**, 120–127.

254 Y. S. Ho, *J. Hazard. Mater.*, 2006, **136**, 681–689.

255 S. M. Musyoka, H. Mittal, S. B. Mishra and J. C. Ngila, *Int. J. Biol. Macromol.*, 2014, **65**, 389–397.

256 A. E. Ofomaja, *Bioresour. Technol.*, 2010, **101**, 5868–5876.

257 N. Kannan and M. Meenakshisundaram, *Water. Air. Soil Pollut.*, 2002, **138**, 289–305.

258 Y. . Ho and G. McKay, *Process Biochem.*, 1999, **34**, 451–465.

259 D. Park Sangwook NJ,US, H. Barere Aaron NJ,US, F. Wagner Christopher T. NJ,US, P. Kiefer Robert NJ,US and G. Greenhalgh E. Skott PA,US, *Reinforced Biologic Material*, 2009.

260 D. Robati, *J. Nanostructure Chem.*, 2013, **3**, 55.

261 N. Kannan and M. Meenakshisundaram, *Water, Air Soil Pollut.*, 2002, **138**, 289–305.

262 K. L. Tan and B. H. Hameed, *J. Taiwan Inst. Chem. Eng.*, 2017, **74**, 25–48.

263 Markandeya, S. P. Shukla and G. C. Kisku, *Res. J. Environ. Toxicol.*, 2015, **9**, 320–331.

264 J. Yang, M. Yu and W. Chen, *J. Ind. Eng. Chem.*, 2015, **21**, 414–422.

265 P. Saha and S. Chowdhury, in *Thermodynamics*, ed. S. C. E.-M. Tadashi, InTech, 2011, p. Ch. 16.

266 S. Ata, M. Imran Din, A. Rasool, I. Qasim and I. Ul Mohsin, *J. Anal. Methods Chem.*, 2012, **2012**, 1–8.

267 J. N. Putro, A. Kurniawan, S. Ismadji and Y. H. Ju, *Environ. Nanotechnology, Monit. Manag.*, 2017, **8**, 134–149.

268 O. Üner, Ü. Geçgel and Y. Bayrak, *Water, Air, Soil Pollut.*, 2016, **227**, 247.

269 B. A. Fil, M. T. Yilmaz, S. Bayar and M. T. Elkoca, *Brazilian J. Chem. Eng.*, 2014, **31**, 171–182.

270 N. T. Abdel-Ghani, G. A. El-Chaghaby, E. S. A. Rawash and E. C. Lima, *J. Chil. Chem. Soc.*, 2017, **62**, 3505–3511.

271 J. M. Thomas, *J. Chem. Educ.*, 1961, **38**, 138–139.

272 Pradip and D. W. Fuerstenau, *Colloids and Surfaces*, 1985, **15**, 137–146.

273 S. Y. Lee, R. Sankaran, K. W. Chew, C. H. Tan, R. Krishnamoorthy, D.-T. Chu and P.-L. Show, *BMC Energy*, 2019, **1**, 1–22.

274 S. L. Lo, Y. F. Huang, P. Te Chiueh and W. H. Kuan, *Energy Procedia*, 2017, **105**, 41–46.

275 M. I. Jahirul, M. G. Rasul, A. A. Chowdhury and N. Ashwath, *Energies*, 2012, **5**, 4952–5001.

276 C. Wu, V. L. Budarin, M. J. Gronnow, M. De Bruyn, J. A. Onwudili, J. H. Clark and P. T. Williams, *J. Anal. Appl. Pyrolysis*, 2014, **107**, 276–283.

277 O. L. Ki, A. Kurniawan, C. X. Lin, Y. H. Ju and S. Ismadji, *Bioresour. Technol.*, 2013, **145**, 157–161.

278 J. F. González, A. Ramiro, C. M. González-García, J. Gańán, J. M. Encinar, E. Sabio and J. Rubiales, *Ind. Eng. Chem. Res.*, 2005, **44**, 3003–3012.

279 F. Ronsse, in *Biochar: A Regional Supply Chain Approach in View of Climate Change Mitigation*, eds. B. B. Uzun, E. Apaydın Varol, J. Liu and V. J. Bruckman, Cambridge University Press, Cambridge, 2016, pp. 199–226.

280 H. Ben, F. Wu, Z. Wu, G. Han, W. Jiang and A. J. Ragauskas, *Polymers (Basel).*, 2019, **11**, 1387.

281 EBC (2012), *Eur. Biochar Found. (EBC), Arbaz, Switzerland. Version 6.1 19th June,* 2015, 1–22.

282 A. G. Daful and M. R Chandraratne, *Ref. Modul. Mater. Sci. Mater. Eng.*, 2018, 0–9.

283 R. Tareq, N. Akter and M. S. Azam, eds. Y. S. Ok, D. C. W. Tsang, N. Bolan and J. M. B. T.-B. from B. and W. Novak, Elsevier, 2019, pp. 169–209.

284 A. Dieguez-Alonso, A. Funke, A. Anca-Couce, A. Rombolà, G. Ojeda, J. Bachmann and F. Behrendt, *Energies*, 2018, **11**, 496.

285 H. Rezaei, F. Yazdanpanah, J. Choon Lim, A. Lau and S. Sokhansanj, in *Biomass for Bioenergy - Recent Trends and Future Challenges*, IntechOpen, 2019, vol. i, p. 13.

286 E. Lester, C. Avila, C. H. Pang, O. Williams, J. Perkins, S. Gaddipatti, G. Tucker, J. M. Barraza, M. P. Trujillo-Uribe and T. Wu, *Fuel*, 2018, **232**, 845–854.

287 C. Ravikumar, P. Senthil Kumar, S. K. Subhashni, P. V. Tejaswini and V. Varshini, *Sustain. Mater. Technol.*, 2017, **11**, 19–27.

288 P. Basu, in *Biomass Gasification Design Handbook*, ed. P. B. T.-B. G. and P. Basu, Elsevier, Boston, 2010, pp. 27–63.

289 X. S. Zhang, G. X. Yang, H. Jiang, W. J. Liu and H. S. Ding, *Sci. Rep.*, 2013, **3**, 1–7.

290 E. Christensen, G. M. Fioroni, S. Kim, L. Fouts, E. Gjersing, R. S. Paton and R. L. McCormick, *Fuel*, 2018, **212**, 576–585.

291 H. Kawamoto, *J. Wood Sci.*, 2017, **63**, 117–132.

292 S. Kelkar, Z. Li, J. Bovee, K. D. Thelen, R. M. Kriegel and C. M. Saffron, *Biomass and Bioenergy*, 2014, **64**, 152–161.

293 S. B. Kabakcı and Ş. Hacıbektaşoğlu, in *Pyrolysis*, InTech, 2017, vol. i, p. 13.

294 K. Uemura, S. Appari, S. Kudo, J. I. Hayashi, H. Einaga and K. Norinaga, *Fuel Process. Technol.*, 2015, **136**, 73–78.

295 Y. T. Cheng and G. W. Huber, *Green Chem.*, 2012, **14**, 3114–3125.

296 S. D. Shinde, X. Meng, R. Kumar and A. J. Ragauskas, *Green Chem.*, 2018, **20**, 2192–2205.

297 N. Buchtová and T. Budtova, *Cellulose*, 2016, **23**, 2585–2595.

Appendices

Appendix I. Cassava peel and almond hull MFCs

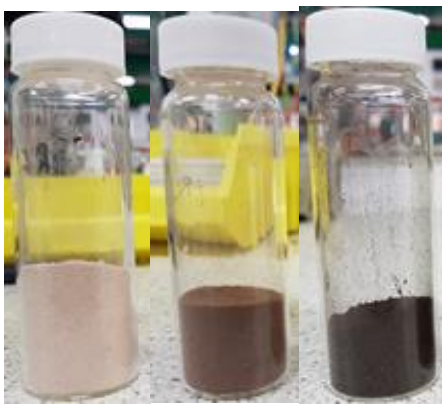

Cassava peel-MFC
(CP 120, CP 170 and CP 220)

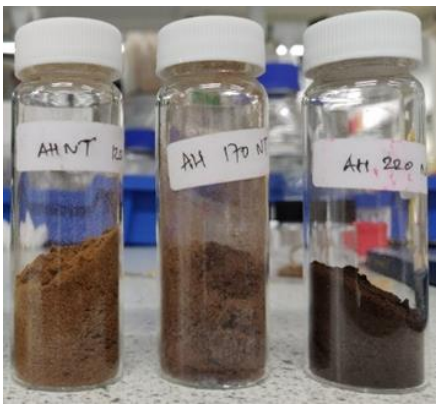

Almond hull-MFC
(AH 120, AH 170 and AH 220)

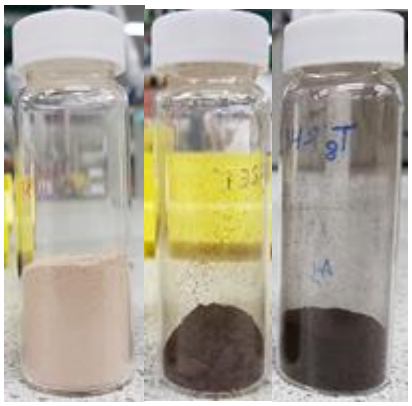

Cassava peel ethanol pretreatment-MFC
(CPET 120, CPET 170 and CPET 220)

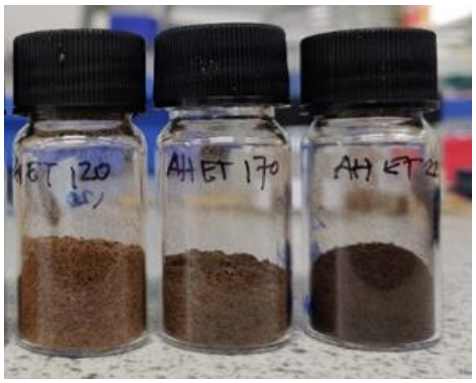

Almond hull ethanol pretreatment-MFC
(AHET 120, AHET 170 and AHET 220)

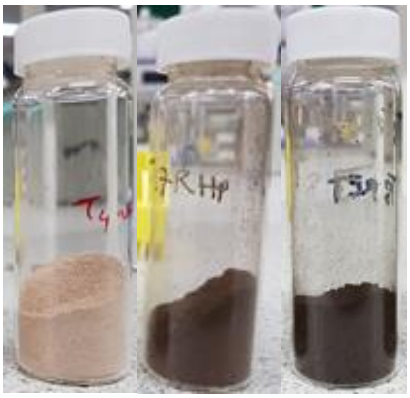

Cassava peel heptane pretreatment-MFC
(CPHP 120, CPHP 170 and CPHP 220)

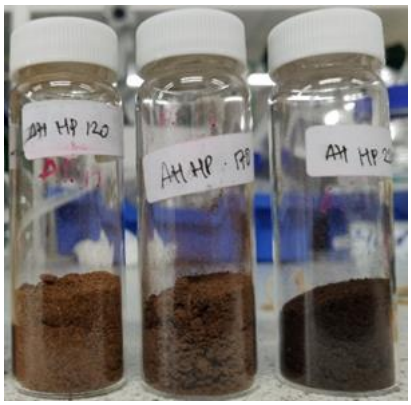

Almond hull heptane pretreatment-MFC
(AHHP 120, AHHP 170 and AHHP 220)

Figure A. 1 MFCs produced from microwave hydrothermal processing (Original in colour)

Appendix II. Cr(VI) adsorption of CPUS 220 at pH 2

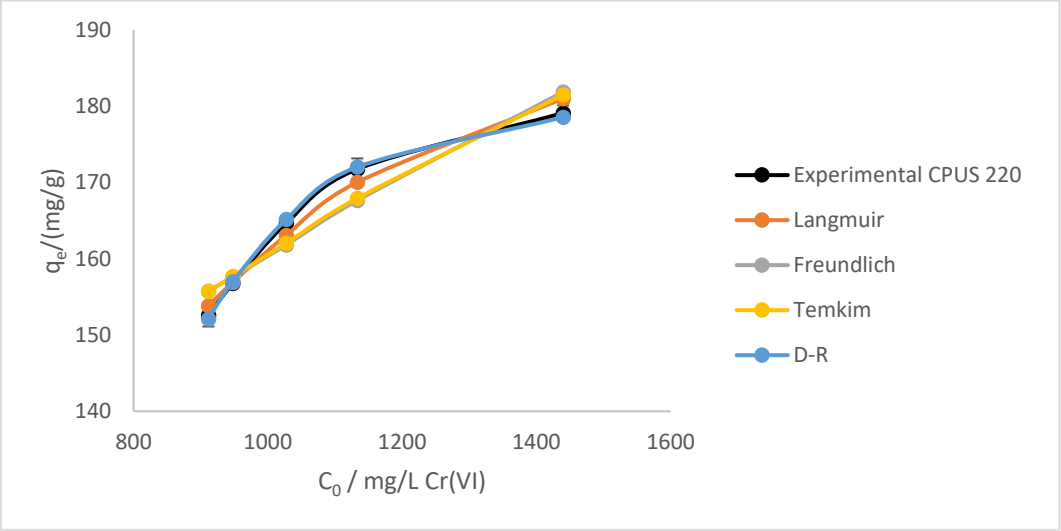

A) Comparison of the isotherm models with experimental CPUS 220 at pH 2

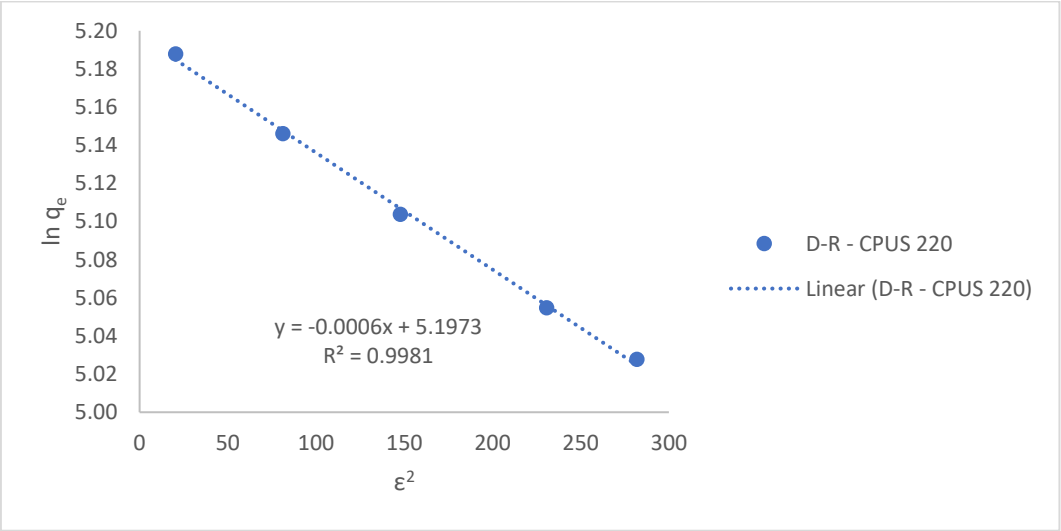

B) Plot ln q_e vs ε^2 of Dubinin–Radushkevich (D-R) CPUS 220

Figure A. 2 A) Comparison of the isotherm models with experimental CPUS 220 at pH 2 and B) plot ln q_e vs ε^2 of Dubinin–Radushkevich CPUS 220 (Original in colour)

Appendix III. Cr(VI) adsorption of AHUS 220 at pH 2

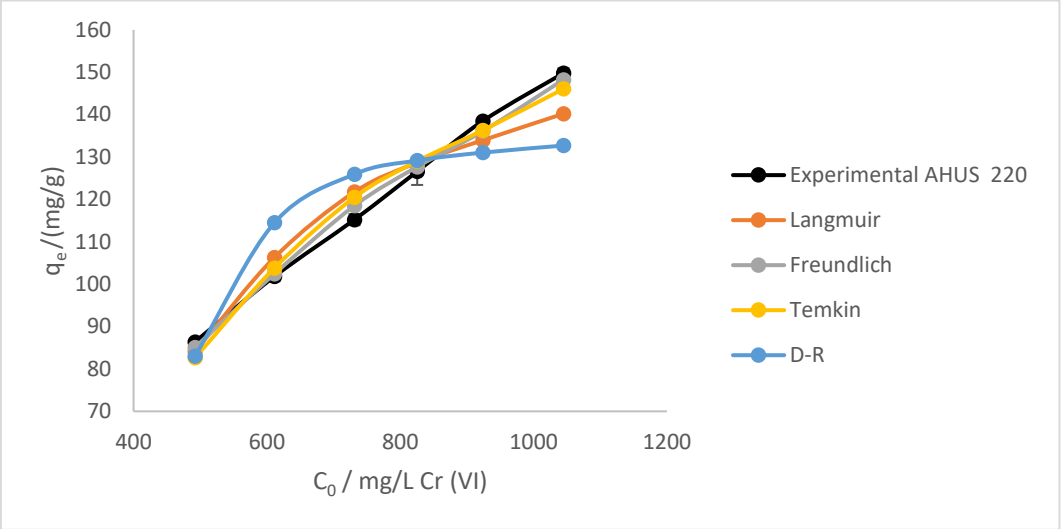

A) Comparison of the isotherm models with experimental AHUS 220 at pH 2

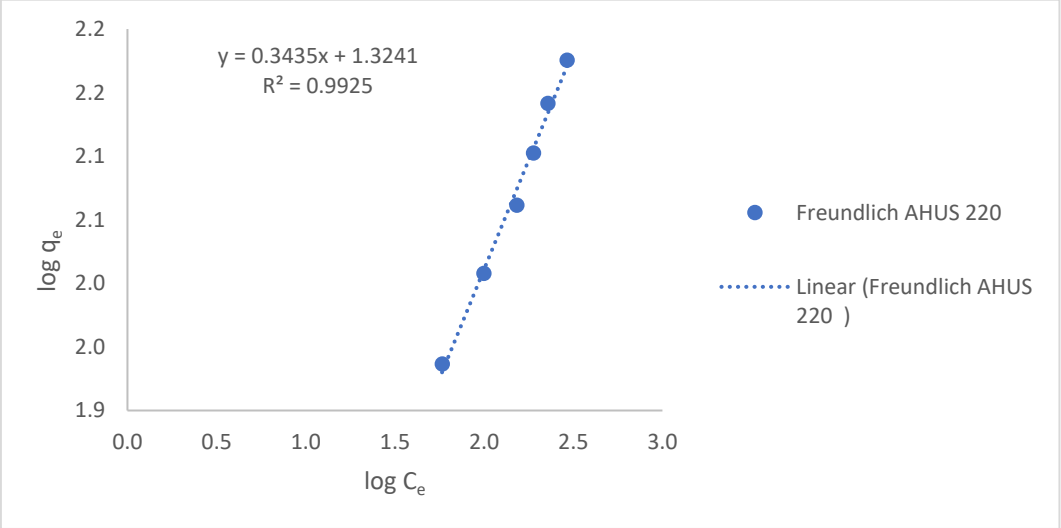

B) Plot of log q_e vs log C_e of Freundlich for AHUS 220

Figure A. 3 A) Comparison of the isotherm models with experimental AHUS 220 at pH 2 and B) Plot log q_e vs log C_e of Freundlich for AHUS 220 (Original in colour)

Appendix IV. C1s XPS spectra of CP 220 MFC before and after adsorption

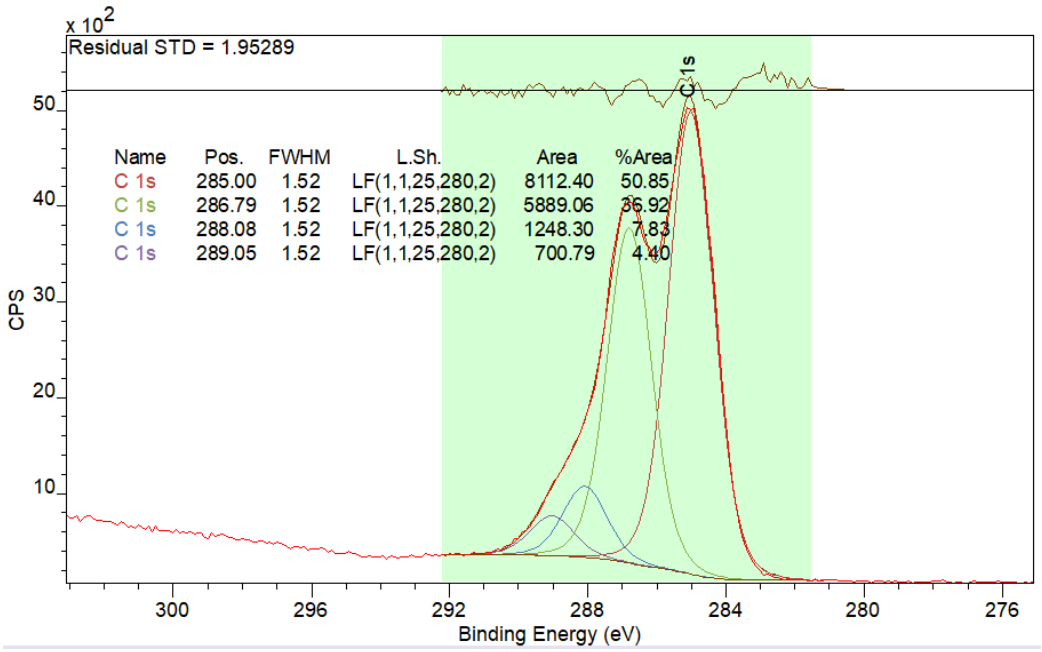

A) C1s XPS spectra of CP 220 before adsorption

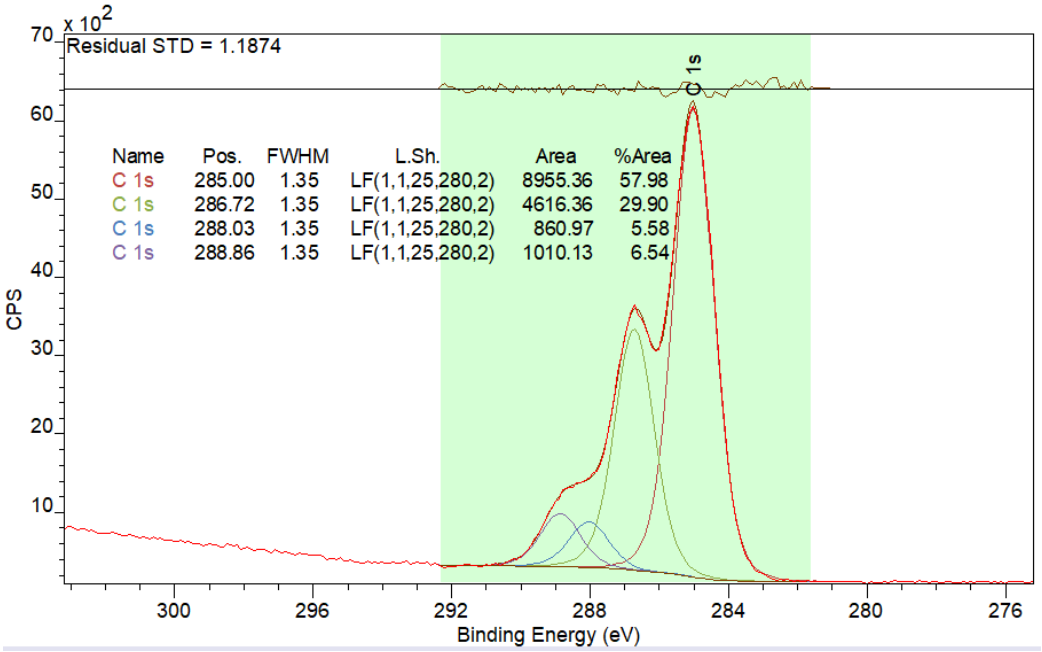

B) C1s XPS spectra of CPST 220 after adsorption with concentration of 300 mg/L Cr(VI) via stirring

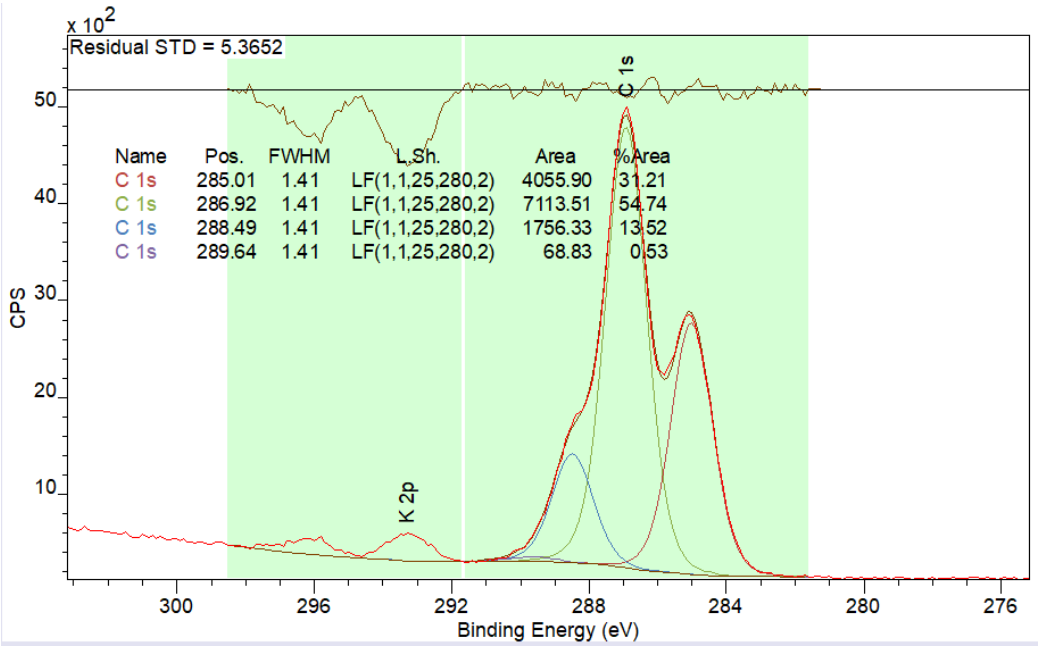

C) C1s XPS spectra of CPUS 220 after adsorption with concentration of 900 mg/L Cr(VI) via ultrasound

Figure A. 4 A) C1s XPS spectra of CP 220 before adsorption, B) after adsorption with concentration of 300 mg/L Cr(VI) via stirring and C) after adsorption with concentration of 900 mg/L Cr(VI) via ultrasound (Original in colour)

Appendix V. C1s XPS spectra of AH 220 MFC before and after adsorption

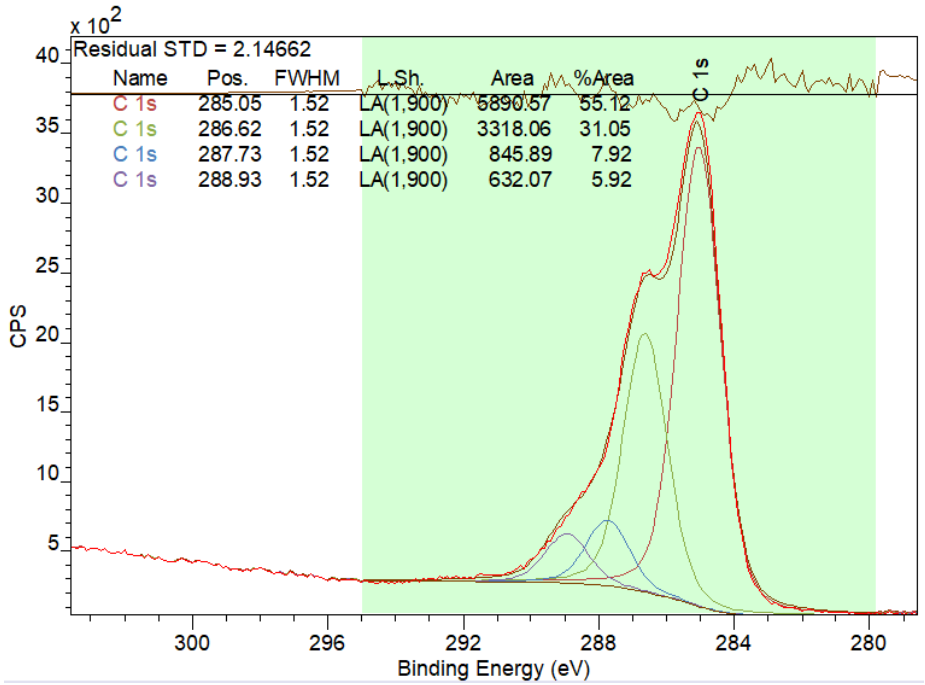

A) C1s XPS spectra for MFC of AH 220 before adsorption

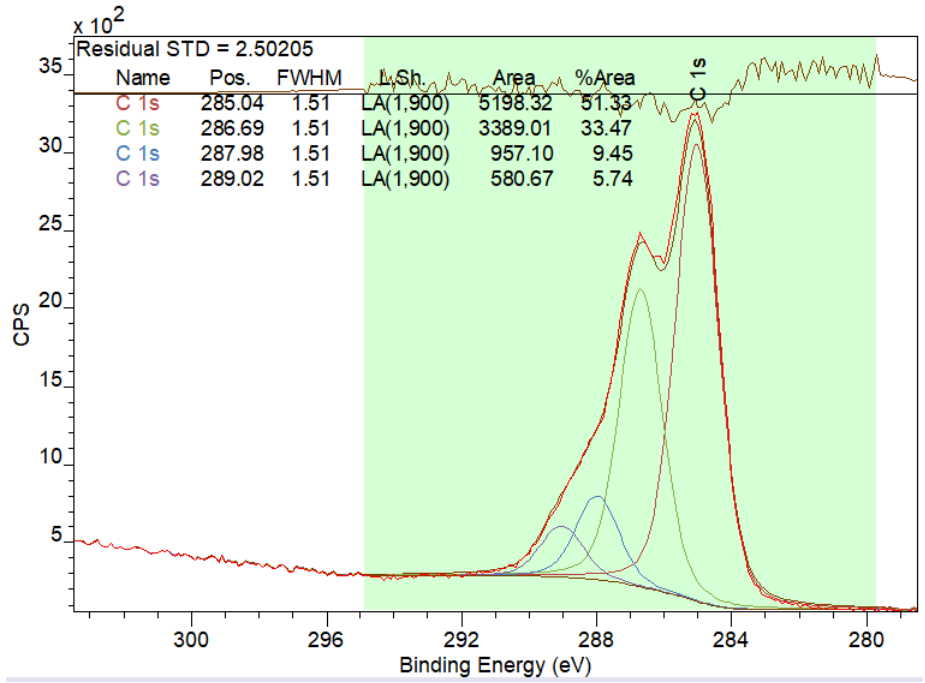

B) C1s XPS spectra for MFC of AHST 220 after adsorption with concentration of 300 mg/L Cr(VI) via stirring

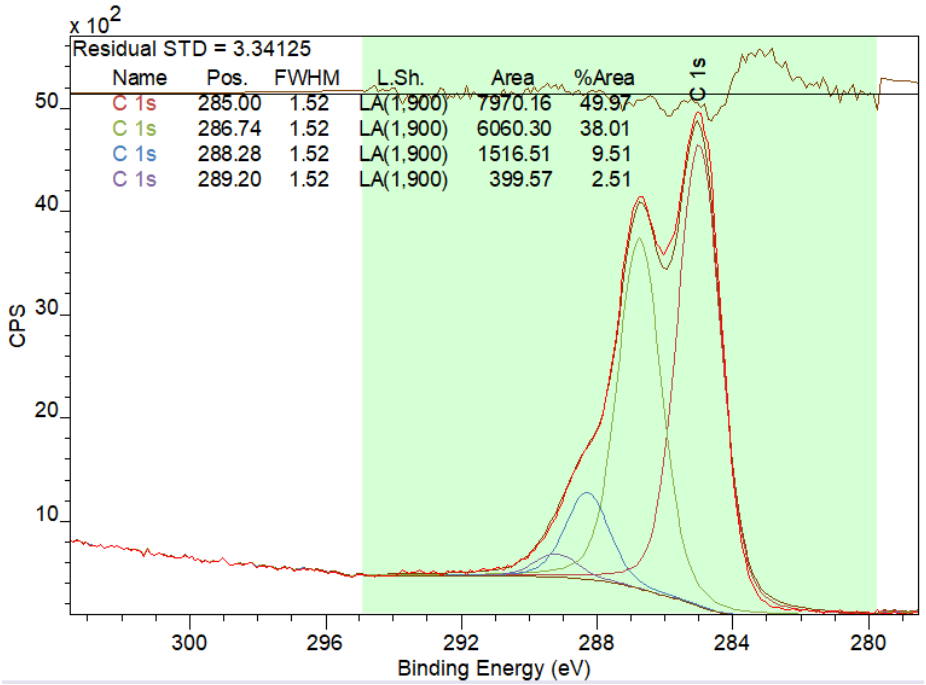

C) C1s XPS spectra for MFC of AHUS 220 after adsorption with concentration of 900 mg/L Cr(VI) via ultrasound.

Figure A. 5 (A) C1s XPS spectra of AH 220 before adsorption, B) after adsorption with concentration of 300 mg/L Cr(VI) via stirring (C) after adsorption with concentration of 900 mg/L Cr(VI) via ultrasound (Original in colour)

Appendix VI. MB adsorption of CPUS 120

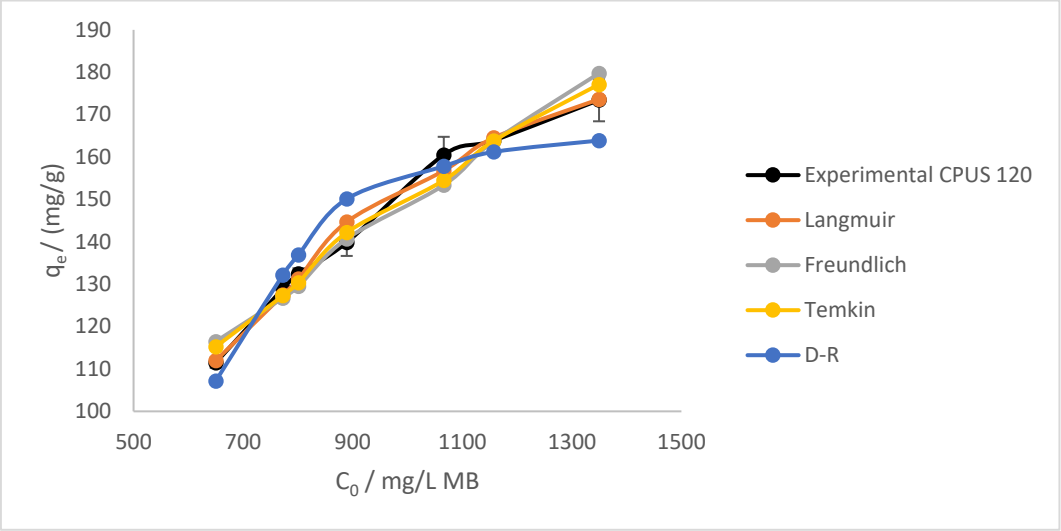

A) Comparison of the isotherm models with experimental CPUS 120

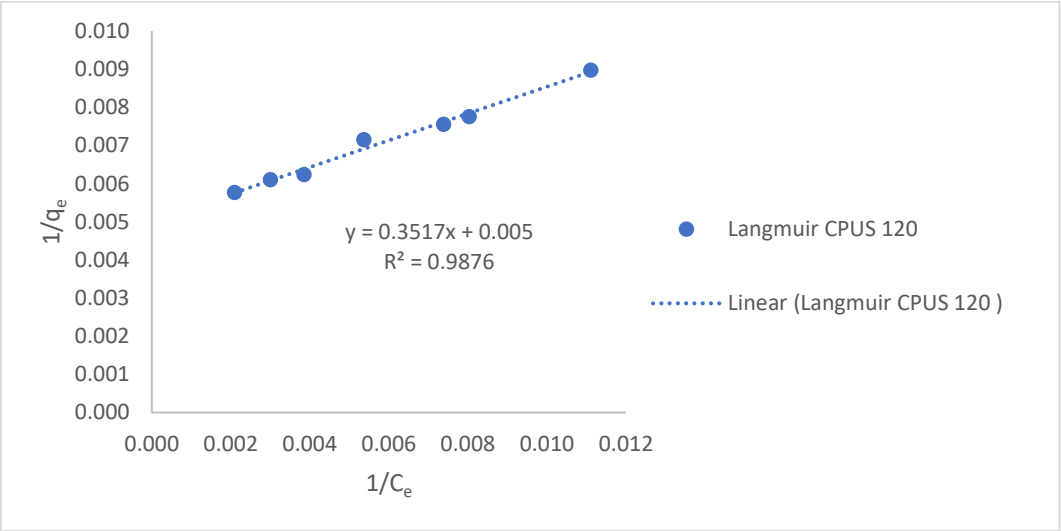

B) Plot of $1/q_e$ vs log $1/C_e$ of Langmuir for CPUS 120

Figure A. 6 A) Comparison of the isotherm models with experimental CPUS 120 and B) Plot $1/q_e$ vs $1/C_e$ of Langmuir CPUS 220 (Original in colour)

Appendix VII. MB adsorption of AHUS 120

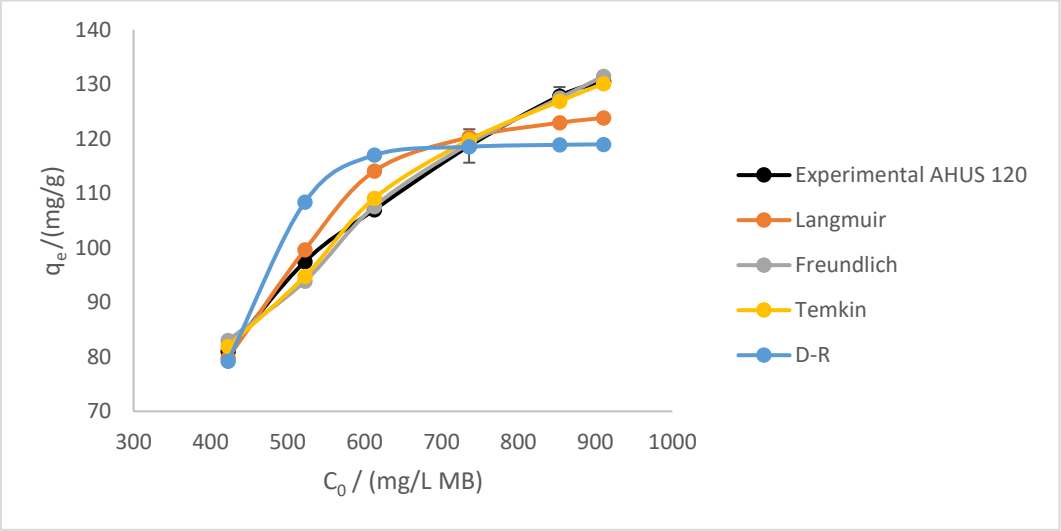

A) Comparison of the isotherm models with experimental AHUS 120

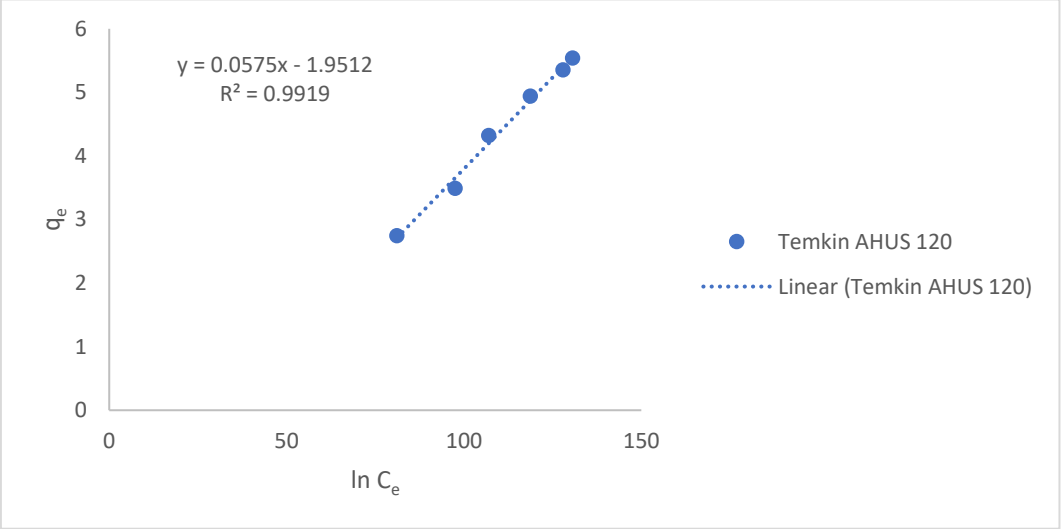

B) Plot of q_e vs ln C_e of Temkin AHUS 120

Figure A. 7 A) Comparison of the isotherm models with experimental AHUS 220 and B) Plot of q_e vs ln C_e of Temkin AHUS 120 (Original in colour)

Appendix VIII. MB adsorption of ACUS

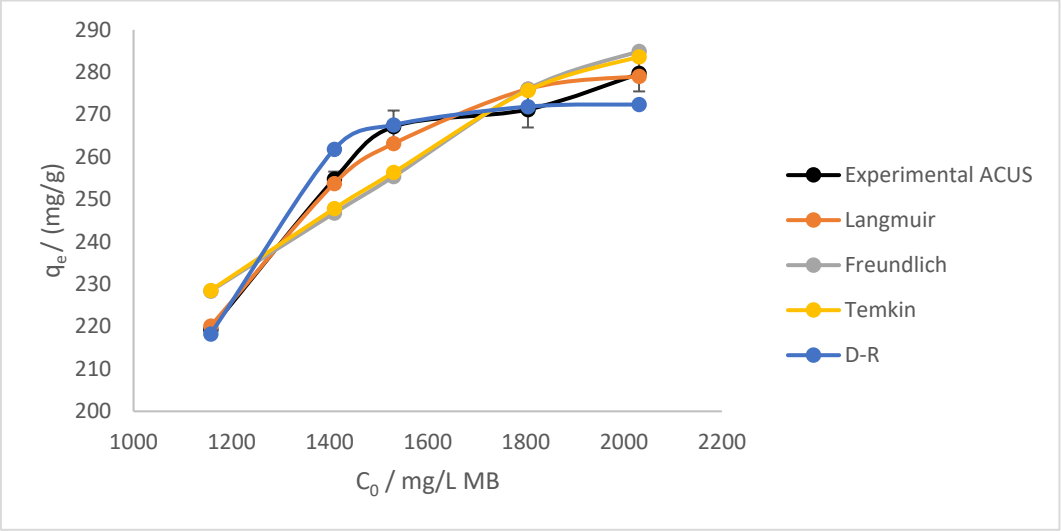

A) Comparison of the isotherm models with experimental ACUS

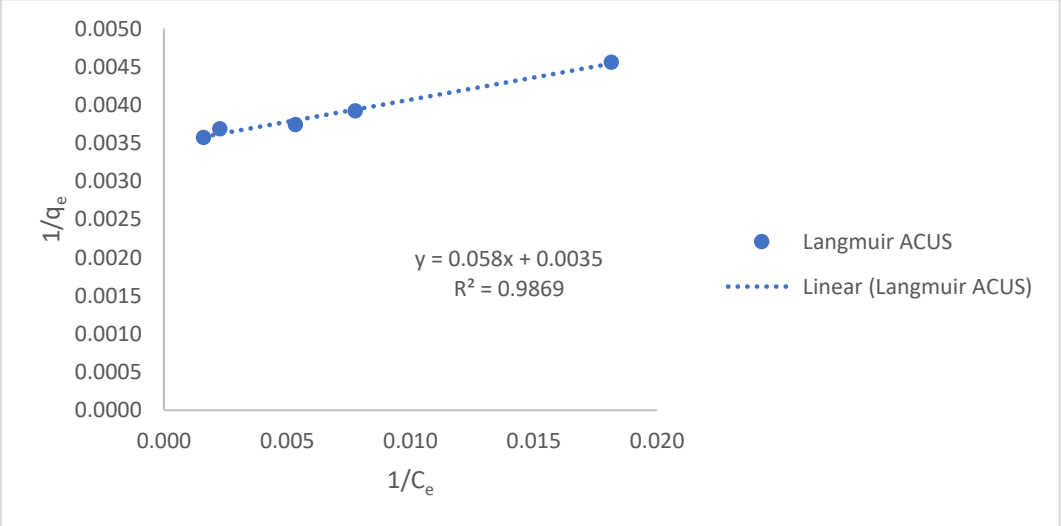

B) Plot of $1/q_e$ vs $1/C_e$ of Langmuir ACUS

Figure A. 8 A) Comparison of the isotherm models with experimental ACUS B) Plot of $1/q_e$ vs $1/C_e$ of Langmuir ACUS (Original in colour)

Appendix IX. C1s XPS spectra of CP 120 and AH 120 MFC

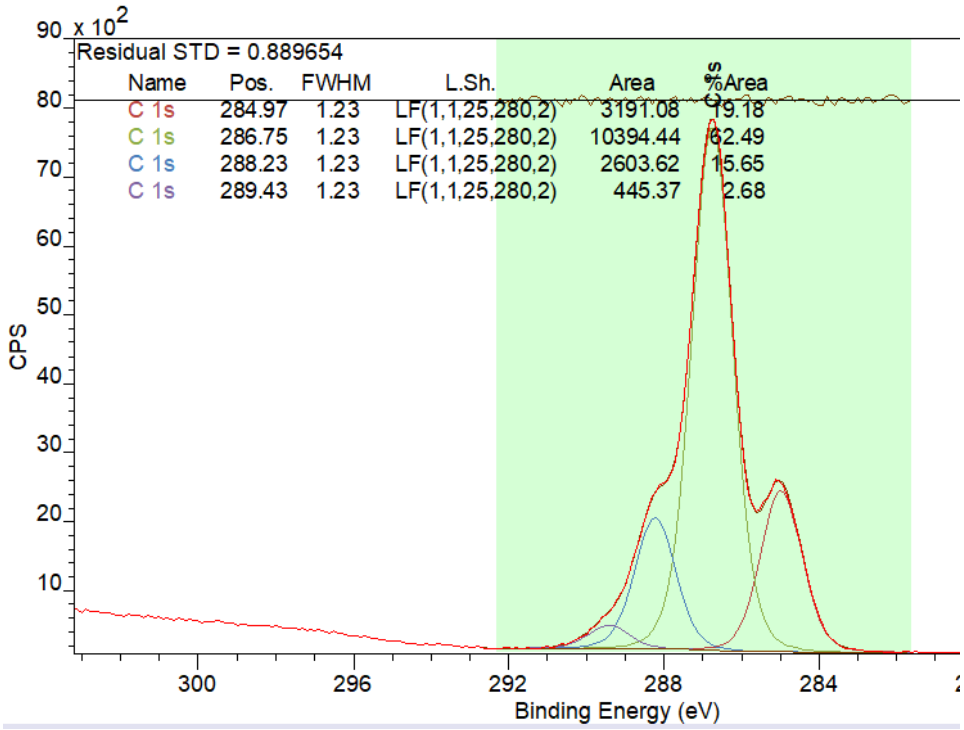

A) C1s XPS spectra of CP 120

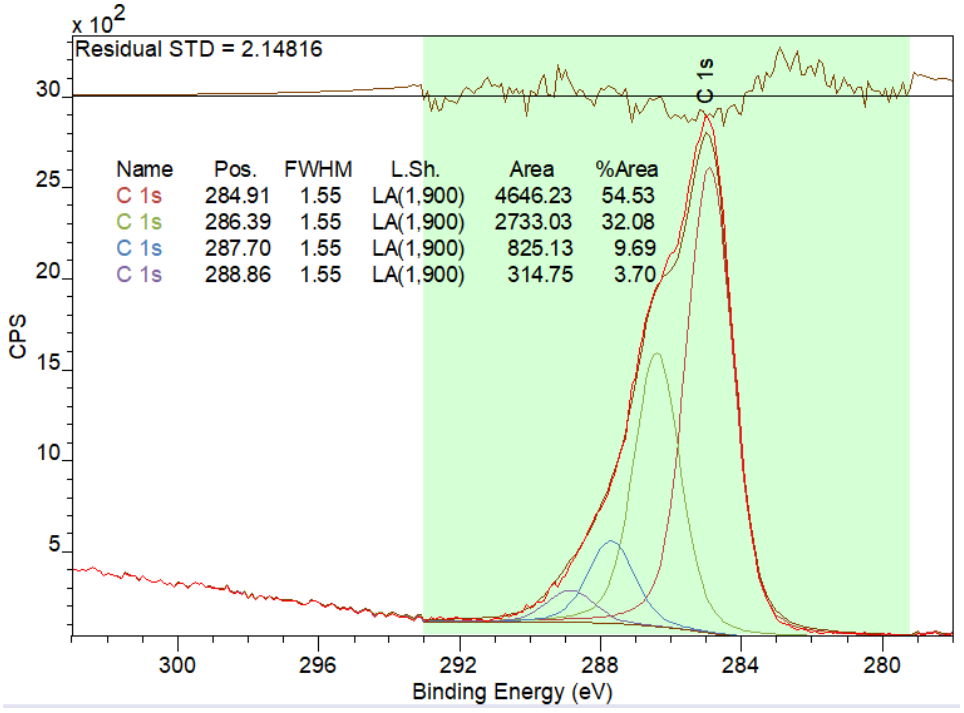

B) C1s XPS spectra of AH 120

Figure A. 9 C1s XPS spectra of CP 120 (A) and AH 120 (B) MFC

Appendix X. *Pseudo*-second order plot of CPUS 220 and AHUS 220

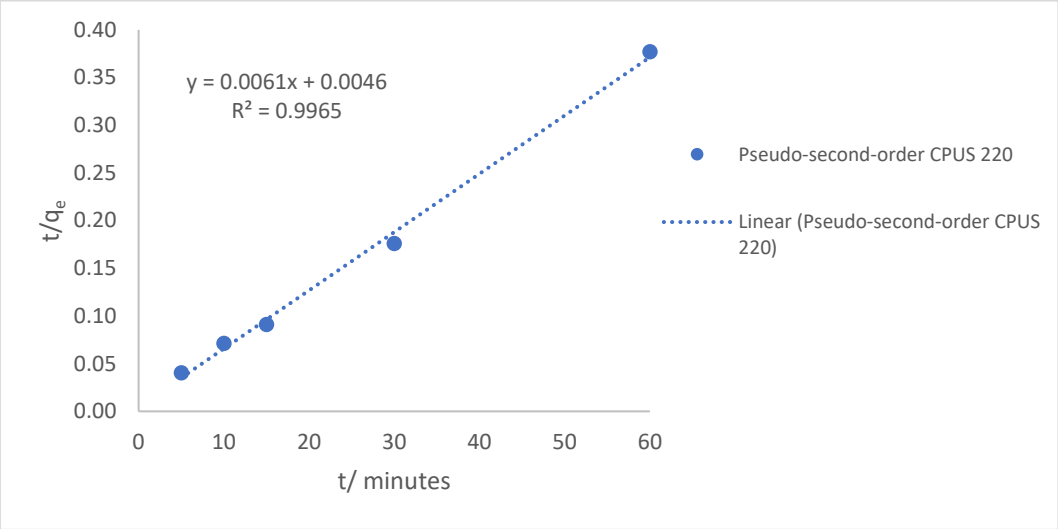

A) Plot t/q_e vs t of *pseudo*-second order CPUS 220

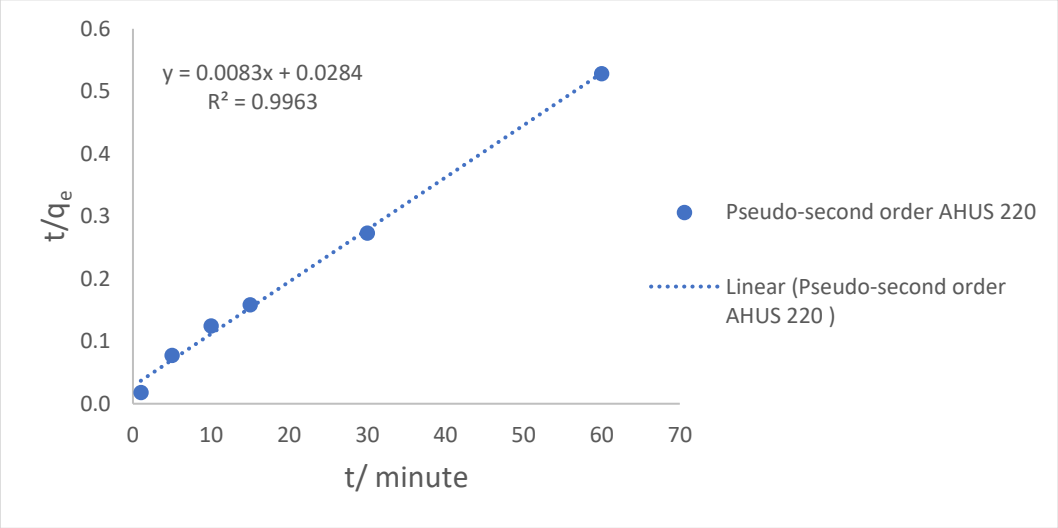

B) Plot t/q_e vs t of *pseudo*-second order AHUS 220

Figure A. 10 A) Plot t/q_e vs t of *pseudo*-second order CPUS 220 and B) Plot t/q_e vs t of AHUS 220 of *pseudo*-second order (Original in colour)

Appendix XI. *Pseudo*-second order plot of CPUS 120 and AHUS 120

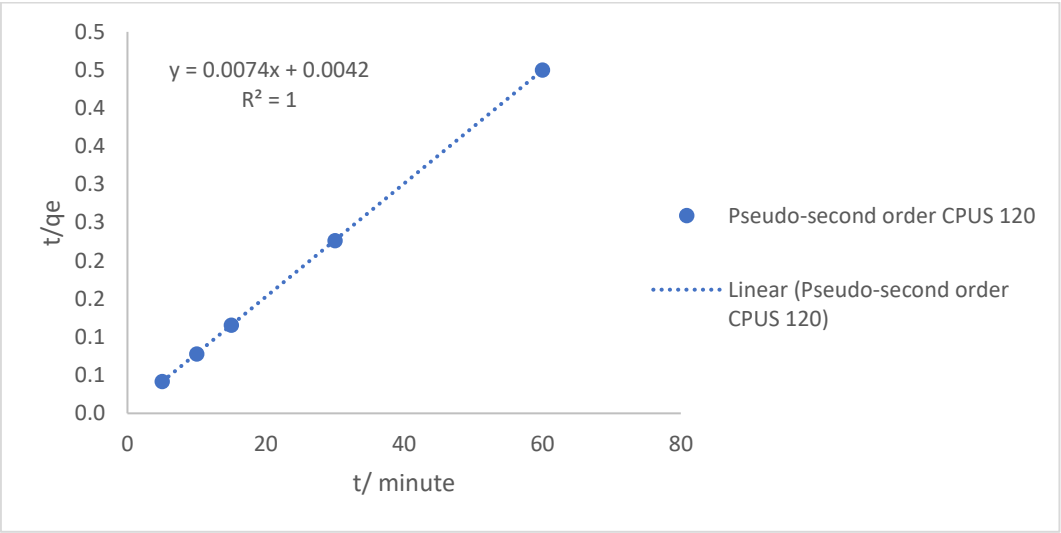

A) Plot t/q_e vs t of *pseudo*-second order CPUS 120

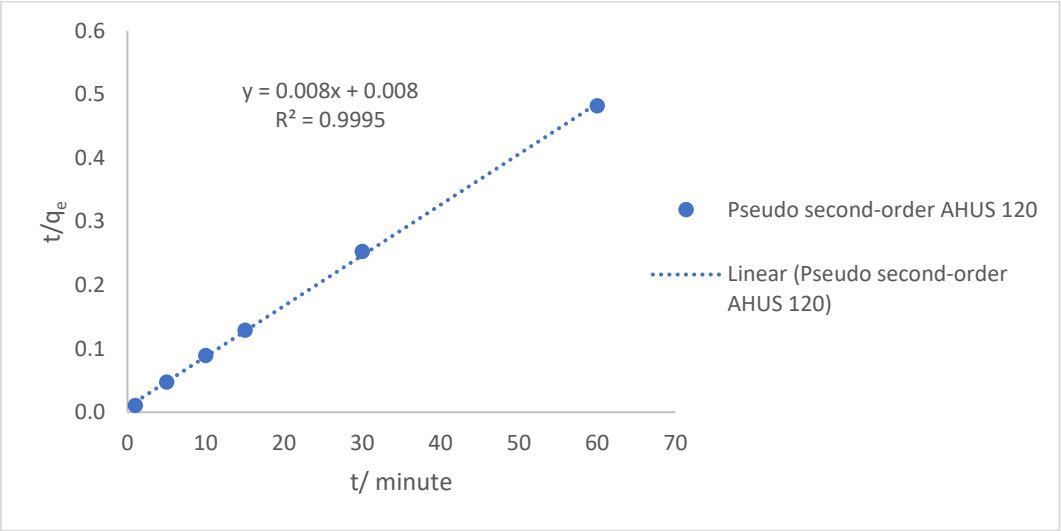

B) Plot t/q_e vs t of *pseudo*-second order AHUS 120

Figure A. 11 A) Plot t/q_e vs t of *pseudo*-second order for CPUS 120 (A) and AHUS 120 (B)

Appendix XII. Thermodynamic parameter plot of CPST 120, AHST 120 and ACST

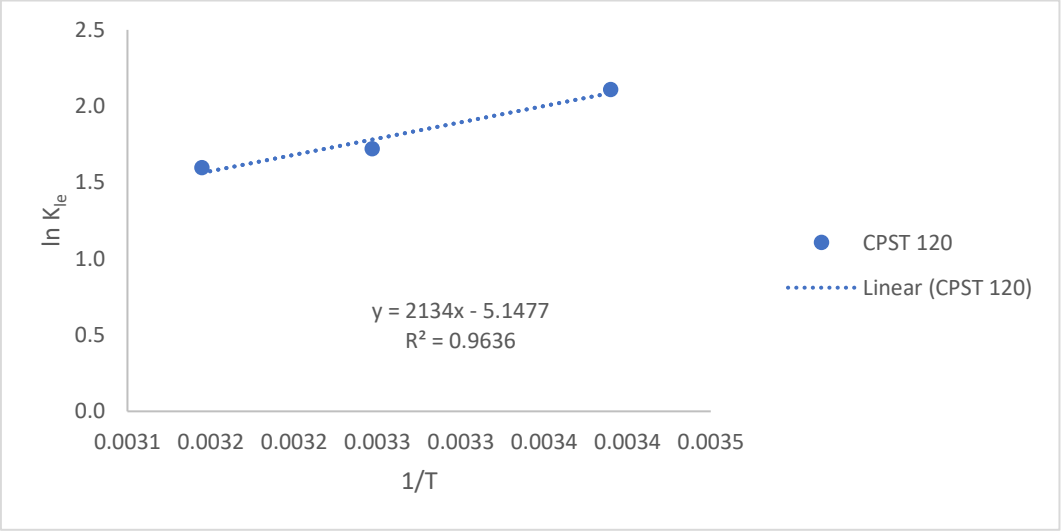

A) Plot ln K_{le} vs 1/T for thermodynamic parameters CPST 120

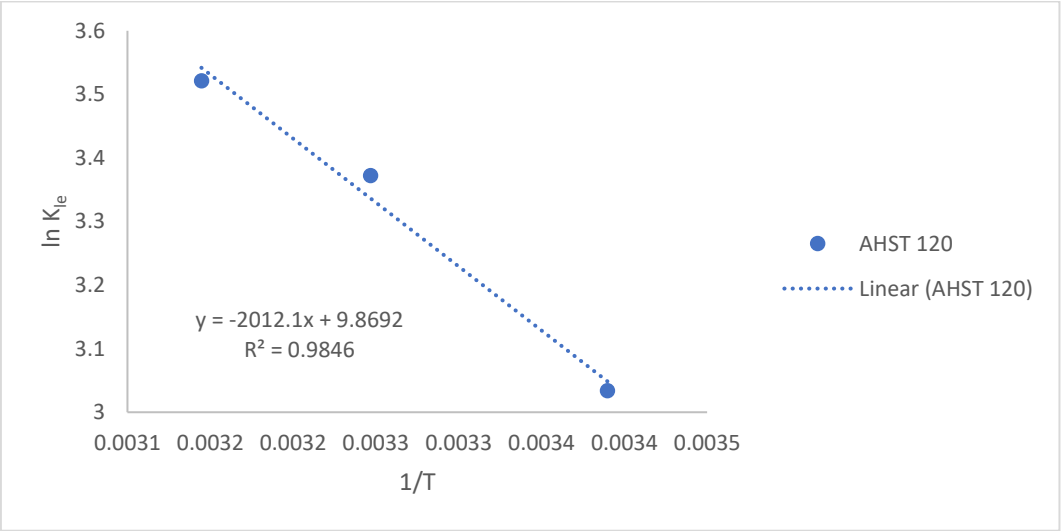

B) Plot ln K_{le} vs 1/T for thermodynamic parameters AHST 120

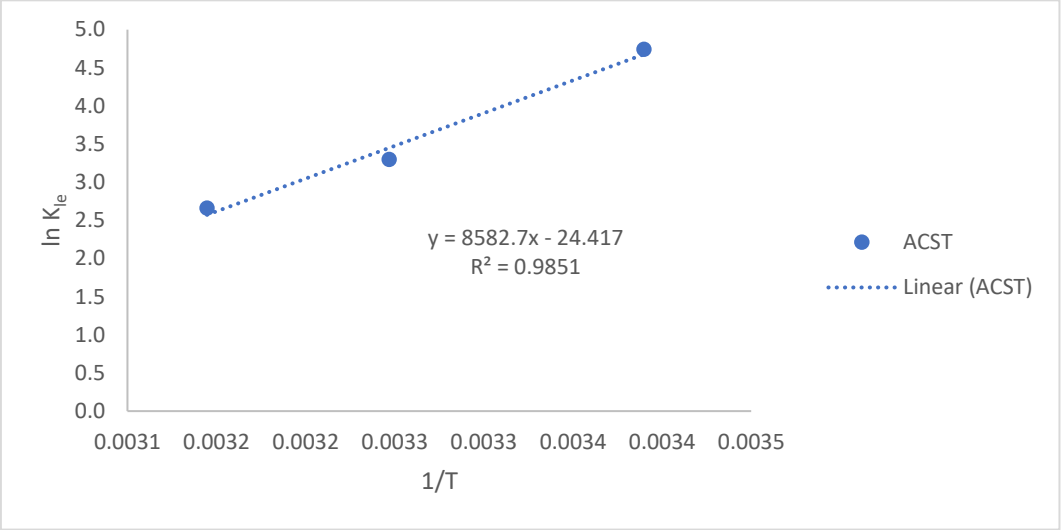

C) Plot ln K_{le} vs 1/T for thermodynamic parameters ACST

Figure A. 12 Plot ln K_{le} vs 1/T for thermodynamic parameters of CPST 120 (A), AHST 120 (B) and ACST (C) (Original in colour)

Appendix XIII. Cassava peel and almond hull chars

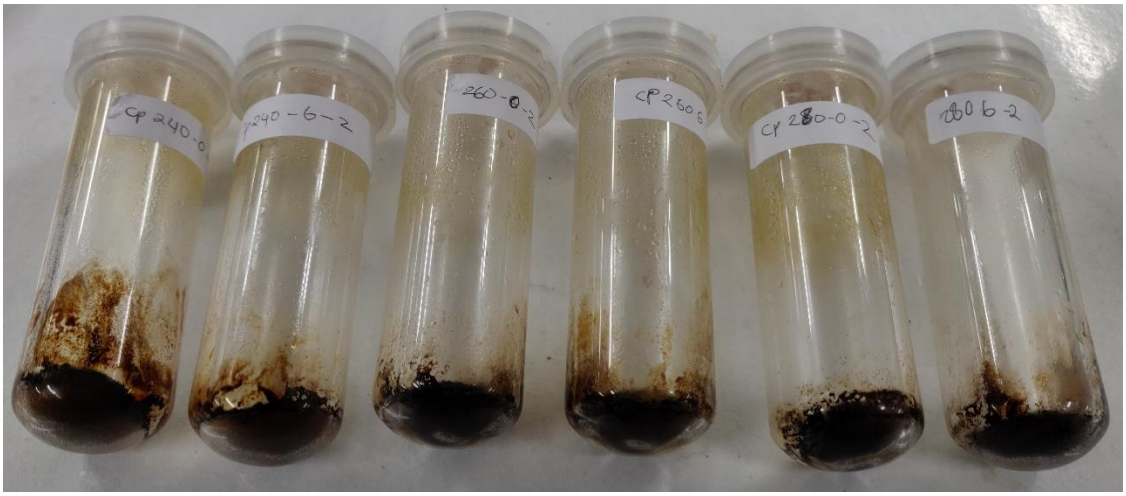

A) Cassava peel char from microwave pyrolysis processing
(T:240 °, 260 °and 280 °C t: 0 and 6 mins)

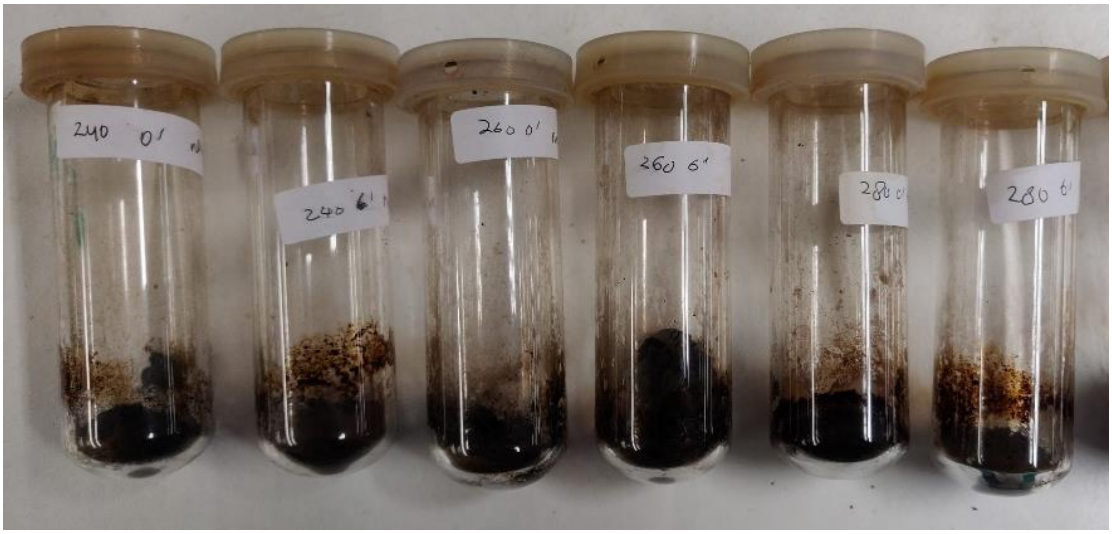

B) Almond hull char from microwave pyrolysis processing
(T:240°, 260 °and 280 °C t: 0 and 6 mins)

Figure A. 13 Cassava peel (A) and almond hull (B) biochar produced from conventional microwave pyrolysis (Original in colour)

Abbreviations

AC – Activated carbon

ADF - Acid detergent fibre

ADL - Acid detergent lignin

AH – Almond hull

AHET - Almond hull ethanol pre-treatment

AHHP - Almond hull heptane pre-treatment

ATR-IR - Attenuated total reflectance infrared spectroscopy

B.E – Binding energy

BET - Brunauer–Emmett–Teller

BJH - Barrett–Joyner–Halenda

C2C - Cradle to the grave

c.a - *circa*

CHN - Carbon, hydrogen and nitrogen analysis

CI -Crystallinity index

CMC - cellulose microfibril

CNC - Cellulose nanocrystal

CNF -Cellulose nanofibril

CP – Cassava peel

CPET – Cassava peel ethanol pre-treatment

CPHP - Cassava peel heptane pre-treatment

CP-MAS - Cross polarization magic angle spinning

CTAB - Cetyltrimethylammonium bromide

DP - Degree of polymerization cellulose

D-R - Dubinin-Radushkevich

DTGA - Derivative thermogravimetric analysis

e.g.- exempli gratia

EC - European committee

EDTA - Ethylenediaminetetraacetic acid

EU - European Union

FAO - Food and Agriculture Organization

FT-IR - Fourier Transform Infrared Spectroscopy

GC-MS -Gas chromatography-mass spectroscopy

GHG - Greenhouse gases

HHV - Higher heating value

HMT- Hydrothermal microwave treatment

HPLC - High-performance liquid chromatography

HPLC - High-performance liquid chromatography

i.e.- id est

L/W - Length /Width

MB - methylene blue

MFC -Microfibrillated cellulose

n.a – not applicable

NB - nota bene

NDF - Neutral detergent fibre

NMR - Nuclear magnetic resonance

SDG - Sustainable development goals

SEM- Scanning electron microscopy

ST - Stirring mode

TAPPI - Technical association of the pulp and paper industry

TEM - Transmission electron microscopy

TEMPO - 2,2,6,6-Tetramethylpiperidine-1-oxyl radical

TGA - Thermogravimetric analysis

US - Ultrasound mode

WRAP - Waste and resources action programme

XPS - X-Ray photoelectron spectroscopy

XRD - X-ray diffraction